Universitat
deGirona

IRON AND IRIDIUM MOLECULAR COMPLEX FOR WATER OXIDATION CATALYSIS

Zoel CODOLÀ DUCH

DOCTORAL THESIS

Iron and Iridium molecular complexes for water oxidation catalysis

Zoel Codolà Duch

2014

Doctoral programme in Chemistry

Supervised by: Dr. Julio Lloret Fillol and Dr. Miquel Costas Salgueiro

Tutor: Dr. Miquel Costas Salgueiro

This manuscript has been presented to opt for the doctoral degree from the
University of Girona

Universitat de Girona

Dr. Miquel Costas Salgueiro and Dr. Julio Lloret Fillol, of Universitat de Girona,

WE DECLARE:

That the thesis entitled Iron and Iridium molecular complexes for water oxidation catalysis, presented by Zoel Codolà Duch to obtain a doctoral degree, has been completed under our supervision and meets the requirements to opt for an International Doctorate.

For all intents and purposes, I hereby sign this document.

Dr. Miquel Costas Salgueiro   Dr. Julio Lloret Fillol

Girona, 5 de Juny de 2014

FULL LIST OF PUBLICATIONS

This thesis is based on a compendium of the following publications:

Chapter III

Highly Effective Water Oxidation Catalysis with Iridium Complexes through the Use of NaIO$_4$. Codolà, Z., M. S. Cardoso, J., Royo, B., Costas, M., Lloret-Fillol, J. Chem. Eur. J 2013, 19, 7203-7213. (Impact factor: 5.831, position 21/152 in Chemistry, multidisciplinary, 1st quartile)

Chapter IV

Efficient water oxidation catalysts based on readily available iron coordination complexes. Fillol, J. L., Codolà, Z., Garcia-Bosch, I., Gómez, L., Pla, J. J., Costas, M. Nat. Chem. 2011, 3, 807-813. (Impact factor: 21.757, position 3/152 in Chemistry, multidisciplinary, 1st quartile)

Chapter V

Electronic Effects on Single-Site Iron Catalysts for Water Oxidation. Codolà, Z., Garcia-Bosch, I., Acuña-Parés, F., Prat, I., Luis, J. M., Costas, M. , Lloret-Fillol, J. Chem. Eur. J 2013, 19, 8042-8047. (Impact factor: 5.831, position 21/152 in Chemistry, multidisciplinary, 1st quartile)

Chapter VI

Evidence for an Oxygen Evolving Fe–O–Ce Intermediate in Iron-Catalysed Water Oxidation. Codolà, Z. Gómez, L., Kleespies, S.T., Lawrence Q., Costas, M., Lloret-Fillol, J. Submitted to *Nature Communications* in 2014. (Impact factor: 10.015, position 3/56 in multidisciplinary sciences, 1st quartile)

LIST OF ABBREVIATIONS

μ-Mebbp	6,6"-(4-methyl-1H-pyrazole-3,5-diyl)di-2,2'-bipyridine
12-TMC	1,4,7,10-tetramethyl-1,4,7,10-tetraazacyclododecane
13-TMC	1,4,7,10-tetramethyl-1,4,7,10-tetraazacyclotriecane
AB	Acid-Base
acac	acetyl acetonate
ADP	Adenosine diphosphate
ATP	Adenosine triphosphate
ATR	Attenuated total reflectance
bpfxc	5, 15-bis-(pentafluorophenyl)-10-(2,7-di-tert-butyl-5-carboxy-9,9-dimethyl-9H-xanthene-4-yl)corrole
bpi	pyridine-2-ylmethyl
bpp	3,5-bis(2-pyridyl)pyrazolate
bpy	2,2'-bipyridine
btpyan	1,8-bis(2,2':6',2''-terpyridyl)anthracene
CAN	$[Ce^{IV}(NH_3)_6(NH_4)_2]$
cod	1,5-cyclooctadiene
Co-Pc	Cobalt phthalocyanine
Co-Po	Co-porphirin
Cp*	1,2,3,4,5-pentamethylcyclpentadiene
CSI-HRMS	High resolution mass spectrometry with a cryospray attachment
CV	Cyclic Voltammetry
D1	One of the two protein subunits that form the reaction core of the PSII. Donor site.
D2	One of the two protein subunits that form the reaction core of the PSII. Acceptor site.
DC	Direct Coupling
dCIP	2,6-dichlorophenolindophenol
deep	4,4'-bis(ethoxy-carbonyl)-2,2'-bipyridine
DFT	Density functional theory
DIQ-bpy	N,N-bis[(isoquinolin-1-yl)methyl][6-(pyridin-2-yl)pyridin-2-yl]methanamine
DLS	Dynamic Light Scattering
DPA-bpy	N,N-bis(2-pyridinylmethyl)-2,2'-bipyridine-6-methanamine
DPV	differential pulse voltammetry
EDS	Energy-dispersive X-ray spectroscopy
EDX	Energy-dispersive X-ray spectroscopy
EPR	Electron Paramagentic Ressonance spectroscopy
ESI-MS	Electrospray Mass Spectrometry
ET	Electron Transfer
EXAFS	Extended X-ray Absorption Fine Structure
Fd	Ferrodoxine
FNR	Ferrodoxin-NADP$^+$ reductase
FT-IR	(Fourier Transform) Infrared spectroscopy
GC-MS	Gas chromatography–mass spectrometry
H$_2$cppd	1,4-bis(6'-carboxylate-pyrid-2'-yl)-pyridazine acid
H$_2$cpph	1,4-bis(6'-carboxylate-pyrid-2'-yl)-phtalazine acid

Hbpp	2,2'-(pyrazole-3,5-diyl)dipyridine
Hedta	ethylenediaminetetraacetic acid
His	Histidine residue
HOMO	Highest occupied molecular orbital
ICP-MS	Inductively coupled plasma mass spectrometry
ITO	$Sn^{IV}O_2$-doped In_2O_3
k^2,C^2,C^2-NHC	k^2,C^2,C^2-1,3-diphenylimidazol-2-ylidene
KIE	Kinetic isotopic effect
LUMO	Lowest unoccupied molecular orbital
mcbpen	*N*-methyl-*N'*-carboxymethyl-*N,N'*-bis(2-pyridylmethyl)ethane-1,2-diamine
mcp	*N,N'*-dimethyl-*N,N'*-bis(2-pyridylmethyl)-cyclohexane-1,2-diamine
Me_2NHC	N-dimethylimidazolin-2-yldiene
$^{Me2}Pytacn$	1-(2'-pyridylmethyl)-4,7-dimethyl-1,4,7-triazacyclononane
Me_6tren	tris(N,N'-dimethylaminoethyl)amine
MeCN	CH_3CN
men	*N,N'*-dimethyl-*N,N'*-bis(2-pyridylmethyl)-ethane-1,2-diamine
$^{Me}Py_2tacn$	1-(di(pyridin-2-yl)methyl)-4,7-dimethyl-1,4,7-triazacyclononane
MOF	Metal-Organic Framework
N4Py	N,N-bis(2-pyridylmethyl)-N-(bis-2-pyridylmethyl)amine
$NADP^+/NAPH$	Nicotinamide adenine dinucleotide phosphate
Nafion	sulfonated tetrafluoroethylene based fluoropolymer-copolymer
NaPi	phosphate buffer
NHC	N-heterocyclic carbene
NMR	Nuclear Magnetic Resonance
NP	Nanoparticles
OEC	Oxygen Evolving Complex
OECD	Organization for Economic Cooperation and Development
OTf	CF_3SO_3 anion
Oxone	potassium peroxysulfate
P680	PSII Primary Donor
P700	PSI Primary Donor
$PaPy_3H$	*N,N*-bis(2-pyridylmethyl)-amine-*N*-ethyl-2-pyridine-2-carboxamide
PCET	Proton Coupled Electron Transfer
pdp	*N,N'*-bis(2-pyridylmethyl)-2,2'-bipyrrolidine
Ph	Pheophytin
pic	Picolyl ligand
POM	Polyoxometalate
ppm	Part per milion
ppy	2-phenylpyridine
PQ_x	Plastoquinone x
PS	Photosensitizer
PSI	Photosystem I
PSII	Photosystem II
PTCBI	3, 4, 9, 10-perylenetetracarboxylic acid bisbenzimidazole
py	pyridine

PY5	2,6-bis(bis(2-pyridyl)methoxymethane)pyridine
qpy	qpy = 2,2':6',2'':6'',2'''-quaterpyridine
RDS	Rate determining step
rR	Resonance Raman Spectroscopy
S_{0-4}	Different redox states of the Kok cycle
salpd	propane-1,3-diylbis(salicylideneiminate
SHE	Standard Hydrogen Electrode
Sl	N,N'-Bis(salicylidene)ethylenediaminecobalt (II)
Slp	N,N'-bis(salicylaldehyde)-1,2-phenylenediamine
SO	Sacrificial Oxidant
STEM	Scanning transmission electron microscopy
TAML	tetraamido macrocyclic ligand
tBu-OOH	tert-butyl hydrogen peroxide
TDMImp	5,10,15,30-tetrakis-(1,3-dimethylimidazolium-2-yl)porphyrin
TEM	Transmission Electron Microscopy
terpy	2,2':6',2'' - terpyridine
TG/DTA	thermogravimetric/differential thermal analyses
TGG	triglycylglycine
TMC	1,4,8,11-tetramethyl-1,4,8,11-tetraazacyclotetradecane
TMPyP	tetra-(N-methylpyridyl)porphyrinato
TOF	Turnover frequency
TON	Turnover number
TPA	tris(2- methylpyridyl)amine
tpfc	tpfc = 5, 10, 15-tris(pentafluorophenyl)corrole
tpym	tris-(2-pyridyl)methane
USD	United States dollar
UV-Vis	Ultraviolet-Visible spectroscopy
WO	Water Oxidation
WOC	Water Oxidation Catalyst
XANES	X-ray Absorption Near Edge Structure
XAS	X-ray absorption spectroscopy
XPS	X-ray photoelectron spectroscopy
XRD	X-ray diffraction
Yz	Tyrosine residue
η	Overpotential

LIST OF FIGURES

refluxing in MeOH (Right).[196] [a] Light-driven conditions ([Ru(bpy)$_2$(deeb)][PF$_6$)$_2$ as PS and Na$_2$S$_2$O$_8$ as SO, in NaPi buffer, pH 7.2) 76

LIST OF TABLES

LIST OF SCHEMES

ACKNOWLEDGEMENTS

GRAPHICAL ABSTRACT

Chapter IV. Efficient water oxidation catalysts based on readily available iron coordination complexes (p.123)

$$H_2O + 4Ce(IV)$$

WOC

$$O_2$$

$$4Ce(III) + 4H^+$$

$$H_2O$$

Chapter V. Electronic effects on single-site iron catalysts for water oxidation (p.133)

$$2 H_2O \qquad O_2 + 4H^+$$

E

-NO$_2$
-CO$_2$Et
-Cl
-H

Increase in Reactivity

$$4 Ce^{IV} \qquad 4 Ce^{III}$$

Chapter VI. Evidence for an oxygen evolving Fe–O–Ce intermediate in iron-catalysed water oxidation (p.143)

electron aceptor

Tyr$_z$

-e

Lewis acid

-e

electron aceptor

Lewis acid

Chapter VII. Results and discussion (p.165)

Chapter VIII. General Conclusions (p.205)

ANNEX (p.209)

TABLE OF CONTETNS

SUMMARY

Harness light from the sun is one of the major goals towards the substitution of fossil fuels. Nature has developed a sophisticated system to store the radiant energy in the chemical bonds of the carbohydrates, through water and carbon dioxide. This process has been perfected for millions of years and the development of an artificial system to replicate the natural photosynthesis is extremely challenging. Towards the design of these energy conversion schemes based on sunlight a key step is the water oxidation. The water oxidation provides the electrons needed for the production of fuel. However, an efficient catalyst is required to overcome the uphill energy transformation required for this multi-electronic transfer.

Initially, we focused our attention on the 3rd row transition metal Iridium, which is a well-established robust and efficient metal for the water oxidation. A carbene-type family of compounds has been studied with the aim to find some keys to unravel mechanistic details and structural preferences which benefits the oxidation of water.

Nevertheless, state of the art of molecular catalysts using abundant metals such as manganese, cobalt, copper and iron constitute ideal models for catalyst development based on abundant and benign metals. Elucidation of the active species and the O-O bond formation mechanism mediated by these metals is key for the rational catalyst design. Therefore, first row transition metals have been employed for preparing coordination compounds with well-known oxidative robust ligands. Iron complexes of this kind have been previously studied in C-H and C=C oxidation reactions, and in this thesis they have been proved to be excellent catalysts for the water oxidation, exhibiting turnover numbers >350 and >1000 using Ce^{IV} and $NaIO_4$ respectively. Isotopic-labeling experiment evidenced that all of the O_2 was exclusively originated from water, and the negligible amounts of CO_2, together with the absence of nanoparticles indicated that no major oxidation of the ligand takes place, in favor to a homogeneous mechanism. Also the systematic tuning of the electronic effects on $[Fe(OTf)_2(^{Me2}Pytacn)]$ impacted directly on the water oxidation efficiency, reinforcing the molecular nature of the complexes operating in a homogeneous phase.

Mechanistic studies and characterization of intermediates have been pursued, with the final aim of understanding the requirements for the design improved iron-based catalysts. The characterization by high resolution mass spectrometry (CSI-HRMS) and resonance Raman spectroscopy (rR) of a novel oxo-bridged iron-cerium complex constitutes the first direct observation of a heterodimetallic core in a synthetic WO catalyst. These species can be construed as the closest structural and functional model for the essential heterodimetallic Mn^V–O–Ca^{II} center involved in the water oxidation event in PSII.

RESUM

L'aprofitament de la llum com a font d'energia és una de les alternatives més prometedores per tal de substituir els combustibles fòssils. La natura ha desenvolupat un sofisticat sistema d'emmagatzematge d'energia solar en els enllaços químics dels carbohidrats, mitjançant H_2O i CO_2. Aquest procés ha sigut perfeccionat al llarg de milions d'anys. Per tant, el desenvolupament de sistemes artificials capaços d'imitar la fotosíntesi natural és extremadament complicat. De camí cap al disseny de sistemes per a la conversió d'energia lumínica, un pas clau és l'etapa d'oxidació de l'aigua. L'oxidació de l'aigua proporciona els electrons necessaris per la producció de combustible. Malauradament, la presència d'un catalitzador és necessària per superar aquesta transformació multielectrònica, ja que requereix una elevada energia.

Inicialment, vam focalitzar l'estudi en l'Iridi, metall de la 3ª sèrie de transició ben establert com a catalitzador robust i eficient per l'oxidació d'aigua. L'estudi d'una família de compostos amb lligands tipus carbè es va dur a terme amb l'objectiu d'identificar aspectes claus per entendre detalls mecanístics i estructurals, beneficiosos per l'oxidació catalítica de l'aigua.

Tot i això, els sistemes catalítics actuals que utilitzen metalls com el manganès, cobalt, coure o ferro constitueixen models ideals pel desenvolupament de catalitzadors basats en metalls abundants i benignes. Entendre quines són les espècies actives i el mecanisme a través del qual es forma l'enllaç O-O són passos clau cap al disseny racional de catalitzadors. Per tant, s'han utilitzat metalls de la 1ª sèrie de transició per preparar complexos de coordinació amb lligands resistents a medis oxidants. Complexos de ferro com els que utilitzarem en aquesta tesi, ja havien sigut prèviament estudiats com a catalitzadors per l'oxidació d'enllaços C-H i C=C. Aquí es demostra que també són competents per a l'oxidació d'aigua, exhibint un elevat nombre de cicles catalítics, >350 i >1000 en presència de Ce^{IV} i $NaIO_4$ com a oxidants de sacrifici. L'estudi mitjançant marcatges isotòpics evidencia que l'oxigen generat prové exclusivament de l'aigua. La quantitat negligible de CO_2 i l'absència de nanopartícules són indicatius d'una oxidació mínima del lligand, fet que suggereix un mecanisme homogeni. L'efecte directe en l'eficiència del catalitzador al modular els efectes electrònics mitjançant la modificació del lligand del complex $[Fe(OTf)_2(^{Me2}Pytacn)]$, reafirma la homogeneïtat del procés.

Finalment s'han realitzat estudis mecanístics i de caracterització d'intermedis amb l'objectiu d'entendre aspectes claus per a la millora dels catalitzadors de ferro. La caracterització mitjançant espectrometria de masses d'alta resolució (CSI-HRMS) i ressonància Raman, ha permès detectar un nou dímer de ferro-ceri unit per un pont oxo. Aquesta és la primera observació directa d'un centre heterodimetàl·lic en un catalitzador d'oxidació de l'aigua, el qual constitueix el model estructural i funcional més proper al centre de Mn^V-O-Ca^{II} present en el PSII.

RESUMEN

El aprovechamiento de la luz como fuente de energía solar es una de las alternativas más prometedoras para sustituir los combustibles fósiles. La naturaleza ha desarrollado un sofisticado sistema de almacenamiento de energía solar en los enlaces químicos de los carbohidratos, mediante agua y CO_2. Este proceso ha sido perfeccionado a lo largo de millones de años. Por lo tanto, el desarrollo de sistemas artificiales que imitan la fotosíntesis natural es extremadamente complejo. De camino al diseño de sistemas para la conversión de energía lumínica, una etapa clave es la oxidación del agua. Oxidar la molécula de agua proporciona los electrones necesarios para la producción de combustible pero la presencia de un catalizador es estrictamente necesaria para superar esta transformación multielectrónica, la cual requiere una elevada energía.

Inicialmente, focalizamos la investigación en el Iridio, metal de la 3ª series de transición bien establecido como catalizador robusto y eficiente para la oxidación de agua. El estudio de una familia de compuestos con ligandos tipo carbeno se llevó a cabo con el objetivo de localizar puntos mecanísticos y estructurales claves para la oxidación catalítica del agua,

Los sistemas catalíticos actuales que utilizan metales como el manganeso, cobalto, cobre o hierro constituyen modelos ideales para el desarrollo de catalizadores basados en metales abundantes i benignos. Entender cuáles son las especies activas y el mecanismo a través del cual se forma el enlace O-O, son pasos clave hacia el diseño racional de catalizadores. Por lo tanto, se han utilizado metales de la 1ª serie de transición para preparar complejos de coordinación con ligandos resistentes a la oxidación. Complejos de hierro como los utilizados en esta tesis ya habían sido previamente estudiados como catalizadores para la oxidación de enlaces C-H y C=C. Aquí se demuestra que también son competentes para la oxidación de agua, con un elevado número de ciclos catalíticos, >350 i >1000 en presencia de Ce^{IV} y $NaIO_4$. El estudio mediante marcaje isotópico indica que el oxígeno generado proviene exclusivamente del agua. La cantidad despreciable de CO_2 i la ausencia de nanopartículas indican una menor descomposición del ligando, a favor de un mecanismo homogéneo. El impacto directo en la eficiencia del catalizador al modular los efectos electrónicos mediante la modificación del ligando del complejo $[Fe(OTf)_2(^{Me2}Pytacn)]$ sostiene la homogeneidad del proceso.

Finalmente se han realizado estudios mecanísticos y de caracterización de intermedios con el objetivo de comprender aspectos calves para la mejora de los catalizadores de hierro. La caracterización mediante espectrometría de masas de alta resolución (CSI-HRMS) i resonancia Raman, ha permitido detectar un nuevo dímero de hierro-cerio unido por un puente oxo, que consiste en la primera detección de un centro heterodimetálico en un catalizador de oxidación de agua. Esta especie se puede concebir como el modelo estructural i funcional más cercano al centro de Mn^V-O-Ca^{II} presente en el PSII.

CHAPTER I.

GENERAL INTRODUCTION

I. GENERAL INTRODUCTION

I.1.   World Energy Demand

Fossil fuels reservoirs are becoming extinct. The increase of the energy demand expected for the following years (**Figure I.1**, left), led by a fast expansion of population and the increase of energy consumption by the non-OECD[*] members (Organization for Economic Cooperation and Development) (**Figure I.1**, right), combined with the current largest economic growth makes the present energetic system unmaintainable.[1] Tightly connected to the fossil fuels exploitation is the global warming, consequence of the emissions of greenhouse gases. The increase of the CO_2 concentration in the atmosphere is behind the raise of global surface temperature during the last century, 0.74 ± 0.18 °C, and is causing new extreme weather patterns, the rise of the sea level, expansion of deserts and retreat of the glaciers.
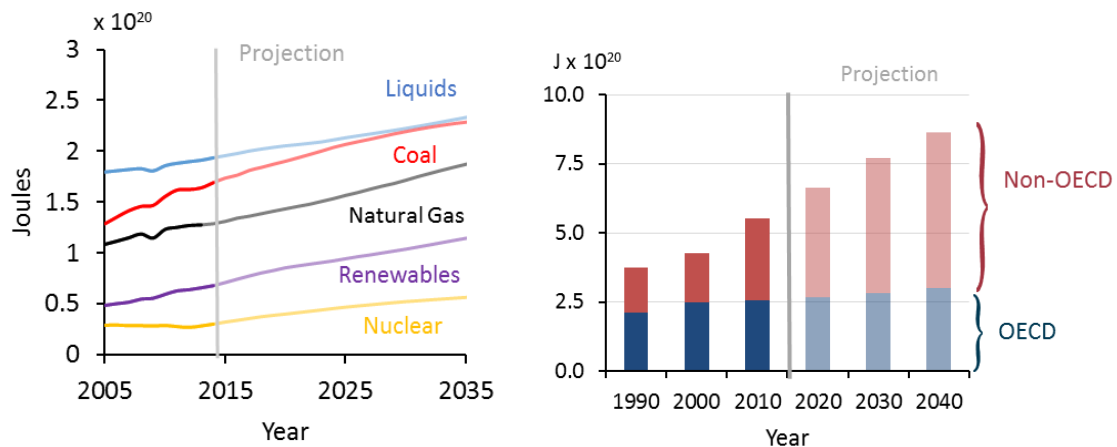
Figure I.1. Left) Projection of world energy use by fuel type, 2005-2030. Energy consumption (in Joules) comprises commercially traded fuels only. Excluded are fuels such as wood, peat and animal waste which are unreliably documented in terms for consumption statistics. Right) Projection of the worldwide energy consumption of OECD and non-OECD members. Adapted with permission from IEO2013.[1]

Therefore, carbon-neutral and sustainable fuels, economically comparable to the current ones, are required to achieve the fossil fuels substitution in large scale. Due to its availability and density, solar energy is an optimum energy source, but the development of amenable production of renewable free-CO_2 energy carriers is still required. The Earth insolation resource base exceeds all other renewable energy sources combined and it is exploitable in mostly all planet regions. On a clear day, ~1 kJ·s^{-1}m^{-2} can strike the surface. Nevertheless, the requirement of a permanent supply is a difficult task because of the day/night cycles of energy production. To overcome the out-of-phase sunlight energy consumption/production, a convenient energy storage system is

---

[*] OECD member countries (January 2014): Australia, Austria, Belgium, Canada, Chile, Czech Republic, Denmark, Estonia, Finland, France, Germany, Greece, Hungary, Iceland, Ireland, Israel, Italy, Japan, Korea, Luxembourg, Mexico, Netherlands, New Zealand, Norway, Poland, Portugal, Slovak Republic, Slovenia, Spain, Sweden, Switzerland, Turkey, United Kingdom, United States.

required. Extensive efforts are currently being devoted to improve the methods to harvest and store the sunlight to achieve a really efficient, low-cost, non-wasting, and sustainable energy source. Among the proposals for the energy storage, chemical bonding is envisioned as one of the most promising alternatives due to its high energy density, being Natural Photosynthesis a mechanism to reflect on.

I.2. Light Harvesting And Energy Storage In Nature: The Photosynthesis

Nature through the so-called Photosynthesis is able to harvest the energy of the sun and store it into carbohydrates by reducing carbon dioxide (**See Equation I.1**) using water as the primary source of electrons and protons. The photosystem consists in 2 main mechanisms, the light reactions and the light-independent reaction, forming together a very complex machinery. In the light reactions, 3 enzymes embedded in the thylakoid membrane of the chloroplasts of higher green plants, algae, and cyanobacteria are involved; Photosystem II (PSII), Cytochrome b_6f and Photosystem I (PSI) (**Figure I.2-3**).[2,3] PSII is the first enzyme involved in the light-dependent reactions and its role is to provide electrons for the reduction of plastoquinone (PQ, quinone-type molecule located in the chloroplast) to plastoquinol (PQH_2), as well as protons to help in the creation of a proton gradient for the synthesis of ATP. Cytochrome b_6f catalyzes the electron transfer from PQH_2 to plastocyanin (PC, a Cu-containing protein), linking the two light-dependent enzymes, whereby introducing protons into the thylakoid space. Finally, PSI uses light energy to mediate the electron transfer from plastocyanin to ferredoxin (Fd, an iron-sulfur protein), which in turn reduces $NADP^+$ to NADPH. In addition, the proton gradient created across the chloroplast membrane is used by ATP synthase for the concomitant synthesis of ATP (**Equation I.2**). NADPH and ATP will be consumed to transform the atmospheric carbon dioxide into carbohydrates by the Calvin cycle (**Figure I.3**, **Equation I.3**). This reserves energy into the primary energy-store, i.e. carbohydrates, which are consumed when recombined with O_2. The electronic recovery of the mechanism is achieved by oxidizing water, a process taking place in PSII (**Figure I.2**). More in-depth into the PSII, its core consists of a two homologous subunits, D1 and D2 proteins. During the photosynthesis, the surrounding light harvesting complexes (chlorophyll and carotenoids, LHC2) capture photons (**Figure I.2,top**), provoking their excitation and delivers the energy by resonance energy transfer through a linked network of those antenna molecules to the reaction center P_{680} (in LHC1, the PSII core in **Figure I.2**), a chlorophyll dimer. The charged chlorophyll complex ($P_{680}*$) is quenched by transferring one electron (becoming P_{680}^+) to a nearby pheophytin (Ph, the primary acceptor), located in D2 (the acceptor side) and then, by several electron transfer events reduces plastoquinones PQ_A and PQ_B (PQ, **Figure I.2**)

which further transfers electrons to the plastocyanin (**PC, Figure I.2**) in Cyt.b_6f and to the Ferrodoxin-NADP$^+$ reductase in PSI (FNR).
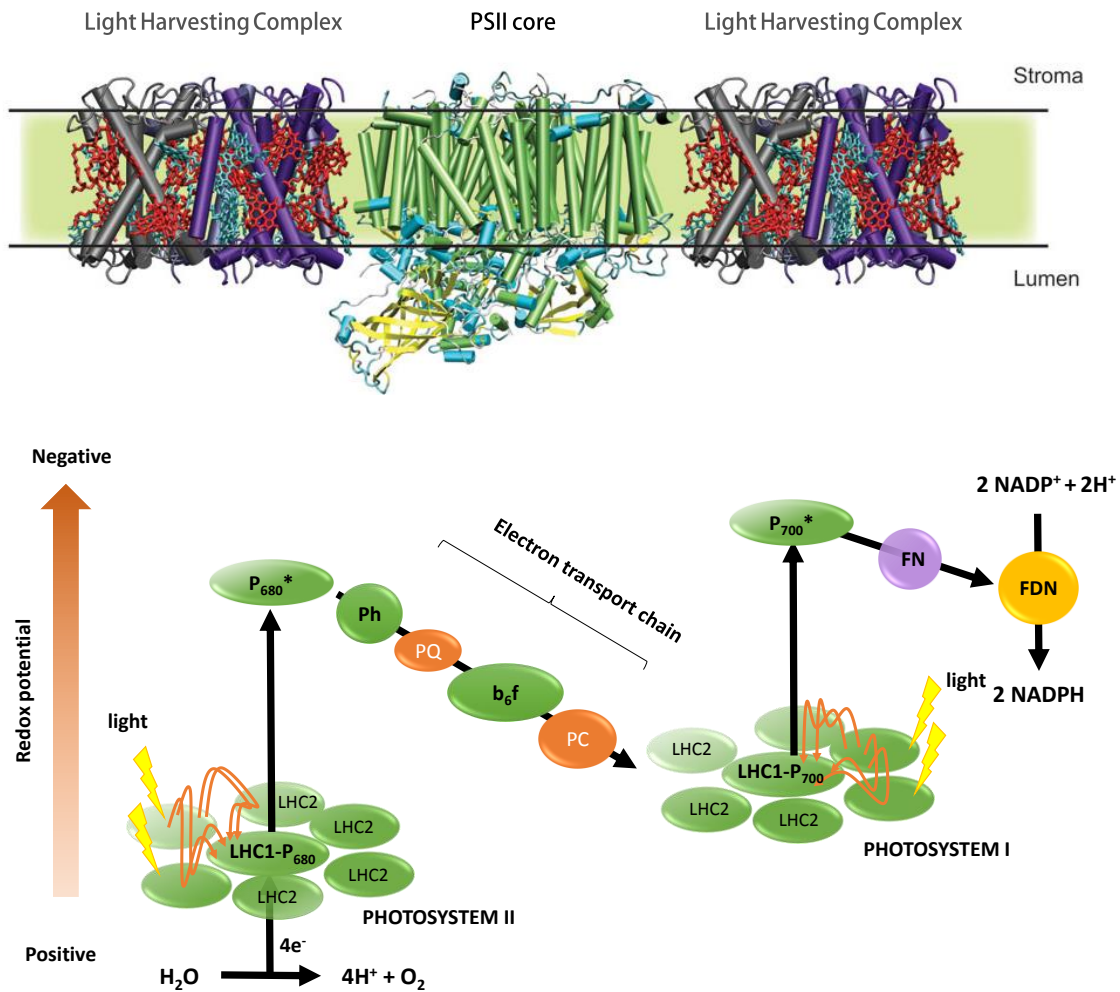
Figure I.2. Top, two light harvesting complexes (LHC2) surrounding the PSII core (LHC1), which contains proteins D1, D2, as well as the OEC. Image reproduced, with permission, from *Nature Chem.*.[4] Bottom, the "Z-scheme" of the photosynthesis describes the oxidation/reduction changes during the light dependent reactions for the synthesis of NADPH. The vertical axis represents the reduction potential of a particular species. Ph = Pheophytin, PQ = Plastoquinone, PC = Plastocyanin, b_6f = Cytochrome b_6f, FN = ferredoxin, FDN = Ferrodoxin-NADP$^+$ synthase, LHC2 = light harvesting complex, LHC1-P_{680} and P_{700} = light harvesting complexes containing reaction centers, located in PSII and PSI respectively.

PQH_2 will be reoxidized to PQ by releasing two protons into the thylakoid lumen. In the donor side (D1) positive charge is delivered to the Yz (Tyrozine-161) to restore P_{680}, resulting in a tyrosine radical (Yz$^\bullet$) and a proton. Yz$^\bullet$ will finally oxidize a metalloenzyme known as the oxygen evolving complex (OEC) which can store up to four oxidizing equivalents, until reduced by the oxidation of a water molecule.[5]

$$(1) \qquad H_2O + CO_2 \xrightarrow{h\nu} [CH_2O] + O_2$$

$$(2) \qquad 2H_2O + 2NADP^+ + 3ADP + 3P_i \xrightarrow{h\nu} 2H^+ + O_2 + 2NADPH + 3ATP$$

$$(3) \qquad 6CO_2 + 18ATP + 12NADPH + 12H_2O \longrightarrow C_6H_{12}O_6 + 18ADP + 18P_i + 12NADP^+ + 6H^+$$
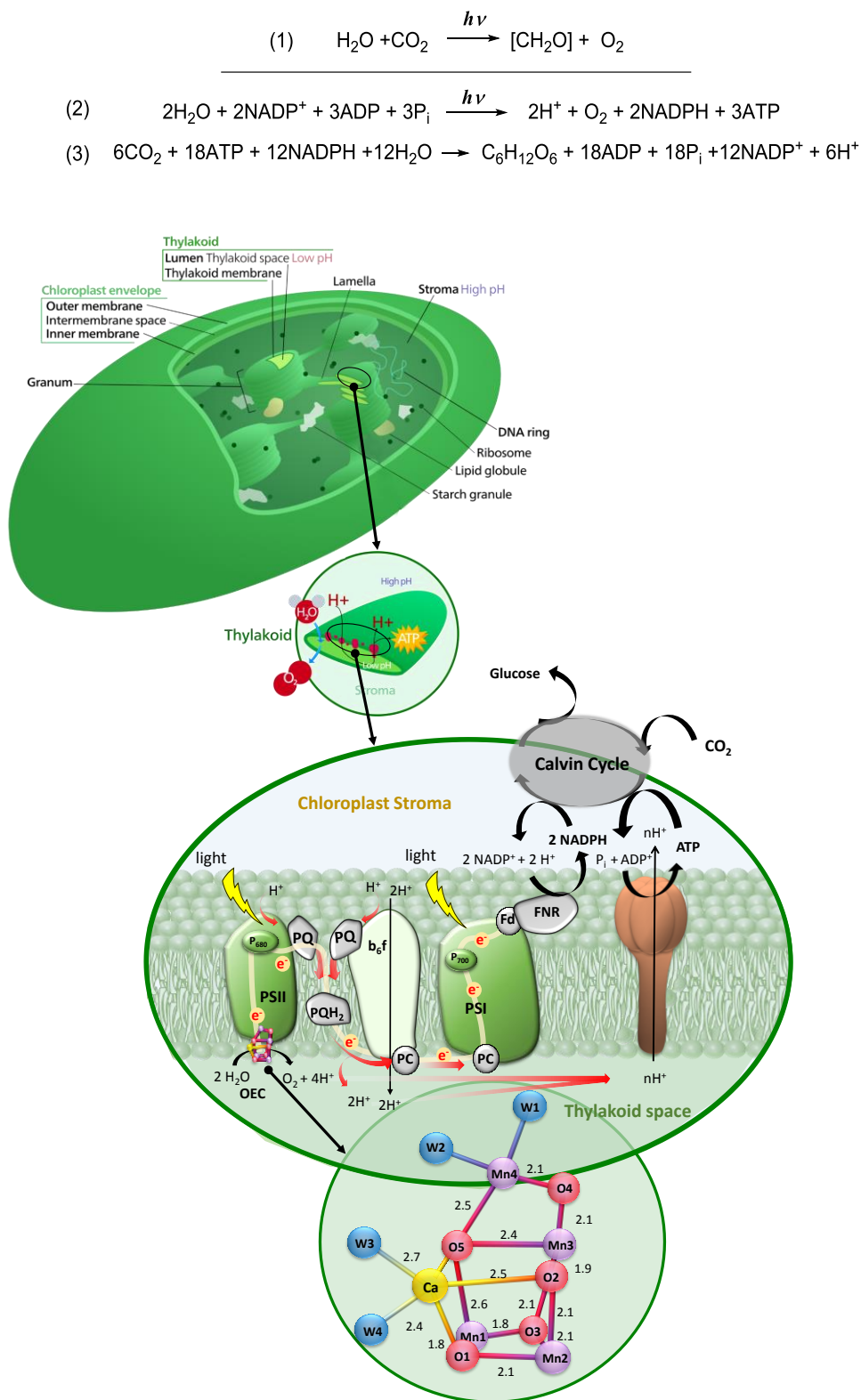
Figure I.3. Schematic diagram of a green-plant chloroplast (top) and magnification of the thylakoid membrane and the oxygen evolving complex (OEC). Manganese atoms (purple) and calcium (yellow) are bonded by oxo bridges (red). Bonds lengths (in angstroms) were calculated from X-ray data.[6] Four water molecules (in blue) were observed close to the cluster (2.1 and 2.4 Å).

To reproduce the photosynthesis artificially is one of the most ambitious scientific goals of our society. However a better understanding of the essential components is still required to produce efficient artificial photosynthesis schemes: i) the light harvest, ii) the charge separation, iii) the water oxidation, iv) the proton and electron transport and v) the CO_2 fixation. Because multiple electronic and protonic stages are required for the CO_2 reduction and the H_2O oxidation, these charge-transfer steps bottlenecks the development of efficient artificial photosynthesis. Indeed, the production of H_2 or $CO/CH_3OH/CH_4$ from H^+ or CO_2 as energetic storage molecules provides a simple alternative to the dark process in the photosynthetic scheme, being the proton reduction (**Equation I.5**) the easier process to achieve.[7] Therefore, water oxidation could (**Equation I.6**) plays a crucial role in the exploitation of the sunlight towards the design of efficient water splitting (**Equation I.4**, global equation) systems.

$$(4) \quad 2H_2O \xrightarrow{h\nu} 2H_2 + O_2 \qquad \begin{array}{l} \Delta G^o = 4.92 \text{ eV} \\ (113 \text{ Kcal·mol}^{-1}) \end{array}$$

$$(5) \quad 4H^+ + 4e^- \longrightarrow 2H_2$$

$$(6) \quad 2H_2O \longrightarrow O_2 + 4H^+ + 4e^-$$
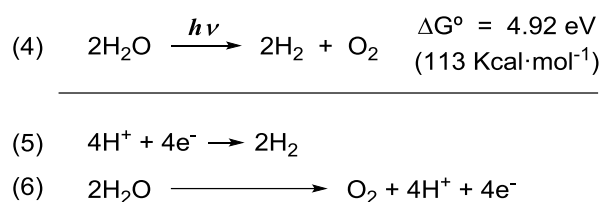
I.2.1 The Oxygen Evolving Complex

In Nature, the OEC is the leading actor of the water oxidation, producing oxygen (byproduct of the reaction) in a rate above 300 O_2 molecules·s^{-1} (per unit of OEC).[8] This manganese complex placed in the LCH1 in PSII can store up to four oxidizing equivalents from tyrozine (Yz), while building up the sufficient oxidizing power to oxidize water and recover the initial state. This sequential redox process is known as Kok cycle and consists in 5 stages (S-states): four oxidizing equivalents collection (from S_0 to S_4) and a light-independent O_2 release ($S_4 \rightarrow S_0$), being S_1 (2 Mn^{III}, 2 Mn^{IV}), the dark-stable state. There is still controversy about how the O-O bond formation takes place and the oxidation states of the Mn atoms at S_4. Proposals are i) the nucleophilic attack of the water to a highly electrophilic $Mn^V=O$ species (or Mn^{IV}-oxyl radical), and ii) the coupling reaction between a biradical.[9] The two mechanisms differ upon formation of the S_3-state. For the biradical coupling pathway an additional water molecule must bind to the cluster, triggering an expansion of the structure. The additional water substrate forms the oxyl radical in S_4 (Siegbahn model).[10]

Nowadays, the catalytic structure of the OEC remains elusive. In 2004, a cubane Mn_3O_4Ca cluster bridged by oxo atoms and connected with the fourth Mn via one of the μ-oxo groups was reported by Ferreira and coworkers.[11] Afterwards, different positions of metal ions and ligands were determined with high precision energy density maps.[12] Following concerns that the OEC is being reduced during data collection, Extended X-ray Absorption Fine Structure (EXAFS) experiments with lower X-ray exposure were performed. Nevertheless the large amount

of metal atoms in the OEC difficult data interpretation and three possible geometries were proposed by Yano *et al.*[13] A recent publication reported the most accurate crystal structure determination ever performed of PSII, with a resolution of 1.9Å, where a distorted cubane-like Mn_3O_4Ca cluster remains as the most plausible conformation of the OEC, which is bound to an additional manganese atom by and oxo bridge that fulfill the oxygen evolving center cluster (Mn_4O_5Ca, **Figure I.2**).[6] In the OEC surrounding, molecules of water were found coordinated to the metal centers and linking the Mn cluster to the Yz and the last one to a nearby histidine (D1-His 190). D1-His190 seems to play a crucial role on the photosynthesis providing an exit pathway for protons and rendering the water oxidation process thermodynamically favorable ($\Delta G = -8.4 kcalmol^{-1}$).[14] Despite the high precision, authors admit that data is still insufficient in order to reveal the detailed structure of the water splitting catalytic center. Indeed, distances obtained by X-ray crystallography and EXAFS are slightly different, suggesting that the cluster may also suffer from photoreduction by radiation and the data does not represent exclusively the structure of the S_1-state, but a superposition of reduced states.[10]

Because of its technological relevance, major research efforts are currently on going to unravel the mechanism of the OEC and to develop artificial photosystems and heterogeneous photocatalytic materials to imitate its reactivty.[15,16] Due to the extreme oxidizing chemistry associated with the oxidation of water, the OEC is not playing alone in this task. Indeed, surrounding protein residues mediates the water oxidation by modulating the redox potentials and providing exit pathways for the substrate and products.[17] PSII orchestrates the whole catalytic reaction dealing with the inevitable side-reactions (leaks) occurring when O_2 is present. Diverse self-healing mechanism has been well-developed by Nature to prevent over-oxidation due to the formation of superoxides, peroxides and singlet oxygen, which can damage nearby organic species.[18,19] This feature represents a major issue for the development of a synthetic and stable functional model. Thus, artificial water oxidation becomes a complicated reaction to mimic using a simple, synthetic, non-proteic catalyst but because of its revolutionary impact in the field of renewable energies, its development has become an attractive challenge for the scientific community.

I.3. Basic Considerations For The Development Of Artificial Water Oxidation Catalysts

I.3.1 Electrolysis of water

The oxidation of water molecules (the oxygen formally is O^{2-}) could yield mainly to six different products: hydroxide radicals, oxyl radicals, hydrogen peroxide, hydrogen superoxide, oxygen and ozone. Its standard potentials at pH = 0 *vs* SHE are included in **Scheme I.1**.[20-25] The

most thermodynamically favorable product of the water oxidation is the 4 electron oxidation to O_2 (1.23 V), which under standard conditions (1 bar, 25ºC) and considering the expansion of the produced gas (O_2) the thermodynamic potential required is 1.48 V.[26] The very high potential required for the ideally-uncatalyzed stepwise water oxidation make the process energetically inefficient and economically unfeasible. Therefore, the use of a catalyst is absolutely required to accomplish the reaction at a lower potential and high rate, and hopefully close to the thermodynamic energetic parameters of the 4-electron water oxidation to O_2.
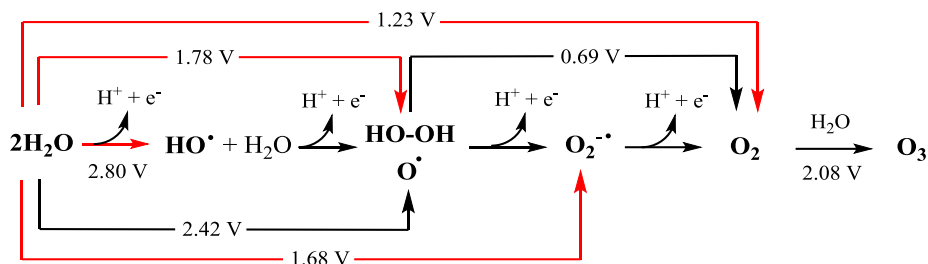
Scheme I.1. Standard reduction potentials *vs* SHE at pH 0.0 for the oxidized species produced during the electrolysis of water. The O_2 Latimer diagram is highlighted in red.

I.3.2 Catalyst design

Towards the research of the optimum catalyst for the water oxidation, some critical aspects must be considered: i) the water oxidation reaction is a multi-step redox process, and redox active compounds would be ideal platforms to assist this process by storing oxidizing equivalents and avoid the formation of very reactive radical products. While only selected organic compounds have suitable redox properties,[27] metal oxides and coordination complexes opens a broad spectrum of possibilities. In addition, the accumulation of oxidizing power by the catalyst can be very much helped by stepwise proton-coupled electron-transfer (PCET) processes, which lowers the thermodynamics by avoiding highly charged intermediates. Moreover, the presence of multiple redox active sites (e.g. OEC-PSII) could prevent a high accumulation of positive charge by sharing it through each one of the redox sites. For coordination complexes, ligands can also play a very important role by stabilizing the different oxidation states of the redox metal cores. Indeed, a high valent intermediate can be partially stabilized by ligands with a high charge density donor character (basic ligands). Anionic donor ligands are the paradigm to achieve a great stabilization of the high oxidation states; however they tend to hydrolyze easily. Besides, non-innocent ligands can be very helpful to delocalize the positive charge and store it out from the metal center, facilitating the accumulation of oxidizing equivalents. Nevertheless, careful must be taken to do not overstabilize the high valent M=O species, otherwise the O-O bond formation would be hampered. A right balance between redox potential and reactivity has to be found for a specific system.

Organic ligands present the important drawback of being oxidized under the strong oxidizing conditions required for the water oxidation yielding considerable structural changes. A recent proposal came up with the idea of using discrete metal-oxides as already oxidized ligands.[28] Group 5 or 6 metals have the proper degree of oxophilicity to generate discrete anionic metal-oxide structures, known as polyoxometalates. This inorganic ligands can be used to form complexes with redox active metals, avoiding the oxidation of the ligand. Nevertheless, it has been observed that these ligands are particularly easily hydrolyzed under the usual catalytic conditions.

A catalytic reaction will be very much helped by a good affinity between the catalyst and the substrate. Thus, oxophilic active sites may facilitate the water oxidation. This trend is reflected in the formation of terminal metal-oxo species. The electronic structures of oxo-metal complexes were introduced by Carl Ballhausen (B) and Harry Gray (G) based on experimental and theoretical investigations, leading to the B&G model.[29] In simple terms, the earliest transition metals (e.g. Ti, Nb, W) forms highly stable metal oxides with relatively inert strong M-O bond. A triple oxo-metal bond is expected for d^0 metals. By filling up electrons into the d orbitals, the π oxo-metal bonds are reduced, as electrons fill the $\pi*$ oxo-metal orbitals to finally lead to a single M-O bond, which is not stable. The impossibility to form the M-O species after electrons fill the $\pi*$ oxo-metal orbitals is what is call the "oxo wall".[30] Therefore, metals from groups 5 to 7 are good candidates for the catalyst design because its M-O species has a great equilibrium between stability and reactivity. Finally, the catalyst topology is also very important to facilitate the O-O bond formation by disposing the metal-oxo to react.

In summary, the ideal catalyst should combine a highly-oxidant core, with a robust and basic ligand which facilitates the O-O bond formation (structurally) and the O_2 release (electronically). Thus, improvements towards an efficient Water Oxidation Catalysts (WOCs) will be very much helped by a detailed mechanistic understanding.

I.3.3 The O-O bond formation step and the dioxygen release

The O-O bond formation can occur via two different pathways: i) a water nucleophilic attack over a highly electrophilic M-O unit, resulting in a $2e^-$ reduction of the metal center (acid base mechanism, **Scheme I.2**, AB) and ii) the interaction of two oxyl-metal radical units (direct coupling, **Scheme I.2**, DC), resulting in a $1e^-$ reduction per metal core. The acid base mechanism is favored by electrowithdrawing ligands which makes the oxo-ligand more electrophilic and therefore more susceptible to suffer the nucleophilic attack of water molecule. Moreover, the assistance of an internal (included on the ligand structure) or external proton acceptor, by binding the water molecule, can be helpful to orientate the attack. On the other hand, the DC mechanism

will be favored by increasing the spin density on the oxygen atoms and by facilitating (electronic and sterically) the dimeric interaction.
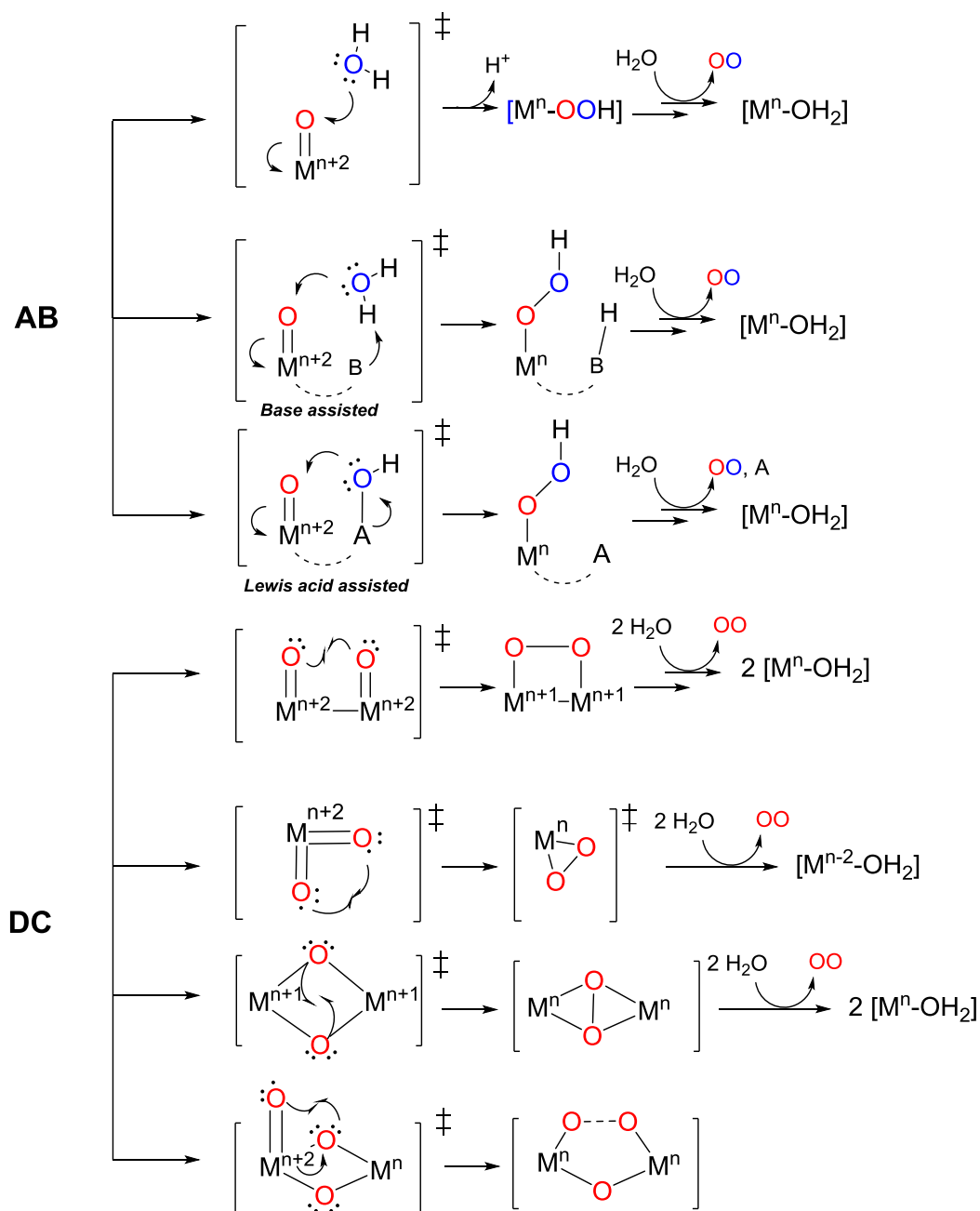
Scheme I.2. Mechanistic proposals for the O-O bond formation in the acid-base (AB) and direct coupling (DC) water oxidation. In the AB mechanism, dashed lines indicates cooperation in both internal (being part of the ligand) or external scenarios.

The reductive elimination of dioxygen is crucial for the recovery of the catalyst and this reaction rate can be also rate determining. The energy barrier for this step can be related to many different factors (electronics, stability of the intermediate, subsequent oxidations). Although, the design of the catalyst needs to facilitate this step, usually is the less energetically demanding.

Once a potential family of catalysts is designed, fast-screening techniques may facilitate the study of their performance as water oxidizing catalysts.

I.3.4 Approaches towards the artificial photosynthesis

In the PSII, Nature uses a complex system that harvest light and release electrons to power the reduction of the plastoquinone. This loss of electrons is compensated by the OEC towards the water oxidation. Focused on the catalytic process occurring in the OEC, water oxidation can be studied by using an oxidant driving force such as electric current, chemical oxidants or photochemical excitation. Advantages of using sacrificial oxidants (SOs) are the straightforward analysis of bulk solutions, the facile measurements of TON and TOF (turnover numbers and turnover frequencies), the fast screenings, the simple methodologies for establishing kinetics, and also the study of the intermediates,[31] which will help in understanding the reaction mechanisms. Oxo-transfer agents such as hypochlorite (ClO^-), Oxone (SO_5^-), periodate (IO_4^-), persulfate ($S_2O_8^{2-}$) and electron-transfer complexes like $[Ce^{IV}(NH_3)_6(NH_4)_2]$ (CAN), $[Co^{III}(NH_3)_5Cl]^{2+}$ or $[Ru^{III}(bpy)_3]^{3+}$ (bpy= 2,2' bipyridine) are common SOs used in WO because of their high oxidation potential, which must be enough to oxidize the water oxidation catalyst (WOC). Because SOs are usually used in large amounts (from 10 to $>10^5$ eq) it has to be considered that oxo-transfer salts can be the real source of oxygen and generally, single electron oxidants (CAN and $[Ru(bpy)_3]^{3+}$) are preferred. Those SOs do not mimic the conditions desired for an artificial photosystem and therefore data obtained must be considered with caution.[31]

Closer to the Nature are systems which work under the presence of photosensitizers (PS) (**Scheme I.3**) and ultimate oxidants as electron acceptors.
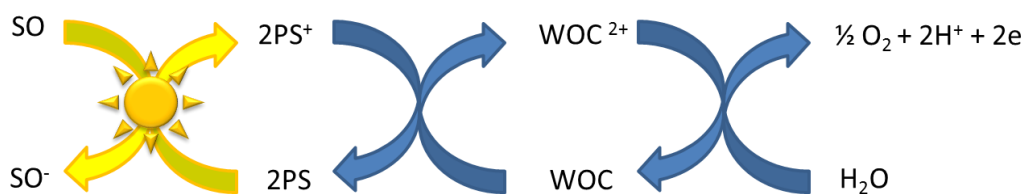
Scheme I.3. Schematic light-driven water oxidation mechanism. SO stands for the sacrificial oxidant (usually $Na_2S_2O_8$) and PS for the photosensitizer (usually $[Ru(bpy)_3]^{2+}$). A first electron transfer is photoinduced by the excitation and oxidation of the PS (PS → PS*→PS$^+$), reducing the SO ($S_2O_8^{2-}$ to SO_4^{2-} and $SO_4^{\cdot\ -}$). The PS$^+$ oxidizes the catalyst, which accumulates four oxidizing equivalents to finally oxidize a water molecule.

After every catalytic cycle, 4 equivalents of protons *per* molecule of oxygen are released, lowering the pH in solution. Because the thermodynamic reduction potential is pH dependent (E = 1.23 - 0.059·pH V *vs* SHE), as more water is oxidized, higher is the potential required. To maintain a constant pH and avoid the activity depletion, it is common to use buffered solutions.

Nevertheless, the possible influence of these buffers in the mechanism or even in the formation of the real catalytic species must be taken into account.

I.4.   State Of The Art: Water Oxidation Catalyst Based On Noble Metals

All the potentials reported herein will be referred vs SHE (standard hydrogen electrode). It's important to consider the pH to make reasonable comparisons among complexes. Besides, TON stands for moles of oxygen produced per moles of added catalyst (or precatalyst) and TOF is the maximum TON per second observed.

During the last 30 years, both homogeneous and heterogeneous water oxidation catalysts (WOCs) have been developed. While heterogeneous materials are nowadays leading the field in terms of potential applicability in devices, the study of homogeneous molecular catalysts is essential for mechanistic understanding, accessing the identification of intermediates and facilitating the kinetic interpretation. Is worth mentioning that differentiation between homogeneous/heterogeneous catalysis in this field has been found particularly difficult, and sometimes, also misleading. The harsh conditions of the reaction usually provokes that homogeneous systems transform into amorphous metal oxides and the true active species are difficult to identify. In this regard, only a limited number of catalysts have been shown to proceed through well-defined molecular entities. This introduction will be focused on well-defined homogeneous systems due to their intrinsic relevance in the WO mechanistic understanding.

Very important discoveries and developments have been achieved in the field of water oxidation and it is notably the exponential growth of activity in the field during the last 10 years (**Figure I.4**). Seminal studies on earth's-scarce ruthenium[32,33] and more recently iridium[34-36] metals, both combined with development of novel organic ligand frameworks, have led to the discovery of highly effective WOCs, with TON and TOF similar to the Natural OEC.[8,37]
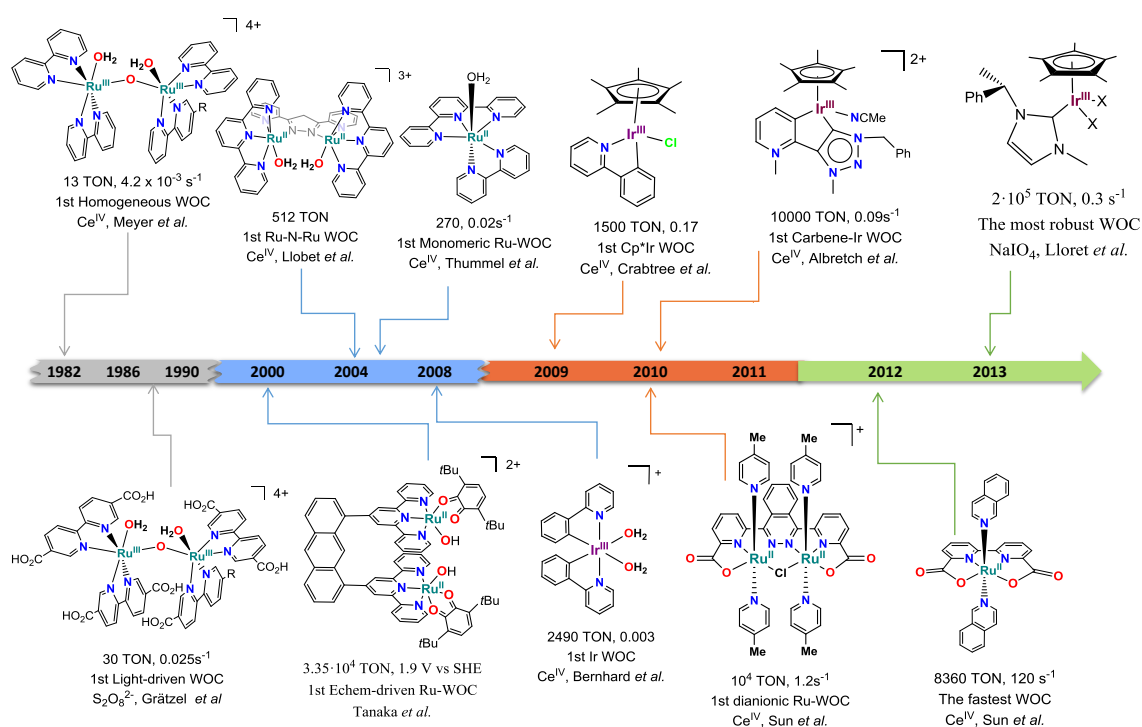
Figure I.4. Time line with the most emblematic Ruthenium and Iridium WOCs. TON, TOF (s⁻¹), relevance of the discovery, sacrificial oxidant and the corresponding author are included. Echem-driven stands for electrochemical driven water oxidation.

I.4.1 Ruthenium Water Oxidation Catalysts

I.4.1.1. Dinuclear Ru-based WOCs

Ruthenium-based catalysts are the most extensively studied systems. A pioneering example of ruthenium homogeneous WOC was reported by Meyer *et al.* in 1982 (**Figure I.5, 1a**).[38,39] The dinuclear complex [Ru$_2$(μ-O)(bpy)$_4$(H$_2$O)$_2$](ClO$_4$)$_4$·4H$_2$O (bpy = 2,2'-bipyridine) known as the "blue dimer" led to oxygen evolution in the presence of CAN as SO in a 0.1 M HClO$_4$ aqueous solution, with a TON value of ca. 13. 4.6 TON of O$_2$ were produced after 2 h of bulk electrolysis at 1.58 V vs SHE (pH 1, TfOH). The analogous phenantroline dimer was also found active. The mechanism for the Ce^{IV}-driven water oxidation catalyzed by the "blue dimer" has been deeply investigated. However, despite the large number of mechanistic studies, there is still controversy in identifying the O-O bond formation pathway. The most supported mechanism is the AB on Ru^{IV,V} or Ru^{V,V}.[40,41] The replacement of bpy by 4,4′-dichloro- or 5,5′-dichloro substituted bpy almost showed the same activity of its predecessor (2.7 TON with CAN, 2 TON at 1.54 V vs SHE)[42] but the key improvement was the inclusion of carboxylic groups in the 5',5' positions of the bipyridine, which lowered the WO-onset† to 1.3-1.4 V (**Figure I.5, 1b**). For the thermal water oxidation, up to 75 TON were reported by using Co^{3+} ions as electron acceptor

---

† The onset potential is the potential at which the catalytic current starts.

(H_2SO_4 1M). Alternatively to the formation of a $[Ru^V=O]_2$ intermediate (AB pathway), a mechanism involving the formation of a μ-peroxo complex $[Ru_2^{III}-O-O-Ru_2^{III}]$ from $[Ru^{IV}-OH]_2$ was also proposed (DC pathway). Taking advantage of the lower overpotential[‡] of **1b**, light-driven oxygen evolution was achieved in aqueous buffered solution (pH 7) with $[Ru^{II}(bpy_{COMe})_3]^{2+}$ (bpy_{COMe} = 4,4'-dicarboethoxy-2,2'-bipyridine) as photosensitizer and $Na_2S_2O_8$ as a sacrificial electron acceptor with an efficiency of 30 TON.[43]
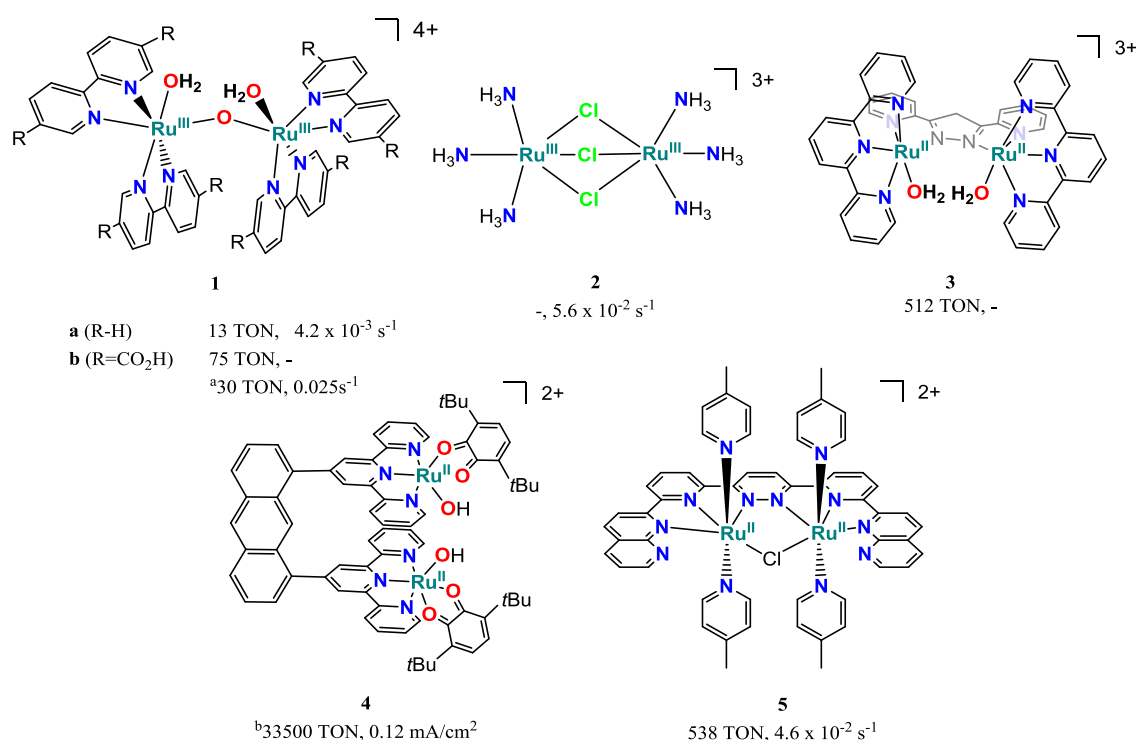
Figure I.5. Selected dimeric Ru complexes active in the water oxidation reaction. TON (moles of O_2 generated per moles of complex) and TOF (TON·s^{-1}) are indicated below the structures when available. TON and TOF values are based on Ce^{IV}-driven water oxidation unless stated. [a] Light driven water oxidation conditions ($[Ru(bpy)_3]^{2+}$ as PS and $Na_2S_2O_8$ as SO). [b] Electrochemical-driven water oxidation, at 1.9 V vs SHE.

Later, in 1999, Kaneko *et al.* found that the simple $[(NH_3)_3Ru(\mu-Cl)_3Ru(NH_3)_3]^{2+}$ (**Figure I.5, 2**) was also an active complex for the water oxidation using Ce^{IV} as oxidant. Parallel to the oxygen evolution (k_{O2} = 5.6 x 10^{-2} s^{-1}), a deactivation pathway involving N_2 production (k_{deac} = 1.4 x 10^2 L·M^{-1}·s^{-1}) was detected and reduced by 17-fold by supporting the catalyst on Nafion.[44] Early attempts to improve the efficiency of μ-oxo diruthenium complexes involved the use of dinucleating ligands. To this end, Llobet and co-workers described a diruthenium complex $[Ru_2^{II}(\mu-OAc)(bpp)(terpy)_2]^{3+}$ (terpy = 2,2':6',2'' - terpyridine), where the two metal atoms were not connected by an oxo-bridged but instead by Hbpp (2,2'-(pyrazole-3,5-diyl)dipyridine) ligand. The aim of this approach was to favor O-O bond formation by means of spatially arranging. The

---

[‡] Overpotential (η) is referred to the difference between the potential experimentally observed for a catalytic event and the thermodynamically determined reduction potential for this process (in this case for the WO, which V_{thermo} = 1.23 - 0.059·pH).

two $[Ru^{IV}(O)]$ atoms were disposed in a manner in which the two putative terminal oxo ligands had the right orientation and in close proximity to favor the direct coupling reactivity.[45] Besides, the lack of oxo bridging ligands (when compared to the blue dimer) was envisioned to prevent the catalyst decomposition by reductive cleavage of the bridge or by the formation of the thermodynamically favored *trans*-dioxo structure. Mechanistic studies with isotopic labelling proved that the O-O bond formation occurs intramolecularly[45] (**Scheme I.4, DC**) and the efficiency in water oxidation attained by this strategy slightly improved the pioneer Meyer's blue dimer. TON was substantially enhanced up to 250 when the catalyst was supported in Nafion.[46] Subsequently, it was reported that under optimized conditions the homogeneous $[Ru_2^{II}(\mu\text{-}Ac)(bpp)(terpy)_2]^{2+}$ catalyst improve up to 512 TON.[47]
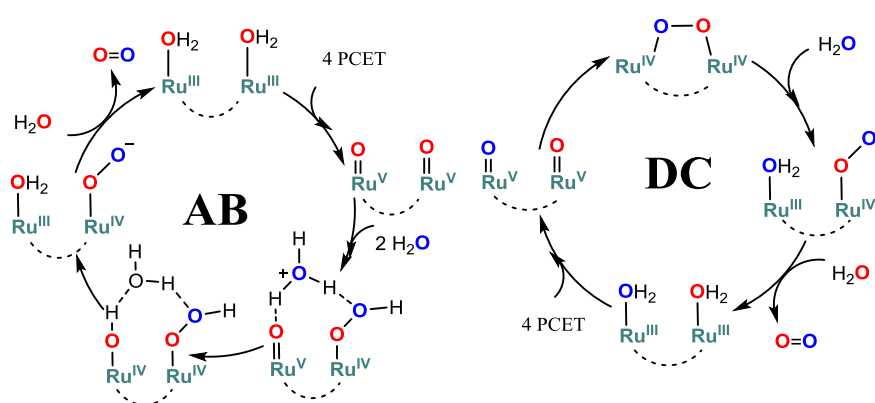
Scheme I.4. Scheme of the two general mechanistic proposals, including the acid base (left)[48,49] and the direct coupling (right, intra or intermolecular) pathways for the O-O bond formation.[50]

Back to 1998, Tsuge and Tanaka reported a $[Ru(OH_2)(quinone)(terpy)]^{2+}$ complex which depending on the pH of the media, the aqua ligand released protons without the formation of a μ-oxo dimer.[51] Taking advantage of this process, the dinuclear complex $[Ru_2(OH)_2(Q)(btpyan)]^{2+}$ (btpyan = (1,8-bis(2,2':6',2''-terpyridyl)anthracene, Q = 3,6-di-*tert*-butyl-1,2-benzoquinone) was designed by linking the terpy backbones to an anthracene moiety (**Figure I.5, 4**) with the aim to achieve two adjacent M=O moieties towards the O-O bond.[52,53] Because the compound was not water-soluble, it was supported on an ITO electrode (indium tin oxide) to study its redox behavior in aqueous media. A strong anodic current was observed at 1.7 V (pH 4) and O_2 was produced until the pH decreased to 1.2 (500 TON). 40 h of electrolysis carried out by readjusting the pH yielded a total TON of 6730. Further optimization and by applying a higher V (1.9 V vs SHE) 33500 TON were obtained. Due to the lack of O_2 production observed for the monomeric compound, the intramolecular DC mechanism was proposed. The authors proposed that the quinone ligand facilitates the Ru-OH oxidation to Ru=O by an intramolecular ET, inducing radical character in the oxo ligand, and facilitating the direct coupling. The resulting Ru-O-O-Ru undergoes two single electron oxidations, a first one localized at the quinone and a second at the

metal, affording a $[(Q)Ru^{III}$-O-O-$Ru^{III}(Q)]^{4+}$, from where O_2 dissociates with concomitant binding of two H_2O molecules to the reduced Ru^{II} centers. The replacement of the quinone by a bpy moiety and the consequent loss of catalytic activity provided a strong argument in favor of the quinone role as redox non-innocent ligand. Surprisingly DFT calculations in gas phase supported a O-O bond formation *via* a DC mechanism where the formal oxidation state of the Ru atoms remains unchanged at +2. $[Ru_2(O_2^-)(Q^{-1.5})_2(btpyan)]^0$ complex was formed by the removal of four protons before the four electron oxidation takes place. From this reduced species, the first 2e⁻ oxidation $([Ru_2(O_2^-)(Q^{-0.5})_2(btpyan)]^{2+})$ occurs at low potentials (0.6 V). Because the second 2e⁻ oxidation was also pure ET, it was required much higher potentials (1.54 V) to yield $[(Ru^{II})_2(O_2^-)(Q)_2(btpyan^{·+})]^{4+}$. From here, the mechanism was closed by the liberation of an O_2 molecule (recovering $[(Ru^{II})_2(Q)_2(btpyan)]^{4+}$).[54] This mechanism is unusual since the single O-O bond formation occurs at lower redox potentials than the subsequent oxidations to yield dioxygen.
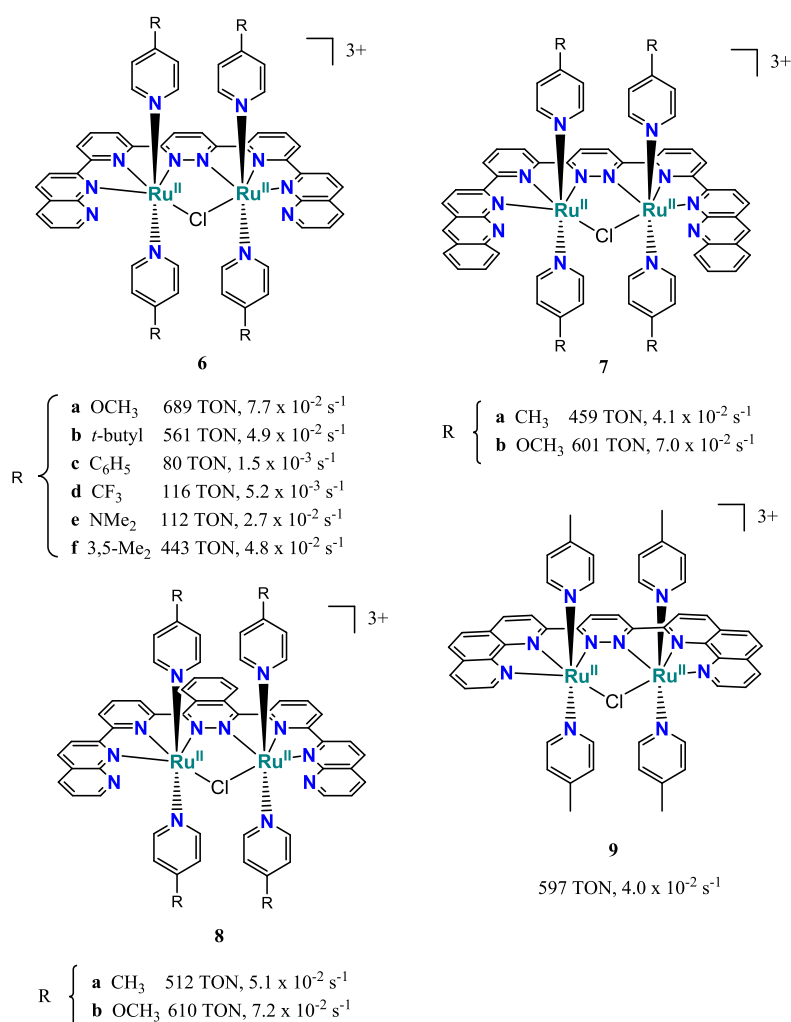
Figure I.6. Dimeric Ru^{2+} WOCs reported by Thummel and coworkers.[55]

Inspired on the alternative structural design of Tanaka and Llobet groups, replacing the labile μ-oxo bridge of the blue dimer for a robust backbone, Thummel and coworkers reported a

series of dimeric Ru^{II} WOCs with neutral bis-tridentate nitrogen-based ligands (**Figure I.5, compound 5**[56] and **Figure I.6**).[55] The two metal cores held in the same plain of the backbone, linked by a chloride bridge. The axial positions were occupied by different monodentate pyridine-based ligands, yielding a facile-tunable family of complexes with two Ru atoms disposed in a *cis*-position to each other. Using CAN as oxidant, TONs between 80-690 and TOFs ranging (0.15-7.7)$\cdot 10^{-2}$ s^{-1} were reported.

More recently, based on the complexes reported by Thummel *et al.* and inspired by the presence of oxygen-rich ligands within the OEC surroundings, Sun and coworkers included a negatively charged biscarboxylato bridge, with the aim to decrease the oxidation potential needed for the WO. This perspective became crucial to enhance the catalytic performance. Complexes $[Ru^{II}_2(cppd)(pic)_6]^+$ (**Figure I.7, 10**, H_2cppd = 1,4-bis(6'-carboxylate-pyrid-2'-yl)-pyridazine acid, pic = 4-picoline)[57] and $[Ru^{II}_2(cpph)(pic)_4(\mu-Cl)]^{2+}$ (**Figure I.7, 11,** H_2cpph = 1,4-bis(6'-carboxylate-pyrid-2'-yl)-phtalazine acid) [58] were synthetized and tested as WOC with CAN as SO. The difference among them resides in the *cis* and *trans* orientation of the two Ru centers. While the O-O bond was facilitated by a DC mechanism for the *cis* complex (**11**) AB or even an intermolecular DC was expected for the *trans* (**10**). Both catalysts were also found active under light-driven conditions (different substituted $[Ru(bpy)_3]^{2+}$ as PSs and $Na_2S_2O_8$ as SO), with TONs ranging 185-370 and 60-580 and TOF values of 0.11-0.26 and 0.1-0.83 s^{-1} (function of the PS) for complexes **10** and **11**, respectively. [58,59] Complex **11** was superior in both Ce^{IV}-driven and light-driven WO because the DC mechanism usually favors a lower onset (against the AB pathway) for the water oxidation.

A similar mechanistic scenario was studied by Llobet and co-workers, using *trans*-$\{[Ru^{II}(tpym)(H_2O)]_2(\mu-bpp)\}(PF_6)_3$ (**Figure I.7, 12**) and *cis*-$\{[Ru^{II}(terpy)(H_2O)]_2(\mu-bpp)\}(PF_6)_3$ (**Figure I.5, 3**) complexes (tpym = tris-(2-pyridyl)methane, bpp = 3,5-bis(2-pyridyl)pyrazolate).[60] Unexpectedly, kinetic studies of the *trans*-Ru-OH$_2$ complex (**12**) pointed towards a second-order behavior on [Ru], indicating a dimeric intermolecular DC. Labelling experiments showed that, when reacting the Ru^{IV}=O dimer with excess of CAN in ^{18}O labelled water the main O$_2$ isotope formed during the first TON was the ^{16}O$_2$ (c.a. 100%). This observation points towards a DC mechanism where a very slow exchange of of the M=O moieties with the oxygen atoms of the water take places, reinforcing the kinetics studies. Is important to notice that the labelling scenario proposed by the authors will only fit for DC scenarios where M=O exchange is below 10%. Indeed, differentiating between AB and DC mechanisms is no longer possible by labelling studies when oxygen exchange reaches 10%.

Later on, the pyrazolate bridge (μ-bpp, complex **3**) was subtle modified (**Figure I.7, 13**, μ-Mebbp = 6,6''-(4-methyl-1H-pyrazole-3,5-diyl)di-2,2'-bipyridine) to improve the complex stability and robustness. TON and TOF, 22.6 and 6.8$\cdot 10^{-2}$ s^{-1} , were slightly enhanced (TON and

TOF for **3** were 18.3 and $1.5 \cdot 10^{-2}$ s^{-1}) under the same conditions, but more interesting, the labelling experiments indicated a change of mechanism, from DC to AB.[61] Due to the *cis*-orientation of the metal cores, this data reveals close activation energy barriers between two O-O bond formation pathways.

Therefore, the design of complexes topologically disposed for a facile intramolecular direct coupling between M=O moieties seems to facilitate the oxygen production. The introduction of anionic ligands improve the catalytic performance while reduces the redox potential required to achieve the oxidation of water under a more appropriate photosynthetic scheme. Besides, the singular electrochemically powered WO shows a very convenient model, yielding high TON in a less oxidative environment, potentials applied are still too high (> 1.7 V) for a further applicability.

10
4740 TON, 0.28 s^{-1}

11
10400 TON, 1.2 s^{-1}

12
9.6 TON, 3.1 x 10^{-2} s^{-1}

13
22.6 TON, 6.8 x 10^{-2} s^{-1}
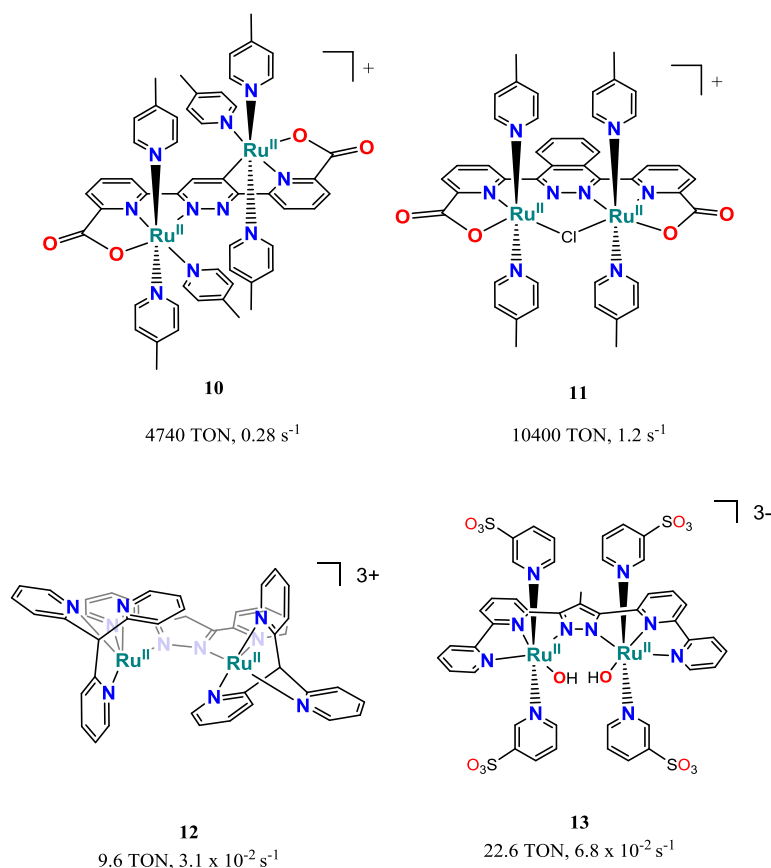
Figure I.7. The most actives dimeric Ru^{2+} WOCs, reported by Sun and coworkers (**10**, **11**) and complexes employed by Llobet and coworkers (**12**, **13**) for mechanistic studies.

I.4.1.2.   Mononuclear Ru-based WOCs

Since the discovery of the blue dimer for the WO, only multi-metallic complexes were found to be good WOCs and thus, it was believed that monomeric complexes were not suitable to carry out the reaction.[62] However, in 2005 Zong and Thummel[56] discovered a monomeric

complex able to oxidize water without entailing two metal-cores for the formation of the O-O bond. The Ru complex (**Figure I.8, 5'**) was synthetized by using 2,2'-(4-(tert-butyl)pyridine-2,6-diyl)bis(1,8-naphthyridine) as the backbone ligand and 4-substitued pyridines occupying the axial positions.[56] A sterically hindered complex, containing 7'-*t*Bu substituted 1,8-naphthyridine ligand afforded the same activity (**Figure I.10**, **28**), suggesting a mononuclear process. In light of this, and because no ligand exchange was detected after the catalysis (^{1}H-NMR, ESI-MS), a tentative mechanism was proposed involving a 7th coordinated Ru^{IV} species generated by the coordination of a water molecule to a highly electrophilic 16e$^-$ Ru^{IV} intermediate. The concomitant 18e$^-$ species was further oxidized to Ru^{VI}=O by the SO and the O-O bond formation took place at the following step. Otherwise, Meyer and Sakai groups independently reported new mononuclear Ru-WOCs ([Ru(terpy)(NN)(OH$_2$)]$^{2+}$ (NN = bpy (Sakai) and NN = 2,2'-bipyrimidine (Meyer)) with aqua ligands. Their mechanistic studies pointed towards an AB mechanism (**Scheme I.4**), where a 6th coordinate [Ru^V=O]$^{3+}$ triggered the O-O bond formation, generating a concomitant Ru^{III}-OOH species. Further oxidation by CAN liberated dioxygen, closing the catalytic cycle.[63-65]

5
538 TON, 4.6 x 10^{-2} s^{-1}

5'
260 TON, 1.4 x 10^{-2} s^{-1}
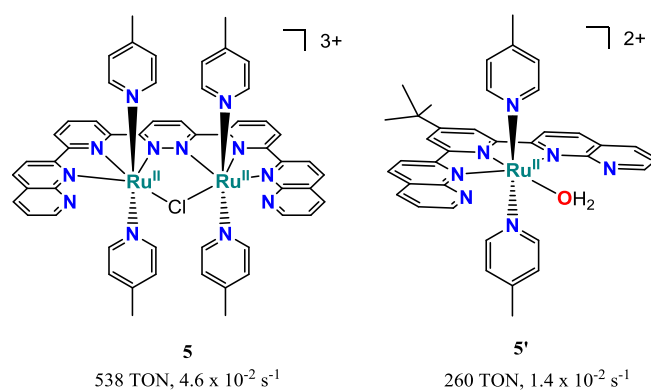
Figure I.8. A chloro-bridged diruthenium complex (**5**) and its analogous monomer (**5'**) reported by Thummel and coworkers.

For [Ru(terpy)(bpy)(OH$_2$)]$^{2+}$ (**14**), the catalytic activity was remarkably improved by including different groups (EtO and MeO) at the 4th position of the terpy moiety (i.e. the 4'-ethoxy substituted complex increased both TON (690) and TOF (1.1·10^{-1} s^{-1})).[66] This improvement was related to the higher basicity of the oxo ligand as well as the lower redox potential required for the formation of the Ru^V=O. Careful examination of the electronic effects on both terpy and bpy moieties indicated a strong correlation between catalyst activity and stability depending on the position and identity of the substituent group on the ligands. Higher TON but lower TOF were achieved by electrowithdrawing groups in the bpy, while electrodonating groups accelerated the rate by decreasing the catalyst robustness.[67,68] However, the contrary effect was observed for the substituted terpy. This was rationalized by the π-backbonding to the most labile group, which was

bpy. Thus, a fine balance between electron density at the metal and π-backbonding to the most labile ligand is key for a fast and robust complex.

In a more elaborated mechanistic proposal, besides the nucleophylic attack of a water molecule the authors contemplated a competing reaction in which O_2 was produced by O abstraction from nitrates (from CAN).[68] This consideration arises from the detection of an unexpected O_2 isotopic distribution (labelling experiments). Due to the detection of NO_2 by laser cavity ring-down spectroscopy and the observation of a prominent signal corresponding to $[Ru(tpy)(bpy)OCe(NO_3)_5]^+$ by ESI-MS, which was fragmented into $[Ru^{III}\text{-}OO]^+$ by MS/MS experiments, the authors concluded that Ce^{IV} ion may play a role in weakening the N-O bond, allowing the O-O bond formation between the ruthenyl species and a nitrate anion.

Modifications on the tridentate (NNN) or bidentate (NN) moieties of the original complex **14a** resulted in a large family of mononuclear [Ru(NNN)(NN)L] compounds (**Figure I.9**) active in catalytic water oxidation.[64,65,69,70,71] In addition, [Ru(NNN)(pic)_2L] complexes as well as [Ru(NNNN)(pic)_2], containing a tetradentate backbone (pic = 4-picoline ligand; NNNN = tetradentate ligand; L = water or halogen, **29**) were also reported active (**Figure I.10**).

$R^1, R^2 = H$ **L**

H$_2$O	270 TON, 1.9 x 10^{-2} s^{-1}	**14a**
Cl	390 TON, 2.0 x 10^{-2} s^{-1}	**14b**
Br	450 TON, 1.5 x 10^{-2} s^{-1}	**14c**
I	570 TON, 1.9 x 10^{-2} s^{-1}	**14d**
4-MePy	135 TON, 0.3 x 10^{-2} s^{-1}	**14e**

$R^1 = t$Bu $R^2 = H$ **L**

Cl	667 TON, 0.6 x 10^{-2} s^{-1}	**14f**
I	701 TON, 7.9 x 10^{-2} s^{-1}	**14g**

$R^1 = H$ $R^2 = t$Bu, L = Cl   218 TON, 0.3 x 10^{-2} s^{-1} **14h**

$R^1, R^2 = t$Bu, L = Cl   94 TON, 0.03 x 10^{-2} s^{-1} **14i**

15-20

L = Cl   R

Me	190 TON, 3.9 x 10^{-2} s^{-1}	**15a** / **15b**
OMe	110 TON, 3.2 x 10^{-2} s^{-1}	**15c**
NO$_2$	260 TON, 3.7 x 10^{-3} s^{-1}	**15d**
CO$_2$Et	570 TON, 8.5 x 10^{-3} s^{-1}	

L = H$_2$O   -, 1.6 x 10^{-2} s^{-1} **16a**

L = Cl   n.d.   **16b**

L = H$_2$O   -, 3.6 x 10^{-2} s^{-1} **17a**

L = H$_2$O   *in*: 8 TON, 2.6 x 10^{-2} s^{-1} **18a**
        out: 14 TON, 5.2 x 10^{-2} s^{-1} **18b**

R^1, R^2

H	400 TON, 0.2 x 10^{-2} s^{-1}	L = Cl	**19a**
H	450 TON, 2.8 x 10^{-2} s^{-1}	L = H$_2$O	**19b**
Me	60 TON, 0.5 x 10^{-2} s^{-1}	L = H$_2$O	**19c**

$R^1 = $Me, $R^2 = $H 155 TON, 0.8 x 10^{-2} s^{-1} L = Cl   **19d**

$N_{trans \text{ to L}}$ L

H$_2$O	**3200 TON**, 1.8 x 10^{-2} s^{-1}	**20a**
Cl	**1170 TON**, 0.1 x 10^{-2} s^{-1}	**20b**
I	**1135 TON**, 2.8 x 10^{-2} s^{-1}	**20c**

$N_{cis \text{ to L}}$ 1 TON, 0.1 x 10^{-2} s^{-1} **20d**

CH   L = Cl

CH$_{cis \text{ to Cl}}$ 66 TON, 0.1 x 10^{-2} s^{-1} **20e**

CH$_{trans \text{ to Cl}}$ 9 TON, 0.5 x 10^{-2} s^{-1} **20f**

L = Cl   n.d.   **21**

21-23

148 TON, 1.0 x 10^{-3} s^{-1} **22**

4.6 TON, 1.0 x 10^{-3} s^{-1} **23**

123 TON, 3.0 x 10^{-3} s^{-1} **24**

Figure I.9. Selected mononuclear ruthenium WOCs type [Ru(NNN)(NN)L] with different polypyridil ligands. TON and TOF are obtained from different literature sources and they are not suitable for comparisons due to the different experimental conditions. CAN was used as SO.

4-MePy	95 TON, 0.2 x 10^{-2} s^{-1}		**25a**
H$_2$O	300 TON, 3.7 x 10^{-2} s^{-1}		**25b**
Cl	370 TON, 0.5 x 10^{-2} s^{-1}		**25c**
Br	140 TON, 0.4 x 10^{-2} s^{-1}		**25d**
I	**378 TON, 16.1 x 10^{-2} s^{-1}**		**25e**

R = H   L

R = tBu, L = Cl   310 TON, 0.4 x 10^{-2} s^{-1} **25f**

350 TON, 2.3 x 10^{-2} s^{-1} **26**

152 TON, 0.8 x 10^{-2} s^{-1} **27**

260 TON, 1.1 x 10^{-2} s^{-1} 416 TON, 2.7 x 10^{-2} s^{-1}
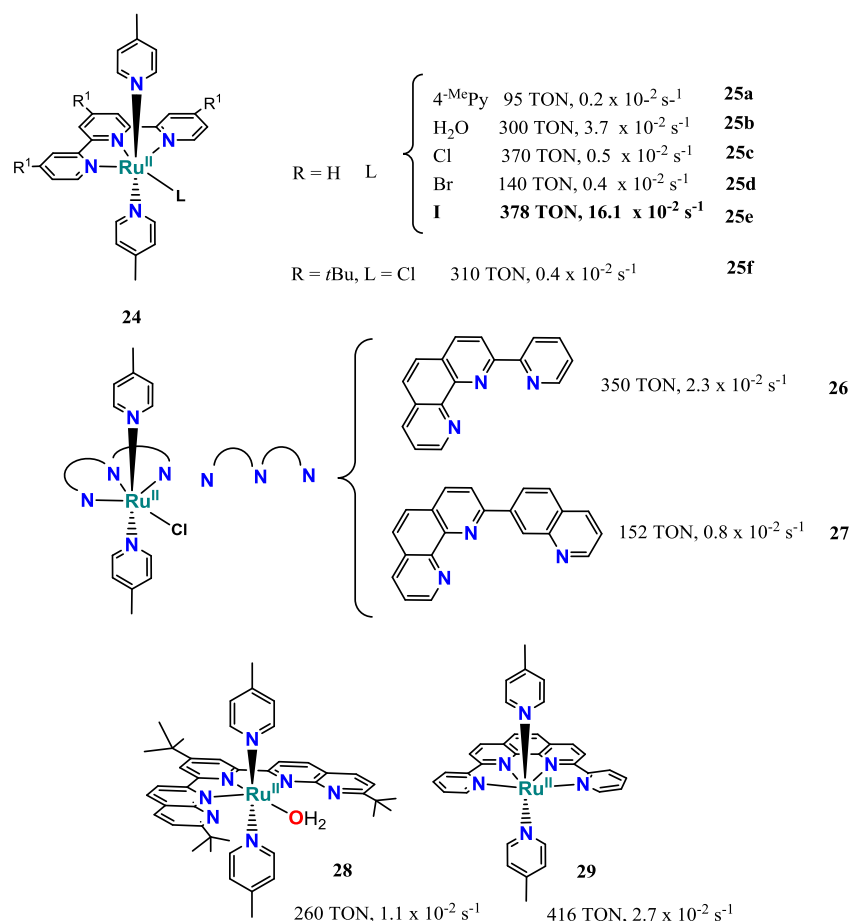
Figure I.10. Selected mononuclear ruthenium WOCs types [Ru(NNN)(pic)$_2$] and [Ru(NNNN)(pic)$_2$] with different polypyridil ligands. TON and TOF are obtained from different literature sources and they are not suitable for comparisons due to the different experimental conditions. CAN was used as SO.

Deeper in the ligand design, Thummel and Fujita found that the topology of an ancillary ligand could be crucial for the water oxidation reaction. While complex **20a** was found highly active, **20d** was not at all, despite having a N atom proximal to the labile position of the complex which can assist the water nucleophilic attack.[72] The role of the axial ligand was studied by Berlinguette and coworkers. While Thummel and coworkers did not observed ligand exchange in **14b** after recover it from a catalytic reaction, ^{1}H-NMR studies showed a clear exchange between Cl and H$_2$O,[65,67] a process that was accelerated at low pH. Thus, the mechanism for **14b** resembles the proposal of Meyer *et al.* instead of undergoing a coordination sphere expansion. Further insight into the mechanism was obtained by Sakai and coworkers. An alternative DFT-based proposal contemplate the possibility of a Ru^V=O - oxo-hydroxocerium(IV) radical coupling path.[73]

But is one site really enough? Recently, complexes [(terpy)(5,5'-X$_2$-bpy)Ru^{IV}(μ-O)Ru^{IV}(terpy)(O)(OH$_2$)]$^{4+}$ (X = H or F, **13**), generated from the dimerization of [Ru^{II}(terpy)(5,5'-X$_2$-bpy)(OH$_2$)]$^{2+}$ and [Ru^{VI}(terpy)O$_2$(H$_2$O)]$^{2+}$, were found efficient and robust WOCs. Slow

dinucleation of the monomeric species was observed under electrolysis. The dimeric Ru_2^{IV} species was fully characterized (by XRD, UV-Vis, Raman spectroscopy and electrochemistry) and its formation was proposed to be initiated by the dissociation of a bpy ligand from its monomer precursor. This process took place when the metal core is oxidized to $Ru^V=O$, due to the strong *trans*-effect of the latter. Then, $Ru^V=O$ was further oxidized to $Ru^{VI}(O)_2$ and reacted with a more reduced Ru center to generate the dimeric species. Electrochemical-driven water oxidation yielded a TOF of 1.2 s^{-1} (monomer) and 0.7 s^{-1} (dimer) and TON of 14930 and 6683 after 10 h respectively (1.8 V *vs* SHE at pH 1). Interestingly, after 8 h of electrolysis, the current density was found similar for both compounds, indicating that the dimer was fully formed from the monomeric species. The dimer ruggedness was impressive, with no sign of fatigue after 10 h. Although the mechanism was proposed to follow an AB pathway in both cases, authors affirm that the presence of two metal cores linked by an oxo bridge was essential to allow a fast ET and release the charge that suffers a single-site complex during the several oxidations. Nevertheless, this was not really reflected in the TOF observed.[74]
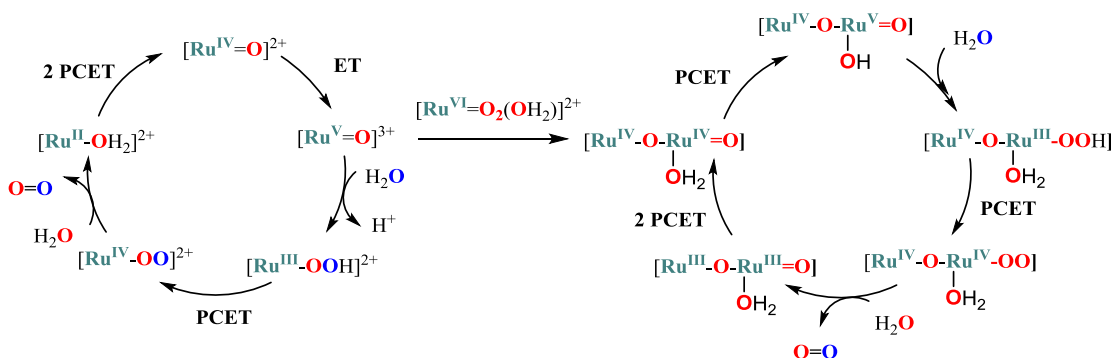
Scheme I.5. Double mechanism proposed by Llobet et al., including the monomeric catalytic cycle proposed by Meyer et al. (left)[63] and the gate to the dimeric process (right).[74]

Back to the Thummel proposal, a singular 7th coordinated μ-(HOHOH)-$[Ru^{IV}(ONNO)(pic)_2]^{3+}$ species (ONNO = 2,2'bipyridine-6,6'-dicarboxylate) was isolated and characterized with X-ray diffraction by Sun and coworkers (**Figure I.11**).[75] Following the new findings on mononuclear Ru WOCs, Sun and coworkers reported an analogous family of complexes by introducing modifications in complex **11** (**Figure I.11**, **30**). Due to the low oxidation potential required to achieve the $Ru^{IV}=O$ species (0.57 V vs SHE), the $Ru^{IV}=O$ intermediate was isolated from catalytic experiments (by precipitation with NH_4PF_6) with low amounts of sacrificial oxidant (60 eq).

30
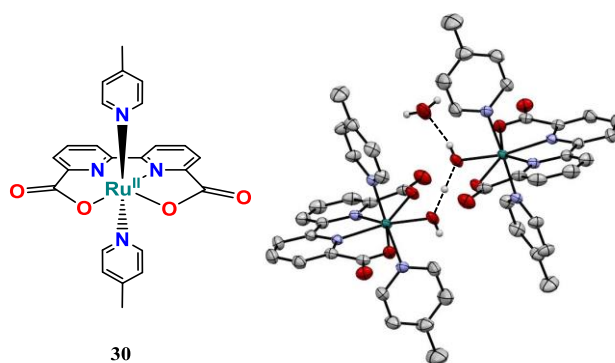
Figure I.11. Left, structure of [Ru^{II}(ONNO)(pic)$_2$]. Right, crystal structure of the isolated species μ-(HOHOH)-[Ru^{IV}(ONNO)(pic)$_2$]$^{3+}$, after a water oxidation catalysis with 60 eq. of CAN.

When Sun and coworkers investigated **25a** ([Ru(terpy)(pic)$_3$]), they realized that one picoline ligand was exchanged by H$_2$O to generate an octahedral intermediate.[76] Therefore mechanistic proposals from Thummel and Meyer may be both valid, as a function of the catalyst employed. The above mentioned [Ru(ONNO)(pic)$_2$] (**Figure I.11, 30**), analogous to the biscarboxilato dimeric compounds, was also found highly active.[8] The isolated 7th coordinated compound and the DFT calculations served altogether to propose a mechanism towards an intermolecular interaction between two monomeric units (**Scheme I.6**).[77] Two important points were extracted from the study of this compound: a) the introduction of a dianionic ligand reduces the potential required for the water oxidation to a level where the light-driven reaction can be carried out ([Ru(bpy)$_3$]$^{2+}$ as the PS and Na$_2$S$_2$O$_8$ or [Co(NH$_3$)$_5$Cl]Cl$_2$ as SO)[78] b) if the mechanism is base on the intramolecular direct coupling, this could be facilitated by modifying the axial picoline ligands by isoquinolines, taking advantage of the π-stacking interaction between the aromatic rings, lowering the barrier for the radical coupling of the Ru-O species (**Scheme I.6**). As a result, complex **31** (**Figure I.12**) was synthetized and the impressive TOF of 300 s^{-1} was achieved under optimized conditions. This O$_2$ production rate is similar to the activity found for the PSII (100 – 400 s^{-1}). Mechanistically, the binuclear radical coupling pathway between two units of Ru^V=O was supported by both experimental (kinetics) and DFT calculations.[8] Later modifications on the axial position derived into a large family of [Ru(ONNO)(N)$_2$] complexes with impressive activities (**Figure I.12**).[79,80] Also very interesting was the observation that after the modification of the equatorial bridge for a more rigid unit (1,10-phenanthroline-2,9-dicarboxylate), the O-O bond formation pathway became a monomeric process (AB mechanism), where the dicarboxylate ligand probably assisted the nucleophilic attack of the water molecule.[32] The study of the electronic effects by different 4-substituted pyridyl ligands showed that electrowithdrawing groups enhance the WO activity while electrodonating enhanced the longevity of the catalyst.[81] However, the observed non-covalent interaction[8] was definitively more effective than pure electronic effects. Taking advantage of the low overpotential (onsets usually

below 1.25 V at pH 7) of this family of extraordinarily active WOCs, visible light driven WO was carried out by photo-generated $[Ru(bpy)_3]^{3+}$ within a typical three component SO-PS-WOC system (SO was $S_2O_8^{2-}$). Nevertheless, the activity was not as impressive as for the Ce^{IV}-driven catalysis. Indeed, TON of 218 and 232 and TOF around 0.3 s^{-1} where observed for compounds **31** and **34**. As a major problem, the pH dropped dramatically from 7 to 2 after the first run, shifting the onset for the WO at higher potentials, stopping the catalytic activity. Using a substituted PS with higher oxidative potential and recycling the catalyst by raising up the pH with NaOH and adding a new batch of PS and SO, 579 TON were achieved. A quantum efficiency of 17.1% at 473 nm was reached for the best catalyst of the series (**30** containing a 4-Br substituted pyridine as the pic ligand, TON = 250, TOF = 0.33 s^{-1}).[82]

30

2010 TON, 14.7 s^{-1}
[a] 100 TON, 6 x 10^{-2} s^{-1}

31

8360 TON, 120 s^{-1}
[b] 218 TON, 0.3 s^{-1}

32

[c] 4563 TON, 31s^{-1}

33

[c] 1702 TON, 70 s^{-1}

34

[c] 55400 TON, 286 s^{-1}
[b] 232 TON, 0.3 s^{-1}

35

[d] 336 TON, 9.2 x 10^{-2} s^{-1}

[e] **36**
a R^1,R^2 = H   2032 TON, 137 s^{-1}
b R^1= Me, R^2 = H   2365 TON, 146 s^{-1}
c R^1= H, R^2 = Me   550 TON, 150 s^{-1}
d R^1= Me, R^2 = Br   4050 TON, 176 s^{-1}

[e] **37**
a R^1 = H, R^2 =NO$_2$ 1094 TON, 3.4 s^{-1}
b R^1= Me, R^2 = Br   1150 TON, 4.5 s^{-1}
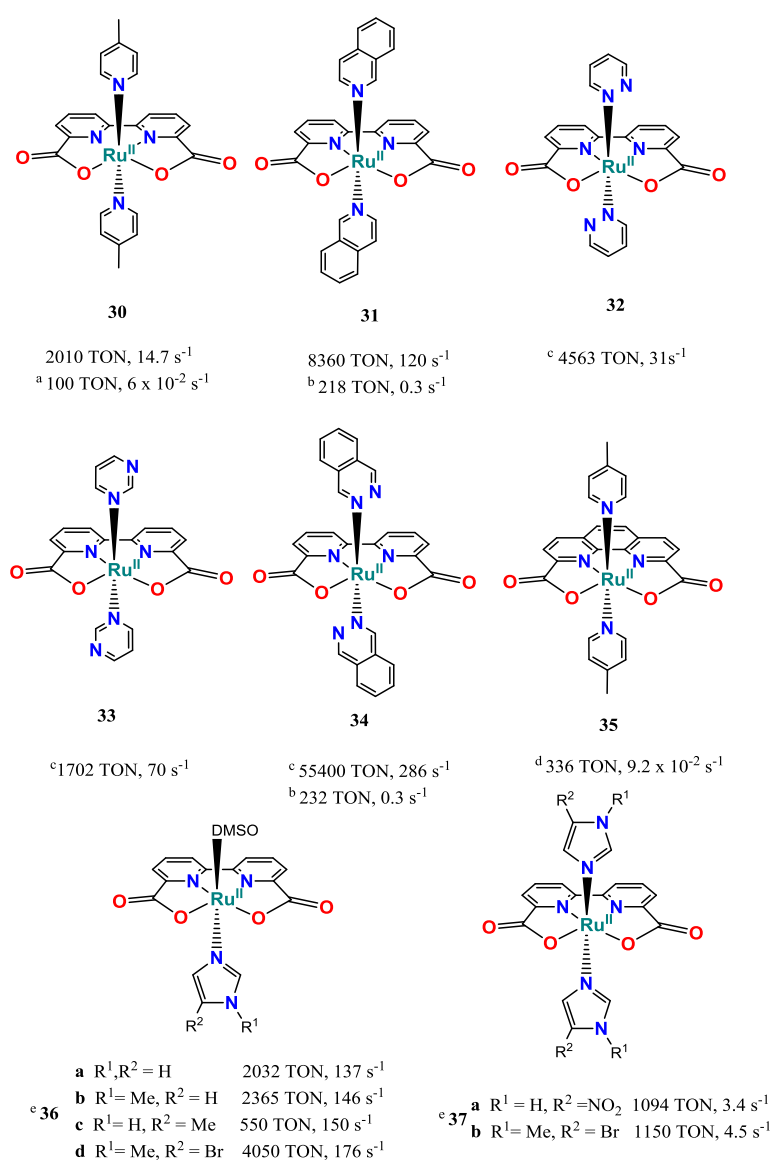
Figure I.12. [a] Light-driven WO, using $[Ru(bpy)_3]^{2+}$ as PS and $[Co(NH_3)_5Cl]Cl_2$ as SO. [b] Light-driven WO, using $[Ru(bpy)(4,4'-CO_2Et-bpy)_2]^{2+}$ as PS and $Na_2S_2O_8$ as SO. [c] TON and TOF are not recorded under the same conditions,

thus they are not comparable. [d] Under the same conditions, complex **30** performance was 1200 TON, 4.5 s^{-1} (TON, TOF). [e] Under the same conditions, complex **30** performance was 2000 TON with a TOF of 41.2 s^{-1}.

To gain in robustness, complex **30** was modified at the axial positions using a methylene spacer to connect two monomeric units and facilitate the direct coupling (**Figure I.13**). Electrochemistry indicates no electronic communication between the two metals and the onset was comparable to its monomeric precursor (1.21 V). Upon testing in thermal WO, the dimer produced 20780 TON (*per* dimer). This value resulted one order of magnitude higher than its monomeric precursor (1550 TON) and the authors decided to study the effect of different bridging spacers within the same structure. Taking advantage of a much-easily tunable imidazole ligand, compounds **30b** and **30c** were synthetized and tested as WOC. 16690 and 21660 TON (per dimer) were obtained respectively. Optimizing the conditions for **30c** (25 nM [Ru]$_2$, 10mM [Ce^{IV}]), a TON of 42840 was achieved, with an initial TOF of 40 s^{-1}. Kinetics pointed towards a reaction rate first order dependent on the dimeric complex, opening the possibility of an intramolecular DC mechanism. The electrodeposition of the compound on ITO shows a catalytic current at η = 100 mV, in neutral aqueous solution. Contrarily, monomers lose their activity upon immobilization, reinforcing the requisite of an intramolecular pathway and providing a mechanistic proposal reminiscent to Tanaka's work (complex **4**).[83] Interestingly, in contrast to catalyst **31** which its catalytic activity was reduced with the concentration (TON value of 3000 and TOF value of 1.7 s^{-1} for a 100 nM of [Ru], versus 8360 TON, 120 s^{-1} for a 15 μM of [Ru], **Figure I.13**), catalysts **30c** improved from 33550 TON to 42840 TON by decreasing [Ru] from 62.5 to 25 nM (the TOF (40 s^{-1}) was constant for the whole 12.5-62.5 nM range).
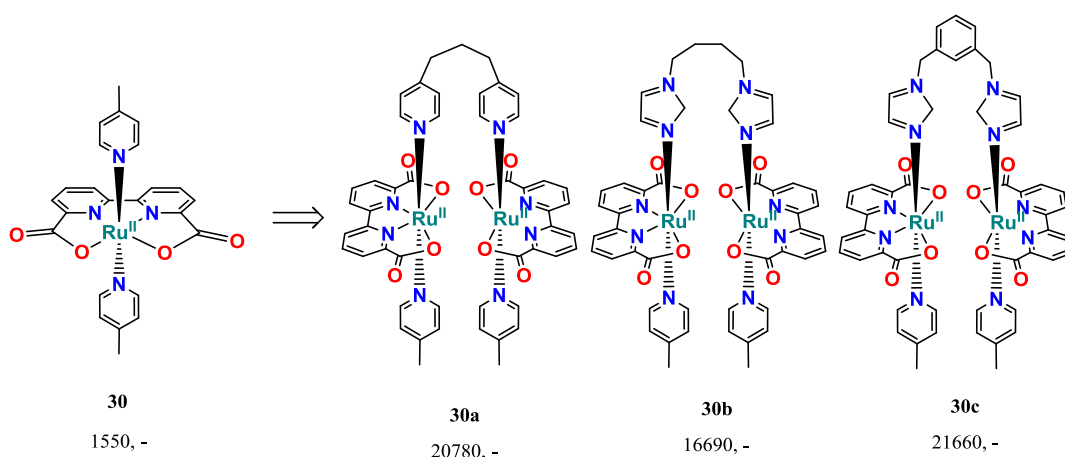
Figure I.13. Dimerized structures of the ruthenium WOC 30 by using different methylene spacers. TON values were obtained upon addition of the catalyst (0.05 μM) to an aqueous solution of HOTf (pH 1), containing CAN (5mM). TOF values were not available.

Recently, [Ru^{II}(ONNO)(NHC)(OH$_2$)]$^+$ (NHC = 1,3-dimethylimidazolium-2-ylidene) was studied as WOC. The complex had an onset potential for the water oxidation at 1.5 V (pH 1, η =

0.33) and the activity for the thermal water oxidation driven by Ce^{IV} was lower than the expected for a Ru(ONNO)-type complex (63 TON, 0.04 s^{-1}). Kinetic studies and DFT pointed to a second-order reaction, first order on Ru, thus indicating a single-site mechanism (AB pathway) and emphasizing again with the diversion of catalytic mechanisms, depending on the first coordination sphere.[84] The lower activity reported, when compared with previous reported Ru(ONNO)-type complexes (**Figure I.12**) indicates the importance of having a robust N-donor axial ligand, avoiding its replacement for a solvent molecule, which diminishes the catalytic efficiency.

Considering the important role of the isoquinoline on the O_2 production of mononuclear Ru compounds, facilitating the DC interaction, Zhao and coworkers replaced the 4-picoline ligand moieties of the Ru-WOC [Ru^{II}(DPA-bpy)(OH$_2$)](PF$_6$)$_2$ (DPA-bpy = N,N-bis(2-pyridinylmethyl)-2,2'-bipyridine-6-methanamine) for isoquinolines (DIQ-bpy = N,N-bis[(isoquinolin-1-yl)methyl][6-(pyridin-2-yl)pyridin-2-yl]methanamine) to provide insights on this π-stacking effect. However, it was observed a contrary effect on the TON (from 20 to 2). The authors proposed that in the case of an AB mechanism, an intermolecular noncovalent interaction should prevent the attack of the water molecule on the high-valent Ru=O.[85]
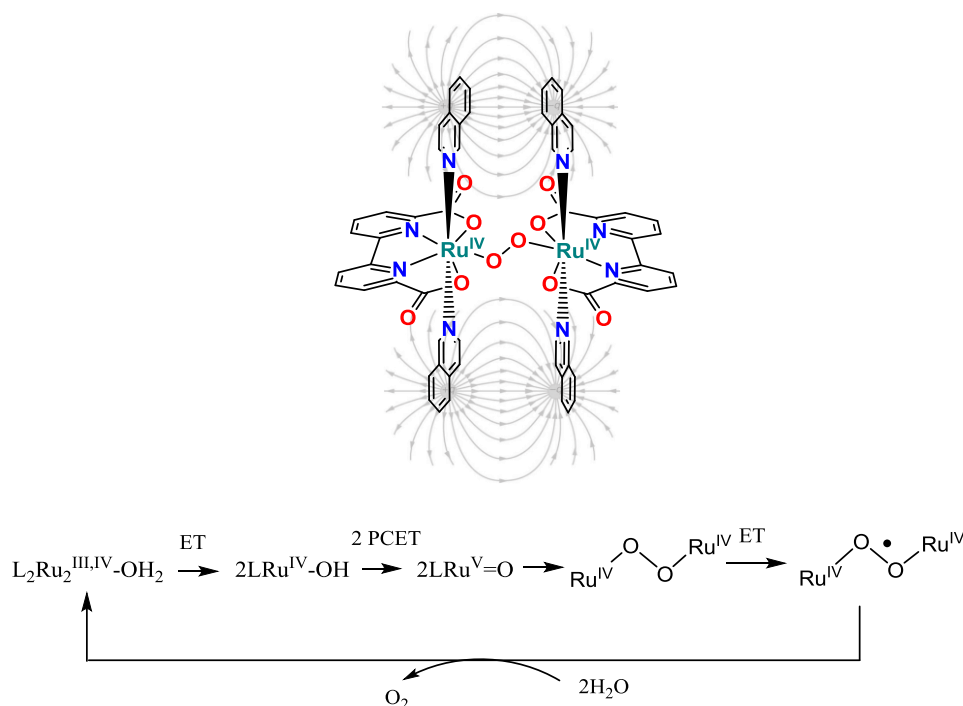
Scheme I.6. Catalytic mechanism proposal for the Ru-WOC intramolecular process and illustration of the intermolecular coupling pathway favoured by the π-stacking between isoquinoline moieties.

An step forward was done by Sun and coworkers by using a modified compound **30** integrated to a multiwalled carbon nanotube coated on ITO by non-covalent π-stacking interactions (**Figure I.14**, **EC**). At pH 7, the WO-onset occurs at 1.15 V (η = 280 mV) and by applying 1.4 V, both H_2 (from the Pt counter electrode) and O_2 (from the ITO-modified electrode)

evolved, the latter with a TOF of 0.3 s^{-1} and a TON of 11000 after 10 h of electrolysis.[86] Taking advantage of the low catalytic overpotential for the WO (160 mV at neutral pH, NaPi buffer) of **30**, different photoelectrochemical (PEC) devices were designed (**Figure I.14**, **PEC**).[87] Initially, the catalyst supported on Nafion was combined with a dye-sensitized nanostructured TiO$_2$ on FTO modified with a PS ([Ru(4,4'-PO$_3$H$_2$-bpy)(bpy)$_2$]$^{2+}$) as the anode (**Figure I.14**, **PEC 1**). Pt was the cathode. Photocurrent was generated upon illuminating the PEC, with a TON and TOF of 16 and 7.5·10^{-3} s^{-1}. Because TiO$_2$ conduction band was not reductive enough for the H$_2$ production, a small negative bias of 0.13 V was applied. Due to the strongly acidic Nafion membrane, the PEC experienced a low efficiency. Therefore, alternatively to the Nafion membrane, the complex was modified with an N-(3-(triethoxysilyl)propyl)isonicotinamide ligand in one of its axial positions and was immobilized directly on the nanostructured TiO$_2$ particles (**Figure I.14**, **PEC 2**). The new PEC device produced both hydrogen and oxygen by applying an external bias of 0.2 V (pH 6.8, 0.1 M NaPi buffer) with a high photocurrent (1.7 mA·cm^{-2}).[88]
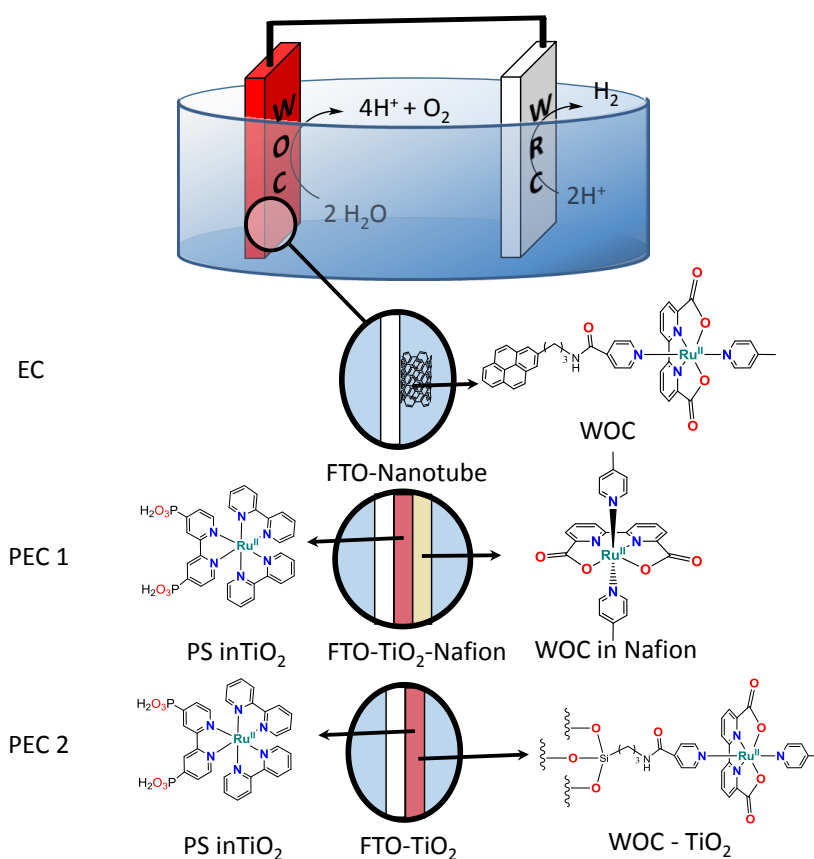
Figure I.14. Alternative water splitting systems design by Sun and coworkers containing different anodes. The EC is an electrochemical cell powered by an applied voltage. PEC stands for a photoelectrochemical cell powered by both light and an external current. To increase the absorption spectrum to the visible range, a PS complex was anchored to TiO$_2$.

Monomeric Ru-WOCs have provided a new vision towards the development of water oxidation catalyst. While DC mechanism seems to be the most efficient and robust pathway for the water oxidation, with low overpotentials, dimeric compounds are not strictly required. Indeed, the O-O bond formation can be achieved intermolecularly by two monomeric units. This gives a great opportunity to the homogeneous WO, due to the simpler ligand design. Moreover, another key point which is reinforced by mononuclear complexes is the participation of anionic ligands to facilitate the oxidation of the metal center by lowering the redox potential. Besides the impressive activity reported for those compounds (TOF close to 300 s^{-1}), further improvements are still required to maintain this activity in the light-driven WO and to deal face to face the OEC.

I.4.1.3.   Ruthenium Polyoxometalates

The oxidative decomposition of the organic ligands is a common deactivation pathway during the water oxidation, because of the harsh conditions where the reaction is carried out. Hill, Bonchio and their respective coworkers independently proposed the use of pure inorganic ligands such as polyoxometalates (POM) as a strategy to overcome the degradation processes. Nevertheless, these ligands are not immune to degradation processes such as hydrolysis. The ruthenium polyoxometalate, **Ru$_4$POM** (**Figure I.15**) was found to be active and robust in both thermal and light-driven conditions. Its structure was based on two γ-SiW$_{10}$O$_{36}$$^{8-}$ units connected by a [Ru$_4$(μ-O)$_4$(μ-OH)$_2$(H$_2$O)$_4$]$^{6+}$ core, in which Ru^{IV} atoms were disposed in an adamantane-like arrangement. Bonchio *et al.* reported that in the presence of Ce^{IV}, water oxidation took place with high TOF (0.125 s^{-1}) and TON (500). Kinetics were first-order on catalyst, suggesting that the four Ru atoms were involved in the multielectronic and multiprotonic process.[89,90] Insight into the mechanism was obtained by Bonchio and coworkers. From Ru$_4$^{IV} ([Ru^{IV}$_4$(H$_2$O)$_4$(μ-O)$_4$(μ-OH)$_2$(γ-SiW$_{10}$O$_{36}$)$_2$]$^{10-}$), three quasi-reversible redox couples (0.48, 0.61 and 0.86 V) and a last non-reversible anodic wave at 1.06 V were attributed to the formation of [Ru$_4$^{V}], being the latter the competent active species. The sequential Ru oxidation was confirmed by UV-Vis. The first oxidation (Ru^{V}Ru$_3$^{IV}) takes place easily under oxygen atmosphere and can be reversed by ascorbic acid, as confirmed by EPR, resonance Raman (rR) and DFT calculations. Addition of 1eq of Ce^{IV} yielded an EPR silent Ru$_2$^{V}Ru$_2$^{IV} characterized by rR. Addition of 2eq of CAN to Ru^{V}Ru$_3$^{IV} yielded an EPR active paramagnetic system which was consequently associated with Ru$_3$^{V}Ru^{IV}. No more changes were observed upon addition of Ce^{IV}, thus Ru$_4$^{V} (predicted by DFT) was not observable. The intramolecular direct coupling pathway is neglected due to geometrical constraints and an intermolecular interaction did not fit with the obtained first order kinetics, thus only the AB pathway was reasonable for the O-O bond formation.[91]

Hill and coworkers performed electrochemical studies and observed a catalytic process taking place at a redox potential below 1.21 V vs SHE.[31] Consequently, [Ru(bpy)$_3$]$^{3+}$ could be

used as SO. 17.8 TON were recorded and control experiments with the non-active RuCl$_3$ pointed towards Ru$_4$POM as the real catalyst.[28] Light-driven WO was carried out using Nas$_2$S$_2$O$_8$ as SO and Ru(bpy)$_3^{2+}$ as PS. 180 TON and an initial TOF of 0.08 s^{-1} were reported. However lowering the concentration of the catalyst and increasing persulfate, up to 350 TON were achieved.[92] The substitution of the central heteroatom of the POM, Si^{4+} by P^{5+} did not affect the complex structure, but increased the overall charge by one unit. Although this change impacts in the redox properties of the POM, similar catalytic activities and redox potentials were observed.[93] Bonchio and coworkers anchored the Ru$_4$POM in a multiwalled nanotube which was deposited on ITO (indium tin oxide) to make an oxygen-evolving anode for the electrochemical-driven water oxidation.[94] The performance of this new device had remarkable efficiency (34 TON, 0.085 s^{-1}), operative voltage (overpotential of 0.6 V), current density and operational stability.

Ru$_4$POM
180 TON, 0.08 s^{-1}
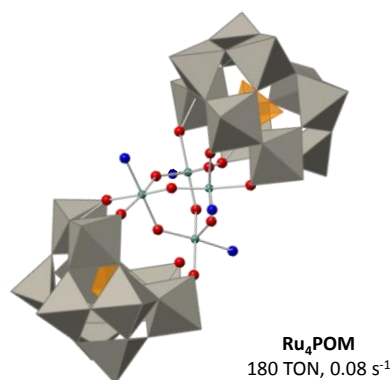
Figure I.15. Ru$_4$POM. Ru (in green) and oxygen (in red) atoms belonging to the core are drawn in ball & stick style. The grey polyhedra is W$_{10}$O$_{36}^{8-}$ and the orange, the Si atom.

I.4.2 Iridium Water Oxidation Catalysts

I.4.2.1. Chemical-driven water oxidation using CAN

Since the eighties, it is well known that metal dioxides based on Ru, Ir and Pt can catalyze the Ce^{IV} and Ru(bpy)$_3^{3+}$-driven water oxidation reactions.[95-101] Among them, Iridium oxides were found long-lived and very active WOCs with low overpotentials, showing both very high electrochemical and photochemical rates.[102] Nevertheless, it was not until 2008 when the first iridium complex was studied as WOC. Moreover, this was the first organometallic complex tested for the water oxidation. In the presence of CAN, a family of [Ir^{III}(ppy)$_2$(OH$_2$)]$^+$ derivates (ppy=2-phenylpyridine) produced O$_2$ with a slow rate but for a long period of time (6 - 8 days). Indeed, through ligand modifications, the energy of the HOMO was found to be highly tunable and consequently it was argued that the oxidation potentials could be easily controlled. The increase of Ir$^{III/IV}$ redox potential was associated with a decline of the electronic density at the metal center,

which leaded to a slight increase of the catalytic activity, from 2200 TON up to 2760 TON and from $0.3 \cdot 10^{-2}$ to $0.4 \cdot 10^{-2}$ s^{-1} (TOF). DFT studies concluded that the ability to tune the electronics of both catalyst and photosensitizer may facilitate photo-driven half reactions or full water splitting devices.[103] Later on, Crabtree, Macchioni and coworkers explored the versatility of Cp*Ir complexes in WO (Cp* = 1,2,3,4,5-pentamethylcyclopentadiene). The "half-sandwich" iridium complexes showed an enhanced catalytic efficiency with regard to the previously described organometallic compounds (**Figure I.16, 39-44**).[35,104,105]
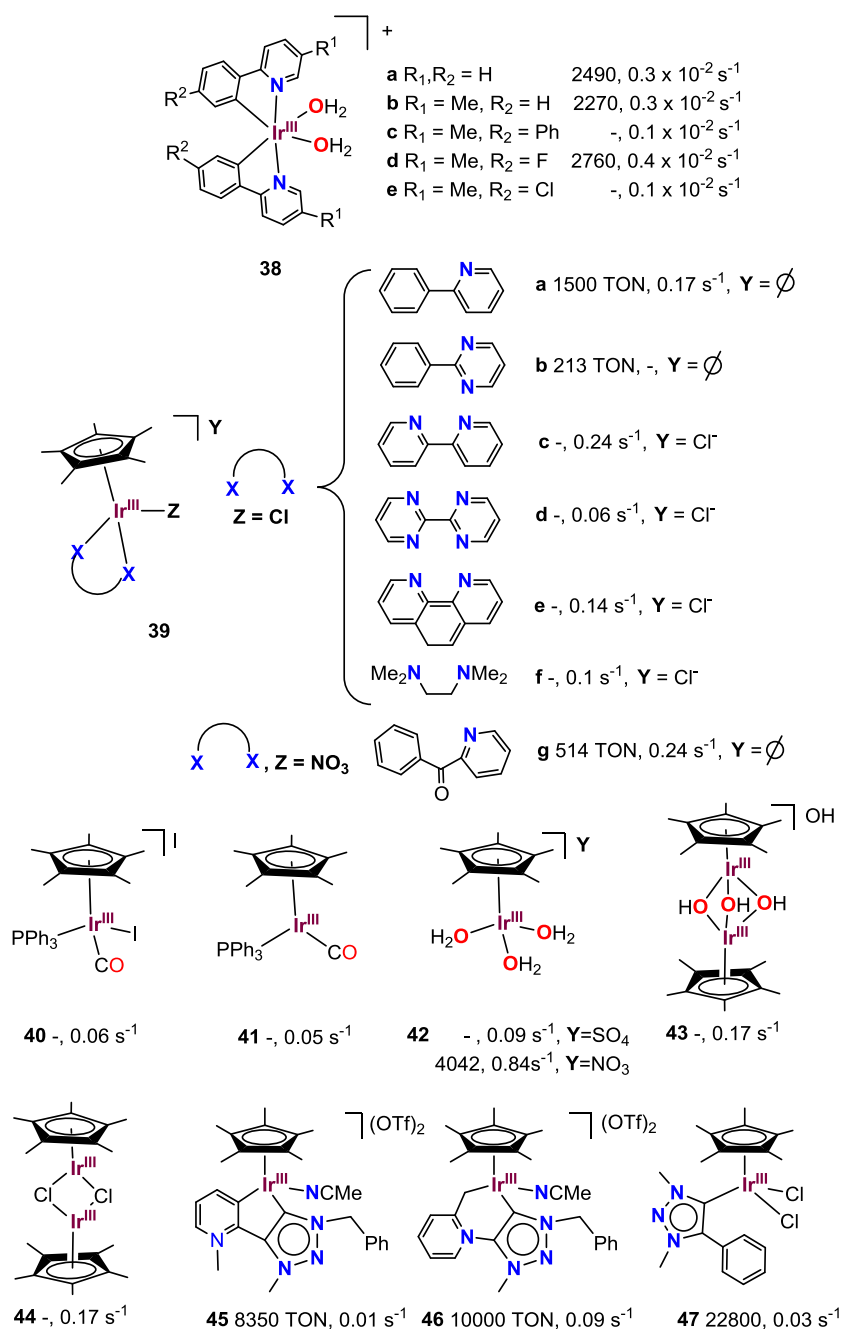
Figure I.16. TON and TOF values are highly sensitive, and very dependent on the concentration of both catalyst and oxidant. Values belonging to different sources are not directly comparable. Nevertheless, a qualitative comparison is informative.

Complexes **39-**type clearly improved the TOF reported by Bernhard and coworkers up to that moment, but it was the introduction of bidentate carbene type ligands the key to raise one order of magnitude the TON of the Ir WOCs (**Figure I.16, 45 and 46**). It was suggested that the high electronic flexibility (resonance) of the carbene-type ligand could stabilize both the low oxidation state species (carbene acts as a neutral ligand) and the oxidized species (zwitterionic form).[36] Another carbene-based complex reported by the same group, compound **47**, has the highest TON achieved for any Ir WOC, using CAN as SO. This complex was also found photo-electrochemically active. Using hematite as a photoanode, a pH-dependent light-induced current was observed at 1.23V.[106]

Crabtree, Brudvig and coworkers also reported an analogous example, $Cp*Ir(k^2,C^2,C^2-NHC)Cl$ ($k^2,C^2,C^2-NHC = k^2,C^2,C^2$-1,3-diphenylimidazol-2-ylidene), which contained a C-chelate carbene (**Figure I.17, 49**). The Ce^{IV}-driven WO rate was 0.13 s^{-1}, and a different lag phase was observed, when compared to complex **39a**. Kinetics indicated almost 2nd order on Ir, and authors suggested that NHC may be lost under catalytic conditions forming compound **42**, which contributes to the catalysis. The WO activity was also tested using the milder SO $NaIO_4$, exhibiting a much higher rate (~ 0.25 s^{-1}). Caution must be taken when using oxo-transfer oxidants due to the possibility of oxygen formation via disproportionation of the oxidant. First insights on WO intermediates were obtained by CV of complex **49** in MeCN. Under those conditions, a quasi-reversible wave was observed at 0.9 V. This reversibility points towards a partially stable Ir^{IV} intermediate, which was chemically generated from Ir^{III} by the addition of $[Ru(bpy)_3]^{3+}$ and analyzed by EPR. A metastable low-spin d^5 Ir^{IV} with S=1/2 was detected. The intermediate decomposed into EPR silent byproducts. The same experiment with compound **39a** did not generate any signal in the EPR and authors concluded that NHC ligand was providing a greater stability to the high-valent $[Cp*Ir^{IV}(NHC)Cl]^+$ intermediate.[107] Cp*Ir compounds bearing monodentate NHC ligands were also found actives for the WO reaction, with TON much closer to the $[Ir(bpy)_2(OH_2)_2)]^+$ but retaining TOFs of Cp*-type complexes (**Figure I.17, 48**). Oxidized species observed by ESI-MS upon addition of CAN were related to $[IrCp* = O]^+$, $[IrCp*(OH)_3]^+$, $[IrCp* = O \cdot 2Na]^+$ and $[IrCp*(O)_2 \cdot 2Na]^+$.[108] Later on, Macchioni and coworkers showed that in fact these oxidations were not at the metal center, but on the Cp* moiety (See next section).[109]
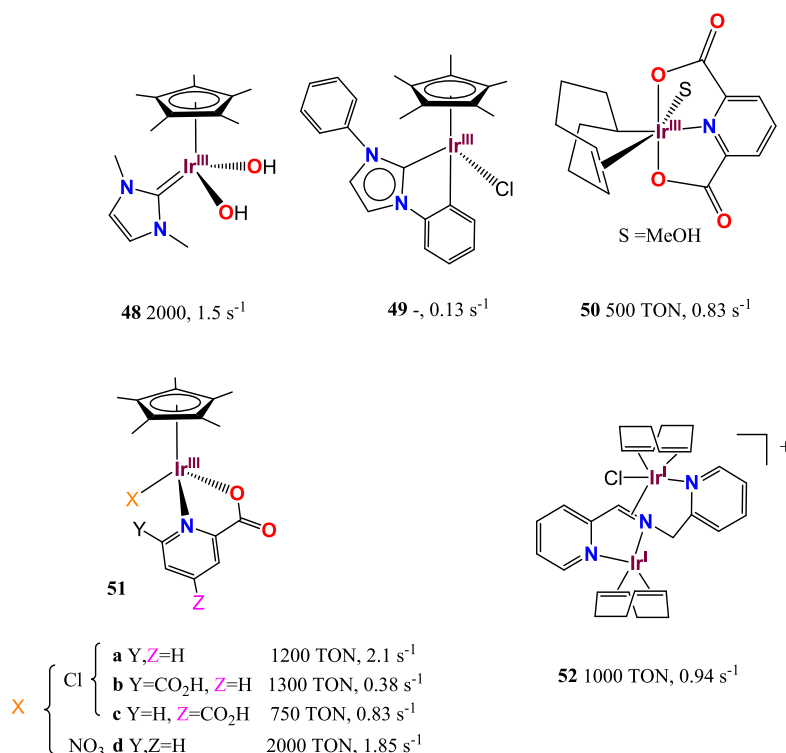
Figure I.17. Carbene based complexes (**48-49**) reported by Reek, Crabtree and coworkers, complexes containing carboxylate ligands (**50-51**) reported by Macchioni *et al*., and an example of an organometallic free-Cp* IrWO complex (**52**) reported by de Bruin *et al*.

Following the successful introduction of anionic ligands (pyridine carboxylate) in the design of Ru WOCs, a similar strategy was followed for Ir compounds, maintaining the Cp* moiety. The new complexes, $[Cp*Ir(\kappa^2\text{-N,O})X]$ (k^2-N,O = 2-pyridinecarboxylic acid, 2,4-pyridinecarboxylic acid or 2,6-pyridinecarboxylic acid, X = Cl⁻ or NO₃⁻) (**Figure I.17, 51**) and the *free*-Cp* $[Ir(\kappa^3\text{-N,O,O})(1\text{-}\kappa\text{-}4,5\text{-}\eta^2\text{-}C_8H_{13})(MeOH)]$ (κ^3-N,O,O = 2,6-pyridinedicarboxylic acid) (**Figure I.17, 50**) were found suitable for the WO. While long-term activities were found similar to the previous examples, initial TOF were outstanding, being **51a** the fastest Ir WOC reported so far using CAN as SO (TOF 4.8 s⁻¹, conditions: [Ir]= 0.5 μM, [Ce^{IV}] = 20 mM).[110]

Another interesting *free*-Cp* Ir WOC $[(cod)ClIr(\mu\text{-bpi})Ir(cod)]PF_6$ (bpi = (pyridine-2-ylmethyl) (pyridine-2-ylmethylene) and cod = 1,5-cyclooctadiene) was reported by de Bruin and coworkers with good TON and TOF (1000, 0.94 s⁻¹) (**Figure I.17, 52**).[111] Kinetic studies agree with first order on both Ir and Ce^{IV}.

I.4.2.2.   Homogeneous *vs* Heterogeneous: The Fate of the Ligand

Colloidal iridium oxides have been well documented to be excellent water oxidation catalysts.[95,96,112-114] Therefore, since the discovery of the first organometallic iridium WOCs and due to the harsh conditions were the catalysis takes place (Ce^{IV}-driven WO), the distinction

between homogeneous and heterogeneous catalysts during the water oxidation has been a primary focus of discussion, and state of the art technics (NMR, ESI-MS, UV-Vis, DLS, TEM, powder XRD, XPS…) has been employed to shed some light on this controversy.

The presence of a broad UV/Vis absorption band centered at 570-590 nm region of the spectrum has been related to the presence of colloidal IrO_2 in solution for many years. For this reason, the formation of this chromophore upon addition of CAN has been interpreted as a clear evidence of ligand degradation.[115] However, this band can also arise from a d-d transition of distorted octahedral Ir^{IV} center and the association to iridium oxides without further evidences is a non-reliable indicator.[116]

Three years after the publication of the first organometallic iridium WOC, Rheingold and coworkers found that the most relevant Ir complexes (**38a, 39a, 42, 45, 46, 48**) experimented a fast modification of the ligand structure upon titration with CAN (UV-Vis, HNMR, ESI-MS).[115] UV-Vis spectra of those catalysts in the presence of CAN showed the growth of an absorbance at 550-650nm, which was proposed to belong to IrO_x NPs. As pointed by Crabtree and coworkers, this may be alternatively explained by the formation of Ir^{IV} molecular species, absorbing in the same range. Despite of that, no oxygen was produced until several equivalents of the oxidant were consumed and important changes were observed by ^{1}H-NMR and ESI-MS, pointing towards the oxidation of the Cp* moiety.[115] STEM (scanning tunneling electron microscopy) analysis of dried samples pointed towards Ir-NPs associated with Ce atoms instead of the expected free Ir-rich aggregates.

On the other hand, Fukuzumi and coworkers demonstrated that slight modifications of the chelate ligand had a deep effect in the reactivity as well as in the nanoparticle (NP) formation. $[IrCp*(4,4'-R-2,2'-bpy)(OH_2)]^{2+}$ (**39c(OH$_2$)$^{2+}$**) was taken as platform, and the bpy moiety was modified with R = OH, OMe, Me or COOH groups. The WO activity with CAN was evaluated and TOF ranging from 0.05 to 0.75s^{-1} were found. For the best WOC (R = OH), TOF increased gradually during the reaction, reaching the highest value of the series. In a subsequent run, this TOF was kept from the beginning, indicating the presence of a stable catalyst generated from the starting complex. It was characterized as IrO_x insoluble NP. Nevertheless, those particles were found more active than conventional iridium oxide and TG/DTA (thermogravimetric / differential thermal analyses) and XPS (X-ray photoelectron spectroscopy) measurements suggested the presence of small amounts of carbonaceous residues, contributing to this higher efficiency, demonstrating that the choice of the precursor is crucial to achieve a highly active compound.[117]

A deep NMR study performed by Macchioni and coworkers following the evolution of Cp*Ir in water oxidation conditions (CAN as SO) showed how the Cp* moiety was oxidized in

its –C-CH$_3$ positions to form alcohols, aldehydes or acid derivatives before breaking and producing acetic or formic acid. DFT calculations confirmed that such functionalization could take place at the quaternary carbon and CH$_3$ protons with similar activation energies to the intramolecular attack of the superoxide resulting from the O-O bond formation in a η^1-O$_2$ coordination mode.[109] Further experimental studies with H$_2$O$_2$ showed the oxidative degradation preferentially occurring at the quaternary carbon atoms.[118] To avoid this process, Macchioni and coworkers used HEDTA (ethylenediaminetetraacetic acid) as ligand, taking advantage of its well-known strong donating properties suitable for the stabilization of high valent intermediates. TON of 12000 and TOF of 0.1 s^{-1} using CAN as SO were comparable to the best Ir catalysts reported.[119] Deeper into the oxidation process of the Cp*, Macchioni and coworkers were able to intercept three different intermediates during the oxidative transformation of the Cp* moiety (**Scheme I.7**). Interestingly, different oxidants (H$_2$O$_2$, CAN and NaIO$_4$) triggered the same transformations; the oxidation to an unconventional epoxide Ir^{III}-O-Cp* species which, after addition of a water molecule, evolves to double ketone-functionalized Cp*(O)$_2$-Ir complex. One of the ketone groups was then coordinated to the metal. Further unidentified oxidative transformations end up with the complete degradation of the Cp*. The isolated epoxide species, a mixtures of intermediates, and the initial compound produced O$_2$ in a similar TOF (CAN as SO), suggesting a common single molecular species which provides most of the catalytic activity.[120]
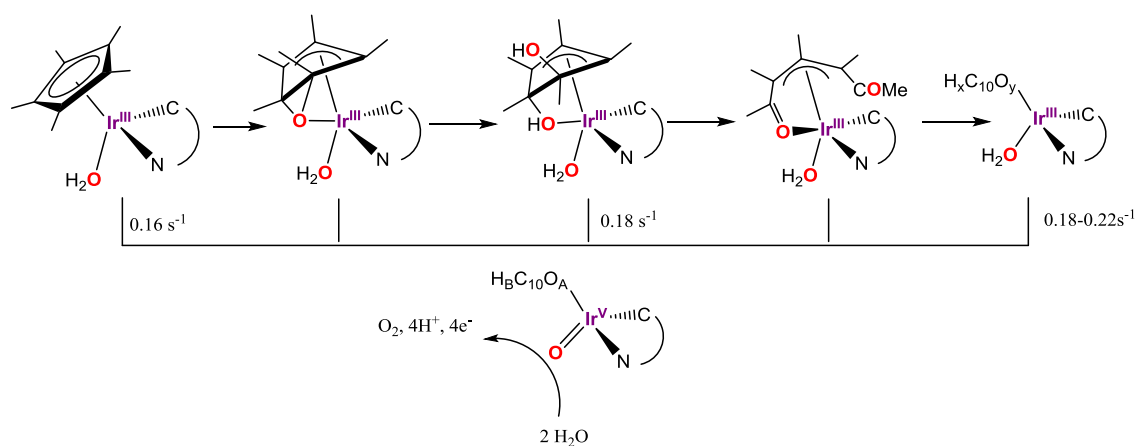
Scheme I.7. Initial complex and oxidized intermediates detected. TOF of the starting compound (left), the isolated intermediate (center) and of mixtures resulting from the oxidative process with different eq. of CAN or H$_2$O$_2$ (right) were reported.

Junge, Beller and coworkers carried out a deep study to elucidate the homogeneity of the catalysis under the presence of CAN. Complexes **53-59** (**Figure I.18**) and heterogeneous iridium oxides were compared by *in-situ* X-ray absorption spectroscopy (XAS). XANES (X-ray Absorption Near-Edge Structure, first resonance after the edge jump) were useful to differentiate between oxidation states of the active species and EXAFS (Extended X-ray Absorption Fine

structure, high kinetic energy range) allowed the differentiation by type, number and distance of neighboring atoms to the X-ray absorber. Under water oxidation conditions, XANES data pointed to a significant contribution of Ir^{IV} species for all the Ir^{III} complexes. By comparison with IrO_2, EXAFS revealed that both $IrCl_3$ and $Ir(acac)_3$ retained the initial salt precursor structure at some extent (~70% and ~60% respectively). This was similar for catalyst **53** (1:1 precurssor : $Ir^{IV}O_2$). However, for catalyst **56** only 18% of Ir^{III} was observed, indicating that a large amount of the initial complex has been transformed into NPs. In good agreement, HAADF-STEM images showed NP sizes smaller than 1 nm for $IrCl_3$, while no NP were detected for **56**, due to bigger particle size, above the 10 μm range. Moreover, three different-sized IrO_2 samples were synthetized on porous supports (7.3 nm, 7.7 nm and 1-3 nm) and tested as WOC to compared against commercially available IrO_2 (1-3 nm). The biggest the size of the particle, the lowest the catalytic activity. Indeed, the TOF of the smallest synthetized NP was similar to $IrCl_3 \cdot xH_2O$ but lower than the reported for $Ir(acac)_3$. Altogether seems to indicate that starting from Ir complexes (precursors), a first phase of the reaction is dominated by active homogeneous catalyst (high TOF) which turns gradually into nano-sized Ir^{IV}=O WOCs (conversion rates are strictly depending on the precursor). Finally, the catalytic activity vanishes due to the agglomeration of NP during the course of the reaction.[121]
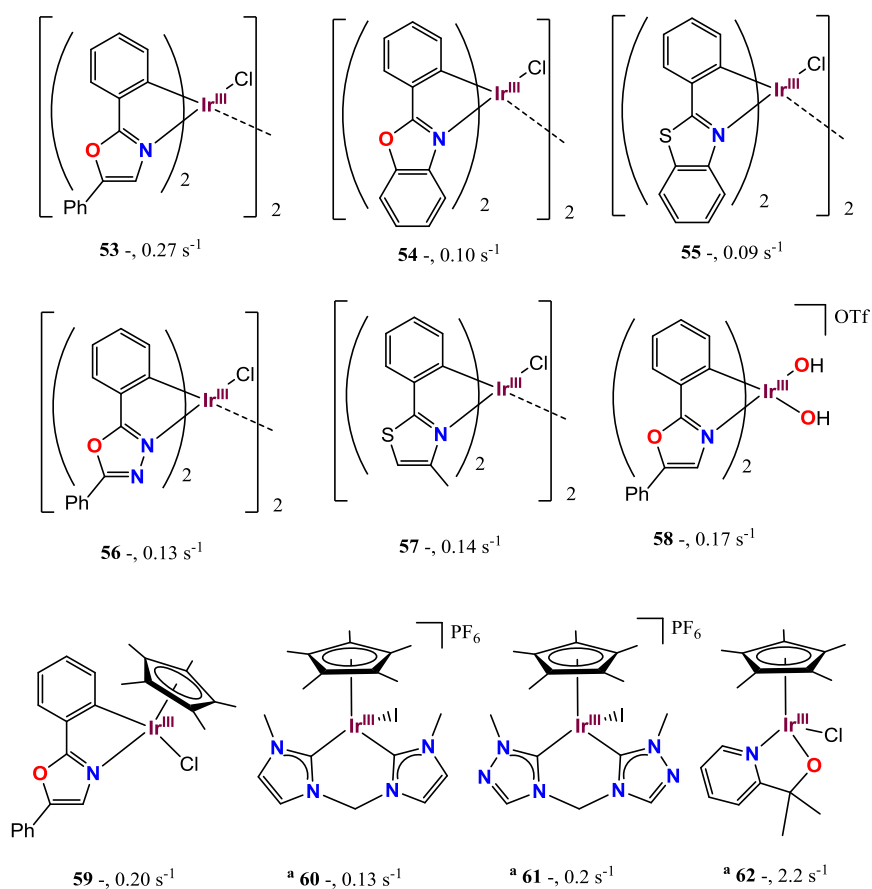
53 -, 0.27 s^{-1} **54** -, 0.10 s^{-1} **55** -, 0.09 s^{-1}

56 -, 0.13 s^{-1} **57** -, 0.14 s^{-1} **58** -, 0.17 s^{-1}

59 -, 0.20 s^{-1} ^{a} **60** -, 0.13 s^{-1} ^{a} **61** -, 0.2 s^{-1} ^{a} **62** -, 2.2 s^{-1}

A sophisticated strategy using an elongated dicarboxylate bipyridine (bpy-dc) or phenylpyridine (ppy-dc) bridging ligands attached to Cp*Ir as a link between $Zr_6(\mu_3$-O$)_4(\mu_3$-OH$)_4$(CO$_2$H) cuboctahedral subunits providing a highly porous and oxidatively-robust metal organic framework (MOF) structure (**Figure I.19**) was carried out to avoid the degradation pathways involving multiple molecules and facilitate the characterization of the catalyst after the reaction. The MOF was found to catalyze Ce^{IV}-driven water oxidation, and its recovery and characterization after the catalysis exhibited an oxidative degradation on the Cp* rings. The active species was identified by NMR and ESI-MS as a [(bpy-dc)Ir(OH$_2$)$_2$(XCl] (X= formate or acetate groups).[122] Further support on the MOF stability was obtained by PXRD and ICP-MS.
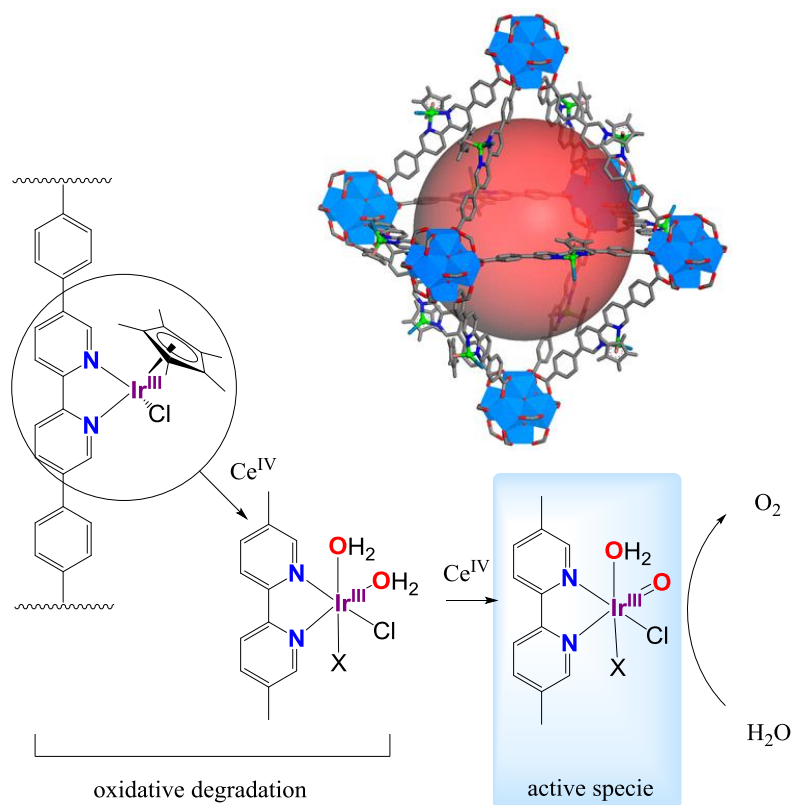
Figure I.19. MOF structure consisting on $Zr_6(\mu_3$-O$)_4(\mu_3$-OH$)_4$(CO$_2$H) units linked by an elongated iridium complex of formula [Cp*Ir^{III}(bpy-dc)Cl]+. The release of the Cp* generates the catalytic species, highlighted in the picture. Adapted with permission from ref. [122], copyright (2012) American Chemical Society.

The studies focused on Iridium complexes for the WO carried out by Fukuzumi, Macchioni, Beller, Lin and coworkers it could be argued that in many cases a biphasic catalytic behavior takes place; in a first phase of the reaction, the most active species are generated from the initial iridium complexes (precatalyst) but during the course of the reaction, IrO$_x$ NP are

formed and the WO rate decreases while increases the size of the aggregation, explaining the fast depletion of the TOF.

I.4.2.3.   Iridium Salts As Precatalysts For The Water Oxidation

Simple and commercially available iridium salts were in fact very efficient precatalysts for the water oxidation (See Summary of the water oxidation catalysts), as demonstrated by Beller and coworkers. The activities reported for these salts turn out to be highly sensitive to experimental conditions and detection methods.[104,123] While Crabtree and coworkers found a TOF of $7 \cdot 10^{-3}$ s^{-1} for $IrCl_3 \cdot xH_2O$,[104] Beller $et\ al.$ reported a value 12-fold higher. Interestingly a TOF of 0.47 s^{-1} was detected when an aged sample of the chloride salt (dissolved in water for 15 days) was used instead of a freshly prepared sample (TOF = 0.084 s^{-1}). Ir(acac)$_3$ (acac = acetyl acetonate) was also found very active (TOF = 0.33 s^{-1}). However, IrO_2 exhibits a different behavior when compared to the other salts, having a much lower rate.[123]

I.4.2.4.   Sodium Periodate As A Milder Oxidant For the Water Oxidation

As mentioned above, the use of $NaIO_4$[116] is not completely accepted for the water oxidation due to the possibility of being itself the source of oxygen. Labelling studies are not useful to understand the mechanism due to the fast oxo exchange with water. However, in favor of this oxidant there are several important advantages: i) it is a milder oxidant (1.6 V vs SHE) than CAN or Oxone, ii) it is stable between pH 2 to 7.5, iii) an O-O bond is not present like in oxone, tBuOOH or H_2O_2 and iv) so far catalysts that produce oxygen with $NaIO_4$ also oxidize water in the presence of CAN (iron and iridium compounds).

Since its first appearance on iron WOCs (2010 and 2011 (**Chapter III of this thesis**)) its use has been extended to Ir-WOCs to avoid working in acid pHs and in a way to slow down the fast ligand oxidation which takes place in the presence of Ce^{IV}. Firstly, Crabtree and coworkers employed periodate with a Wilkinson type catalyst.[124] Interestingly, this compound rapidly decomposes in the presence of CAN but, in the presence of $NaIO_4$ a high TOF was reported. Further studies with a series of Ir-WOCs (**39c** SO$_4$ instead of Cl, **42, 60-62**) showed that the milder oxidant led to a reduced degradation of the catalysts, in part because of the higher pH. UV-Vis spectroscopy and DLS (dynamic light scattering) argue against formation of NPs, which in combination with the lack of CO_2 in the headspace (detected by GC-MS) pointed towards a homogeneous process. Partial ligand oxidation was observed after a catalytic run, but it was in much lower extent than when Ce^{IV} was used as SO. For instance, an impressive TOF of 2.2 s^{-1} was reported for compound **62** under those conditions.[116]

Electrodeposition of IrO_x on the surface electrodes has been used as an indication of catalyst degradation under WO. A convenient method to measure mass change on an electrode relies on the converse piezoelectric effect. Briefly, if a mass change occurs at the surface of the piezoelectric working electrode (gold-coated quartz crystal electrode connected to the nanobalance), the frequency of the resonant vibration shifts depending on the magnitude and sign of the change in mass. Sauerbrey equation relates this change and the gain or loss in mass can be calculated at the $ng \cdot cm^2$ scale. Under electrochemical-driven conditions, complex **62** (OTf replaces Cl) do not form any deposit and was concluded to be an homogeneous WOC. Nevertheless, for complex **42** the electrodeposition was clear.[125]

By this time, our group was working on a similar family of complexes to the ones reported by Reek *et al.*,[108] but using periodate as SO. A comprehensive study using both SO (CAN and $NaOI_4$), and including kinetics, NMR, ESI-MS, and DLS was carried out to understand how a milder oxidant can influence the catalytic activity (see **Chapter III**). With the aim of determining the impact of hydroxyl groups and their keto-enol tautomerism on catalysis, Papish and coworkers included OH and OMe in the 4,4'- and 6,6'-postions of the bpy moiety of the complex **39c** (**Figure I.20, 63a-c**) and they measured the WO activity using $NaIO_4$ at different pH (3-6).[126] The use of this milder oxidant was found beneficial for the process, avoiding the formation of NP (DLS). Initial rate studies showed a rate enhancement at high pH for OH-containing compounds. This behavior was related to ligand deprotonation, improving the electron-donating character of the ligand. The use of electrochemistry or $[Ru(bpy)_3]^{3+}$ as SO rather than CAN or $NaIO_4$, led to oxidation of the complex, but no oxygen evolution was detected.[127] Following this work, a very recent investigation of the pH-activity tendency using $NaIO_4$ as SO showed a change of one order of magnitude in the TOF when increasing the pH from 5.5 to 7.2. Because complex **63f** does not contain any OH in its structure, it was argued that the increase of TOF relies on the deprotonation of the aqua ligand (Papish catalyst contained Cl). First-order dependence on the precatalyst was obtained at low catalyst concentrations. Spectroscopic analysis connects the 590 nm-absorbing species with the active catalyst. The formation of such species was strongly dependent on the reaction conditions, in particular to small [SO/Ir] ratios. Another less-active species was detected under higher amounts of SO, absorbing at 600 nm. DLS and TEM identified the later as 120 nm – NP while the former (590nm absorption species were separated by ultrafiltration) as 0.5 – 2 nm small IrOx clusters. The authors suggested that the lower TOF for **63d** was related to the higher stability of the complex, preventing the formation of small IrO_x clusters and evolving to a less active dimer containing chelate ligands (*vide infra*, **Scheme I.8**).[128]

The formation of IrO_x nanoparticles in different $Cp*Ir^{III}$ precursors was studied under the presence of $NaIO_4$, by combining UV-Vis and real time DLS.[129] It was found that chelate ligands (2,2'-bipyridine, 2-phenylpyridine) conferred an extra stability to the complexes, strongly

evading the NP formation. The observation of a chromophore at 570-590 nm by UV-Vis was related to a d-d transitions of distorted octahedral Ir^{IV} center, which might be the active species responsible for water oxidation.

			Papish *et al.*			
				TOF (x 10^3 s^{-1})		
			pH	a	b	c
			3	0	0	0
			4.5	50	90	4.3
			5	83	127	14
			5.6	223	353	14
			6	367	373	18

a $R^1 = OH$, $R^2 = H$
63   **b** $R^1 = H$, $R^2 = OH$
c $R^1 = OMe$, $R^2 = H$

d X=Y=CH, $R^1 = R^2 = H$ 7200, 0.28 s^{-1}
e X=Y=CH, $R^1 = H$, $R^2 = OH$ 6700, 3.75 s^{-1}
f X=CH, Y=N, $R^1 = R^2 = H$ 6700, 5.2 s^{-1}
g X=N, Y=CH, $R^1 = R^2 = OH$ 6330, 2.2 s^{-1}

Fujita *et al.*
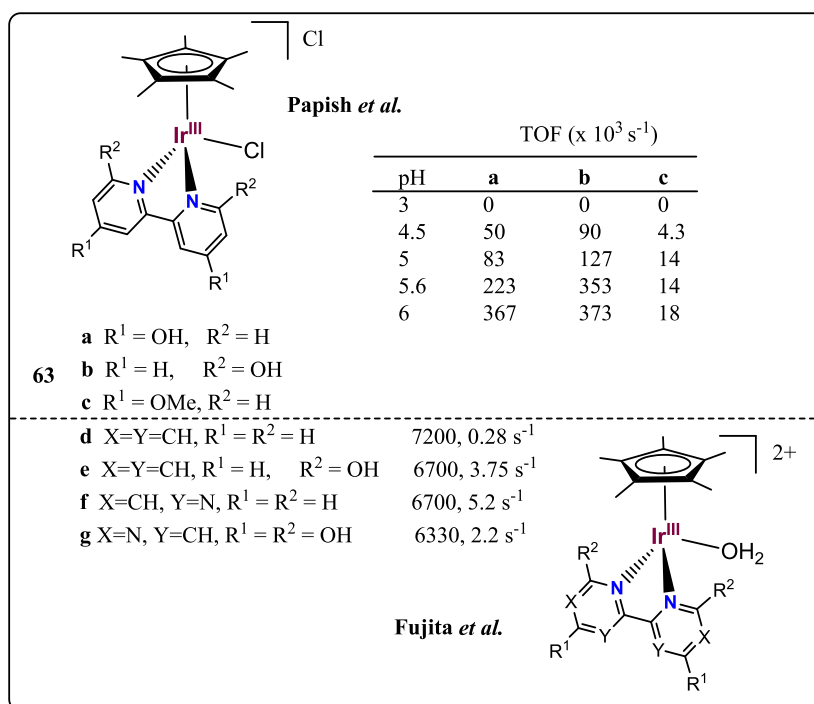
Figure I.20. Top) pH effect on TOF for the $NaIO_4$-driven water oxidation with an $[Ir^{III}Cp^*(bpy)Cl]^+$ WOC, and bottom) TON and TOF for $[Ir^{III}Cp^*(X)(OH_2)]^{2+}$ (X stands for bipyridine or bipyrimidie), complexes at 50mM NaPi buffer (pH 7.2)

Indeed, the formation of the 570-590 nm signal was found reversible by the addition of a reducing agent (MeOH), thus indicating that the band is in fact an oxidized species. According to Crabtree *et al.*, dynamics of NP formation are strongly depended on both catalyst concentration and pH and the amount of NP and the growth rate are regulated by the solution potential and the presence of inorganic salts or organic co-solvents. The presence of chelating agents were found effective in preventing the particle formation, and therefore complexes such as **39a**(OH), **39c**(OH) and **62**(OH) (OH replaces Cl), which contains strongly chelating ligands, catalyzed the WO in the homogeneous phase,[129] in agreement with previous electrochemical studies (*vida supra*).[125] However, these complexes were not the "true" catalyst because under oxidative conditions they suffered a complete oxidative damage of the Cp* moiety, while maintaining the chelating ligand intact, generating the homogeneous WOC with a characteristic blue color (related to NP in the past). Electrophoresis suggested the presence of well-defined Ir-cations, and TEM-EDX (transmission electron microscopy-energy-dispersive X-ray spectroscopy), XPS (X-ray photoelectron spectroscopy), ^{17}O-NMR, rRaman spectroscopy data and DFT are consistent with the formation of a dimeric species with formula $[Ir^{IV}(pyr-CMe_2O)(OH_2)_2(\mu-O)]_2^{2+}$ (**Scheme I.8**),

that might be the resting state. A different precursor bearing the same chelate ligand was found equally effective for both water and C-H oxidation, in agreement with the mechanism proposed.[130]
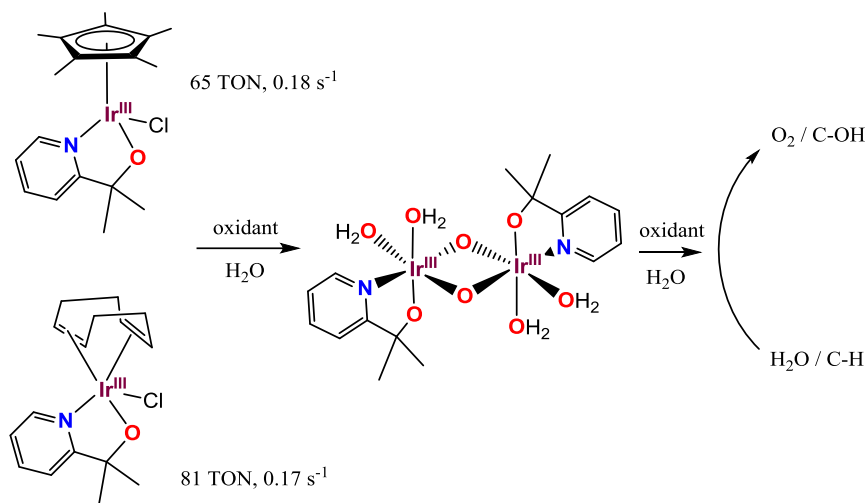
Scheme I.8. Proposed "true" catalyst formed during the NaIO$_4$-driven water oxidation. Chelate ligands remains intact, providing a carbonaceous moiety to the IrO$_x$ catalyst, making more effective the catalysis.

I.4.2.5. Mechanistic insights for the Ir-catalyzed water oxidation

Mechanistic studies becomes very complicated when a drastic transformation take place on the catalyst. Earlier kinetic studies carried out by Crabtree, Macchioni,[35,105] and coworkers indicate first order on the metal (AB mechanism). In analogy to the single-site ruthenium catalyst, two PCET steps from Ir^{III} are proposed to yield the catalytically active Ir^V=O species. [35,105] The possibility to use NaIO$_4$ to avoid the formation of NP provided a new opportunity to extract some valuable information. In that way, Crabtree and coworkers proved the viability of the DC mechanism with a series of Cp*Ir^{III} dimers. Among the precursors tested, complexes bearing monodentate NHC ligands were found to generate NP, and corresponding dimeric analogs did not exhibit rates that depend on their nuclearity, or on the distance between metals. However, the bis-pyridine-pyrazolide ligand was resistant to oxidative degradation (**Figure I.21, 64 and 64b**) and could be studied, exhibiting first order kinetics on [Ir]. In addition, the dimeric structure exhibits a lower O$_2$ evolution rate when compared with the mononuclear counterpart. The electrochemical behavior of both mono and dimetallic complexes were found very similar. The sum of this data discarded a cooperative mechanism, and the nucleophilic attack of the water molecule on Ir^V=O (**AB** pathway) was supported for this system.[131]

I.4.2.6. Light-driven water oxidation with Irdium complexes

Recently, Bonchio and coworkers reported an iridium complex active under light driven conditions. The organometallic compound was firstly evaluated using NaIO$_4$ and CAN as sacrificial oxidants, reaching TOF of 0.12 and 0.2 s^{-1} respectively (**Figure I.21, 65**). ^{1}H-NMR and

GC-MS analysis indicates the partial decomposition of the organic ligand, releasing 4 TON of CO_2. The light driven WO was carried out in a $NaHCO_3/Na_2SiF_6$ buffer at pH 5.2, employing $[Ru(bpy)_3]^{2+}$ (PS) and Na_2SO_8 (SO). O_2 evolution was observed in a rate (TOF) between $(2-5)$ $\cdot 10^{-3}$ s^{-1} reaching 37% of conversion after 5 h of irradiation and a quantum yield of 3.8% (photons absorbed / O_2 produced). The reaction rate was concentration-dependent, the lower the catalyst loading, the higher the TOF. A control experiment with $IrCl_3$ produced 4.2 TON, with a TOF of $1.25 \cdot 10^{-3}$ s^{-1}, values lower than for the complex. In addition, EPR studies suggested the presence of an Ir^{IV} species as an intermediate under irradiation conditions.[132]
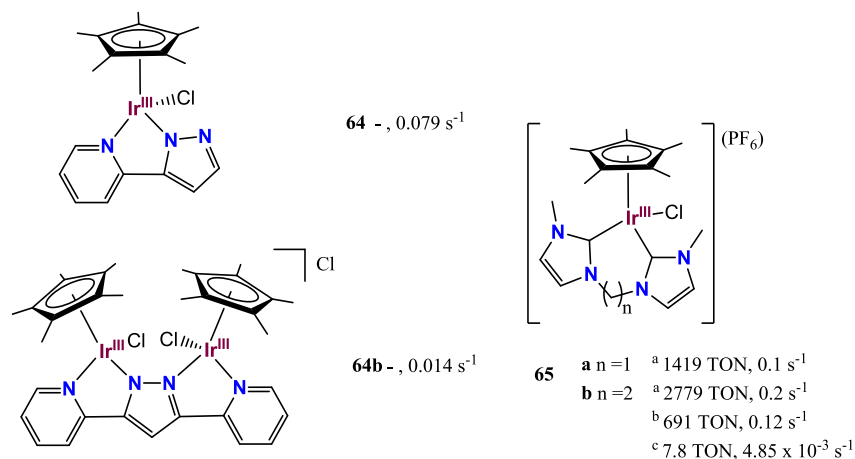
Figure I.21. 64b is the dimeric complex of **64**, reported by Crabtree *et al*. [131] **65**, is the light driven WOC reported by Bonchio *et al*.[132]

I.5. State Of The Art: Water Oxidation Catalyst Based On First Row Transition Metals

The limited abundance of novel metals in the earth-crust ($\approx$1ppb), and their high prices in the market (**Table I.1**) restrict their use in large scale. Therefore, development of water oxidation catalysts based on first row transition metals may be regarded as an attractive alternative because these metals are relatively abundant, cheap, and in addition, they are generally less toxic than heavy metals.[133]

Table I.1. Abundance, production and market prices of well-known metals that catalyses water oxidation.

	Abundance on Earth's Crust (%) [134]	Production (tons) [135]	$USD/Ton[134,136]
Iron	6.3%	7.2×10^8	27
Manganese	0.11	6.2×10^6	1460
Copper	7×10^{-3}	6.5×10^6	8950
Cobalt	3×10^{-3}	1.7×10^4	$3.6 \cdot 10^4$
Ruthenium	9.9×10^{-8}	0.12	$2.1 \cdot 10^6$
Iridium	4×10^{-8}	3	$14.8 \cdot 10^6$

The most relevant examples reported until 2014 of homogeneous water oxidation catalysts based on first row transition metals are summarized in **Figure I.22** (*vida infra*). A detailed description of WOCs based on first row transition metals is included in the following sections.
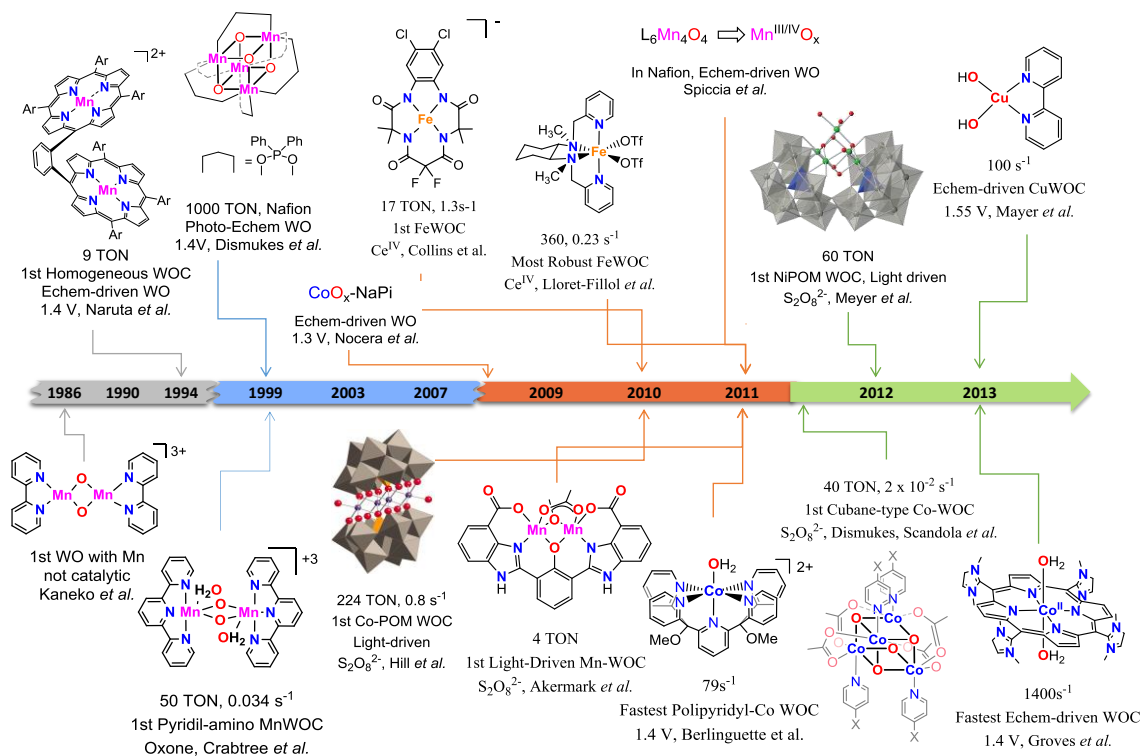
Figure I.22. Time line with the most emblematic first row transition metal WOCs. TON, TOF (s^{-1}), breakthrough, oxidation method the corresponding authors are included. Echem-driven stands for electrochemical driven water oxidation, and Photo-Echem is used for a system powered by a combination of light and electrical current.

I.5.1 Manganese Water Oxidation Catalysts

I.5.1.1. Mn in PSII

The PSII active site for the water oxidation, the oxygen evolving complex (OEC), is constituted by three manganese and a calcium atoms bridged by four oxygens in a cubane-distorted cluster ($CaMn_3O_4$). An external Mn atom bound through an oxo bridge to this cluster consummates the Mn_4O_5Ca structure. This complex leads the water oxidation reaction in PSII, which supplies protons and electrons to reduce NADPH and synthetize ATP. To the date, the mechanism is not completely understood. Indeed, steps such as the O-O bond formation are still under debate.[9,10] Understanding fundamentals of the OEC reactivity could be key for the rational development of functional artificial photosystems. In the last decade, valuable information has been extracted by applying a model chemistry approach towards the understanding of operative mechanisms occurring on biological systems. In this context, analogous synthetic compounds to

the OEC have been designed to get insight on the water oxidation. However few structural models containing Mn oxides arranged as a cluster has been found active catalysts for the water oxidation. The most important examples are detailed below.

I.5.1.2.   Bioinspired Mn₄O₄ Models

The synthesis, characterization of model coordination complexes in different oxidation states, and the study of its reactivity has contributed substantially to the understanding of the role of metal complexes in biological processes. A paradigm is the understanding of the OEC at the atomic level, which has been found extremely complicated. In this regard, the use of synthetic manganese coordination complexes is a powerful tool to unravel the basic chemical principles, and elemental steps that operate in the water oxidation reaction at the OEC. The first examples towards the design of synthetic structural models of the OEC were through the study of robust tetranuclear manganese complexes with the general formula $L_6Mn_4O_4$ (L^- = diarylphosphinate ligand, (p-R-C_6H_4)$_2$PO$_2^-$ (R = H, alkyl, OMe)). Complexes of general formula $L_6Mn_4O_4$ have the following reactivity (**Scheme I.9**) **i**) abstraction of four hydrogen atoms from amines or phenols, yielding two water molecules by triggering a notable structural change on the cubane, forming the so-called "pinned butterfly" $[L_6Mn_4O_2]$[137,138] **ii**) O$_2$ photo-release with a concomitant loss of a bridging anion (Ph$_2$PO$_2^-$), generating the "butterfly complex $[L_5Mn_4O_2]^+$. This photochemistry, exclusive for cuboidal-type manganese complexes, was initiated by the photoexcitation of the Mn-O charge transfer band of the initial cubane $L_6Mn_4O_4$ complex by UV-light, in the gas phase (laser desorption/ionization mass spectrometry, LDS-MS).[139,140] Taken together these reactivities, Dismukes and coworkers glimpsed a mechanism towards the production of O$_2$ from water in a closed cycle, along the reverse mechanism **i**. However, O$_2$ did not photodissociate in liquid phases. The insolubility in water and most organic solvents of $L_6Mn_4O_4$ was a major issue for the investigations, but it was overcomed by supporting the cluster on Nafion. This allowed the system to function in the presence of water. Photoelectrochemical driven water oxidation was observed at 1 - 1.4 V vs SHE. During photoelectrolysis for 65h, the membrane passed a net charge equivalent to 1000 turnovers per cluster.[141] The reversible release of one equivalent of ligand (connection between path **i** and **ii**, butterfly →pinned butterfly, **Scheme I.9**) and the capture of two water molecules and release of 4 protons (reverse path **i**) were proposed to draw a mechanistic scheme.
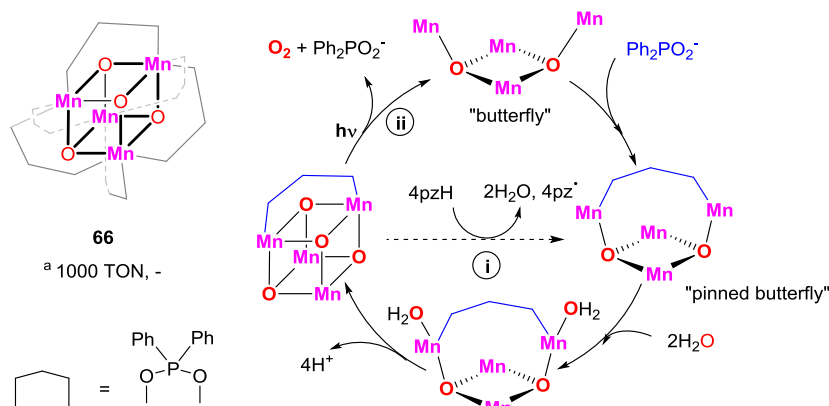
Scheme I.9. Proposed structural rearrangement of the manganese cluster during the water oxidation. Only one phosphinate ligand (in blue) was included in the catalytic cycle to emphatize the coordination/decoordination process. pzH is phenothiazine. [a] Photoelectrochemical TON obtained for the $L_6Mn_4O_4$ cluster supported on Nafion after 65h at 1.4V.

Later on, Spiccia and coworkers proved that $L_6Mn_4O_4$ clusters supported on Nafion are transformed into Mn^{2+} (birnessite), which in turn is electro-oxidized into $Mn^{III/IV}$-O_x nanoparticles (NP), true responsible species of the water oxidation.[142] XAS studies before and after loading the cluster in Nafion and after the bulk electrolysis at 1.2 V vs SHE showed substantial structural changes (**Figure I.23**). Firstly, upon supporting the complex on the membrane, a Mn^{II} (confirmed by XANES) surrounded by six oxygen-donors with disordered second sphere (EXAFS) was observed, indicating a full transformation of the original cluster. The input of electrical current shifted the near edge structure (XANES) to higher energies (oxidation state for Mn was 3.8-3.9), similar to what expected for an oxidized cubane. However EXAFS reveals spectral differences in comparison to what is expected for a cubane complex, indicating that $L_6Mn_4O_4$ was not the true catalyst. Further electrocatalytic studies with layered MnO_2 NPs supported on FTO (fluorine-doped tin oxide working electrode) revealed its efficiency for the WO in alkaline media (pH > 8). The onset potential was found constant at 1.5 vs SHE until pH 9, when sharply shifted to negative potentials ($\eta_{pH\,8}$ = 700 mV, $\eta_{pH\,9}$ = 480 mV). Spectroscopic studies indicated the presence of Mn^{3+} on the surface of the layer at high pH, while below pH 9 a reversible disproportionation reaction yielding the formation of Mn^{2+} and Mn^{4+}, with the onset again on higher potentials (1.5 V). Those experiments pinpointed Mn^{3+} as an essential precursor for the electrocatalysis.[143]
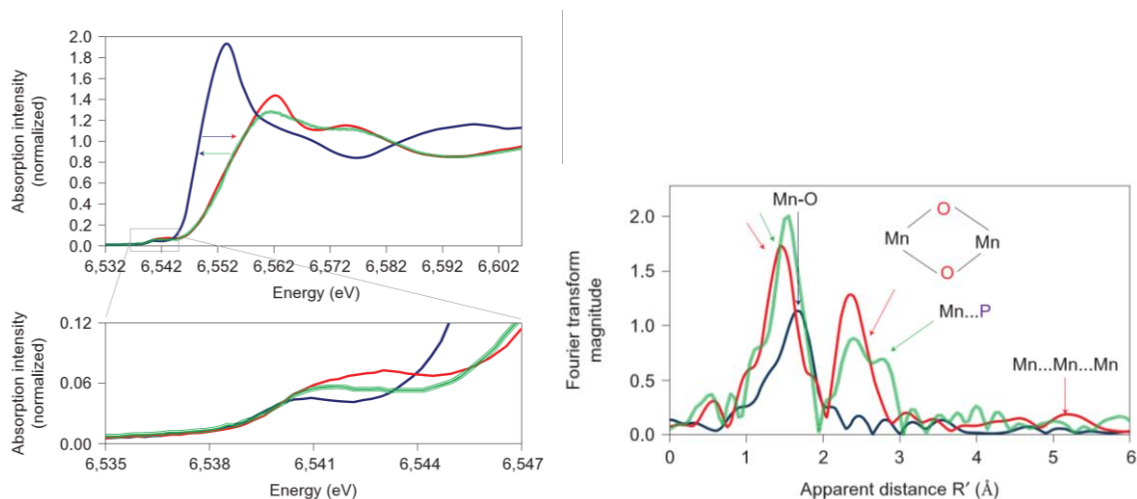
Figure I.23. Comparison of Mn K-edge XAS spectra. Green: [Mn$_4$O$_4$L$_6$]ClO$_4$, L=(MeOPh)$_2$PO$_2^-$, in acetonitrile; blue: [Mn$_4$O$_4$L$_6$]$^+$ in Nafion; red: the electro-oxidized product of [Mn$_4$O$_4$L$_6$]-Nafion. The data is represented as **left**) XANES and magnification of pre-edge; **right**) Fourier transform of the EXAFS labelled with bonding interactions responsible for the peaks. Reprinted by permission from Macmillan Publishers Ltd ref. [142], copyright (2011)

I.5.1.3.   Biomimetic models including a Lewis acid

Calcium is an essential cofactor for the water oxidation but its role in the OEC is still under debate. Different possible roles of the Ca^{2+} has been considered; i) the Ca^{2+} atom may act as a Lewis acid, binding the water substrate and enhancing its nucleophilicity making more reactive towards a Mn^V(O) pendant, lowering the barrier for the O-O bond formation, ii) Ca^{2+} atom may modify the hydrogen bonding network between Yz and the Mn cluster, affecting the PCET iii) Ca^{2+} atom may tune the pK$_a$ and redox potential values of the cluster to facilitate the water oxidation.[144]

The preparation of structural analogues of the OEC containing a calcium atom with the aim to clarify its role has been found synthetically challenging. The first example was reported in 2005 when Christou *et al.* synthetized a complex, [Ca$_2$Mn$_{13}$O$_{10}$(OH)$_2$(OMe)$_2$(O$_2$CPh)$_{18}$(H$_2$O)$_4$; Mn^{IV}, Mn^{III}$_{10}$, Mn^{II}$_2$) possessing two Mn$_4$O$_4$ cubes attached to a central, planar Mn$_3$O$_4$ unit, to which two Mn-Ca are attached above and below the plane.[145,146] Within this structure, a subunit possessing a distorted Mn$_3$CaO$_4$ cubane-like topology, analogous to the native OEC. A similar motif was obtained by Powell, Reedijk and coworkers[147,148] when 2 eq. of an *in situ* formed Schiff base (E)-3-((2-hydroxy-3-methoxybenzylidene)amino)propane-1,2-diol (**L**) was mixed with CaCl$_2$, NaN$_3$, and MnBr$_2$ yielding a [CaMn^{III}$_3$Na(**L**H)$_3$(μ_4-O)(N$_3$)$_3$(MeOH)]Cl·2H$_2$O. The [Mn$_3$CaNa] cluster was tested as WOC and it was found able to produce small amounts of dioxygen when oxone, NaOCl or tert-butyl hydrogen peroxide (*t*BuOOH) were used as sacrificial oxidants (< 4 TON, calculated from the reported plots obtained by the Clark electrode). Later on, Nayeri and coworkers found that CaMnO$_3$ (perovskite-type structure) and Ca$_2$Mn$_3$O$_8$ (layered

structure) materials, yielded from the 800 ºC-heated mixtures of disodium malonate, $MnCl_2$, and $CaCl_2$, and $CaCO_3$ and $MnCO_3$ respectively, were able to catalyze the thermal water oxidation (CAN as SO) with TOF of $1.2 \cdot 10^{-3}$ s^{-1}. Even using the photogenerated $[Ru(bpy)_3]^{3+}$ (from $[Ru(bpy)_3]^{2+}$, and $[Co^{III}(NH_3)Cl]Cl_2$ as SO, in acetate buffer) water oxidation was observed in low rates.[149] Alternatively, Borovik et al. reported an elegant method to aggregate a group II cation in the second coordination sphere. The calcium-manganese hydroxo-bridged compound with the general formula $[15\text{-crown-}5 \supset Ca^{II}\text{-}(\mu\text{-OH})\text{-} Mn^{III}(MST)]^+$ was prepared by mixing $Ca(OTf)_2$, 15-crown-5 and monomeric $[Mn^{II}MST]^-$ (MST = N,N',N''-[2,2',2''-nitrilotris(ethane-2,1-diyl)]tris(2,4,6– trimethylbenzene-sulfonamido) complex. The Mn-OH-Ca obtained mimicked structurally the oxygen evolving complex. This compound enhanced the O_2 reduction rate by 2 orders of magnitude when compared with the $[Mn^{II}MST]^-$ complex solely, demonstrating that the presence of a Ca^{2+} atom in red-ox processes is key, in relevance with the OEC.[150] Closer to the real structure of the OEC, a $[Mn_3CaO_4]^{6+}$ model was successfully synthetized and characterized by Agapie and coworkers.[151] These authors were focused in the possibility to include different Lewis acid ions in the cluster structure and evaluate the electrochemical properties. Reduction potentials were found dependent on the Lewis acidity of the redox-inactive metal incorporated, supporting the redox modulator role of Ca^{2+} in the OEC.[144,152,153] The lower the pK_a of the $M(aqua)^+$ ion (proportional to the Lewis acidity of the redox-inactive metal), the higher the redox potential of the Mn centers, due to the lower electron density on the metal.[153] However, a deviation from the trend (Sr^{2+} and Ca^{2+} exhibit the same redox) and the intriguing observation that only the replacement of Ca^{2+} for Sr^{2+} partially maintain the function of the enzyme,[154] remain puzzling observations awaiting explanation. In addition, the incorporation of the external Mn atom to fully reproduce the OEC structure remain as a synthetic challenge that maintains this field very active for synthetic inorganic chemists.

I.5.1.4.   Manganese Porphyrin Complexes

Porphyrin and corrole-type ligands have been widely used for oxidative transformations due to their capacity to stabilize high oxidation states. The first report of their application in the water oxidation reaction was reported by Naruta and coworkers in 1994. The authors introduced a family of dimeric Mn-porphyrin complexes formed with two units of tetraarylporphyrins (aryl moieties = $4\text{-}t\text{BuC}_6H_4$, $2,4,6\text{-Me}_3C_6H_2$, and C_6F_5) linked by a 1,2-phenylene bridge and produced oxygen electrochemically when the potential was set up above 1.4 V vs SHE (**Scheme I.10, 67**). The highest activity reported, 9.2 TON, was observed for the C_6F_5 aryl-substituted Mn-porphyrin at 2 V. The origin of the activity was related to the spatial disposition of the two Mn-porphyrin units, which facilitate a face to face intramolecular interaction between the two Mn=O units.[155] Authors postulated that the O-O bond formation proceed through a direct coupling mechanism between the two Mn=O units. However, the detection and characterization of a Mn^V-porphyrin

intermediate ([Mn^V=O TMPyP], TMPyP = tetra(N-methylpyridyl)porphyrinato) remained elusive until 1997,[156] when Mn$_2$^{V}=O(OH) was detected (by UV-Vis, resonance raman (rR) and EPR spectroscopy) and characterized as the responsible species of the O-O bond formation (**Scheme I.10, 67**).[157] On the other hand, by using stopped-flow spectroscopy the complex [Mn^{III}TMPyP] (TMPyP = tetra(N-methylpyridyl)porphyrinato) was found to be highly reactive for olefin epoxidation and oxo-transfer in the presence of carbamazepine and halogens (to hypohalite, OBr$^-$ and OCl$^-$).[156,158]

The incorporation of a sulfonated porphyrin [4,4',4'',4'''-(porphyrin-5,10,15,20-tetrayl)tetrabenzenesulfonate] Mn complex within a thin layer of poly(terthiophene) yielded a film which was electrodeposited over ITO as a working electrode, and tested for the water oxidation.[159] A substantial increase of current (from 0.88 V, pH 7) was achieved by light-irradiation. The negligible current observed by electrolysis at 1-1.1 V confirmed that light was essential for the production of O$_2$. Interestingly, the homogeneous complex was not active under the same conditions. Selective oxidation of water to O$_2$ occurs prior to chloride oxidation when using seawater as the solvent. An AB water oxidation mechanism is expected to compete with the formation of HClO which spontaneously equilibrates to form Cl$_2$. Due to the negligible production of chlorine, the mechanism is expected to go towards a direct coupling. No further evidences were reported to discern between mechanistic scenarios.

Mn complexes based on corrole ligands resulted to be good compounds to stabilize high-valent ion metals.[160-165] Faster rates for the oxidation of alkenes,[162] phosphine and dimethylsulfoxide were achieved,[163] and the electrochemical-driven water oxidation at 0.8 V vs Ag/AgNO$_3$ (in a CH$_2$Cl$_2$ / CH$_3$CN (2:3, v/v) solution containing 30 μL of an aqueous solution of (*n*-Bu)$_4$NOH (10% in water)) was observed.[164,165] Towards the understanding of the mechanism, HRMS and UV-Vis studies indicated that the product of the reaction between Mn^V=O (chemically generated by 1.4 eq. *t*BuOOH in MeCN) and a hydroxide ion (from an CH$_3$CN/H$_2$O (1:1 v/v) solution of (*n*-Bu)$_4$NOH, 0.2 M) yield a Mn^{IV} complex, which in turn evolves to a Mn^{III}-OH complex within a few minutes. Therefore it was postulated that O-O bond is formed by the two-electron reduction of the Mn^V, and the concomitant Mn^{III} hydroperoxy complex is further oxidized (e.g. by unreacted Mn^V) to a Mn^{IV} peroxide intermediate (detected by UV-Vis and HRMS). The later finally liberates O$_2$ by disproportionation or reductive elimination. (**Scheme I.9, 68**).
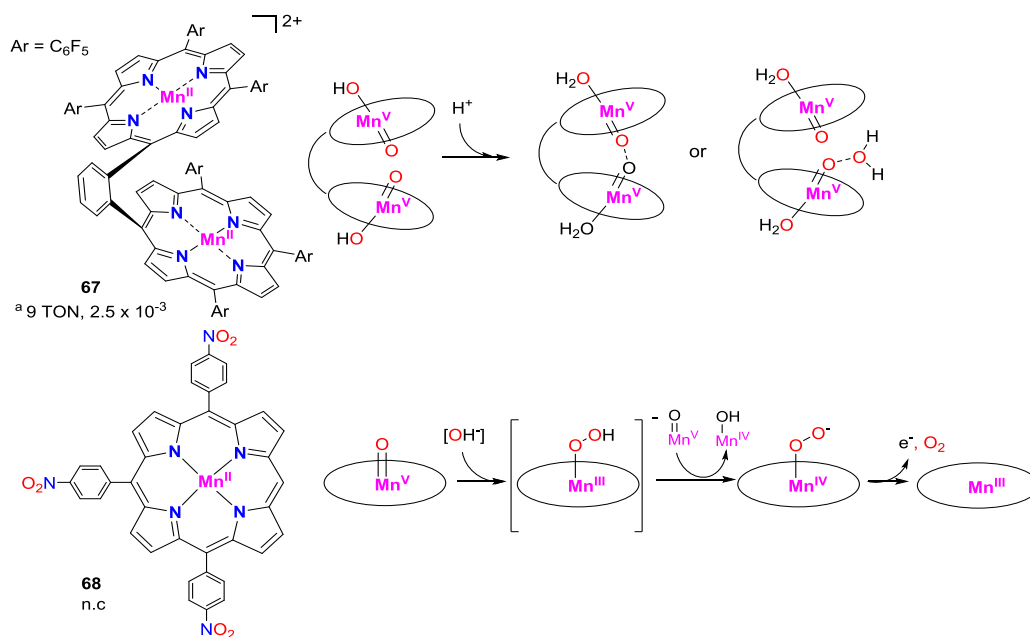
Scheme I.10. Top) First homogenous WOC based on first row transition metals. The active species for the water oxidation was suggested to be Mn^V. Ar = C_6F_5. Bottom) Proposed acid base mechanism for the water oxidation with Mn corrole-type complexes. [a] Electrochemical-driven water oxidation at 1.4V vs SHE. n.c. Not catalytic. Numbers reported in the figure stands for TON and TOF values.

I.5.1.5. Manganese Pyridine-amino Complexes

Organic ligands based on amino and pyridine moieties are very appealing for the design of simple and robust complexes for water oxidation. In 1986 Kaneko *et al.* reported the oxidation of water meditated by [$Mn_2(\mu\text{-}O)_2(bpy)_2$] using CAN as sacrificial oxidant (**Figure I.24, 69**). However, the reaction was not catalytic and oxygen was only observed at the surface of unsolved particles, suggesting that water oxidation was a heterogeneous process.[166]
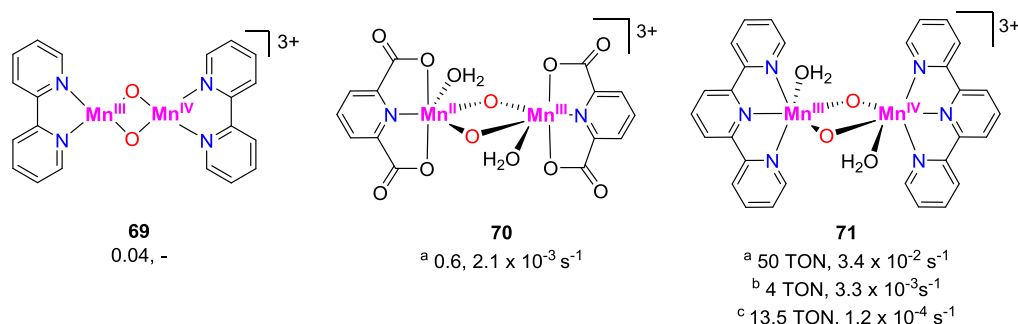
Figure I.24. Selected examples of pyridine based manganese complexes studied in oxygen evolution. [a] Oxone (HSO_5^-) was the sacrificial oxidant (SO).[167] [b] NaOCl was the SO. [c] Activity recorded when the catalyst was supported on a clay, CAN was the SO.[168] Numbers reported in the figure stands for TON and TOF values.

The severe oxidizing and low-pH conditions that implies the use of CAN as sacrificial oxidant was shown to be an important issue for the stability of manganese complexes based on

pyridine-amino ligands[169] and its replacement by alternative milder oxidants such as OCl[-] or HSO$_5$[-] (Oxone) resulted in a way to reach catalytic activity.[168] In this reagard, Brudvig and coworkers reported that [Mn$_2$[III,IV](μ-O)$_2$(terpy)$_2$](NO$_3$)$_3$ (terpy = 2,2´:6´,2´´-terpyridine, **Figure I.24, 71**) produced O$_2$ by using OCl[-] or oxone as sacrificial oxidants (4 TON and > 50 TON respectively) but not when using CAN.[167,170]

Mechanistic studies performed by the same authors showed a first-order dependence of reaction rates in the concentration of [Mn$_2$[III,IV](μ-O)$_2$(terpy)$_2$]$^{3+}$ and zero order on oxone. The resting state, determined by ultraviolet–visible (UV–vis) and electron paramagnetic resonance (EPR) spectroscopy, was the initial [Mn$_2$[III,IV](μ-O)$_2$(terpy)$_2$]$^{3+}$ complex. The thermodynamically favorable coordination of Oxone led to the formation of two possible isomers, produced by the two coordination vacancies available at the two metals cores (Mn[III] or Mn[IV]), preferring the interaction with the more electrophilic site (Mn[IV]). However, the high energetic barrier for the O-O bond cleavage and the concomitant two-electron oxidation of Mn[IV] to Mn[VI] inhibits the reaction, accumulating an inactive Mn[IV] species [(terpy)Mn[III](μ-O)$_2$Mn[IV]-(HSO$_5$)(terpy)]$^{3+}$. In equilibrium to this inactive species, the energetically less favored intermediate [(terpy) (HSO$_5$)-Mn[III](μ-O)$_2$Mn[IV](terpy)]$^{3+}$, which is catalytically competent, was oxidized to [(terpy)Mn[V](O)(μ-O)$_2$Mn[IV](terpy)]$^{3+}$ (best described as Mn$_2$[IV/IV]-oxyl radical) and this further reacted with water liberating dioxygen. The O-O bond cleavage for the formation of the formal Mn[V] was determined to be rate determining under excess of oxone (**Scheme I.11**).[171,172]

Competing with this pathway, [(terpy)Mn[V](O)(μ-O)$_2$Mn[IV](terpy)]$^{3+}$ could react with the resting state [Mn$_2$[III,IV](μ-O)$_2$(terpy)$_2$]$^{3+}$ to form the catalytically inert [Mn$_2$[IV,IV](μ-O)$_2$(terpy)$_2$]$^{4+}$ species. Independently synthesized [Mn$_2$[IV,IV](μ-O)$_2$(terpy)$_2$]$^{4+}$ sustained the inactivity of this species, probably due to the impossibility of being two-electron oxidized to Mn[VI] by oxone. The inverse correlation between the catalytic activity and the concentration of [Mn$_2$[IV,IV](μ-O)$_2$(terpy)$_2$]$^{4+}$ in solution (X-ray absorption spectroscopy) indicated that the comproportionation process (Mn[V,IV] + Mn[III,IV] $\rightarrow$ Mn[IV, IV]) was faster than the water oxidation. Hence, it was concluded that catalytic activity of the [(terpy)Mn[V](O)(μ-O)$_2$Mn[IV](terpy)]$^{3+}$ must be higher than that initially inferred by considering all the manganese complex to be active, due to the small amount of the latter that is actually contributing in the reaction. (**Scheme I.11**).[172]

DFT calculations support the catalytic reaction towards a formal [(terpy)Mn[V](O)(μ-O)$_2$Mn[IV](terpy)]$^{3+}$, and a water molecule with an accessible energetic barrier of 23 kcal·mol^{-1}.[173] The studies also manifested radical character of the Mn[V]–oxo moiety better described as Mn[IV]–oxyl that have a large positive impact on the formation of the O-O bond. Later on, *ab inito* molecular dynamic simulations suggested that the thermodynamic accessibility of the hydroperoxo species was critical and rate-limiting. An alternative deactivation mechanism was proposed towards the cleavage of one μ-oxo bridge to generate a poorly-catalytic [Mn[IV]O(μ-

O)Mn^{IV}(O)]$^{4+}$ dimer.[174] Labeling studies showed that at low concentration of oxone, the incorporation of ^{18}O from H$_2$^{18}O in O$_2$ increased. Therefore, the nucleophilic attack of the water molecule to [(terpy)Mn^V(O)(μ-O)$_2$Mn^{IV}(terpy)]$^{3+}$ yielding [(terpy)Mn^{III}(OOH)(μ-O)$_2$Mn^{IV}(terpy)]$^{2+}$ under low oxone concentration is favoured in certain extend.[175,176]
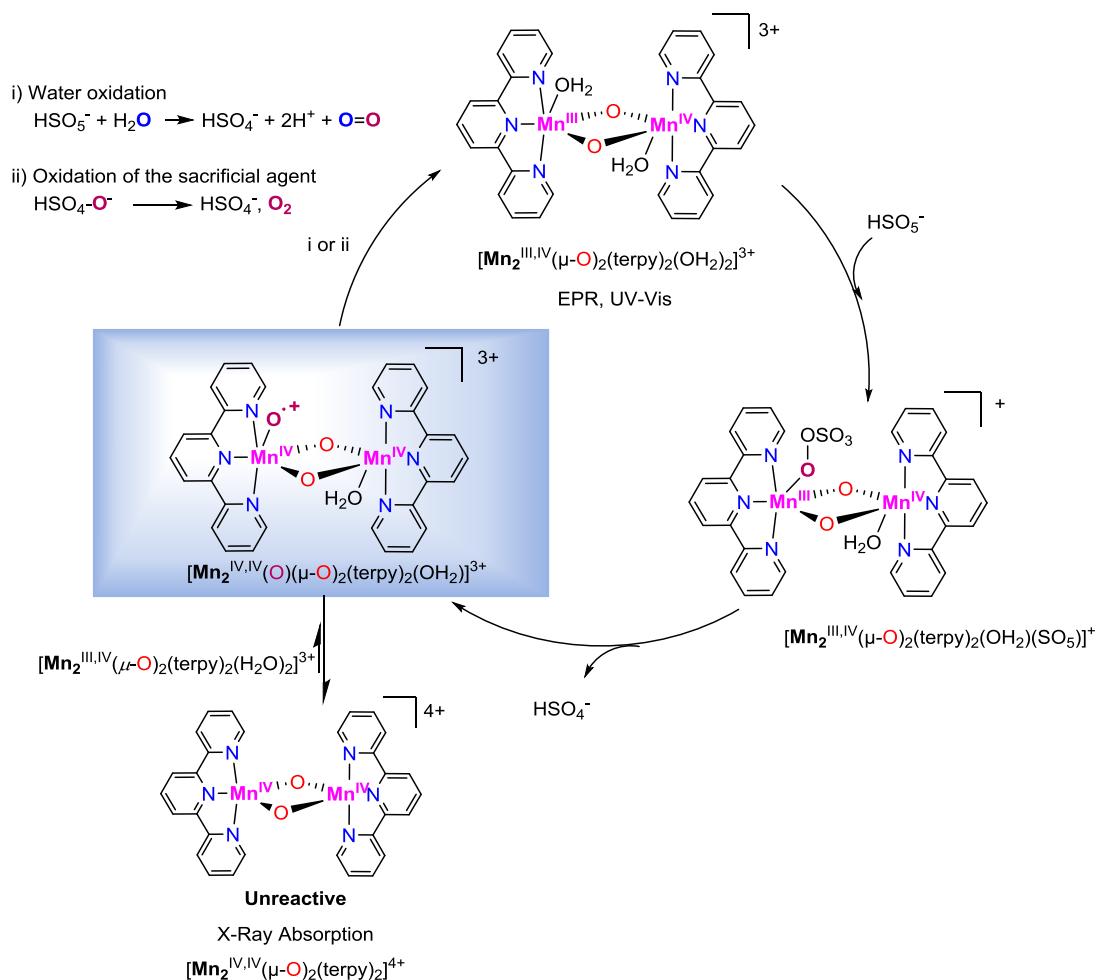
Scheme I.11. Mechanism proposed for the oxidation of water with [Mn$_2$^{III,IV}(μ-O)$_2$(terpy)$_2$(H$_2$O)$_2$]$^{3+}$ (terpy = 2,2':6,2''-terpyridine) when using Oxone as oxidant. The proposed intermediate responsible for the oxygen release has been highlighted.

The use of CAN as an outer sphere single electron oxidant is preferred to avoid parallel sources of O$_2$ not arising from H$_2$O. However the low pH of Ce^{IV} solutions is an important issue for the stability and few ligands can maintain its stability under these harsh conditions. To avoid this process, Yagi and Narita adsorbed the manganese complex into different layered compounds (e.g. kaolin or mica). This strategy was also implemented to allow the mono-electronic oxidation of the inactive Mn^{IV} centers to Mn^V. A maximum TON of 14 was observed and the stability of the entire [Mn$_2$^{III,IV}(μ-O)$_2$(terpy)$_2$]$^{3+}$ / clay material after 30min of treatment with CAN was confirmed by EXAFS.[168,177] This was a remarkable result since it indicates a real catalytic water oxidation activity. However, the real nature of the catalyst is difficult to be identified.

Nevertheless, clay adsorbed complexes can be used to elucidate fundamental details in the water oxidation ability of Mn complexes. For instance, electronic effects, introduced by ligand modification, could be evaluated by studying the catalytic activity in water oxidation (WO) of a series of $[Mn_2^{III,IV}(\mu-O)_2(R-terpy)_2]^{3+}$ (R-terpy = 4'-substituted 2,2':6',2''-terpyridine) under the presence of CAN. Strong correlation between $E_{1/2}$ of $Mn_2^{III,IV}$ /$Mn_2^{IV,IV}$ and the second-rate constant (k_2) for the catalytic activity was observed. The higher the reduction potential, the higher the k_2 observed.[178]

Focused on the degradative side reactions of the complex under harsh conditions, a very promising alternative was reported by Nepal and Das,[179] assembling the catalyst in a well-defined pore of a robust MOF $(Cr_3(\mu-O_3) (CH_3COO)_6)$ providing extra-stability to the complex towards acidic and oxidant conditions and blocking its diffusion between pores or to the external solution. This methodology resulted in a 20-fold improvement of the catalytic activity with respect to the previously reported by Brudvig and coworkers. Fourier transformed infrared (FTIR), EPR, UV–vis, and elemental analysis supported the intact presence of $[Mn_2^{III,IV}(\mu-O)_2(terpy)_2]^{3+}$ after the reaction with oxone as sacrificial oxidant. Even more interesting was the activity observed when CAN was used as SO. TOF of 40 h^{-1} was reported for more than 7 days of catalysis, being one of the few report of a "true" homogeneous WO catalyst based on manganese.[180]

Complementarily to those works, the electrochemical generation of the $[Mn_2^{IV,IV}(\mu-O)_2(terpy)_2]^{4+}$ revealed the dimerization of this complex to a thermodynamically stable linear tetranuclear Mn cluster $[Mn_4O_5(terpy)_4(H_2O)_2]^{6+}$, linked through a μ-oxo bridge. This compound was shown to be spontaneously formed when $[Mn_2^{IV,IV}(\mu-O)_2(terpy)_2]^{4+}$ was dissolved in water. The resulting tetramer cannot be further oxidized under electrochemical conditions neither by oxone. The light-driven WO (with $[Ru(bpy)_3]^{2+}$ as PS and $Na_2S_2O_8$ as SO) yielded similar amounts of O_2 as in the blank reaction.[181] However, once adsorbed on kaolin, the tetramer was found active using CAN as sacrificial oxidant **(Scheme I.12)**.[182]
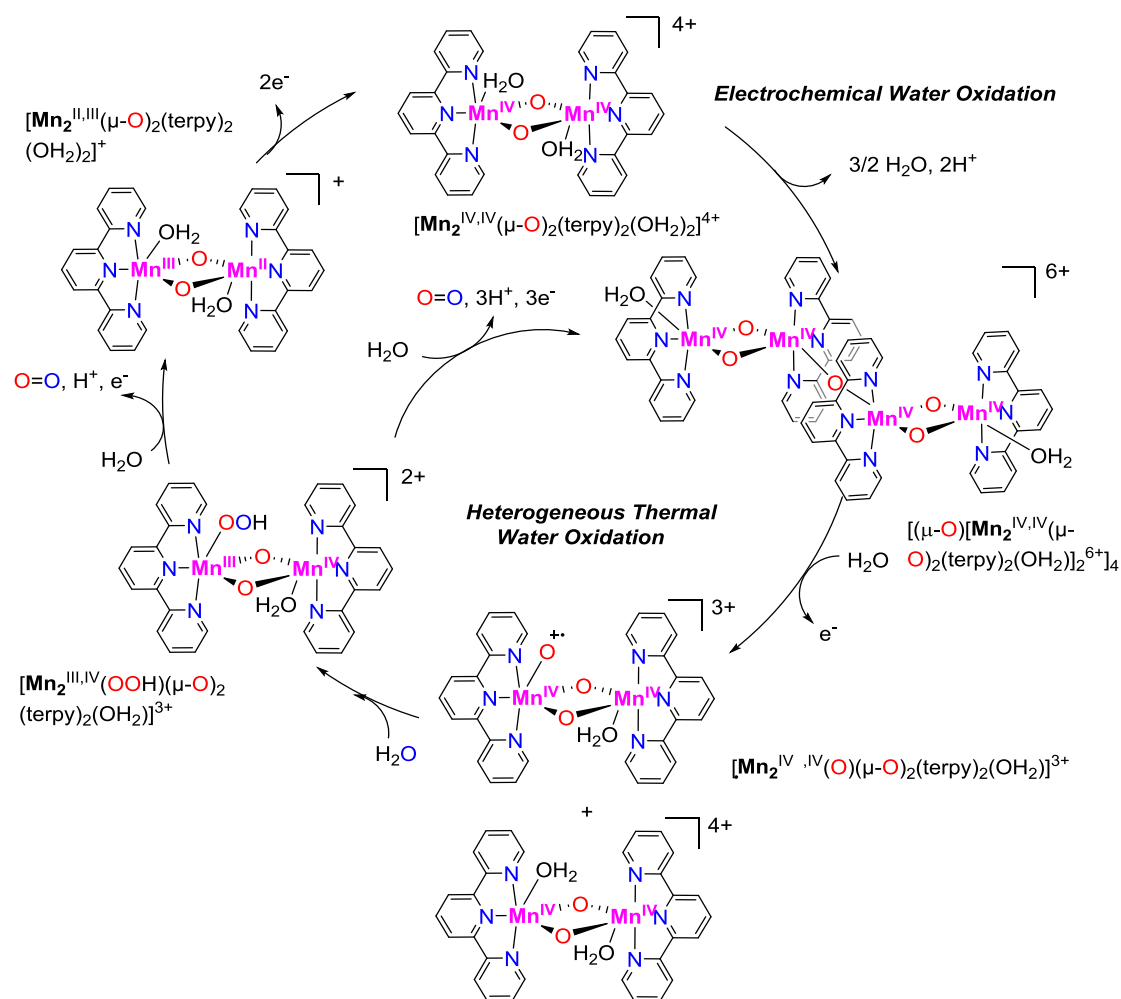
Scheme I.12. Catalytic cycles proposed for the water oxidation with the tetrameric Mn species. The external cycle was proposed for the activity observed under electrochemical conditions, where $Mn_2^{IV/IV}$ dimerizes upon addition of current. The internal path corresponds to the heterogeneous system (tetramer supported on clay), when CAN is used as sacrificial oxidant.

Another interesting complex was reported in 2005 by McKenzie and co-workers. $[Mn^{II}_2(mcbpen)_2(H_2O)_2](ClO_4)_2$ (mcbpen = *N*-methyl-*N'*-carboxymethyl-*N,N'*-bis(2-pyridylmethyl)ethane-1,2-diamine) produced oxygen under the presence of large excess of *tert*-butylhydroperoxide (*t*BuOOH) as sacrificial oxidant.[183] On the basis of ESI-MS spectrometry and UV spectroscopy, the authors proposed a mechanism scheme (**Scheme I.13**) where an initial Mn^{II} dimer was cleaved and oxidized to monomeric $[Mn^{III}(mcbpen)(OH)]^+$ species and a new dimerization took place upon extrusion of a water molecule, to give a short-lived $[Mn^{III}_2(mcbpen)_2(\mu\text{-}O)]^{2+}$ intermediate, detected by ESI-MS and UV-Vis. A subsequent oxidation was proposed to generate a "diamond-core"-type dimer, $[Mn^{IV}_2(mcbpen)_2(\mu\text{-}O)_2]^{2+}$, which collapses releasing O_2 and regenerating the initial $[Mn^{II}_2(mcbpen)_2(H_2O)_2]^{2+}$ species. Surprisingly, evolution of $^{34}O_2$ along with some $^{32}O_2$ was observed in labeling studies using 95% $H_2^{18}O$ (no $^{36}O_2$ was observed).[184,185] 15,000 TONs were achieved without apparent oxidative

damage, neverthless tBuOOH is known to evolve O_2 *via* one-electron radical-type pathways and therefore the exact amount of oxygen produced from the water oxidation reaction could not be established. While the system was also active with oxone as SO, the use of single electron outer sphere oxidants such as CAN or $[Ru(bpy)_3]^{3+}$ results in substoichiometric O_2 evolution.[183] The analogous dimeric intermediates, $[Mn^{IV}_2(mcbpen)_2(\mu\text{-}O)_2](ClO_4)_2$ and $[Mn^{IV}_2(bpmg)_2(\mu\text{-}O)_2](ClO_4)_2$ (bpmg = 2-[[2-[bis(pyridin-2-ylmethyl)amino]-ethyl](methyl)amino]acetic acid), were isolated by Anderlund and coworkers but no O_2 was detected after treatment with CAN, nor with oxone, in contrast to the proposal by McKenzie.[186] A remarkable different coordination (2-picoline was replaced by the free methyl carboxy moiety) was observed when Anderlund *et al.* reproduced the synthetic procedure reported by McKenzie *et al*. Unfortunately, the sum of observations did not shed light into the nature of the O_2 formed.

(a)

72
ª15,000 TON, -

(b)
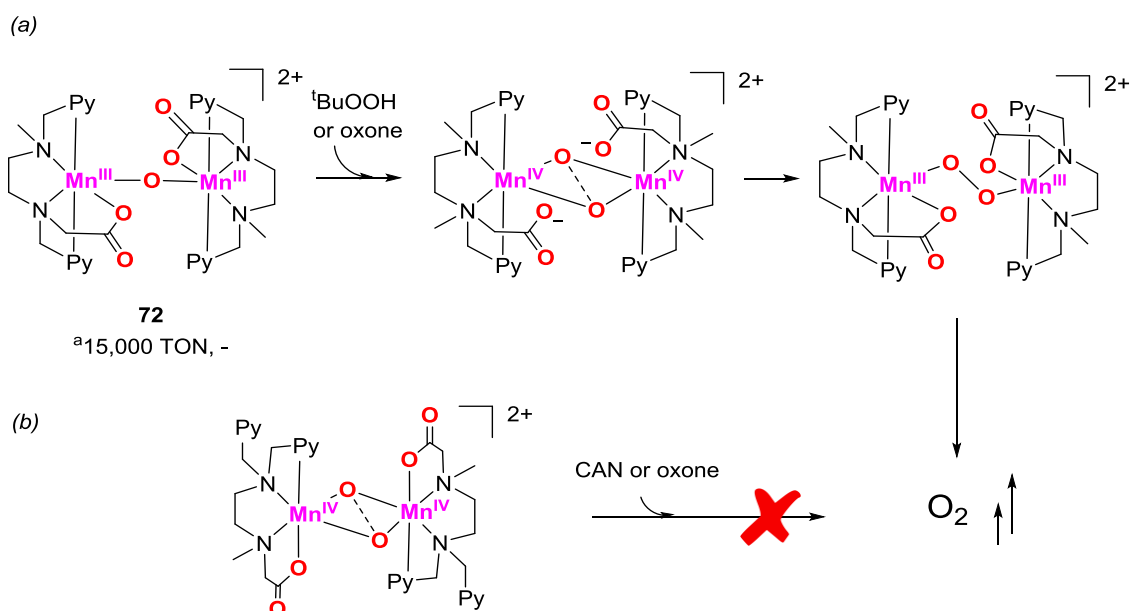
Scheme I.13. a) Collapse of the diamond core proposed by McKenzie et al. and b) Unreactive intermediate isolated by Anderlund and co-workers. tBuOOH was the SO.

The effective comparison between WOCs is usually difficult due to the different catalytic conditions employed for different complexes. An attempt to uniform results among selected dimeric manganese complexes was carried out by Styring and co-workers (**Table I.2**).[187] The results summarized in **Table I.2** shows that the complex reported by Crabtree and Brudvig *et al.* can be considered superior in terms of O_2 evolution rates. Again, it was highlighted that oxo-transfer sacrificial oxidants (H_2O_2, oxone, ClO⁻ or tBuOOH) produces catalytic amounts of O_2, while the use of pure electron-transfer agents (CAN or $[Ru(bpy)_3]^{3+}$) do not proceed under homogeneous conditions.

Table I.2. Comparison of oxygen evolution rates [$mM_{O2}\,min^{-1}\,M_{metal}^{-1}$] for selected manganese complexes for the water oxidation under the same catalytic conditions: 2 mM of catalyst, 50 eq of sacrificial oxidant. The rate was detected 2 min after the addition of the SO using a Clark electrode.

[$Mn_2^{II,II}(\mu\text{-}OAc)_2(bpmp)_2$]$^+$

73

[$Mn_4^{IV,III,II,II}(\mu\text{-}O)_4(tphpn)_2$]$^{3+}$

74
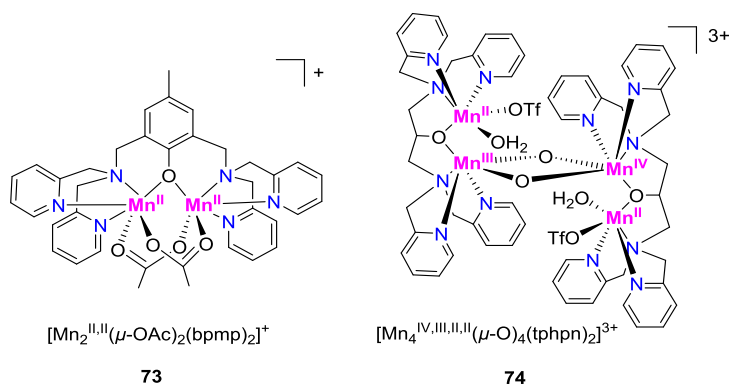
Compound	$H_2O_2^a$	^tBuOOH	HSO_5^-	ClO^-	Ce^{4+}
73	33	1	16	n.d.	n.d.
74	>500^b	34	105	n.d.	n.d.
72	7.5	traces	38	traces	n.d.
71	1.8	36	>500^b	7	n.d.

n.d. non oxygen detected above the lower detection limit of 1 $mM_{O2}min^{-1}M_{metal}^{-1}$. 2 equiv. of H_2O_2 added. ^{b}O$_2$ evolution faster than the upper detection limit of the Clark electrode.

Recently, Brudvig *et al.*[188] studied [Mn(PaPy$_3$)(NO$_3$)](ClO$_4$)] (**75**, PaPy$_3$H = *N,N*-bis(2-pyridylmethyl)-amine-*N*-ethyl-2-pyridine-2-carboxamide) (**Figure I.25, 75**), which showed water oxidation activity using oxone as SO (4 TON and 1.4·10^{-2} TON·s^{-1}). In contrast, [Mn(N4Py)OTf]OTf] (N4Py = 1,1-di(pyridin-2-yl)-*N,N*-bis(pyridin-2-ylmethyl)methanamine (**Figure I.25, 76**) and [Mn(PY5(OH$_2$)](ClO$_4$)$_2$ (PY5 = 2,6-bis(bis(2-pyridyl)methoxymethane)-pyridine)) showed very low and non-oxygen evolution (**Figure I.25, 77**) under the same conditions (**Figure I.25**). The authors suggested that [Mn(PaPy$_3$)(NO$_3$)](ClO$_4$)] was robust enough to avoid protonation and the anionic *N*-donor moiety increases the stability of the high-valent intermediate competent for the oxygen evolution.

75
4 TON, 1.4 x 10^{-2} s^{-5}

76
-, 1.4 x 10^{-3} s^{-1}

77
n.d
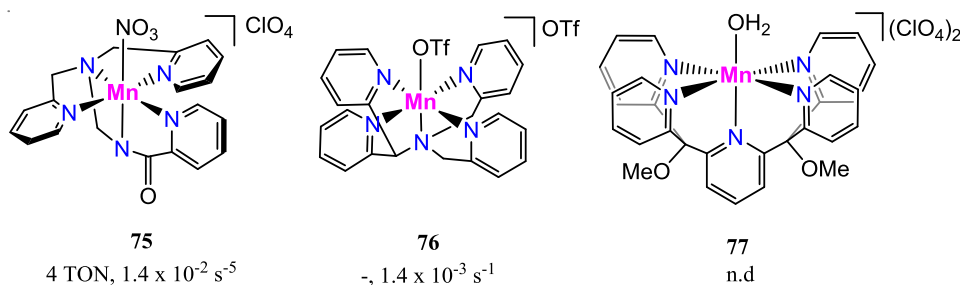
Figure I.25. Mn complexes tested for the water oxidation, using Oxone as sacrificial oxidant.

A clay support was again key for the WO catalyzed by the complex $[Mn_2(TPA)_2(\mu\text{-}O)_2]^{2+/3+}$. While negligible TON was reported for the homogeneous water oxidation with Ce^{IV} as SO, once anchored the activity became higher (2.6 TON and TOF of $5.2 \cdot 10^{-3}$ s^{-1}). STEM (Scanning transmission electron microscopy) and EDS (Energy-dispersive X-ray spectroscopy) do not show formation of NP. A signature of a $Mn^{IV,IV}$ intermediate was detected by UV-Vis and EPR and the intermediate could be isolated (XRD). The adsorption on clay of the isolated species $Mn^{III,IV}$ and $Mn^{IV,\ IV}$ was confirmed by UV-Vis, EPR and XRD, and the data suggested the structure was conserved for both. 2.4 and 1.9 TON were observed upon addition of CAN, respectively. Because no ^{18}O exchange was observed in the oxo-bridge ligands (IR spectroscopy), the authors proposed a mechanism where the N-donor site is decoordinated and replaced by an oxo moiety that will further react with a water molecule.[189]

While the main goal is to finally achieve the light driven water oxidation, since 1985 there are few successful examples. Mn(III) salen complexes where found able to liberate oxygen in the presence of an excess of *p*-benzoquinone and irradiation with visible light. The O_2 evolution proceeded with a concomitant reduction of the *p*-benzoquinone to semiquinone. The activity was highly sensitive to the structure. $[Mn(salpd)(H_2O)]^{2+}$ (salpd = propane-1,3-diylbis(salicylideneiminate)) is one of the most active complexes reported. Kinetic studies showed that the rate of dioxygen evolution was first-order dependent on the Mn(III) complex and half-order on quinone concentrations. Rates were strongly dependent on the pH of the reaction medium, but solvent independent. [190-192]

An effort to mimic the electron transfer between chlorophyll, tyrosine, and the OEC that leads the water oxidation reaction in the PSII was carried out by Styring and co-workers. They assembled a photosensitizer (e.g., a ruthenium based complex), through a tyrosine to a monomeric and a dimeric manganese-based complexes. The authors observed, on the basis of EPR spectroscopy and optical flash photolysis techniques, photon driven stepwise electron transfer from the Mn complex to the tyrosine and finally to the Ru complexes mimicking the electronacceptor site of PSII. [193-195]

The first pure homogeneous water oxidation catalyst working in the presence of an outer sphere single electron transfer oxidant ($[Ru(bpy)_3]^{3+}$ (bpy = 2,2'-bipyridine)) was the dimeric $[Mn_2(dCIP)(OMe)(CH_3CO_2)]$ (dCIP = 2-(3-(7-carboxy-1*H*-3λ^4-benzol[*d*]imidazol-2-yl)-2-hydroxyphenyl)-1*H*-benzo[*d*]imidazole-4-carboxylic acid).[196] $[Mn_2(dCIP)(OMe)(CH_3CO_2)]$ was found capable of carrying out the WO with a TON of 25 and TOF of 0.027 s^{-1}. Interestingly, crystallization in hot methanol yielded a tetrameric structure of the compound, reminiscent of the OEC cluster (**Figure I.26, 78**). Labeling studies with 5.8% ^{18}O-enriched water were in agreement with a water oxidation process and the catalyst was found competent for the light-driven process

with a TON of 4 ($Na_2S_2O_8$ as SO and $[Ru(bpy)_3]^{2+}$ or $[Ru(bpy)_2(4,4'-CO_2Et-bpy)](PF_6)_2$ as photosensitizers).

78

25 TON, 2.7×10^{-2} s^{-1}

[a] 4 TON, -
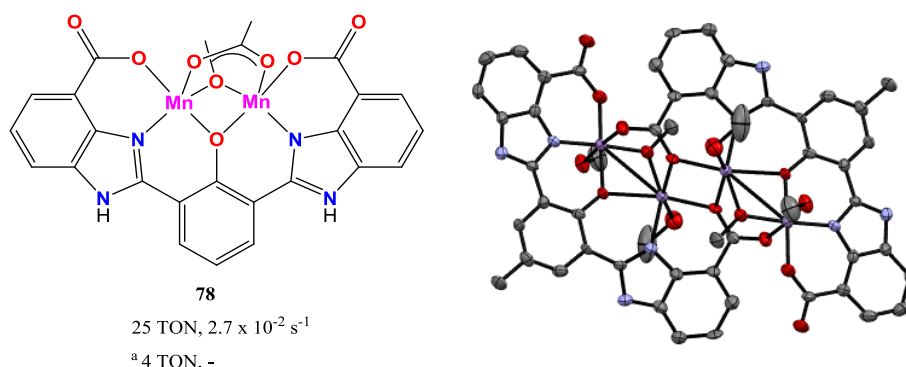
Figure I.26. Left) Line drawing of the first homogeneous Mn-WOC working with monoelectronic oxidants. Right) X-ray crystal structure at 50% probability level of the biomimetic complex formed upon refluxing in MeOH.[196] [a] Light-driven conditions ($[Ru(bpy)_2(4,4'-CO_2Et-bpy)](PF_6)_2$ as PS and $Na_2S_2O_8$ as SO, in NaPi buffer, pH 7.2)

I.5.2 Early Work On Cobalt, Iron And Copper As Alternative Metals For The Water Oxidation

The first reports related to the homogeneous water oxidation catalysis by first row transitions metals dates from the early 80s. Selected salts and complexes were identified as promising water oxidation catalysts working in neutral or basic conditions, in the presence of buffers. The use of stoichiometric electron acceptors (usually $[Ru(bpy)_3]^{3+}$) was a common approach to generate the four oxidizing equivalents needed for the water oxidation.

Initially, Shafirovich and coworkers reported that simple Co^{II} ions were efficient water oxidation catalysts (WOC) in the presence of $[Ru(bpy)_3]^{3+}$, being active above pH 5 in phosphate buffer (NaPi).[197] The catalytic activity stopped due to the precipitation of oxidized Co species from solution because the active specie was removed from the solution-phase reaction. The mechanism was studied by stopped-flow but kinetics were found complicated and very dependent on the initial concentrations of both the catalyst and the sacrificial oxidant. At pH 6.5-7.2 (0.025 M phosphate, 0.1 M ionic strength, 25ºC) with $(1-10) \cdot 10^{-5}$ M Ru^{III}, $(1-10) \cdot 10^{-4}$ M Ru^{II} and $(1-6) \cdot 10^{-6}$ M Co^{II}, first order kinetics on $[Co^{II}]$ and second order on [Ru] were reported.[198] A $[Co^{IV}]$ intermediate was postulated as the active species.

By this time, Elizarova and coworkers also reported water oxidation by bipyridyl complexes based on first-row transition metals (Co, Cu and Fe).[99] Cobalt was also found active coordinated with ammonia, ethylendiamine and oxyacids but the yields reported were nearly stoichiometric. The use of sulfonated phtalocyanines as ligands in basic media (NaOH, pH 9-10)

were also useful for the oxygen production, being Fe and Co complexes the most active metals with turnover numbers of 10. A similar value was reported for the Co-Porphyrin complex.

I.5.3   Cobalt Water Oxidation Catalysts

Until 2008, water oxidation research was mainly focused on ruthenium and manganese. While those systems remained in solution during electrocatalysis, allowing their mechanistic study, cobalt salts precipitated after few catalytic cycles, complicating its mechanistic study. But in 2008 cobalt reemerged, held on by Nocera's group.[199] They observed that the cobalt precipitate remained active in the heterogeneous phase and took advantage of that by supporting the catalyst on an electrode surface (by electrodeposition). These modified electrodes exhibited a highly improved long-term water oxidation activity. In light of this, the Co-complexes were relaunched and several research groups have developed homogeneous Co systems aiming at the understanding in molecular scale of the water oxidation mediated by cobalt. However, likewise in iridium WO catalysts, simple Co^{2+} ions and cobalt-oxides are active catalyst for the oxygen production and a great effort is usually needed to distinguish between homogeneous and heterogeneous systems.

I.5.3.1.   Cobalt Polyoxometalates

The first homogeneous Co-WOC was reported in 2010. Craig L. Hill and coworkers proposed the use of carbon-free polytungstate ligands (polyoxometalates such as $P_xW_xO_x$ and $Si_xW_xO_x$) to carry out the water oxidation in a robust environment (**Figure I.27**).[200] They found $[Co_4(H_2O)_2(PW_9O_{34})_2]^{10-}$ (Co$_4$POM, **Figure I.27, 79**) able to produce O_2 in a high rate (TOF of 5 s^{-1}, 75 TON) in phosphate buffer (pH 8), using $[Ru(bpy)_3]^{3+}$ as the SO. Authors provided several data in agreement with the stability of the compound in solution (UV-Vis, ^{31}P NMR). The addition of bpy to chelate possible free CoO_x species decreased the O_2 yield from 67% to 48%, indicating that at least CoO_x originated from aqueous Co^{2+} is not the dominant catalyst. The recyclability of the Co$_4$POM was proved by IR. By addition of an excess of $[Ru(bpy)_3]^{2+}$ after the reaction, Na$_8$Ru(bpy)$_3$-Co$_4$POM precipitates. The infrared spectrum of the solid showed signals consistent with the presence of the initial POM structure, and the recycled material showed an O_2 yield of 49% (58 TON, by the addition of new batch of $[Ru(bpy)_3]^{3+}$), in good agreement with the first-round catalysis. However, this evidence did not rule out the possibility of a second catalyst (Co$_4$POM fragment or heterogeneous CoO_x) being as well active for the WO. A high current was also observed by electrochemistry at low overpotential ($\eta = 0.44$ V, pH 8), and slightly below the Ru^{3+}/Ru^{2+} redox couple (1.21 V vs SHE, $\eta = 0.45$ V), as expected for the activity observed using Ru^{3+} as SO. The light-driven oxidation yielded a turnover of 224 (yield of O_2 ($[O_2]/[SO]^0) = 45\%$), with an initial quantum yield (O_2 produced / absorbed photons, in %) of 30%.[201] The activity was limited by the depletion of the SO (persulfate) and no evidence of particle formation was observed

by DLS. Moreover, Burmazovic and coworkers showed that under basic pH (6-10) the compound has a great stability (data from HRMS), in favor to a homogeneous catalytic process. By labeling studies (^{17}O-NMR spectroscopy) they suggested that the specific binding mode of the water ligand in a protected cavity of this Co-POM can be key for the water oxidation.[202]

However, a detailed study (electrochemistry, kinetics, UV-Vis, SEM, and EDX) of the system by Finke *et al.* showed that Co$_4$POM in phosphate buffer solution (pH 8) was slowly hydrolyzed, releasing Co^{II} (from a 500 µM solution of Co$_4$POM, 11.6% of Co^{II} was liberated, determined by linear sweep voltammetry). The identical O$_2$ evolution time course was observed by bulk electrolysis (1.3 V) for a 3 h aged catalyst (500 µM) and for a free Co^{2+} solution (58 µM [Co(NO$_3$)$_2$] = 11.6% [Co$_4$POM]). This data strongly suggested that under that electrochemical conditions the main catalytic activity arises from the electrodeposited CoO$_x$.[203]

Nanosecond laser flash photolysis carried out by Scandola and coworkers showed that the hole scavenging§ from Ru(bpy)$_3$$^{3+}$ in the Co$_4$POM during the light-driven WO was limited for freshly prepared solutions, while it was improved for aged complexes. The observed electrochemical water oxidation onset for a fresh solution of complex, 1.5 V vs SHE, was too high to be achieved by [Ru(bpy)$_3$]$^{3+}$ (1.21 V) and thus, it was argued that the reaction cannot be carried out neither in dark (chemical generated [Ru(bpy)$_3$]$^{3+}$), nor in photochemical conditions with the starting Co$_4$POM complex. Because Co(NO$_3$)$_2$ was not able to reduce [Ru(bpy)$_3$]$^{3+}$ at the 0-100 ms time scale, the formation of the catalytic species was postulated to arise from the starting Co$_4$-POM.[204]

In a later publication, Finke *et al.* found that hydrolysis of the Co$_4$-POM was strongly dependent on the reaction conditions and thus it is very important to determine which catalyst is the legitimate under the conditions employed. Indeed, homogeneous water oxidation catalysis was observed at higher potentials (>1.5 V vs SHE, where Co$_4$-POM is apparently more stable) and low concentrations of catalyst (2.5 µM) (those conditions favors WO by discrete Co$_4$POM units). A new irreversible oxidation wave (1.45 V) was found 200 mV more positive than Co(NO$_3$)$_2$, and the amount of aqueous [Co^{2+}] found in solution (170 nM) did not form the sufficient CoO$_x$ needed for the amount of oxygen produced (bulk electrolysis at 1.6 V with 200 nM Co(NO$_3$)$_2$ do not show measurable O$_2$ evolution). Therefore, this data suggest that under those conditions, water oxidation is produced by a homogeneous catalyst. However, an additional question stands for whether the Co$_4$POM transform into heterogeneous CoO$_x$ under the oxidative conditions. A post-bulk electrolysis (60 s) analysis of the solution shows a 50 nM increase of Co^{2+} in solution, something that would account for all the catalytic activity observed, as long as the Co^{2+} species formed under oxidative conditions belong to the highly catalytic heterogeneous

---

§ Ru(bpy)$_3$$^{3+}$ is generated by quenching Ru(bpy)$_3$$^{2+}$* (excited state achieved by a 355nm laser) with Na$_2$S$_2$O$_8$ in a <10ns timeframe and the reaction with the catalyst (the recovery of the Ru(bpy)$_3$$^{2+}$, chromophore at 450nm) is monitored in the ms timescale 450nm.

CoO$_x$ species.[205] Hence, the observed partial instability of the Co$_4$POM after the electrolysis did not shed light on the true catalyst. Also a follow-up study using the conditions employed by Scandola and coworkers in the laser flash photolysis studies[206] (*vida supra*) did not show oxygen evolution. Therefore, a proper mechanistic interpretation requires also the measurement of O$_2$ evolution, something problematic on fast time scales.[207]

Hill and coworkers quantified the amount of Co^{2+} (aq.) released from Co$_4$POM using cathodic adsorptive stripping voltammetry (CAdSV) and by extracting the soluble anionic catalyst with a toluene solution of tetraethylammonium nitrate (the strong interaction between the cation and the anion allows the extraction of the POM from water) for further quantification of the aqueous phase by inductively coupled plasma mass spectrometry (ICP-MS). Both methods showed the presence of 3.5% of free Co. The extraction of the Co$_4$POM (for the ICP-MS analysis) produced the loss of ~98% of the catalytic activity, indicating the amount of free metal was not enough to account for the WO. The authors put emphasis again in the importance of the reaction conditions, being pH, ionic strength, buffer composition, and concentration variables that substantially modifies the POM stability and reactivity.[206] Moreover, EXAFS studies revealed the integrity of the structure under catalytic conditions with chemical oxidant, without evolution of cobalt oxides.[208] Because Co$_4$POM was found stable after the catalysis, the hydrolytic fragmentation proposed by Scandola and coworkers (*vide supra*) can only be expected if the active species can revert into the original complex again.

In the process of studying the reaction mechanism, Finke and coworkers observed a self-oxidation process of both Co$_4$POM and [Ru(bpy)$_3$]$^{3+}$, leading to the precipitation of a POM-[Ru(bpy)$_3$]$^{2+}$ species. This process was in competition with the O$_2$ production. Using catalytic conditions for which O$_2$ evolution was maximized, a kinetic study of the Co$_4$POM was carried out. While CoO$_x$ was found superior for the WO in terms of reaction rates, kinetic analysis showed that under the conditions reported the most abundant catalyst was Co$_4$POM. The determination of the rate law was masked by decomposition pathways but kinetics indicate common oxidative species for both O$_2$ production and ligand oxidation, being the later process favored, therefore indicating, according to the authors, a limitation for future applications.[209]

Due to the numerous degradation pathways and the strong dependency on the WO conditions, there are still no indications for the rational design of Co-POM WOCs. However, other examples were reported as active compounds for the oxygen production. The keggin-type POM K$_7$[Co^{III}Co^{II}(H$_2$O)W$_{11}$O$_{39}$] (**Figure I.27, 80**) was found active for the light-driven (TON$_{max}$ = 360, TOF$_{max}$ = 0. 5 s^{-1}) and thermal (TON$_{max}$ = 15, TOF$_{max}$ = 0.06 s^{-1}) water oxidation, with an O$_2$ yield of 30% and 60%, respecively.[210] No nanoparticles were detected (by DLS, CV, FT-IR, EDX, laser flash photolysis) and the catalyst was recyclable, showing similar activities as the freshly prepared sample. The electrochemical onset for the water oxidation was observed at 0.97

V, easily accessible for the hole-scavenging (1.12 V vs SHE was reported for $[Ru(bpy)_3]^{3+}$), favoring the homogeneity of the mechanism.[210]
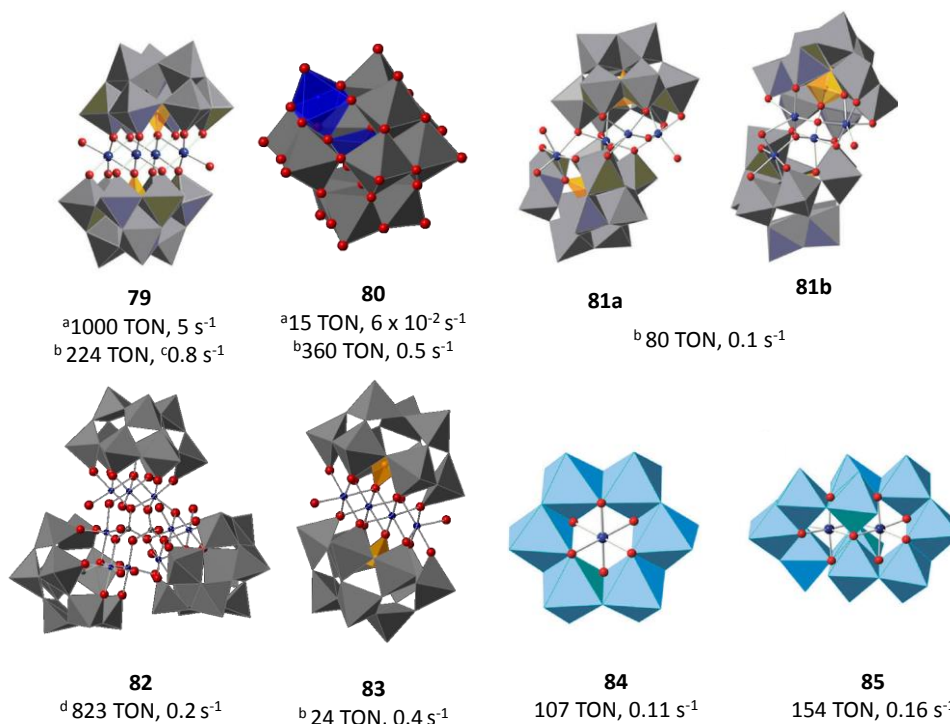
Figure I.27. X-ray crystal structure in combination with ball-and-stick and polyhedral representations of CoPOM WOCs adapted from reference [211] with permission from The Royal Society of Chemistry. **79**) $[Co_4(H_2O)_2(PW_9O_{34})_2]^{10-}$, **80**) $[Co^{III}Co^{II}(H_2O)W_{11}O_{39}]^{7-}$, **81 a and b**) isomers of $[\{Co_4(\mu\text{-}OH)(H_2O)_3\}(Si_2W_{19}O_{70})]^{11-}$, **82**) $\{Co_9(H_2O)_6(OH)_3(HPO_4)_2(PW_9O_{34})_3\}^{16-}$ **83**) $\{Co_4(H_2O)_2(SiW_9O_{34})_2\}\cdot n H_2O\}^{10-}$, crystal obtained from another source [212] **84**) $[CoMo_6O_{24}H_6]^{3-}$, and **85**) $[Co_2Mo_{10}O_{38}H_4]^{6-}$. Oxygen is in red, cobalt in blue, phosphorous in grey (figure 80) and polyhedra CoO_6 (**80**), WO_6 and MoO_6 are dark blue, grey and light blue (**84, 85**) respectively. Si and P are drawn as translucent orange polyhedra. [a] $[Ru(bpy)_3]^{3+}$ was the SO. [b] Light driven WO ($Na_2S_2O_8$, $[Ru(bpy)_3]^{2+}$). [c] TOF was calculated graphically. [d] NaOCl was the SO and TON were obtained by 4 cumulative additions of SO.

$[\{Co_4(\mu\text{-}OH)(H_2O)_3\}(Si_2W_{19}O_{70})]^{11-}$ (**Figure I.27**, two isomers (**81a and 81b**) in 1:1 ratio) was obtained trying to isolate the analogous Si-centered Co_4POM by Hill and coworkers.[213] Under illuminated conditions ($[Ru(bpy)_3]^{2+}$ and $S_2O_8^{2-}$, pH 9), 80 TON were reported, with an initial TOF of 0.1 s^{-1} and an O_2 yield around 24%. The compound gradually decomposed into $[\{Co(H_2O)\}(\mu\text{-}H_2O)_2K\{Co(H_2O)_4\}(Si_2W_{18}O_{66})]^{11-}$ and $[Co(H_2O)SiW_{11}O_{39}]^{6-}$ but due to the much slower activity observed with the isolated byproducts, the initial POM was considered an active WOC.

Another example able to catalyze the thermal WO was reported by Mascarós and coworkers, consisting in a triple Keggin-type POM containing a nonacobalt core ($\{Co_9(H_2O)_6(OH)_3(HPO_4)_2(PW_9O_{34})_3\}^{16-}$ (**Figure I.27, 82**).[214] In this study, electrolysis of the Co_9POM (in pH 7 NaPi buffer) at 1.41 V vs SHE resulted in the formation of an electrodeposited

film, containing cobalt and phosphorous, which maintains its activity when transferred to a control buffered solution. The addition of a chelate ligand (2,2'-bipyridin (bpy)) during the bulk electrolysis resulted in a 40-fold decrease of the current and no CoO_x film was detected after the electrolysis. At the end of the reaction, $([Co(bpy)_3]^{3+})_4Na_4[Co_9POM]$ precipitated from the solution. This compound could be prepared by the addition of $[Co(bpy)_3]^{3+}$ to a solution of Co_9POM. The cyclic voltammetry showed a peak at 0.75 V and a catalytic onset at 1.1 V. Upon addition of bpy, the signal at 0.75 V disappeared. This observation, together with the lack of film deposition under the presence of bpy suggest that no CoO_x is present when bpy is added in solution and therefore the remaining catalytic activity arises from an homogeneous WOC. This homogeneity was reinforced using NaOCl as sacrificial oxidant. Up to 800 TON of O_2 per metal were accumulated by several loadings of NaOCl (dissolved in sodium phosphate buffer (NaPi) pH=8). The maximum TOF observed was 0.2 s^{-1}. No sign of fatigue was detected for one-week aged catalyst solutions. Moreover, addition of bpy does not change the O_2 yields and no NP were detected by DLS. Because heterogeneous catalysis were not completely excluded in the electrochemical studies, a subsequent article using the insoluble Cs^+ salt of **82** as a doping agent into a carbon electrode, showed a robust catalytic process under a large range of pH.[215] Control experiments using 125 μM of Co_3O_4 showed 2-3 times less activity than 2 μM of Co_9POM, thus reinforcing the catalytic activity of the polyoxomethalate.

A sandwich-type cobalt containing silicotungstate $[Co_4(H_2O)_2(SiW_9O_{34})_2]^{12-}$ (**Figure I.27, 83**) was also isolated and tested as WOC by Patzke *et al.* under light-driven conditions $([Ru(bpy)_3]^{2+}$ and $S_2O_8^{2-})$. TON of 24 and TOF of 0.4s^{-1} (at 20 μM and 42 μM of catalyst, respectively) were reported. Systematic stability tests (spectroscopy, light scattering and microscopy) supported the presence of the entire complex. Interestingly a CoPOM-PS intermediate (PS = $[Ru(bpy)_3]^{2+}$) was formed in the initial stages of the reaction. This compound was found to precipitate under dark conditions when the complex was added to a $[Ru(bpy)_3]^{2+}$ solution (Na_2SiF_6 buffered medium), or could be recovered after 15 min of illumination, by centrifugation of the solution (according to ATR FT-IR). The catalytic activity could be reactivated at least twice by the addition of the Co-POM/PS, but not by introducing fresh SO or PS to the remaining supernatant liquid, indicating that the Co-POM has been completely immobilized in the Co-POM/PS form. The analogue Ru-POM/PS was also reported therein.[216]

Finally, a family of Co-POM with molybdenum $([CoMo_6O_{24}H_6]^{3-}$ and $[Co_2Mo_{10}O_{38}H_4]^{6})$ (**Figure I.27, 84 and 85**) were found photochemically actives. DLS ruled out the formation of colloidal particles and TON of 107 and 154 were obtained after 30 min of irradiation.[217] Under their experimental conditions, TOF for **84** and **85** (0.11 and 0.16 s^{-1}) were found higher than for Co_4POM (**77**) (TOF = 0.08 s^{-1}).

I.5.3.2. Porphyrin-like Cobalt WOCs

Few examples of cobalt complexes containing organic ligands are reported as water oxidation catalysts. In an early work, Elizarova *et al.* found that cobalt phthalocyanines or porphyrines catalyzed the oxidation of water by $[Ru(bpy)_3]^{3+}$.[218] Based on these examples, the photocatalytic WO was well established for both families of complexes. A bilayer of an n-type semiconductor (PTCBI = 3, 4, 9, 10-perylenetetracarboxylic acid bisbenzimidazole, **Figure I.28**, left) and the cobalt phthalocyanine (Co-Pc) supported on ITO showed a high photoanodic current at 0.2 V under the presence of TEA. This current was not observed in the dark or using an ITO/Co-Pc electrode. Indeed, in a dry cell of the PTCBI/Co-Pc it was observed a photovoltage of 0.5 V indicating the formation of a p-n junction in the interphase. Therefore the organic bilayer can work as a photoelectrode in water by transferring the electrons from the Co-Pc/water interphase to the semiconductor by applying a bias. Further investigations indicates that the light was exclusively absorbed by the PTCBI, acting as the photosensitizer. Removing TEA (source of electrons) from the media, the electrons were obtained from the conversion of OH⁻ into O_2. At pH 11 (NaOH), the water splitting took place very efficiently at an applied bias potential of 0.5 V *vs* SHE (η = -0.08 V, 2000 TON in 1 hour).[219]

On the other hand, Sakai and coworkers (**Figure I.28**, upper right) studied the light-driven WO with Co-porphyrin (Co-Po) systems ($[Ru(bpy)_3]^{3+}$ as PS, $S_2O_8^{2-}$ as SO).[220] A dramatic pH dependence on the TOF values was observed, decreasing ~6 fold from pH 11 to pH 12 or pH 10 (0.17 s⁻¹ at pH 11). No NP were detected (DLS), kinetic studies pointed towards 2nd order on the catalyst, and DFT supported the presence of radical character on the oxo atom of Co^{III} or Co^{IV} oxyl species. Hence, the oxyl-metal radical coupling (DC) seemed the most plausible mechanism. (**Figure I.28**, lower right). The oxidation state of the cobalt in the rate determining step remained unclear. Deactivation of the catalytic activity was related to oxidative cleavage of the ligand (detected by ESI-MS).
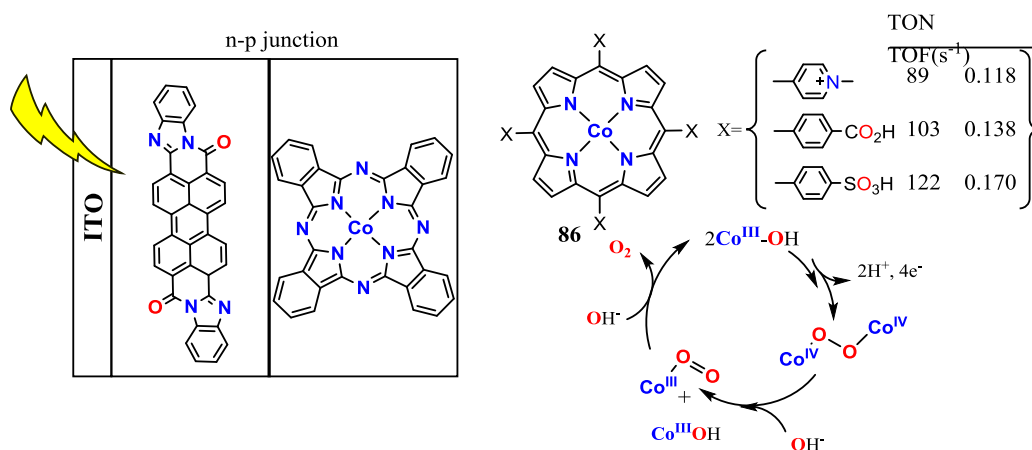
Figure I.28. Left) Scheme of the photochemical n-p junction Co-Pc/PTCBI/ITO and, right) different Co-Po complexes, its catalytic activity for the light-driven WO (10µM of Co-Po) at pH 11 (NaPi buffer) and its mechanistic proposal.

A "xanthene-hangman" corrole, [Co^{III}(bpfxc)] (**Figure I.29**, **87** bpfxc = 5, 15-bis-(pentafluorophenyl)-10-(2,7-di-tert-butyl-5-carboxy-9,9-dimethyl-9H-xanthene-4-yl)corrole) was also found electrochemically active when immobilized in Nafion films, with a TOF close to 0.8 s^{-1} when the potential was setup to 1.6 V vs SHE (pH =7).[221] The authors argued that the hanging moiety (the acid-base functionality placed over the face of the corrole) assists in the intramolecular proton transfers by preorganizing the water molecule within the system, having a decisive role for the water oxidation. Because the current onset occurs above the first oxidation event (Co^{IV} or $Co^{III\bullet}$) the authors favored $Co^{IV\bullet}$ as the catalytic species. The homogeneous catalysis was reinforced because the onset was above to the expected for CoO_x NP,. [Co^{III}(tpfc)(py)$_2$] (**Figure I.29**, **88**, tpfc = 5, 10, 15-tris(pentafluorophenyl)corrole and py = pyridine) was also found active.[222] The electrodeposited catalyst produced O_2 with TOF of 0.2 s^{-1} at 1.6 V (vs SHE pH = 7, NaPi) and UV-Vis, ESI-MS, SEM, and EDX supported a molecular catalytic system derived from the initial complex (precatalyst) upon dissociation of the pyridine group from the cobalt. The WO rate was found [NaPi] dependent, suggesting a base assisted proton transfer process in the O-O bond formation.

87
-, 0.8 s^{-1}

88
-, 0.2 s^{-1}

89 L= H_2O or OH^-

R= **a** TDMImP **b** TM4PyP **c** TTMAP
-, 1400s^{-1}
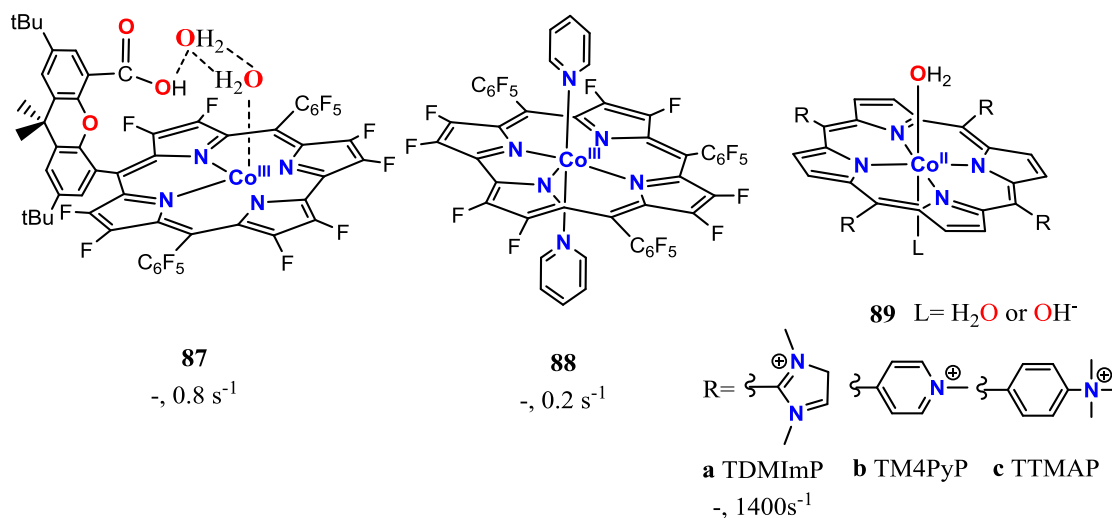
Figure I.29. Corrole and porphyrin cobalt complexes for the water oxidation. TOF reported here were all under electrochemical conditions.

A family of cationic cobalt porphyrins (**Figure I.29, 89**) was also found able to catalyze the oxidation of water.[223] The most active complex, Co^{II}(TDMImp(OH$_2$)) ([Co-5,10,15,30-tetrakis-(1,3-dimethylimidazolium-2-yl)porphyrin]), had an onset potential of 1.4 V (vs SHE) in neutral water (0.2M NaPi buffer, pH 7) and sustained oxygen evolution was observed during several hours with a rate constant (k_{cat}) of 1400 s^{-1}.[223] EDTA or ion exchange resins did not affect the catalytic activity, indicating that cobalt oxides are not formed during the reaction. This was

supported by dispersive X-ray spectroscopic analysis of the electrode surface. Because no redox processes were observed from Co^{III} for Co-TDMImP (probably the intermediates were short-lived), the mechanistic study was carried out using the Co-TM4PyP catalyst (TM4PyP = Co–5,10,15,20-tetrakis-(N-methylpyridinium-4-yl)porphyrin). Mechanistically in agreement with the above mentioned Co-corrole mechanism, the accumulation of two positive charges on the Co^{III} (resting state), pointed towards a cation radical $Co^{IV\bullet}$ as the active species. From Co^{III}-TM4PyP, the porphyrin ring was oxidized at 1.34 V generating $^+$P-Co^{III}-OH (the analog Ga^{III}-TM4PyP complex had this redox event at 1.33 V). Then a second anodic oxidation is overlapped the current onset, at 1.52 V, suggesting the oxidation to the catalytically competent $^+$P-Co^{IV}-O. Interestingly, no catalytic activity was observed in unbuffered H_2O solutions. However, the catalysis was not exclusively observed with NaPi buffer (i.e. catalysis takes place with bicarbonate, phthalate…) and therefore the buffer base is expected to play several key roles, leading the proton transfer for the formation of the active species, in the O-O bond formation (rate determining step), but also in the inhibition of the activity (**Scheme I.14**).
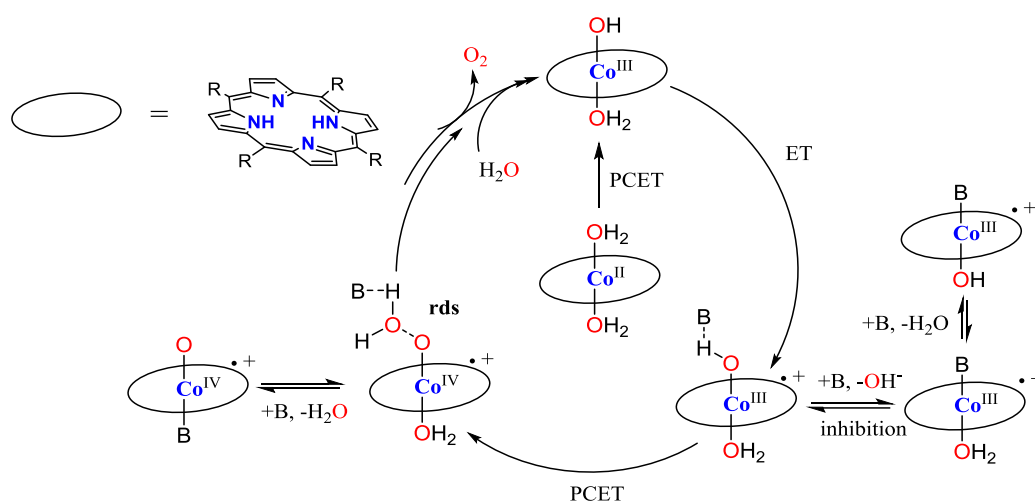
Scheme I.14. Proposed electrochemical mechanism for the base-assisted water oxidation driven by Co-porphyrins. B is the buffer anion.

I.5.3.3.   Polipyridylamino Cobalt Complexes

Strong chelation, robustness and high electron-donation play crucial roles in the rational ligand design when high valent M=O species are intermediates or even the active species in a catalytic mechanism. Pyridyl-amino ligands accomplish those requirements and for this reason they have been widely used as ideal platforms for the oxidation chemistry. However, few examples were reported for the cobalt catalyzed WO. Initially, Berlinguette and coworkers focused their study on $[Co^{II}(PY5)(OH_2)](ClO_4)_2$ **(Figure I.30, 90)** which in aqueous media showed an irreversible oxidation at ~1.4 V (at pH 9.2). This process was assigned to a catalytic behavior occurred upon formation of a $[Co^{IV}OH]^{3+}$ (1.43 V, assigned by square wave

voltammetry). The complex was found to be stable over the pH range of 7.6-10.3, without leading to film deposition under electrochemical conditions. The reaction rate coefficient (k_{cat}) was found 79s^{-1}, but contribution of nanoparticles was not completely ruled out.[224] The stability of the complex, the i_{cat}-pH-independent behavior and the observation that repeated scans do not led into electrodeposition seemed in agreement with a molecular catalysis.[224] However, diluted Co^{2+} (aq) showed a similar behavior. pH-dependent studies showed small different trends for the complex and Co^{2+}(aq) and authors suggested that probably part of the current may arises from a molecular compound. Electrochemistry carried out in mixtures of aqueous KOH and PC (propylene carbonate) suggested different species in solution, but the results were not conclusive. Towards a better understanding, kinetics showed first order on cobalt and on [OH^{-}], suggesting the rate determining step (RDS) is the electrophilic attack of a high valent [Co^{IV}-OH]$^{3+}$ to [OH^{-}], with an observed KIE of 4.7. The alternatively proposed base-assisted deprotonation of [Co^{IV}OH]$^{3+}$ to form [Co^{IV}=O]$^{2+}$ previous to the O-O bond formation was ruled out by DFT due to the high basicity of the resultant oxo, that would not react quickly with OH^{-}. However, kinetic analysis of Co^{2+} does not shed light on the homogeneity of the process.[225]

Later on, Nam, Fukuzumi and coworkers reported a clear example were the heterogeneous material was the real catalyst.[226] Under photocatalytic conditions at pH 7-10, complexes [Co^{II}(Me$_6$tren)(OH$_2$)]$^{2+}$, [Co^{III}(Cp*)(bpy)(OH$_2$)]$^{2+}$, [Co^{II}(12-TMC)]$^{2+}$, and [Co^{II}(13-TMC)]$^{2+}$ (Me$_6$tren = tris(N,N'-dimethylaminoethyl)amine, Cp* = η^5-pentamethylcyclopentadientyl, 12-TMC = 1,4,7,10-tetramethyl-1,4,7,10-tetraazacyclododecane, 13-TMC = 1,4,7,10-tetramethyl-1,4,7,10-tetraazacyclotriecane) were found active WOCs. However, Co(NO$_3$)$_2$ was also found active in those conditions and CO$_2$ was detected together with the O$_2$ evolution for all the complexes. Its degradation was confirmed by ^{1}H-NMR. After 3 min of irradiation, DLS and TEM showed the formation of different sized NP (20-200 nm, depending on the precatalyst), the surface of each were mainly composed of cobalt hydroxide (XPS). Cobalt hydroxides could be converted to active species containing high-valent cobalt ions during the photocatalytic water oxidation. Therefore CoO$_x$ species was the true catalyst. The different activity observed among the catalysts was explained by TG/DTA (thermogravimetric / differential thermal analysis) measurements, revealing that the presence of different amounts of carbon on the NP surfaces modifies the O$_2$ production.

This was not the case for [Co^{II}(qpy)(OH$_2$)$^{2+}$] (**Figure I.30, 91**), qpy = 2,2':6',2'':6'',2'''-quaterpyridine) which homogeneously catalyzed the light-driven [Ru(bpy)$_3$]$^{2+}$ water oxidation (335 TON after 1.5h irradiation at 457nm, pH 8).[227] Only the entire complex was detected by ESI-MS, and DLS analysis did not show the presence of NP. The O$_2$ yield for the thermal WO was 67%, with an initial TOF of 4s^{-1}. The complex was also a good catalyst for photocatalytic proton reduction in aqueous MeCN by the chromophore [Ir^{III}(ppy)$_2$(bpy)]PF$_6$ (ppy=2-phenylpyridine,

bpy=2,2'-bipyridine), being triethanolamine the reductive quencher. The H_2 production was only limited by the light-harvesting process and the stability of the photosensitizer, reaching TON of 890 (5% H_2O in MeCN).

At pH 7.1 (NaPi buffer) the current onset for the Salophen-based cobalt complexes (CoSlp, Slp = N,N'-bis(salicylaldehyde)-1,2-phenylenediamine, **Figure I.30, 92b**, including the red-colored fragment) was low enough to catalyze the light-driven water oxidation (1.1 V vs SHE).[228] The low overpotential observed (η_{90b} = 0.3 V, η_{Co2+} = 0.5-0.6 V) strongly supports the homogeneous catalysis. 17 TON and a quantum yield of ~10-15% were reported, and catalyst stability was confirmed by UV-Vis, DLS and EPR. By laser flash photolysis, a double electron transfer (ET) *per* Co was detected, pointing towards $Co^{IV}=O$ as the active species. The rate for the first ET was remarkably high, being one order of magnitude higher than Co_4O_4.
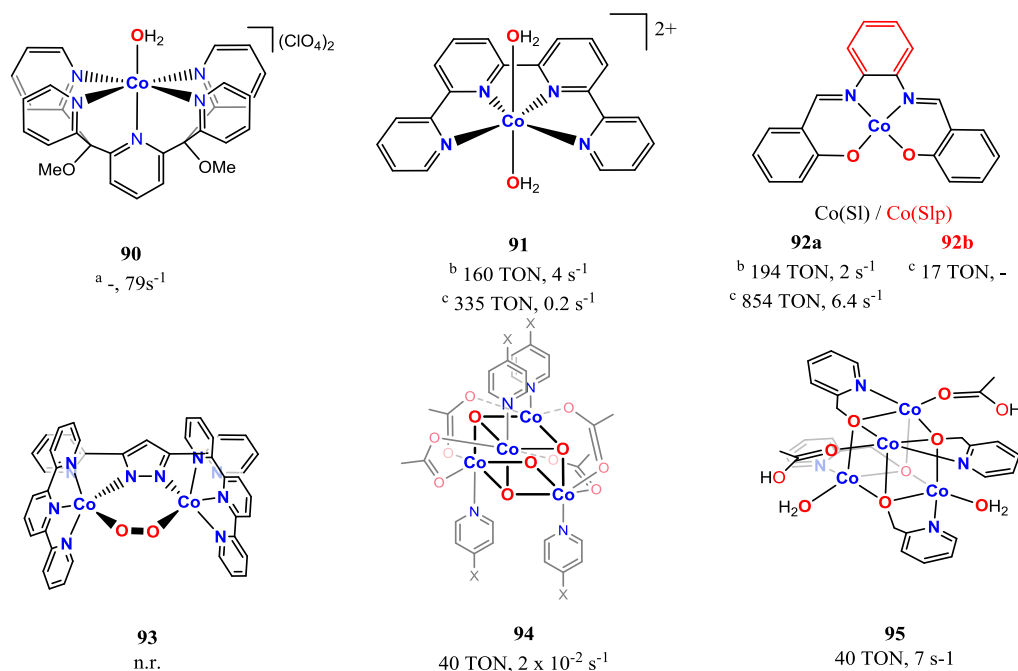
Figure I.30. Polipyridylamino cobalt complexes and cobalt oxide clusters for the water oxidation. n.r.= not reported. [a] Electrochemcial-driven WO. [b] Ru(bpy)$_3$$^{3+}$ as SO. [c] Light-driven WO.

The simpler Co(Sl) (**Figure I.30, 92a**, N,N'-Bis(salicylidene)ethylenediaminecobalt (II)) was also found an effective light-driven WOC, yielding 854 TON and TOF of 6.4 s^{-1}, with a quantum yield of 38.6 % (borate buffer, pH 9). Under non-illuminated conditions (using [Ru(bpy)$_3$]$^{3+}$) a TON of 194 and TOF of 2.0 s^{-1} were reported. The onset of the catalytic wave was at 0.9 V. The catalyst was found hydrolytically stable in borate buffer (UV-Vis, DLS, activity aged solutions = freshly prepared samples) but after the illumination, different-sized NP were detected, together with the presence of CO_2 in the gas phase. A precipitate was isolated after few minutes of irradiation and XPS revealed the absence of Co(II) on its surface, differing from the results reported by Fukuzumi *et al*. (*vida supra*). The isolated solid (probably Co(III) inorganic

species) remained catalytically active for the light-driven WO (lower than the freshly compound), indicating that Co(Sl) acts as a precatalyst.[229]

I.5.3.4. Bioinspired Cobalt Oxide Clusters

The M_4O_4 cubical motif has become an interesting substructure for the development of WOCs since the first observation of the oxygen evolving complex (OEC). Most of the examples are based on Mn due to its analogy to the PSII, but recently Nocera and coworkers found that a Co_4O_4 cubane-like complex was self-assembled during the electrochemical-driven water oxidation by Co^{2+} ions in NaPi buffered water.[230] This observation draw the attention of several groups, which has been focused on the development of molecular cubanes for the water oxidation.

The first molecular Co_4O_4 core was published simultaneously by the groups of Dismukes and Scandola.[231,232] A $Co^{III}_4O_4(Ac)_4(py)_4$ (**Figure I.30, 94**) was found photochemically active in the presence of $[Ru(bpy)_3]^{2+}$ and $S_2O_8^{2-}$ with TON of 40 and a TOF_{max} of 0.02 s^{-1} after 1h of irradiation. Small photodecomposition ($< 5\%$) of the catalyst was observed by ^{1}H-NMR of a solution after a > 5 TON reaction.[231] Using a Co^{2+} concentration equal to the photodecomposition observed for Co_4O_4 no O_2 evolution was observed. Moreover, it was found different lag times and kinetic profiles for Co_4O_4 and Co^{2+}, supporting the presence of different active species. Scandola and coworkers investigated the compound electrochemically. The overpotential was found at 1.32 V (pH 8).[232] The catalytic activity was strongly affected by the concentration of the catalyst and the pH and further electronic modifications (different *para* substituted pyridines: H, Me, t-Bu, OME, Br, COOMe, CN), showed that under irradiation conditions (MeCN:NaBi buffer (10mM, pH 8) 50:50) the primary ET rate (accessible by laser flash photolysis) followed a negative-slope linear Hammett, indicative of an ET favored by electron-rich pyridine ligands. Altogether the data strongly supports the homogeneity of the system.[233] Using the solvent conditions reported above (MeCN:NaBi buffer 50:50) the total consumption of the sacrificial oxidant ($Na_2S_2O_8$, 140 TON) was achieved, in different rates, for all the reported clusters (0.7s^{-1} was the $TOF_{max,}$ $Co^{III}_4O_4(Ac)_4(^{p-OMe}Py)_4$).

I.5.3.5. Unraveling The O-O Bond Formation Mechanism

Heterogeneous cobalt-oxides have been hindering the identification of catalytic species in the cobalt catalyzed electrochemical-driven water oxidation and many questions remain concerning key steps in the mechanism. Based on DFT calculations, the O-O bond formation on a cobalt oxide cubane cluster ($Co_4(\mu-O)_4(OH)_4(OH_2)_8$ model) takes place towards the direct coupling between two $Co^{IV}=O$ groups (best described as $Co^{III}O^\bullet$) with an activation energy of 2.3 kcal/mol.[234] The liberation of O_2 is preceded by the formation of a Co^{III}-O-O-Co^{III} and the subsequent addition of one water molecule which leads the displacement of the O-O bridge

coupled with intramolecular proton transfer, resulting in terminal OOH and OH groups. Towards this idea, Llobet, Stahl and coworkers studied a series of peroxo dinuclear Co^{III} polypyridyl complexes, structurally disposed to favor the DC mechanism.[235] $[Co_2(terpy)_2(\mu\text{-bpp})(\mu\text{-}O_2)]^{3+}$, **(Figure I.30, 93**, terpy = terpyridine and bpp = bispyridilpyrazolate) oxidized water in acidic media (pH 2.1), conditions where CoO_x NP are not stable. Two redox processes (probably Co_2^{III} to Co_2^{IV}) were observed before the onset (1.91 V) (**Scheme I.15**) and a low spin (S = ½) mixed-valent $Co^{III}Co^{IV}$ species was detected by EPR (g = 2.01). O_2 was produced at 2.0 V during two hours bulk-electrolysis with a faradaic efficiency of 77%. The ancillary ligand (terpy) was then replaced for a more basic group (bis-(N-methyl-imidazolyl)-pyridine). As expected for a molecular behavior, the new compound showed a lower onset potential (70 mV below) and higher currents under 2.0 V electrolysis, in agreement with an homogeneous system. However, Co^{2+} arising from decomposition of both complexes was not completely excluded.

Contrarily to the above-mentioned mechanism proposed by DFT calculations on Co_4O_4 species (the low-spin Co^{IV} =O radical) a mechanism towards a nucleophilic attack of the water molecule was proposed by Li and Siegbahn.[236] The mechanism was recalculated considering the optimal protonation state (H_2O or OH) of the model at all stages. Although a high barrier was found (31.6 kcal/mol), a DC process was reported as a less favored pathway and the authors postulated the possible effect of a base acting as a doping agent (in the experimental conditions) or even the role of a larger structure assisting in the [H^+, e^-] release. Focused on this, a novel Co^{II}-based cubane WOC containing a flexible structure based on mono and bidentate acetate and aqua ligands, ($[Co^{II}_4(hmp)_4(\mu_2\text{-}OAc)_2(H_2O)_2]$ (**Figure I.30, 95**, hmp= 2-(hydroxymethyl)pyridine), was reported by Patzke and coworkers to favor the intramolecular direct coupling.[237] TON of 40 and TOF_{max} of $7s^{-1}$ were reported under basic (pH 8-9) light-driven conditions, showing a strong pH-dependency. The complex stability in water was confirmed by CV, UV-Vis and FT-IR and no NP were detected, neither lag-time for the O_2 production (usually observed due to the formation of active CoO_x species). The recyclability was proved by extra-loadings of sacrificial oxidant and the pH re-adjustment, being the activity limited only by the decomposition of the PS. EXAFS and DFT suggested the presence of high-spin Co^{II} centers in the Co_4O_4 systems, which is expected to favor the direct coupling mechanism for this complex due to the higher lability of a M^{II} center.
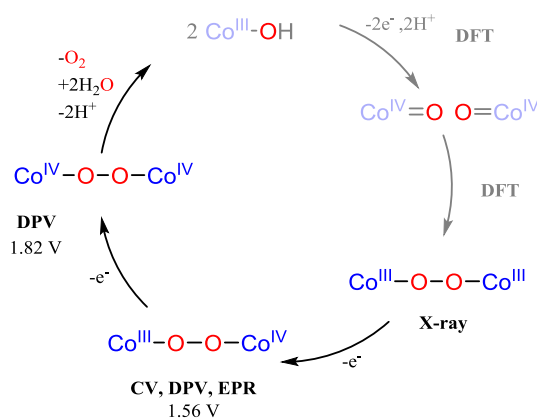
Scheme I.15. DFT (in grey, O-O bond formation based on calculation on the Co_4O_4 cluster by Van Voorhis *et al*.)/experimental (black, O_2 release from the peroxo bridged $[Co_2(tpy)_2(\mu\text{-bpp})(\mu\text{-}O_2)]^{3+}$ reported by Stahl *et al*.) mechanistic proposal for the direct coupling water oxidation. Experimental redox potentials and detection techniques were included for every intermediate observed. CV and DPV are cyclic voltammetry and differential pulse voltammetry. Potentials are reported vs Ag/AgCl, at pH = 2.1

I.5.4 Copper Water Oxidation Catalysts

30 years after the earlier work of Elizarova and coworkers,[99,218] which had the first evidence for the water oxidation meditated by copper ($CuCl_2$, $Cu(bpy)_2Cl_2$ and $Cu(bpy)_3Cl_2$) in presence of $[Ru(bpy)_3]^{3+}$, the first detailed report of catalytic copper driven water oxidation was carried out by Mayer and coworkers. Simple $[(bpy)Cu(\mu\text{-OH})]_2^{2+}$ salts exhibited a large irreversible current with 750mV overpotential at high pHs (pH > 12). The monomeric $[(bpy)Cu(OH)_2]^{2+}$ (**Figure I.31, 96a**) was found dominant in solution (EPR, CV) and a TOF_{max} of $100s^{-1}$ was observed. It was reported the lack of electrodeposition and NP formation in favor to an homogeneous process.[238] Kinetics showed first order on copper (see mechanistic proposal by T.J. Meyer *et al*. in **Figure I.31**). The 6,6'-OH substituted bipyridyl ligand (**Figure I.31, 96b)** was designed to facilitate the PCET as well as the redox potential of the complex by electrodonation.[239] As expected, the overpotential was reduced 200 mV when compared to the unsubstituted system. The catalyst stability was supported by UV-Vis and NMR (>90% of the ligand was recovered after acidification) and a TON of 400 was reported during a bulk electrolysis at 1.1 V vs SHE (pH 12.4, 0.1M NaOAc/NaOH) in a fritted cell (the counter electrode was separated with a membrane to avoid the reduction of the catalyst), with a TOF of $0.4s^{-1}$. Unexpectedly, the study of other 6,6'- and even 4,4'- substituted complexes were not consistent with the lower overpotential observed for the 6,6'-OH derivate. Further analysis of the later suggested a ligand oxidation process (1.55 V) taking place close to the $Cu^{II/III}$ redox wave (1.38 V), that could be involved in lowering the overpotential for the water oxidation. In addition, pH dependent studies indicated that under catalytic conditions, the ligand was in the mono-deprotonated form and DFT studies pointed towards an active species better described as a Cu^{III}-

OH radical rather than Cu^{IV}-OH. Therefore, the deprotonated ligand is acting as an electron transfer mediator in the catalytic cycle, lowering the overpotential for the water oxidation. Nevertheless, the price paid for lowering the potential resulted in a considerable decrease of the TOF when compared to the unsubstituted bipyridyl compound. In addition, the ligand oxidation for the 4,4'-OH substituted bpy was found 0.2 V higher than for the 6,6'-OH, in agreement with the experimental results.

Under appropriate conditions, the use of simple Cu^{2+} salts also performed a sustained WO.[240] In high concentration of CO_3^- or PO_4^{3-} (~1M pH=10.8) kinetics agree with a pH-dependent direct coupling mechanism (2nd order in Cu^{2+} and the activity decreases at lower pH values). The electrodeposited material was found to contribute in the catalysis and the spectroscopical data (UV-Vis and pulsed EPR) pointed towards a [buffer-Cu] complex as the active species. However, first order on Cu was observed in the presence of $NaHCO_3$ (CO_2-saturated, 0.1M, pH 6.7) or acetate buffer (0.1M, pH 6) and thus, both mechanisms, direct coupling and acid/base are compatible for the water oxidation with copper salts.

An electrocatalytic oxidation wave with an onset at 1.1 V (vs SHE in NaPi, pH 11) was also observed for a triglycylglycine Cu^{II} complex $[(TGG)Cu^{II}-OH_2]^{2-}$ (**Figure I.31, 97**).[241] The current was almost stable for long-time-electrolysis and no changes were observed due to electrodeposition, or catalyst decomposition, favoring a robust homogeneous system. Kinetics agree with a single site process, being a formal Cu^{IV}=O the active species where the rate-determining O-O bond formation step takes place with a k_{O-O} of 33s^{-1}, which corresponds to the TOF of the catalytic reaction.
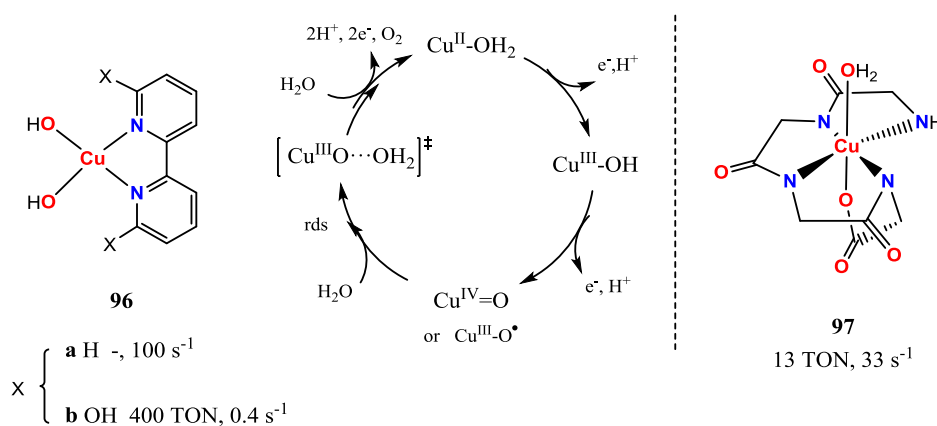
Figure I.31. Schematic representation of the Cu-WOCs, $[(bpy)Cu(\mu-OH)]_2^{2+}$ (left) and $[(TGG)Cu^{II}-OH_2]^{2-}$ (right) and the mechanistic proposal for the electrochemical acid-base water oxidation.[241]

I.5.5   Nickel Water Oxidation Catalysts

The first homogeneous Ni complex was recently reported by Hill and coworkers.[242] A Ni_5-based silicotungstate complex was capable of oxidizing water photochemically, using

$[Ru(bpy)_3]^{2+}$ as PS and persulfate as SO. The measured TON was 60 and quantum yield, 3.8% (**Figure I.32**). A TOF of $1s^{-1}$ was determined under dark conditions using the chemically oxidized PS ($[Ru(bpy)_3]^{3+}$) as SO. Concerning POMs, deep stability studies are always required, and UV-Vis, FTIR and DLS agree with a complex retaining its structure in solution. However electrodeposition of Ni^{2+}-borate (borate was the buffer) was observed at 1.3V. Indeed, it was known that under alkaline media, NiO_x was an efficient and robust electrochemically-driven WOC.[243-245] The preparation of controlled-thickness Ni^{2+}-Bi anodic films with an onset for the WO at 1.2 V was reported by Nocera and coworkers as an alternative to the CoO_x systems, producing O_2 at $1mA/cm^2$ under near-neutral pH.[246] Metal concentration, pH, electrolyte and applied potential were important factors for the correct electrodeposition and the retention of the catalytic activity. Alternatively, Ni^{2+}-Bi films prepared by deposition from $[Ni(en)_3]^{2+}$ or macrocyclic Ni^{II}-amino complexes produced more uniform layers triggering a higher catalytic performance.[247,248] NiO_x generated from simple Ni salts or complexes were also found active for the O_2 production under thermal and light-driven conditions. TON ranging from 2 to 65, and TOF between $0.32\text{-}0.91s^{-1}$ (dark conditions, $[Ru(bpy)_3]^{3+}$ was the SO) and TON of 270-855 (illuminated conditions, using persulfate (2.5mM) as SO and $[Ru(bpy)_3]^{2+}$ (0.12mM) as PS) were obtained using common amino-pyridyl ligands as well as from $Ni(NO_3)_2$ (a TON of 1200 was reported under optimized conditions, $0.6\mu M$ Ni^{II} at pH 8.5) DLS measurements revealed the formation of NPs under both conditions, characterized by SEM, EDX, XPS, XRD and IR as partially reduced nickel oxyhydroxide (β-NiOOH).[249]
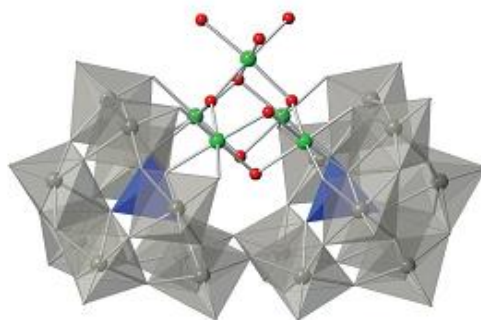
Figure I.32. Crystal structure of $K_{10}H_2[Ni_5(OH)_6(OH_2)_3(Si_2W_{18}O_{66})]\cdot34H_2O$. WO_6 are in gray, SiO_4 in blue, oxygen in red and nickel in green. Reproduced from reference with permission from The Royal Society of Chemistry.[242]

I.5.6 Precedents of Iron Water Oxidation Catalysts

In 2007, Collins and coworkers published the first chemical and spectroscopic evidence of a $Fe^V=O$ species. The strong charge stabilization provided from a tetraamido macrocyclic ligand (TAML) was useful for its isolation and spectroscopic characterization (**Figure I.33**). Due to its extremely high electrophilicity, the opportunity to cleave strong chemical bonds was glimpsed and the water oxidation was achieved upon addition of CAN as a sacrificial oxidant (E^o

= 1.75 V)[31], producing oxygen with a TOF of 1.3s[-1], but exhibiting low TON (**Figure I.33, 98d**).[250] NaIO$_4$ (E° = IO$_4^-$ / IO$_3^-$ = 1.60 V)[31] was also useful for the O$_2$ production and a characteristic oxo-bridged Fe^{IV} signature was observed by UV-Vis spectroscopy. Kinetics indicates first order in [Fe]. Further DFT calculations performed by Crammer and coworkers suggested the formation of a Fe^V=O by two subsequent PCET steps.[251] However the energetic barrier for the O-O bond formation with this intermediate was not attainable (41.5 kcal·mol^{-1}) and the active specie was generated with a new electron oxidation to Fe^V=O (TAML$^{+ \cdot}$) (formally Fe^{VI}), being the formation of the later rate determining with a total barrier of 30 kcal·mol^{-1}. A revision of the reaction mechanism was performed by Siegbahn and coworkers, considering competing pathways, different calculation levels and the presence of nitrate as the source of oxygen for the O-O bond formation.[252] In this case, the water attack was found rate determining with a barrier of 15.4 kcal·mol^{-1}, 4.1 kcal·mol^{-1} lower than the N-O bond cleavage from the nitrate. The low stability of the complex was related to a possible competitive nucleophilic attack of the water on the ligand (10.9 kcal·mol^{-1}).
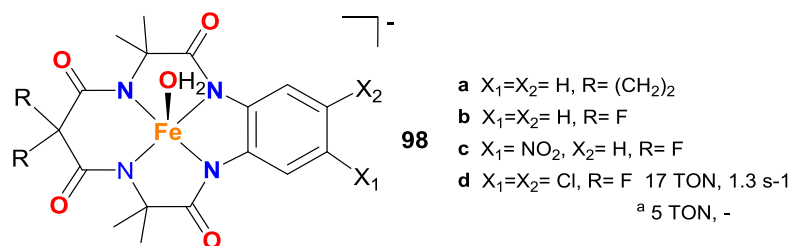
Figure I.33. Schematic representation of the Fe-TAML complexes studied in water oxidation. [a] NaIO$_4$ was used as SO.

The catalytic iron-driven thermal water oxidation was definitively achieved during this Ph.D. research, by a family of iron complexes based on neutral tetradentate aminopyridine ligands (**Chapter IV-V of this thesis**). TOF$_{max}$ of 0.23s[-1] (TON = 360) and 0.06s[-1] (> 1000 TON) were reported when CAN (pH 1) or NaIO$_4$ (pH 2) were used as a chemical oxidants. The availability and modulability of such ligands lead to an extended study of its steric and electronic properties (**Chapter V**) governing the feasibility of the reaction. A mechanism involving a high valent Fe^V=O as the active species, and the detection and characterization of a novel intermediate corresponding to a bimetallic interaction between iron and cerium [O=Fe^{IV}(μ-O)Ce^{IV}], resting state of the reaction) will be also discussed herein (**Chapter IV-VI**).

Reinforcing the mechanism, complexes [Fe^{II}(OTf)$_2$(Pytacn)] were found catalytically active for the stereospecific hydroxylation of alkanes and cis-dihydroxylation of olefins using similar conditions to those ones reported for the water oxidation, being water the source of oxygen and CAN the sacrificial oxidant (**See Chapter VII**).

I.6.   Summary of Water Oxidation Catalysts

Table I.3. Summary of catalytic conditions.

Cat ref.[a]	[Cat] (µM)[b]	[SO] / [PS] (mM)[c]	Onset (η)[d]	Medium	TON (recyclable)[e]	TOF (s^{-1})[f]	Ref
Ruthenium Dimers							
1a	41	2.05 (Ce^{IV})	-	0.1 M HClO$_4$	13	4.2·10^{-3}	38
	1.58 V		1.58 (0.4)	0.1 M HOTf	4.6	-	39
1aCl[g]	300	15 (Ce^{IV})	1.54 (0.37)	0.1 M HOTf	2.7	2.3·10^{-3}	42
1b	20	100 (Ce^{IV})	1.4 (0.19)	0.5 M H$_2$SO$_4$	75	-	43
1b	0.15	5 (S$_2$O$_8^-$) / 0.1 Ru*		NaPi (pH 7)	30	2.5·10^{-2}	43
2	4000	1200 (Ce^{IV})	-	(pH <0 .8)	-	5.6·10^{-2}	44
3	914	93 (Ce^{IV})	1.25 (0.02)	0.1 M HOTf	18.6	1.4·10^{-2}	45
3	80	913 (Ce^{IV})		0.1 M HOTf	512	-	47
3-Nafion	0.25	0.9 (Ce^{IV})	1.37 (0.2)	0.1 M HOTf	250	1.1·10^{-11}	46
4	1.9 V		1.51 (0.52)	CF$_3$CH$_2$OH: H$_2$O (9:1 v/v) 1 M H$_3$PO$_4$/KOH (pH 4)	21	-	52,53
4	1.9 V		1.4 (0.4)	1 M KOH (pH 4)	2400 (33500)		52,53
5-9	66.7	333 (Ce^{IV})	-	HOTf (pH 1)	80-689	1.5·10^{-3} - 7.7·10^{-2}	55
10	0.05	5 (Ce^{IV})	-	HOTf (pH 1)	4740	0.28	58
10 (light)	2.5	10 (S$_2$O$_8^-$) / 0.62 Ru**	1.35 (0.55)	8.3mM NaPi (pH 7.2)	580	0.83	58
11	0.05	5 (Ce^{IV})	1.5 (0.33)	0.1 M HOTf	10400	1.2	58
11 (light)	10.8	9.5 (S$_2$O$_8^-$) / 0.47 Ru**	1.2 (0.4)	8.3mM NaPi (pH 7.2)	370 (12070)	0.26	59
12	1500	100 (Ce^{IV})	1.72 (0.55)	0.1 M HOTf	9.6	3.1·10^{-2}	60
13	1000	100 (Ce^{IV})	1.76 (0.59)	0.1 M HOTf	22.6	6.8·10^{-2}	61
[(terpy)(bpy)Ru^{IV}(µ-O)Ru^{IV}(terpy)(O)(OH$_2$)]$^{4+}$	1.8 V		1.65 (0.48)	0.1 M HOTf	14930	0.7	74
[(terpy)(5,5'-F$_2$-bpy)Ru^{IV}(µ-O)Ru^{IV}(terpy)(O)(OH$_2$)]$^{4+}$	1.8 V		-	0.1 M HOTf	6683	1.2	74
Ruthenium Monomers							
16-17	51	1500 (Ce^{IV})	1.65 (0.48)	0.1 M HNO$_3$	-	1.6-3.6·10^{-2}	64
5', 14-15, 19-21,25-29	66.7	333 (Ce^{IV})	>1.5 (0.33) (20a,d)	0.1 M HOTf	110-1170	3.910^{-2} - 0.37	69,71,72
25a, 25b, 25c (light)	0.5	9.3(S$_2$O$_8^-$)/0.5 Ru*	1.31 (0.51) (25b)	NaPi (pH 7.2)	2, 43, 84		

Cat ref.[a]	[Cat] (µM)[b]	[SO] / [PS] (mM)[c]	Onset (η)[d]	Medium	TON (recyclable)[e]	TOF (s^{-1})[f]	Ref
18,23	1000	100 (Ce^{IV})	-	0.1 M HOTf	8$_{in}$/14$_{out}$	2.6·10^{-2} in 5.2·10^{-2} out	73,253
22,24	125	200 (Ce^{IV})	1.55,1.54 (0.34)	(pH 0.4)	148, 123	1·10^{-3}, 3·10^{-3}	73
30	58.8	600 (Ce^{IV})	1.5 (0.33)/1.25 (0.08)[h]	HOTf (pH 1)	2010	14.7	8
30(light)	9.75	0.28 Co /9.75·10^{-3} Ru*	0.98 (0.16)	NaPi (pH 7.0)	100	6·10^{-2}	78
[Ru^{II}(ONNO)($^{4-Br}$Py)]	10	10(S$_2$O$_8^-$)/0.5 Ru*	1.05 (0.23)	20mM NaBi (pH 7)	-	4.2·10^{-2}	82
	10	10(S$_2$O$_8^-$)/0.5 Ru**		20mM NaBi (pH 7)	251 (518)	0.33	
30a-30c	0.05	5 (Ce^{IV})	-	HOTf (pH 1)	16690-21660	-	83
31	15	600 (Ce^{IV})	1.27 (0.1)[h]	HOTf (pH 1)	8360	120	8
31	10	10(S$_2$O$_8^-$)/0.5 Ru**	0.96 (0.14)	20mM NaBi (pH 7)	218	0.31	82
32	12.4	365 (Ce^{IV})		HOTf (pH 1)	4563	31	79
33	29.9	365 (Ce^{IV})	1.2 (0.03)[h]	HOTf (pH 1)	1702	70	79
34	1.6	365 (Ce^{IV})		HOTf (pH 1)	55419	286	79
34	10	10(S$_2$O$_8^-$)/0.5 Ru**	0.95 (0.13)	20mM NaBi (pH 7)	232 (579)	0.32	82
35	32	167 (Ce^{IV})	1.55-1.65 (0.38-0.48)	HOTf (pH 1)	336	9.2·10^{-2}	32
35 (light)	5	5(S$_2$O$_8^-$)/0.25 Ru*	1.23 (0.43)	20mM NaPi (pH 7.2)	5.5	-	32
36	12	400 (Ce^{IV})	1.43-1.46 (0.26-0.29)	0.1M HOTf	550-4050	137-150	80
37	30	400 (Ce^{IV})	1.34-1.35 (0.17)	0.1M HOTf	1094-1150	3.4-4.5	80
Ru$_4$POM	430	172 (Ce^{IV})	-	(pH 0.8)	500	0.125	89
Ru$_4$POM (light)	5	5 (S$_2$O$_8^-$)/1 Ru*	1.15 (0.35)	20mM NaPi (pH 7.2)	180	8·10^{-2}	92
Iridium							
38	50	1500 (Ce^{IV})	-	(pH < 1)	< 2760	0.1-0.4·10^{-2}	35
39a-f,40-44	5	78 (Ce^{IV})	1.35 (0.53) (39c-d)	(pH 0.89)	< 1500	0.05-0.24	104
42	4.1nmol·cm^{-2}, 1.4 V		1.15 (0.27)	pH 6		1.46	254
39g	0.2	1 (Ce^{IV})	-	0.1M HNO$_3$	514	0.24	105
45-46	20	1000(Ce^{IV})	-	(pH < 1)	8350-10000	0.01-0.09	36
47	5	1000 (Ce^{IV})	1.23	(pH < 1)	22800	0.03	106
48	40	333 (Ce^{IV})	1.3 (pH 4.5)	(pH < 1)	2000	1.5	108
49	4.5	78 (Ce^{IV})	1.4 (pH 7)	(pH 0.89)	-	0.13	107
50-51	0.5-5	10-40 (Ce^{IV})	-	HNO$_3$ (pH 1)	500-2000	0.083-2.1	110
52	50-200	200 (Ce^{IV})	-	(pH < 1)	1000	0.94	111
Ir(acac)$_3$	111		-		-	1177	
[Cp*IrCl$_2$]$_2$	107	170 (Ce^{IV})	-	(pH < 1)	-	1074	123
IrCl3· x H$_2$O	118		-		-	303	

Cat ref.[a]	[Cat] (µM)[b]	[SO] / [PS] (mM)[c]	Onset (η)[d]	Medium	TON (recyclable)[e]	TOF (s⁻¹)[f]	Ref
Aged IrCl$_3$·x H$_2$O	123		-		-	1707	
IrO$_2$	147		-		-	347	
39a	111		-		-	316	
53-59	100	170 (Ce^{IV})	-	(pH < 1)	-	0.09-0.27	[121]
60	2.4	10 (NaIO$_4$)	-	23mM NaOAc (pH 5.3)	-	0.13	[116]
61	2.2	10 (NaIO$_4$)	-	23mM NaOAc (pH 5.3)	-	0.2	[116]
62	0.1	10 (NaIO$_4$)	-	23mM NaOAc (pH 5.3)	-	2.2	[116]
62(OTf)	3300		0.82 (0.0)	0.1 M KNO$_3$ (pH 7)			[125]
62	5	10	-	20mM NaHSO$_3$	65	0.18	[130]
62(COD replaces Cp*)	5	10	-	20mM NaHSO$_3$	81	0.17	[130]
63(a-c)	5	78 (Ce^{IV})	-	(pH < 1)	-	0.24-0.25	[126]
63(a-c)	5	20 (NaIO$_4$)	-	180 mM NaOAC (pH 5.6)	0.64-120	0.064-12	[126]
63(d-g)	5	50 (NaIO$_4$)	-	50 mM NaPi (pH 7.2)	6330-7200	0.28-5.2	[128]
µ-(CH$_2$)$_n$[Cp*Ir^{III}(NHC) Cl$_2$]$_2$ (n=1-4)	10	100 (NaIO$_4$)	-		-	0.22-0.42	[131]
64-64b	10	100 (NaIO$_4$)	1.4 (0.4)	pH 4	-	0.079-0.014	[131]
65a	62	0.38 (Ce^{IV})	-		1419	0.1	[132]
Manganese							
65b	31	0.38 (Ce^{IV})	-		2779	0.2	[132]
65b	32	50 (NaIO$_4$)	-		691	0.12	[132]
65b (light)	25	5 (S$_2$O$_8^-$)/1 Ru*	1.05 (0.13)	50mM Na$_2$SiF$_6$/NaHCO$_3$ (pH 5.2)	7.8	4.85·10^{-3}	[132]
66/Nafion	0.27 nmol supported, 1.2 V + hυ		0.84 (0.05)	0.1M Na$_2$SO$_4$	1000	-	[141]
67	1mM, 2 V		1.7	H$_2$O in MeCN (5%v/v)	9.2	2.5·10^{-3}	[155]
69	181	(Ce^{IV})	-	H$_2$O	0.04	-	[166]
[(µ-O)$_2$Mn$_2$(phen)$_2$]$^{3+}$	3600	(Ce^{IV})	-	0.1 M HNO$_3$ (pH 1)	4.4·10^{-4}	-	[166]
70	125	23 (oxone)	-	0.1M NaOAc-H$_2$SO$_4$ (pH 4.3)	0.6	2.1·10^{-3}	[167]
[(µ-O)$_2$Mn$_2$(phen)$_2$]$^{3+}$	125	23 (oxone)	-	0.1M NaOAc-H$_2$SO$_4$ (pH 4.3)	0.25	3.2·10^{-3}	[167]
71	500	50 (oxone)	-	H$_2$O	50	3.4 ·10^{-2}	[167]
71	12.5	70 (NaOCl)	-	(pH 8.6)	4	3.3·10^{-3}	[170]
71/Kaolin	360/4800	50 (Ce^{IV})	-	(pH 1)	13.5	1.2·10^{-4}	[168]
71/MOF	66.7	266.7(Ce^{IV})	-	HNO$_3$ (pH 1)	-	1.1·10^{-2}	[180]
72	40	3200 (tBuOOH)	-		15000	-	[183]
71-74	Comparative table with different oxidants can be found in I.5.1.3						[187]
75	32	250 (oxone)	-		4	1.4·10^{-2}	[188]

Cat ref.[a]	[Cat] (μM)[b]	[SO] / [PS] (mM)[c]	Onset (η)[d]	Medium	TON (recyclable)[e]	TOF (s^{-1})[f]	Ref
76	32	250 (oxone)	-		-	$1.4 \cdot 10^{-3}$	[188]
$[Mn_2(TPA)_2(\mu\text{-}O)_2]^{2+/3+}$ / clay	18	125 (Ce^{IV})	-		2.6	$5.2 \cdot 10^{-3}$	[189]
78	84	40	-	NaPi (pH 7.2)	25	$2.7 \cdot 10^{-2}$	[196]
78(light)	84	20 (S$_2$O$_8^-$)/10 Ru**	1.65 (0.85)	NaPi (pH 7.2) CV with MeCH:H$_2$O 10%	4	-	[196,255]
Cobalt							
79	3.2 (60 bpy)	1.5 (Ru(bpy)$_3$$^{3+}$) + (0.06 bpy)	1.2 (0.44)	30mM NaPi (pH 8)	75	> 5	[200]
79 (light)	5	5 (S$_2$O$_8^-$)/1 Ru*	-	80mM NaBi (pH 8.0)	224	0.8	[201]
80		(Ru(bpy)$_3$)$^{3+}$)	0.97 (0.27)		15	$6 \cdot 10^{-2}$	[210]
80 (light)	5	5 (S$_2$O$_8^-$)/1 Ru*		80mM NaBi (pH 9.0)	101	0.5	[210]
81	10	5 (S$_2$O$_8^-$)/1 Ru*	0.9 (0.2)	80mM NaBi (pH 9.0)	80	0.1	[213]
82	5	165 (NaOCl)	1.41 (0.65)	0.9M NaPi (pH 8)	173 (823)	0.19	[214]
83	40	5 (S$_2$O$_8^-$)/1 Ru*	1.4 (0.23)	20mM Na$_2$SiF$_6$ (pH 5.8)	23	0.4	[216]
84	3.6	3 (S$_2$O$_8^-$)/0.06 Ru*	1.45 (0.69)	NaBi (pH 8.0)	107	0.11	[217]
85	1.9	3 (S$_2$O$_8^-$)/0.06 Ru*	-	0.1M NaBi (pH 8.0)	154	0.16	[217]
Co^{II} phthalocyanine (light)		0.5 V [ITO/PTCBI(160nm)/CoPC(90nm)]/cm^2. Visible light irradiation	0.2 (-0.38)^i	NaOH (pH 11)	2000 (3500 at 0.6 V)		[219]
86 (light)	10	5 (S$_2$O$_8^-$)/1 Ru*	-	0.1 M NaPi (pH 11)	89-122	0.12-0.17	[220]
87/Nafion	30 nmol/cm^2	1.6 V	1.45 (0.63)	0.1 M NaPi (pH 7)	-	0.8	[221]
88	2.5 nmol/cm^2	1.6 V	1.35 (0.53)	NaPi (pH 7)	-	0.2	[222]
89	500	1.5 V	1.4 (0.58)	0.2 M NaPi (pH 7)	-	1400	[223]
90	130	1.59 V	1.43 (0.74)	0.1 M KPi (pH 9.2)	-	79	[224]
91	$8 \cdot 10^{-4}$	0.8	-	15 mM NaBi (pH 8.0)	160	4	[227]
$[Co^{II}(bpy)_2(OH_2)_2]^{2+}$	$8 \cdot 10^{-4}$	0.8	-	15 mM NaBi (pH 8.0)	70	2.7	[227]
91 (light)	0.2	5 (S$_2$O$_8^-$)/0.128 Ru*	-	15 mM NaBi (pH 8.0)	335	$4.2 \cdot 10^{-4}$	[227]
$[Co^{II}(bpy)_2(OH_2)_2]^{2+}$ (light)	0.2	5 (S$_2$O$_8^-$)/0.128 Ru*	-	15 mM NaBi (pH 8.0)	206	-	[227]
92a	1.6	1.5 Ru(bpy)$_3$$^{3+}$	0.9 (0.2)		194	2	[229]
92a (light)	1.6	5 (S$_2$O$_8^-$)/1 Ru*		80mM NaBi (pH 9)	854	6.4	[229]
92b (light)	100	5 (S$_2$O$_8^-$)/1 Ru*	1.1 (0.28)	NaPi (pH 7)	17	-	[228]
93	250	2 V vs SHE	1.91 (0.80)	0.1M Pi (pH 2)	-	-	[235]
$[Co_2(terpy)_2(\mu\text{-}Me_2bimpy)(\mu\text{-}O_2)]^{3+}$	250	2 V vs SHE	1.84 (0.73)	0.1M Pi (pH 2)			[235]
94	50	35 (S$_2$O$_8^-$)/0.5 Ru*	1.3 (0.5)	80 mM NaBi (pH 8)	40	$2 \cdot 10^{-2}$	[231]

Cat ref.[a]	[Cat] (μM)[b]	[SO] / [PS] (mM)[c]	Onset (η)[d]	Medium	TON (recyclable)[e]	TOF (s^{-1})[f]	Ref
95	60	5 (S$_2$O$_8^-$)/1 Ru*	1.16 (0.46)	50mM NaBi (pH 9)	28	7	[237]
Copper							
96a	10-100	1.35 V	1.3 (0.84)	0.1M NaOAc (pH 13)	-	100	[238]
96b	1000	1.1 V	0.8 (0.3)	0.1M NaOAc (pH 12.4)	400	0.4	[239]
CuSO$_4$	3000	1.3 V	1.05 (0.46)	1M Na$_2$CO$_3$ (pH 10.8)	16	-	[240]
97	1000	1.3 V	1.1 (0.52)	0.25 M NaPi (pH 11)	13	33	[241]
Nickel							
Ni$_5$-POM	2	5 (S$_2$O$_8^-$)/1 Ru*	-	80mM NaBi (pH 8)	60	-	[242]
Iron							
98d	975	180 (Ce^{IV})	-	(pH <1)	18	1.3	[250]

(a) (light) after the catalyst reference number (Cat ref.), indicates a reaction which is activated by a source of light. (b) Initial concentration of catalyst or precatalyst. (c) Concentration and type of photosensitizer (PS) is included for light driven reactions. (d) The onset of the WO is the potential (in V vs SHE) where the catalytic activity begins. The overpotential is the difference (in V) between the experimental and the thermodynamic process; η = Onset-(1.23-0.059·pH) (e) TON (turnover number) = (n(O$_2$) produced / n(catalyst)). (f) TOF (TON·s^{-1}) is usually measured at the initial stage of the reaction (g) 1aCl = [(μ-O)Ru$_2$(bpyCl)$_4$(H$_2$O)$_2$](ClO$_4$)$_4$ (bpy = 4,4′-dichloro-2,2'-bipyridine). (h) Mixture of CF$_3$CH$_2$OH/H$_2$O (v/v 1:2), pH 1. (i) Under dark conditions no anodic current was observed. NaPi = Sodium Phosphate buffer. NaOAc = Acetate buffer. NaBi = Borate buffer. Ru* = [Ru(bpy)$_3$]$^{2+}$. Ru** = [Ru(bpy)(4,4'-(CO$_2$Et)$_2$bpy)$_2$]$^{2+}$. Co = [Co(NH$_3$)$_5$Cl]Cl$_2$.

I.7.   References

1   Conti, J. , Holtberg, P. *International Energy Outlook 2013, Energy Information Administration (EIA), Washington DC, USA*.
2   Barber, J. *Int. J. Photoenergy* **2004,** 6, 43-51
3   Ferreira, K. N., Iverson, T. M., Maghlaoui, K., Barber, J. , Iwata, S. *Science* **2004,** 303, 1831-1838
4   Scholes, G. D., Fleming, G. R., Olaya-Castro, A. , van Grondelle, R. *Nat Chem* **2011,** 3, 763-774
5   Biesiadka, J., Loll, B., Kern, J., Irrgang, K.-D. , Zouni, A. *PCCP* **2004,** 6, 4733-4736
6   Yasufumi, U., Keisuke, K., Jian-Ren, S. , Nobuo, K. *Nature* **2011,** 473, 55-60
7   Kalyanasundaram, K. , Graetzel, M. *Curr. Opin. Biotechnol.* **2010,** 21, 298-310
8   Duan, L., Bozoglian, F., Mandal, S., Stewart, B., Privalov, T., Llobet, A. , Sun, L. *Nat Chem* **2012,** 4, 418-423
9   Betley, T. A., Surendranath, Y., Childress, M. V., Alliger, G. E., Fu, R., Cummins, C. C. , Nocera, D. G. *Phil. Trans. R. Soc. B* **2008,** 363, 1293-1303
10   Cox, N., Pantazis, D. A., Neese, F. , Lubitz, W. *Acc. Chem. Res.* **2013,** 46, 1588-1596
11   Ferreira, K. N., Iverson, T. M., Maghlaoui, K., Barber, J. , Iwata, S. *Science* **2004,** 303, 1831-1838
12   Kamiya, N. , Shen, J.-R. *Proc. Natl. Acad. Sci.* **2003,** 100, 98-103
13   J. Yano, J. Kern, K. Sauer, M. J. Latimer, Y. Pushkar, J. Biesiadka, B. Loll *et al. Science* **2006,** 314, 821-825
14   Sartorel, A., Bonchio, M., Campagna, S. , Scandola, F. *Chem. Soc. Rev.* **2013,**
15   Xiaobo Chen, Shaohua Shen, Liejin Guo , Mao, S. S. *Chem. Rev.* **2010,** 110, 6503-6570
16   Ann Magnuson, Magnus Anderlund, Olof Johansson, Peter Lindblad, Reiner Lomoth, Tomas Polivka, Sascha Ott *et al. Acc. Chem. Res.* **2009,** 42, 1899-1909
17   Yano, J. , Yachandra, V. *Chem. Rev.* **2014,**
18   Rutherford, A. W., Osyczka, A. , Rappaport, F. *FEBS Lett.* **2012,** 586, 603-616
19   Aro, E.-M., Suorsa, M., Rokka, A., Allahverdiyeva, Y., Paakkarinen, V., Saleem, A., Battchikova, N. *et al. J. Exp. Bot.* **2005,** 56, 347-356
20   Tröster, I., Fryda, M., Herrmann, D., Schäfer, L., Hänni, W., Perret, A., Blaschke, M. *et al. Diamond Relat. Mater.* **2002,** 11, 640-645
21   Kraft, A., Wiinsche, M., Stadelmann, M. , Blaschke, M. *Recent research developments in electrochemistry*. Vol. 6 (2003).
22   Wood, P. M. *Biochem J.* **1988,** 253, 287-289
23   Sala, X., Maji, S., Bofill, R., García-Antón, J., Escriche, L. , Llobet, A. *Acc. Chem. Res.* **2013,** 47, 504-516
24   Chaplin, M. *Water structure and science*, (2014).
25   Vanýsek, P. *Electrochemical Series, Handbook of Chemistry and Physics: 93rd Edition*. 5-80 (2012).
26   Neagu, C., Jansen, H., Gardeniers, H. , Elwenspoek, M. *Mechatronics* **2000,** 10, 571-581
27   Mirzakulova, E., Khatmullin, R., Walpita, J., Corrigan, T., Vargas-Barbosa, N. M., Vyas, S., Oottikkal, S. *et al. Nat Chem* **2012,** 4, 794-801
28   Geletii, Y. V., Botar, B., Kögerler, P., Hillesheim, D. A., Musaev, D. G. , Hill, C. L. *Angew. Chem. Int. Ed.* **2008,** 47, 3896-3899
29   Winkler, J. , Gray, H. in *Molecular Electronic Structures of Transition Metal Complexes I* Vol. 142 *Structure and Bonding* (eds David Michael P. Mingos, Peter Day,Jens Peder Dahl) Ch. 55, 17-28 (Springer Berlin Heidelberg, 2012).
30   Poverenov, E., Efremenko, I., Frenkel, A. I., Ben-David, Y., Shimon, L. J. W., Leitus, G., Konstantinovski, L. *et al. Nature* **2008,** 455, 1093-1096
31   Parent, A. R., Crabtree, R. H. , Brudvig, G. W. *Chem. Soc. Rev.* **2013,** 42, 2247-2252
32   Tong, L., Duan, L., Xu, Y., Privalov, T. , Sun , L. *Angew. Chem. Int. Ed.* **2011,** 50, 445-449
33   Yagi, M., Tokita, S., Nagoshi, K., Ogino, I. , Kaneko, M. *Faraday Trans.* **1996,** 92, 2457-2461
34   McDaniel, N. D., Coughlin, F. J., Tinker, L. L. , Bernhard, S. *J. Am. Chem. Soc.* **2007,** 130, 210-217
35   Hull, J. F., Balcells, D., Blakemore, J. D., Incarvito, C. D., Eisenstein, O., Brudvig, G. W. , Crabtree, R. H. *J. Am. Chem. Soc.* **2009,** 131, 8730-8731
36   Lalrempuia, R., McDaniel, N. D., Müller-Bunz, H., Bernhard, S. , Albrecht, M. *Angew. Chem. Int. Ed.* **2010,** 49, 9765-9768
37   Codolà, Z., M. S. Cardoso, J., Royo, B., Costas, M. , Lloret-Fillol, J. *Chem. Eur. J* **2013,** 19, 7203-7213
38   Gersten, S. W., Samuels, G. J. , Meyer, T. J. *J. Am. Chem. Soc.* **1982,** 104, 4029-4030

39   Gilbert, J. A., Eggleston, D. S., Murphy, W. R., Geselowitz, D. A., Gersten, S. W., Hodgson, D. J. , Meyer, T. J. *J. Am. Chem. Soc.* **1985,** 107, 3855-3864

40   Concepcion, J. J., Jurss, J. W., Templeton, J. L. , Meyer, T. J. *Proc. Natl. Acad. Sci.* **2008,** 105, 17632-17635

41   Moonshiram, D., Alperovich, I., Concepcion, J. J., Meyer, T. J. , Pushkar, Y. *Proc. Natl. Acad. Sci.* **2013,** 110, 3765-3770

42   Lai, Y.-K. , Wong, K.-Y. *J. Electroanal. Chem.* **1995,** 380, 193-200

43   Rotzinger, F. P., Munavalli, S., Comte, P., Hurst, J. K., Gratzel, M., Pern, F. J. , Frank, A. J. *J. Am. Chem. Soc.* **1987,** 109, 6619-6626

44   Yagi, M., Osawa, Y., Sukegawa, N. , Kaneko, M. *Langmuir* **1999,** 15, 7406-7408

45   Sens, C., Romero, I., Rodríguez, M., Llobet, A., Parella, T. , Benet-Buchholz, J. *J. Am. Chem. Soc.* **2004,** 126, 7798-7799

46   Mola, J., Mas-Marza, E., Sala, X., Romero, I., Rodríguez, M., Viñas, C., Parella, T. *et al. Angew. Chem. Int. Ed.* **2008,** 120, 5914-5916

47   Bozoglian, F., Romain, S., Ertem, M. Z., Todorova, T. K., Sens, C., Mola, J., Rodríguez, M. *et al. J. Am. Chem. Soc.* **2009,** 131, 15176-15187

48   Bianco, R., Hay, P. J. , Hynes, J. T. *J. Phys. Chem. A* **2011,** 115, 8003-8016

49   Bianco, R., Hay, P. J. , Hynes, J. T. *J. Phys. Chem. B* **2013,** 117, 15761-15773

50   Li, X., Chen, G., Schinzel, S. , Siegbahn, P. E. M. *Dalton Trans.* **2011,** 40, 11296-11307

51   Tsuge, K. , Tanaka, K. *Chem. Lett.* **1998,** 27, 1069-1070

52   Wada, T., Tsuge, K. , Tanaka, K. *Inorg. Chem.* **2000,** 40, 329-337

53   Wada, T., Tsuge, K. , Tanaka, K. *Angew. Chem. Int. Ed.* **2000,** 39, 1479-1482

54   Muckerman, J. T., Polyansky, D. E., Wada, T., Tanaka, K. , Fujita, E. *Inorg. Chem.* **2008,** 47, 1787-1802

55   Deng, Z., Tseng, H.-W., Zong, R., Wang, D. , Thummel, R. *Inorg. Chem.* **2008,** 47, 1835-1848

56   Zong, R. , Thummel, R. P. *J. Am. Chem. Soc.* **2005,** 127, 12802-12803

57   Xu, Y., Åkermark, T. r., Gyollai, V., Zou, D., Eriksson, L., Duan, L., Zhang, R. *et al. Inorg. Chem.* **2009,** 48, 2717-2719

58   Xu, Y., Fischer, A., Duan, L., Tong, L., Gabrielsson, E., Åkermark, B. , Sun, L. *Angew. Chem. Int. Ed.* **2010,** 49, 8934-8937

59   Xu, Y., Duan, L., Tong, L., Akermark, B. , Sun, L. *Chem. Commun.* **2010,** 46, 6506-6508

60   Maji, S., Vigara, L., Cottone, F., Bozoglian, F., Benet-Buchholz, J. , Llobet, A. *Angew. Chem. Int. Ed.* **2012,** 51, 5967-5970

61   Neudeck, S., Maji, S., López, I., Meyer, S., Meyer, F. , Llobet, A. *J. Am. Chem. Soc.* **2013,** 136, 24-27

62   Collin, J. P. , Sauvage, J. P. *Inorg. Chem.* **1986,** 25, 135-141

63   Concepcion, J. J., Jurss, J. W., Templeton, J. L. , Meyer, T. J. *J. Am. Chem. Soc.* **2008,** 130, 16462-16463

64   Concepcion, J. J., Jurss, J. W., Norris, M. R., Chen, Z., Templeton, J. L. , Meyer, T. J. *Inorg. Chem.* **2010,** 49, 1277-1279

65   Masaoka, S. , Sakai, K. *Chem. Lett.* **2009,** 38, 182-183

66   Yagi, M., Tajima, S., Komi, M. , Yamazaki, H. *Dalton Trans.* **2011,** 40, 3802-3804

67   Wasylenko, D. J., Ganesamoorthy, C., Koivisto, B. D., Henderson, M. A. , Berlinguette, C. P. *Inorg. Chem.* **2010,** 49, 2202-2209

68   Wasylenko, D. J., Ganesamoorthy, C., Henderson, M. A., Koivisto, B. D., Osthoff, H. D. , Berlinguette, C. P. *J. Am. Chem. Soc.* **2010,** 132, 16094-16106

69   Tseng, H.-W., Zong, R., Muckerman, J. T. , Thummel, R. *Inorg. Chem.* **2008,** 47, 11763-11773

70   Yoshida, M., Masaoka, S. , Sakai, K. *Chem. Lett.* **2009,** 38, 702-703

71   Kaveevivitchai, N., Zong, R., Tseng, H.-W., Chitta, R. , Thummel, R. P. *Inorg. Chem.* **2012,** 51, 2930-2939

72   Boyer, J. L., Polyansky, D. E., Szalda, D. J., Zong, R., Thummel, R. P. , Fujita, E. *Angew. Chem. Int. Ed.* **2011,** 50, 12600-12604

73   Yoshida, M., Masaoka, S., Abe, J. , Sakai, K. *Chem. Asian J.* **2010,** 5, 2369-2378

74   López, I., Ertem, M. Z., Maji, S., Benet-Buchholz, J., Keidel, A., Kuhlmann, U., Hildebrandt, P. *et al. Angew. Chem. Int. Ed.* **2014,** 53, 205-209

75   Duan, L., Fischer, A., Xu, Y. , Sun, L. *J. Am. Chem. Soc.* **2009,** 131, 10397-10399

76   Duan, L., Xu, Y., Tong, L. , Sun, L. *ChemSusChem* **2011,** 4, 238-244

77   Nyhlén, J., Duan, L., Åkermark, B., Sun, L. , Privalov, T. *Angew. Chem. Int. Ed.* **2010,** 122, 1817-1821

78   Duan, L., Xu, Y., Zhang, P., Wang, M. , Sun, L. *Inorg. Chem.* **2009,** 49, 209-215

79   Duan, L., Araujo, C. M., Ahlquist, M. S. G. , Sun, L. *Proc. Natl. Acad. Sci.* **2012,** 109, 15584-15588

80   Wang, L., Duan, L., Stewart, B., Pu, M., Liu, J., Privalov, T. , Sun, L. *J. Am. Chem. Soc.* **2012,** 134, 18868-18880

81   Duan, L., Wang, L., Inge, A. K., Fischer, A., Zou, X. , Sun, L. *Inorg. Chem.* **2013,** 52, 7844-7852

82   Wang, L., Duan, L., Tong, L. , Sun, L. *J. Catal.* **2013,** 306, 129-132

83   Jiang, Y., Li, F., Zhang, B., Li, X., Wang, X., Huang, F. , Sun, L. *Angew. Chem. Int. Ed.* **2013,** 52, 3398-3401

84   Staehle, R., Tong, L., Wang, L., Duan, L., Fischer, A., Ahlquist, M. S. G., Sun, L. *et al. Inorg. Chem.* **2014,**

85   Vennampalli, M., Liang, G., Webster, C. E. , Zhao, X. *Eur. J. Inorg. Chem.* **2014,** 2014, 715-721

86   Li, F., Zhang, B., Li, X., Jiang, Y., Chen, L., Li, Y. , Sun, L. *Angew. Chem. Int. Ed.* **2011,** 50, 12276-12279

87   Li, L., Duan, L., Xu, Y., Gorlov, M., Hagfeldt, A. , Sun, L. *Chem. Commun.* **2010,** 46, 7307-7309

88   Gao, Y., Ding, X., Liu, J., Wang, L., Lu, Z., Li, L. , Sun, L. *J. Am. Chem. Soc.* **2013,** 135, 4219-4222

89   Sartorel, A., Carraro, M., Scorrano, G., Zorzi, R. D., Geremia, S., McDaniel, N. D., Bernhard, S. *et al. J. Am. Chem. Soc.* **2008,** 130, 5006-5007

90   Sartorel, A., Miró, P., Salvadori, E., Romain, S., Carraro, M., Scorrano, G., Valentin, M. D. *et al. J. Am. Chem. Soc.* **2009,** 131, 16051-16053

91   Sartorel, A., Miró, P., Salvadori, E., Romain, S., Carraro, M., Scorrano, G., Valentin, M. D. *et al. J. Am. Chem. Soc.* **2009,** 131, 16051-16053

92   Geletii, Y. V., Huang, Z., Hou, Y., Musaev, D. G., Lian, T. , Hill, C. L. *J. Am. Chem. Soc.* **2009,** 131, 7522-7523

93   Besson, C., Huang, Z., Geletii, Y. V., Lense, S., Hardcastle, K. I., Musaev, D. G., Lian, T. *et al. Chem. Commun.* **2010,** 46, 2784-2786

94   Toma, F. M., Sartorel, A., Iurlo, M., Carraro, M., Parisse, P., Maccato, C., Rapino, S. *et al. Nat Chem* **2010,** 2, 826-831

95   Kiwi, J. , Grätzel, M. *Angew. Chem. Int. Ed.* **1978,** 17, 860-861

96   Kiwi, J. , Grätzel, M. *Angew. Chem. Int. Ed.* **1979,** 18, 624-626

97   Mills, A. *J. Chem. Soc., Dalton Trans.* **1982,** 1213-1216

98   Kiwi, J., Gratzel, M. , Blondeel, G. *J. Chem. Soc., Dalton Trans.* **1983,** 2215-2216

99   Elizarova, G. L., Matvienko, L. G., Lozhkina, N. V., Parmon, V. N. , Zamaraev, K. I. *React. Kinet. Catal. Lett.* **1981,** 16, 191-194

100   Kiwi, J. , Grätzel, M. *Angew. Chem. Int. Ed.* **1979,** 91, 659-660

101   Lehn, J. M., Sauvage, J. P. , Ziessel, R. *Nouv. J. Chim.* **1979,** 3, 423-427

102   Youngblood, W. J., Lee, S.-H. A., Maeda, K. , Mallouk, T. E. *Acc. Chem. Res.* **2009,** 42, 1966-1973

103   McDaniel, N. D., Coughlin, F. J., Tinker, L. L. , Bernhard, S. *J. Am. Chem. Soc.* **2008,** 130, 210-217

104   Blakemore, J. D., Schley, N. D., Balcells, D., Hull, J. F., Olack, G. W., Incarvito, C. D., Eisenstein, O. *et al. J. Am. Chem. Soc.* **2010,** 132, 16017-16029

105   Savini, A., Bellachioma, G., Ciancaleoni, G., Zuccaccia, C., Zuccaccia, D. , Macchioni, A. *Chem. Commun.* **2010,** 46, 9218-9219

106   Petronilho, A., Rahman, M., Woods, J. A., Al-Sayyed, H., Muller-Bunz, H., Don MacElroy, J. M., Bernhard, S. *et al. Dalton Trans.* **2012,** 41, 13074-13080

107   Brewster, T. P., Blakemore, J. D., Schley, N. D., Incarvito, C. D., Hazari, N., Brudvig, G. W. , Crabtree, R. H. *Organometallics* **2011,** 30, 965-973

108   Hetterscheid, D. G. H. , Reek, J. N. H. *Chem. Commun.* **2011,** 47, 2712-2714

109   Savini, A., Belanzoni, P., Bellachioma, G., Zuccaccia, C., Zuccaccia, D. , Macchioni, A. *Green Chem.* **2011,** 13, 3360-3374

110   Bucci, A., Savini, A., Rocchigiani, L., Zuccaccia, C., Rizzato, S., Albinati, A., Llobet, A. *et al. Organometallics* **2012,** 31, 8071-8074

111   Dzik, W. I., Calvo, S. E., Reek, J. N. H., Lutz, M., Ciriano, M. A., Tejel, C., Hetterscheid, D. G. H. *et al. Organometallics* **2011,** 30, 372-374

112   Harriman, A., Pickering, I. J., Thomas, J. M. , Christensen, P. A. *Faraday Trans.* **1988,** 84, 2795-2806

113   Nakagawa, T., Bjorge, N. S. , Murray, R. W. *J. Am. Chem. Soc.* **2009,** 131, 15578-15579

114   Zhao, Y., Hernandez-Pagan, E. A., Vargas-Barbosa, N. M., Dysart, J. L. , Mallouk, T. E. *J. Phys. Chem. Lett.* **2011,** 2, 402-406

100

115   Grotjahn, D. B., Brown, D. B., Martin, J. K., Marelius, D. C., Abadjian, M.-C., Tran, H. N., Kalyuzhny, G. *et al. J. Am. Chem. Soc.* **2011,** 133, 19024-19027

116   Parent, A. R., Brewster, T. P., De Wolf, W., Crabtree, R. H. , Brudvig, G. W. *Inorg. Chem.* **2012,** 51, 6147-6152

117   Hong, D., Murakami, M., Yamada, Y. , Fukuzumi, S. *Energy Environ. Sci.* **2012,** 5, 5708-5716

118   Zuccaccia, C., Bellachioma, G., Bolaño, S., Rocchigiani, L., Savini, A. , Macchioni, A. *Eur. J. Inorg. Chem.* **2012,** 2012, 1462-1468

119   Savini, A., Bellachioma, G., Bolaño, S., Rocchigiani, L., Zuccaccia, C., Zuccaccia, D. , Macchioni, A. *ChemSusChem* **2012,** 5, 1415-1419

120   Zuccaccia, C., Bellachioma, G., Bortolini, O., Bucci, A., Savini, A. , Macchioni, A. *Chem. Eur. J.* **2014,** n/a-n/a

121   Junge, H., Marquet, N., Kammer, A., Denurra, S., Bauer, M., Wohlrab, S., Gärtner, F. *et al. Chem. Eur. J* **2012,** 18, 12749-12758

122   Wang, C., Wang, J.-L. , Lin, W. *J. Am. Chem. Soc.* **2012,** 134, 19895-19908

123   Marquet, N., Gärtner, F., Losse, S., Pohl, M.-M., Junge, H. , Beller, M. *ChemSusChem* **2011,** 4, 1598-1600

124   Parent, A. R., Blakemore, J. D., Brudvig, G. W. , Crabtree, R. H. *Chem. Commun.* **2011,** 47, 11745-11747

125   Schley, N. D., Blakemore, J. D., Subbaiyan, N. K., Incarvito, C. D., D'Souza, F., Crabtree, R. H. , Brudvig, G. W. *J. Am. Chem. Soc.* **2011,** 133, 10473-10481

126   DePasquale, J., Nieto, I., Reuther, L. E., Herbst-Gervasoni, C. J., Paul, J. J., Mochalin, V., Zeller, M. *et al. Inorg. Chem.* **2013,** 52, 9175-9183

127   Zhang, T., deKrafft, K. E., Wang, J.-L., Wang, C. , Lin, W. *Eur. J. Inorg. Chem.* **2014,** 2014, 698-707

128   Lewandowska-Andralojc, A., Polyansky, D. E., Wang, C.-H., Wang, W.-H., Himeda, Y. , Fujita, E. *PCCP* **2014,**

129   Hintermair, U., Hashmi, S. M., Elimelech, M. , Crabtree, R. H. *J. Am. Chem. Soc.* **2012,** 134, 9785-9795

130   Hintermair, U., Sheehan, S. W., Parent, A. R., Ess, D. H., Richens, D. T., Vaccaro, P. H., Brudvig, G. W. *et al. J. Am. Chem. Soc.* **2013,** 135, 10837-10851

131   Graeupner, J., Hintermair, U., Huang, D. L., Thomsen, J. M., Takase, M., Campos, J., Hashmi, S. M. *et al. Organometallics* **2013,** 32, 5384-5390

132   Volpe, A., Sartorel, A., Tubaro, C., Meneghini, L., Di Valentin, M., Graiff, C. , Bonchio, M. *Eur. J. Inorg. Chem.* **2013,** 665-675

133   Ayres, R. U. *Proc. Natl. Acad. Sci.* **1992,** 89, 815-820

134   Wolfram|Alpha. **2014,**

135   Barbalace, K. *Periodic Table of Elements, environmentalChemistry.com* **1995-2014,**

136   *Johnson & Matthey* **2014,**

137   Ruettinger, W., Yagi, M., Wolf, K., Bernasek, S. , Dismukes, G. C. *J. Am. Chem. Soc.* **2000,** 122, 10353

138   Carrell, T. G., Bourles, E., Lin, M. , Dismukes, G. C. *Inorg. Chem.* **2003,** 42, 2849-2858

139   Ruettinger, W. , Dismukes, G. C. *Inorg. Chem.* **2000,** 39, 1021

140   Yagi, M., Wolf, K. V., Baesjou, P. J., Bernasek, S. L. , Dismukes, G. C. *Angew. Chem. Int. Ed.* **2001,** 40, 2925-2928

141   Brimblecombe, R., Swiegers, G. F., Dismukes, G. C. , Spiccia, L. *Angew. Chem. Int. Ed.* **2008,** 47, 7335-7338

142   Hocking, R. K., Brimblecombe, R., Chang, L.-Y., Singh, A., Cheah, M. H., Glover, C., Casey, W. H. *et al. Nat Chem* **2011,** 3, 461-466

143   Takashima, T., Hashimoto, K. , Nakamura, R. *J. Am. Chem. Soc.* **2011,** 134, 1519-1527

144   Siegbahn, P. E. M. *PCCP* **2014,**

145   Mishra, A., Wernsdorfer, W., Abboud, K. A. , Christou, G. *Chem. Commun.* **2005,** 0, 54-56

146   Mishra, A., Yano, J., Pushkar, Y., Yachandra, V. K., Abboud, K. A. , Christou, G. *Chem. Commun.* **2007,** 0, 1538-1540

147   Hewitt, I. J., Tang, J.-K., Madhu, N. T., Clerac, R., Buth, G., Anson, C. E. , Powell, A. K. *Chem. Commun.* **2006,** 0, 2650-2652

148   Nayak, S., Nayek, H. P., Dehnen, S., Powell, A. K. , Reedijk, J. *Dalton Trans.* **2011,** 40, 2699-2702

149   Najafpour, M. M., Pashaei, B. , Nayeri, S. *Dalton Trans.* **2012,** 41, 4799-4805

150   Park, Y. J., Ziller, J. W. , Borovik, A. S. *J. Am. Chem. Soc.* **2011,** 133, 9258-9261

151   Kanady, J. S., Tsui, E. Y., Day, M. W. , Agapie, T. *Science* **2011,** 333, 733-736

152   Kanady, J. S., Mendoza-Cortes, J. L., Tsui, E. Y., Nielsen, R. J., Goddard, W. A. , Agapie, T. *J. Am. Chem. Soc.* **2012,** 135, 1073-1082

153   Tsui, E. Y., Tran, R., Yano, J. , Agapie, T. *Nat Chem* **2013,** 5, 293-299

154   Brudvig, G. W. *Phil. Trans. R. Soc. B* **2008,** 363, 1211-1219

155   Naruta, Y., Sasayama, M. , Sasaki, T. *Angew. Chem. Int. Ed.* **1994,** 33, 1839-1841

156   Groves, J. T., Lee, J. , Marla, S. S. *J. Am. Chem. Soc.* **1997,** 119, 6269-6273

157   Shimazaki, Y., Nagano, T., Takesue, H., Ye, B.-H., Tani, F. , Naruta, Y. *Angew. Chem. Int. Ed.* **2004,** 43, 98-100

158   Jin, N., Bourassa, J. L., Tizio, S. C. , Groves, J. T. *Angew. Chem. Int. Ed.* **2000,** 39, 3849-3851

159   Chen, J., Wagner, P., Tong, L., Wallace, G. G., Officer, D. L. , Swiegers, G. F. *Angew. Chem. Int. Ed.* **2012,** 124, 1943-1946

160   Gross, Z., Golubkov, G. , Simkhovich, L. *Angew. Chem. Int. Ed.* **2000,** 39, 4045-4047

161   Golubkov, G., Bendix, J., Gray, H. B., Mahammed, A., Goldberg, I., DiBilio, A. J. , Gross, Z. *Angew. Chem. Int. Ed.* **2001,** 113, 2190-2192

162   Liu, H.-Y., Lai, T.-S., Yeung, L.-L. , Chang, C. K. *Org. Lett.* **2003,** 5, 617-620

163   Mandimutsira, B. S., Ramdhanie, B., Todd, R. C., Wang, H., Zareba, A. A., Czernuszewicz, R. S. , Goldberg, D. P. *J. Am. Chem. Soc.* **2002,** 124, 15170-15171

164   Gao, Y., Liu, J., Wang, M., Na, Y., Åkermark, B. , Sun, L. *Tetrahedron* **2007,** 63, 1987-1994

165   Gao, Y., Åkermark, T. r., Liu, J., Sun, L. , Åkermark, B. r. *J. Am. Chem. Soc.* **2009,** 131, 8726-8727

166   Ramaraj, R., Kira, A. , Kaneko, M. *Angew. Chem. Int. Ed.* **1986,** 25, 825-827

167   Limburg, J., Brudvig, G. W. , Crabtree, R. H. *J. Am. Chem. Soc.* **1997,** 119, 2761-2762

168   Yagi, M. , Narita, K. *J. Am. Chem. Soc.* **2004,** 126, 8084-8085

169   Tagore, R., Chen, H., Zhang, H., Crabtree, R. H. , Brudvig, G. W. *Inorg. Chim. Acta* **2007,** 360, 2983-2989

170   Limburg, J., Vrettos, J. S., Liable-Sands, L. M., Rheingold, A. L., Crabtree, R. H. , Brudvig, G. W. *Science* **1999,** 283, 1524-1527

171   Limburg, J., Vrettos, J. S., Chen, H., de Paula, J. C., Crabtree, R. H. , Brudvig, G. W. *J. Am. Chem. Soc.* **2000,** 123, 423-430

172   Tagore, R., Crabtree, R. H. , Brudvig, G. W. *Inorg. Chem.* **2008,** 47, 1815-1823

173   Lundberg, M., Blomberg, M. R. A. , Siegbahn, P. E. M. *Inorg. Chem.* **2003,** 43, 264-274

174   Valles-Pardo, J. L., de Groot, H. J. M. , Buda, F. *PCCP* **2012,** 14, 15502-15508

175   Chen, H., Tagore, R., Das, S., Incarvito, C., Faller, J. W., Crabtree, R. H. , Brudvig, G. W. *Inorg. Chem.* **2005,** 44, 7661-7670

176   Chen, H., Tagore, R., Olack, G., Vrettos, J. S., Weng, T. C., Penner-Hahn, J., Crabtree, R. H. *et al. Inorg. Chem.* **2007,** 46, 34-43

177   Narita, K., Kuwabara, T., Sone, K., Shimizu, K.-i. , Yagi, M. *J. Phys. Chem. B* **2006,** 110, 23107-23114

178   Yamazaki, H., Igarashi, S., Nagata, T. , Yagi, M. *Inorg. Chem.* **2012,** 51, 1530-1539

179   Nepal, B. , Das, S. *Angew. Chem. Int. Ed.* **2013,** 52, 7224-7227

180   Hansen, R. E. , Das, S. *Energy Environ. Sci.* **2014,** 7, 317-322

181   Baffert, C., Romain, S., Richardot, A., Leprêtre, J.-C., Lefebvre, B., Deronzier, A. , Collomb, M.-N. *J. Am. Chem. Soc.* **2005,** 127, 13694-13704

182   Gao, Y., Crabtree, R. H. , Brudvig, G. W. *Inorg. Chem.* **2012,** 51, 4043-4050

183   Poulsen, A. K., Rompel, A. , McKenzie, C. J. *Angew. Chem. Int. Ed.* **2005,** 117, 7076-7080

184   Seidler-Egdal, R. K., Nielsen, A., Bond, A. D., Bjerrum, M. J. , McKenzie, C. J. *Dalton Trans.* **2011,** 40, 3849-3858

185   Sameera, W. M. C., McKenzie, C. J. , McGrady, J. E. *Dalton Trans.* **2011,** 40, 3859-3870

186   Berggren, G., Thapper, A., Huang, P., Eriksson, L., Styring, S. r. , Anderlund, M. F. *Inorg. Chem.* **2011,** 50, 3425-3430

187   Kurz, P., Berggren, G., Anderlund, M. F. , Styring, S. *Dalton Trans.* **2007,** 0, 4258-4261

188   Young, K. J., Takase, M. K. , Brudvig, G. W. *Inorg. Chem.* **2013,** 52, 7615-7622

189   Yatabe, T., Kikkawa, M., Matsumoto, T., Nakai, H., Kaneko, K. , Ogo, S. *Dalton Trans.* **2014,**

190   Ashmawy, F. M., McAuliffe, C. A., Parish, R. V. , Tames, J. *Dalton Trans.* **1985,** 0, 1391-1397

191   Watkinson, M., Whiting, A. , McAuliffe, C. A. *Chem. Commun.* **1994,** 0, 2141-2142

192   Gonzalez-Riopedre, G., Fernandez-Garcia, M. I., Gonzalez-Noya, A. M., Vazquez-Fernandez, M. A., Bermejo, M. R. , Maneiro, M. *PCCP* **2011,** 13, 18069-18077

193   Hammarström, L., Sun, L., Åkermark, B. , Styring, S. *Catal. Today* **2000,** 58, 57-69

194   Jegerschöld, C. , Styring, S. *Biochemistry* **1996,** 35, 7794-7801

195   F. Mamodov, R. S., S. Styring. *Biochemistry* **1988,** 37, 14245

102

196   Karlsson, E. A., Lee, B.-L., Åkermark, T., Johnston, E. V., Kärkäs, M. D., Sun, J., Hansson, Ö. *et al. Angew. Chem. Int. Ed.* **2011,** 123, 11919-11922

197   Shafirovich, V. Y. K., N. K.; Strelets, V. V. . *Nouv. J. Chim.* **1980**, 81

198   Brunschwig, B. S., Chou, M. H., Creutz, C., Ghosh, P. , Sutin, N. *J. Am. Chem. Soc.* **1983,** 105, 4832-4833

199   Kanan, M. W. , Nocera, D. G. *Science* **2008,** 321, 1072-1075

200   Yin, Q., Tan, J. M., Besson, C., Geletii, Y. V., Musaev, D. G., Kuznetsov, A. E., Luo, Z. *et al. Science* **2010,** 328, 342-345

201   Huang, Z., Luo, Z., Geletii, Y. V., Vickers, J. W., Yin, Q., Wu, D., Hou, Y. *et al. J. Am. Chem. Soc.* **2011,** 133, 2068-2071

202   Lieb, D., Zahl, A., Wilson, E. F., Streb, C., Nye, L. C., Meyer, K. , Ivanović-Burmazović, I. *Inorg. Chem.* **2011,** 50, 9053-9058

203   Stracke, J. J. , Finke, R. G. *J. Am. Chem. Soc.* **2011,** 133, 14872-14875

204   Natali, M., Berardi, S., Sartorel, A., Bonchio, M., Campagna, S. , Scandola, F. *Chem. Commun.* **2012,** 48, 8808-8810

205   Stracke, J. J. , Finke, R. G. *ACS Catalysis* **2013,** 3, 1209-1219

206   Vickers, J. W., Lv, H., Sumliner, J. M., Zhu, G., Luo, Z., Musaev, D. G., Geletii, Y. V. *et al. J. Am. Chem. Soc.* **2013,** 135, 14110-14118

207   Stracke, J. J. , Finke, R. G. *ACS Catalysis* **2014,** 4, 909-933

208   Schiwon, R., Klingan, K., Dau, H. , Limberg, C. *Chem. Commun.* **2013,**

209   Stracke, J. J. , Finke, R. G. *ACS Catalysis* **2013,** 79-89

210   Song, F., Ding, Y., Ma, B., Wang, C., Wang, Q., Du, X., Fu, S. *et al. Energy Environ. Sci.* **2013,** 6, 1170-1184

211   Lv, H., Geletii, Y. V., Zhao, C., Vickers, J. W., Zhu, G., Luo, Z., Song, J. *et al. Chem. Soc. Rev.* **2012,** 41, 7572-7589

212   Zhang, L.-Z., Gu, W., Liu, X., Dong, Z., Yang, Y.-S., Li, B. , Liao, D.-Z. *Inorg. Chem. Commun.* **2007,** 10, 1378-1380

213   Zhu, G., Geletii, Y. V., Kogerler, P., Schilder, H., Song, J., Lense, S., Zhao, C. *et al. Dalton Trans.* **2012,** 41, 2084-2090

214   Goberna-Ferrón, S., Vigara, L., Soriano-López, J. , Galán-Mascarós, J. R. *Inorg. Chem.* **2012,** 51, 11707-11715

215   Soriano-López, J., Goberna-Ferrón, S., Vigara, L., Carbó, J. J., Poblet, J. M. , Galán-Mascarós, J. R. *Inorg. Chem.* **2013,** 52, 4753-4755

216   Car, P.-E., Guttentag, M., Baldridge, K. K., Alberto, R. , Patzke, G. R. *Green Chem.* **2012,** 14, 1680-1688

217   Tanaka, S., Annaka, M. , Sakai, K. *Chem. Commun.* **2012,** 48, 1653-1655

218   Elizarova, G. L., Matvienko, L. G., Lozhkina, N. V., Maizlish, V. E. , Parmon, V. N. *React. Kinet. Catal. Lett.* **1981,** 16, 285-288

219   Abe, T., Nagai, K., Kabutomori, S., Kaneko, M., Tajiri, A. , Norimatsu, T. *Angew. Chem. Int. Ed.* **2006,** 45, 2778-2781

220   Nakazono, T., Parent, A. R. , Sakai, K. *Chem. Commun.* **2013,** 49, 6325-6327

221   Dogutan, D. K., McGuire, R. , Nocera, D. G. *J. Am. Chem. Soc.* **2011,** 133, 9178-9180

222   Lei, H., Han, A., Li, F., Zhang, M., Han, Y., Du, P., Lai, W. *et al. PCCP* **2013,** 1883-1893

223   Wang, D. , Groves, J. T. *Proc. Natl. Acad. Sci.* **2013,** 110, 15579-15584

224   Wasylenko, D. J., Ganesamoorthy, C., Borau-Garcia, J. , Berlinguette, C. P. *Chem. Commun.* **2011,** 47, 4249-4251

225   Wasylenko, D. J., Palmer, R. D., Schott, E. , Berlinguette, C. P. *Chem. Commun.* **2012,** 48, 2107-2109

226   Hong, D., Jung, J., Park, J., Yamada, Y., Suenobu, T., Lee, Y.-M., Nam, W. *et al. Energy Environ. Sci.* **2012,** 5, 7606-7616

227   Leung, C.-F., Ng, S.-M., Ko, C.-C., Man, W.-L., Wu, J., Chen, L. , Lau, T.-C. *Energy Environ. Sci.* **2012,** 5, 7903-7907

228   Pizzolato, E., Natali, M., Posocco, B., Montellano Lopez, A., Bazzan, I., Di Valentin, M., Galloni, P. *et al. Chem. Commun.* **2013,** 49, 9941-9943

229   Fu, S., Liu, Y., Ding, Y., Du, X., Song, F., Xiang, R. , Ma, B. *Chem. Commun.* **2013,** 2167-2169

230   Kanan, M. W., Yano, J., Surendranath, Y., Dincă, M., Yachandra, V. K. , Nocera, D. G. *J. Am. Chem. Soc.* **2010,** 132, 13692-13701

231   McCool, N. S., Robinson, D. M., Sheats, J. E. , Dismukes, G. C. *J. Am. Chem. Soc.* **2011,** 133, 11446-11449

232   La Ganga, G., Puntoriero, F., Campagna, S., Bazzan, I., Berardi, S., Bonchio, M., Sartorel, A. *et al. Faraday Discuss.* **2012,** 155, 177-190

233   Berardi, S., La Ganga, G., Natali, M., Bazzan, I., Puntoriero, F., Sartorel, A., Scandola, F. *et al. J. Am. Chem. Soc.* **2012,** 134, 11104-11107

234   Wang, L.-P. , Van Voorhis, T. *J. Phys. Chem. Lett.* **2011,** 2, 2200-2204

235   Rigsby, M. L., Mandal, S., Nam, W., Spencer, L. C., Llobet, A. , Stahl, S. S. *Chem. Sci.* **2012,** 3, 3058-3062

236   Li, X. , Siegbahn, P. E. M. *J. Am. Chem. Soc.* **2013,** 135, 13804-13813

237   Evangelisti, F., Güttinger, R., Moré, R., Luber, S. , Patzke, G. R. *J. Am. Chem. Soc.* **2013,**

238   Barnett, S. M., Goldberg, K. I. , Mayer, J. M. *Nat Chem* **2012,** 4, 498-502

239   Zhang, T., Wang, C., Liu, S., Wang, J.-L. , Lin, W. *J. Am. Chem. Soc.* **2013,**

240   Chen, Z. , Meyer, T. J. *Angew. Chem. Int. Ed.* **2013,** 52, 700-703

241   Zhang, M.-T., Chen, Z., Kang, P. , Meyer, T. J. *J. Am. Chem. Soc.* **2013,** 135, 2048-2051

242   Zhu, G., Glass, E. N., Zhao, C., Lv, H., Vickers, J. W., Geletii, Y. V., Musaev, D. G. *et al. Dalton Trans.* **2012,** 41, 13043-13049

243   Dyer, C. K. *J. Electrochem. Soc.* **1985,** 132, 64-67

244   Gennero de Chialvo, M. R. , Chialvo, A. C. *Electrochim. Acta* **1988,** 33, 825-830

245   Sadiek, I. M., Mohammad, A. M., El-Shakre, M. E. , El-Deab, M. S. *Int. J. Hydrogen Energy* **2012,** 37, 68-77

246   Dincă, M., Surendranath, Y. , Nocera, D. G. *Proc. Natl. Acad. Sci.* **2010,** 107, 10337-10341

247   Singh, A., Chang, S. L. Y., Hocking, R. K., Bach, U. , Spiccia, L. *Energy Environ. Sci.* **2013,** 6, 579-586

248   Singh, A., Chang, S. L. Y., Hocking, R. K., Bach, U. , Spiccia, L. *Catal. Sci. Tech.* **2013,** 3, 1725-1732

249   Chen, G., Chen, L., Ng, S.-M. , Lau, T.-C. *ChemSusChem* **2014,** 7, 127-134

250   Ellis, W. C., McDaniel, N. D., Bernhard, S. , Collins, T. J. *J. Am. Chem. Soc.* **2010,** 132, 10990-10991

251   Ertem, M. Z., Gagliardi, L. , Cramer, C. J. *Chem. Sci.* **2012,** 3, 1293-1299

252   Liao, R.-Z., Li, X.-C. , Siegbahn, P. E. M. *Eur. J. Inorg. Chem.* **2013,** n/a-n/a

253   Vigara, L., Ertem, M. Z., Planas, N., Bozoglian, F., Leidel, N., Dau, H., Haumann, M. *et al. Chem. Sci.* **2012,** 3, 2576-2586

254   Blakemore, J. D., Schley, N. D., Olack, G. W., Incarvito, C. D., Brudvig, G. W. , Crabtree, R. H. *Chem. Sci.* **2011,** 2, 94-98

255   Huang, P., Magnuson, A., Lomoth, R., Abrahamsson, M., Tamm, M., Sun, L., van Rotterdam, B. *et al. J. Inorg. Biochem.* **2002,** 91, 159-172

CHAPTER II.

MAIN OBJECTIVES

II.   MAIN OBJECTIVES

Towards the development of the artificial photosynthesis, the efficient removal of four protons and electrons from the catalytic site to oxidize water is crucial to start the photosynthetic process. The high thermodynamic potential to overcome the water oxidation makes this process kinetically inefficient when driven by simple electrochemical methods and a great effort has been focused on the development of efficient water oxidation catalyst, required to lower the activation barriers, and allowing the process to take place at lower overpotentials and faster rates. The study of the metalloenzyme (oxygen evolving complex) which leads the water oxidation in the natural photosynthesis, and the protein surroundings, have provided some piece of information towards the understanding of this mechanism and towards the rational development of synthetic compounds to reproduce its function, which in turn has helped in proving some key steps of the reaction occurring in Nature.

In this context, and based on the growing interest on developing alternatives to fossil fuels, the aim of this thesis is the rational design of small homogeneous molecular models to oxidize water efficiently. Moreover, the mechanistic investigation through the detection and characterization of key intermediates and the detection of relevant structural features could be helpful in improving the state of the art water oxidation catalysts.

To date, the homogeneous water oxidation is led by efficient, expensive, toxic, and scarce second and third-row transition metals. Therefore, the development of both robust and efficient systems based on readily available, benign, and inexpensive metals is needed. Due to the lack of mechanism understanding, the thermal water oxidation (driven by chemical oxidants), which allows fast and detailed kinetic studies, will be our main objective.

In this regard, we will focus the first part of this thesis on the development of a well-established an efficient metal to catalyze water oxidation. Iridium organometallic complexes will aid towards the understanding of key aspects on the catalysis. In order to unravel the importance of the chelate ligand we planned the use of two different organometallic structures (Scheme 1) to generate the respective iridium complexes and evaluate the O_2 production using cerium ammonium nitrate and sodium periodate as sacrificial oxidants.
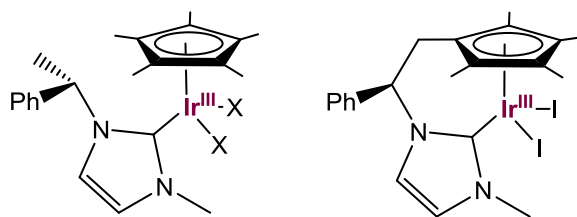
Scheme II.1. Iridium complexes synthetized towards the understanding of the effect of linking the Cp* group to the carbene moiety.

In the next part of this thesis, we moved to first row transition metals, towards the development of element earth abundant and benign catalysts. The robustness towards a highly oxidative environment and the requirement of high oxidation states are key abilities to catalyze with high efficiencies and selectivities the challenging stereospecific C-H hydroxylation, cis-dihydroxylation and epoxidation of olefins, fields were our group has been acquiring expertise in the last decade. Therefore, these systems were thought to be good candidates to explore water oxidation catalysis (Scheme II).
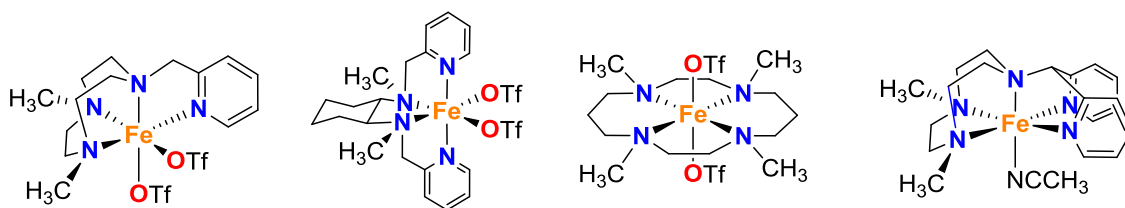
Scheme II.2. Promising iron complexes for the catalytic water oxidation reaction.

Due to the finding of an efficient family of water oxidation catalyst based on iron, the last part of this thesis has been focused on the mechanistic study and intermediate characterization to gain insight towards the rational development of more efficient and robust iron-based systems.

CHAPTER III.

HIGHLY EFFECTIVE WATER OXIDATION CATALYSIS WITH IRIDIUM COMPLEXES THROUGH THE USE OF NaIO₄

This chapter corresponds to the following publication:

Abstract

Exceptional water oxidation (WO) turnover frequencies (TOF=17 000 h^{-1}), and turnover numbers (TONs) close to 400 000, the largest ever reported for a metal-catalyzed WO reaction, have been found by using [Cp*Ir^{III}(NHC)Cl$_2$] (in which NHC=3-methyl-1-(1-phenylethyl)-imidazoline-2-ylidene) as the pre-catalyst and NaIO$_4$ as oxidant in water at 40 °C. The apparent TOF for [Cp*Ir^{III}(NHC)X$_2$] (**1 X**, in which X stands for I (**1 I**), Cl (**1 Cl**), or triflate anion (**1 OTf**)) and [(Cp*-NHCMe)Ir^{III}I$_2$] (**2**) complexes, is kept constant during almost all of the O$_2$ evolution reaction when using NaIO$_4$ as oxidant. The TOF was found to be dependent on the ligand and on the anion (TOF ranging from ≈600 to ≈1100 h^{-1} at 25 °C). Degradation of the complexes by oxidation of the organic ligands upon reaction with NaIO$_4$ has been investigated. ^{1}H NMR, ESI-MS, and dynamic light-scattering measurements (DLS) of the reaction medium indicated that the complex undergoes rapid degradation, even at low equivalents of oxidant, but this process takes place without formation of nanoparticles. Remarkably, three-month-old solution samples of oxidized pre-catalysts remain equally as active as freshly prepared solutions. A UV/Vis feature band at λ_{max}=405 nm is observed in catalytic reaction solutions only when O$_2$ evolves, which may be attributed to a resting state iridium speciation, most probably Ir–oxo species with an oxidation state higher than IV.

CHAPTER IV.

EFFICIENT WATER OXIDATION CATALYSTS BASED ON READILY AVAILABLE IRON COORDINATION COMPLEXES
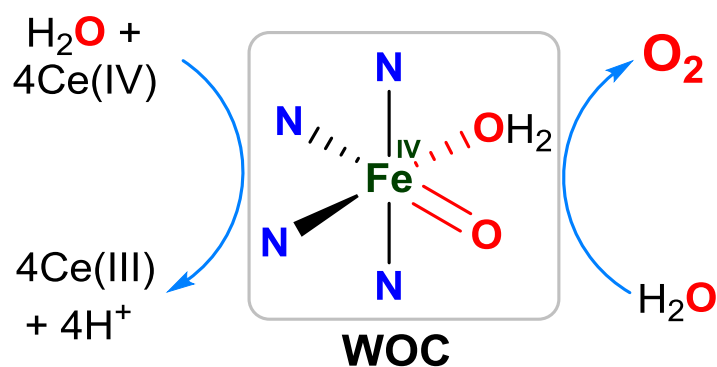
This chapter corresponds to the following publication:

Julio Lloret Fillol, Zoel Codolà, Isaac Garcia-Bosch, Laura Gómez, Juan José Pla & Miquel Costas, Nature Chemistry, **2011**, 3, 807-813.

Julio Lloret Fillol, Zoel Codolà, Isaac Garcia-Bosch, Laura Gómez, Juan José Pla, Miquel Costas
"Efficient water oxidation catalysts based on readily available iron coordination complexes". *Nature Chemistry* **3**, 807–813 (2011)

ABSTRACT

Water oxidation catalysis constitutes the bottleneck for the development of energy-conversion schemes based on sunlight. To date, state-of-the-art homogeneous water oxidation catalysis is performed efficiently with expensive, toxic and earth-scarce transition metals, but 3d metal-based catalysts are much less established. Here we show that readily available, environmentally benign iron coordination complexes catalyse homogeneous water oxidation to give O_2, with high efficiency during a period of hours. Turnover numbers >350 and >1,000 were obtained using cerium ammonium nitrate at pH 1 and sodium periodate at pH 2, respectively. Spectroscopic monitoring of the catalytic reactions, in combination with kinetic studies, show that high valent oxo-iron species are responsible for the O–O forming event. A systematic study of iron complexes that contain a broad family of neutral tetradentate organic ligands identifies first-principle structural features to sustain water oxidation catalysis. Iron-based catalysts described herein open a novel strategy that could eventually enable sustainable artificial photosynthetic schemes.

CHAPTER V.

ELECTRONIC EFFECTS ON SINGLE-SITE IRON CATALYSTS FOR WATER OXIDATION

This chapter corresponds to the following publication:

Electronic Effects on Single-Site Iron Catalysts for Water Oxidation

Zoel Codolà, Isaac Garcia-Bosch, Ferran Acuña-Parés, Irene Prat, Josep M. Luis, Miquel Costas,* and Julio Lloret-Fillol*[a]

Fe

Fe-WOC

Getting in tune: Systematic tuning of the electronic properties of modular non-heme iron coordination complexes can be used to extract important information on the reaction mechanism and intermediates, which, in turn, help to explain the activity of these systems as water oxidation catalysts.

CHAPTER VI.

EVIDENCE FOR AN OXYGEN EVOLVING Fe–O–Ce INTERMEDIATE IN IRON-CATALYSED WATER OXIDATION

This chapter corresponds to the following publication:

Evidence for an Oxygen Evolving Fe–O–Ce Intermediate in Iron-Catalysed Water Oxidation

Zoel Codolà[a], Laura Gómez[a], Scott T. Kleespies[b], Lawrence Que, Jr.[b]*, Miquel Costas[a]*, Julio Lloret-Fillol[a]*

[a]*Institut de Química Computacional i Catàlisi (IQCC) and Departament de Química, Universitat de Girona, Campus de Montilivi, 17071 Girona, Spain*

[b] *Department of Chemistry and Center for Metals in Biocatalysis, University of Minnesota, 207 Pleasant St. S.E., Minneapolis, Minnesota 55455, United States*

*To whom correspondence should be addressed. Email: Julio.lloret@udg.edu; Miquel.costas@udg.edu. larryque@umn.edu

Abstract: The non-heme iron complex α-[Fe^{II}(CF$_3$SO$_3$)$_2$(mcp)] (mcp = (*N,N'*-dimethyl-*N,N'*-bis(2-pyridylmethyl)-1,2-*cis*-diaminocyclohexane) reacts with Ce^{IV} to oxidize water to O$_2$, representing an iron-based functional model for the oxygen evolving complex (OEC) of photosystem II. An intermediate has been trapped, characterized by cryospray ionization high resolution mass spectrometry and resonance Raman spectroscopy, and formulated as [(mcp)Fe^{IV}(O)(μ-O)Ce^{IV}(NO$_3$)$_3$]$^+$, the first example of a well-characterized inner-sphere complex to be formed in Ce^{IV}-mediated water oxidation. The identification of this reactive Fe^{IV}–O–Ce^{IV} adduct may open new pathways to validate mechanistic notions of an analogous Mn^V–O–Ca^{II} unit in the OEC that is responsible for carrying out the key O–O bond forming step.

High-valent iron-oxo species are implicated in important biological and synthetic oxidative transformations.[1, 2, 3] Some of these species have also shown a remarkable competence towards water oxidation to form dioxygen, a reaction that involves O-O bond formation.[4, 5, 6, 7] The reaction is particularly appealing because it has been recognized as one of the bottleneck challenges for the success of artificial photosynthesis, and the identification of iron compounds as efficient catalysts opens novel directions in the quest for systems that could be used on a large scale.[8, 9, 10, 11] In this context, the study of the water oxidation (WO) reaction with chemical oxidants catalyzed by well-defined coordination complexes can clarify fundamental principles underlying the mechanisms of O-O bond formation and cleavage,[12, 13] the latter being at the heart of chemical processes by which aerobic organisms respire.[14] Most remarkably, given the strong parallels between the oxidation chemistry of iron and manganese compounds,[15] it can be envisioned that fundamental chemical insights extracted from studies of O-O bond formation by iron coordination compounds can shed light on intermediates and mechanisms operating at the OEC.

We and others have recently shown that non-heme iron complexes containing tetradentate nitrogen based ligands are competent catalysts for chemically-driven WO.[4, 5, 16, 17] In our systematic studies, we determined that the presence of two *cis* labile sites is required for WO activity and that electronic effects modulate the catalytic efficiency, providing basic principles for catalyst design.[4, 5] Herein, we present evidence for a novel and catalytically relevant reaction intermediate that precedes the oxidation of the water molecule in the case of α-[Fe^{II}(CF$_3$SO$_3$)$_2$(mcp)], **1-α** (Table 1), which we have identified as a particularly active catalyst. This transient species is characterized by high resolution mass spectrometry (CSI-HRMS) and resonance Raman spectroscopy (rR) as a heterobimetallic oxo-bridged iron-cerium complex formed by the reaction of the oxoiron(IV) complex α-[Fe^{IV}(O)(H$_2$O)(mcp)]$^{2+}$ and Ce^{IV}. The Fe(O)(μ-O)Ce(OH$_2$)$_n$ core of this intermediate bears a strong structural resemblance to the Mn(O)(μ-O)Ca(OH$_2$)$_2$ unit found in the natural oxygen evolving center. Most remarkably, the Fe(O)(μ-O)Ce(OH$_2$)$_n$ unit is catalytically competent in water oxidation.

Results and Discussion

[Fe^{II}(CF$_3$SO$_3$)$_2$(mcp)] is known to form two topological isomers, **1-α** and **1-β** (Table 1),[18, 19, 20, 21] which have previously been shown to behave differently as catalysts for C-H and C=C bond oxidations.[19, 21] Given this sensitivity, the abilities of both complexes to act as water oxidation catalysts were explored. In a typical reaction, an aqueous solution of **1-α** or **1-β** (0.5 mL, 12.5 μM, final concentration) was added to an aqueous solution of CAN (9.5 mL,

125 mM, pH = 0.8, final concentration and pH). Gases evolved from these reactions were monitored by manometry and quantified by gas chromatography with a thermal conductivity detector (GC-TCD). Under these conditions (Table 1), **1-α** was highly active and yielded 160 ± 10 and 380 ± 20 TON of O_2, (mol of O_2/mol of catalyst) when using 100 and 12.5 μM catalyst concentrations, respectively. In contrast, very small amounts of O_2 were detected when the same experiment was carried out with its topological isomer **1-β** (4 ± 1 and 5 ± 2 TON, respectively). Therefore, despite the fact that the two complexes differed only in their ligand topology, their activities as water oxidation catalysts were found to be drastically different. Besides O_2, only small amounts of CO_2 were present at the end of the reaction (< 1 TON), indicating that no major ligand oxidation occurred during catalytic O_2 evolution.

Table 1. Water oxidation catalytic activities for **1-α**, and **1-β**.
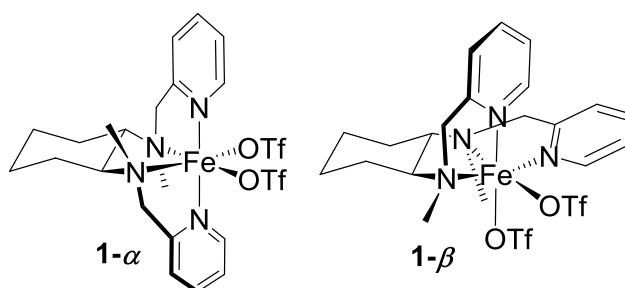
Catalyst	[cat] (μM)	TON O_2[a]	TOF (h^{-1}) [b]	TON O_2[c]	TON CO_2[c]
1-α	100	110 ± 10	580 ± 30	160 ± 10	0.3 ± 0.2
	12.5	360 ± 20	1020 ± 90	380 ± 20	0.4 ± 0.2
1-β	100	4 ± 1	9 ± 1	4 ± 1	0.2 ± 0.1
	12.5	8 ± 2	25 ± 11	5 ± 2	1.1 ± 0.1

Reactions performed in Milli-Q water at 25 ºC. The catalyst (0.5 mL) was injected through a septum into the reaction vessel containing CAN aqueous solution, (9.5 mL, 131 mM; final concentration 125 mM). The initial pH value was 0.8. [a] TON (turnover number) = (n(O_2) produced / n(catalyst)) obtained by manometry. [b] TOF (TON·h⁻¹) measured 5 min after the addition of the catalyst. [c] Values measured by GC-TCD after 3 h of reaction.

Reactions were then analyzed spectroscopically to gain insight into the origin of the dramatic differences in reactivity (Figure 1). The reaction of **1-α** or **1-β** with CAN (3 eq.) in H_2O (final pH =1) resulted in the formation of *α/β*-[$Fe^{IV}(O)(H_2O)(mcp)$]$^{2+}$, **2-α** or **2-β**, respectively. Both exhibited near-IR bands characteristic of $Fe^{IV}(O)$

complexes, namely λ_{max} = 769 nm (ε = 270 M^{-1}·cm^{-1}) for **2-α** and λ_{max} = 778 nm (ε = 280 M^{-1}·cm^{-1}) for **2-β** (Supplementary Fig.1). The use of 3 equivalents of Ce^{IV} to fully transform **1-α,β** to **2-α,β** may be an indication of the high redox potential necessary to oxidize Fe^{III}-OH$_2$ to Fe^{IV}(O). Taking into consideration the Nernst equation, the red-ox potential for the Fe^{III}-OH$_2$/Fe^{IV}(O) couple under the low pH reaction conditions is estimated at ~ 1.4 V vs NHE, which matches that obtained in recent DFT calculations.[22]

Figure 1. **Top)** UV-Vis spectra of **A) 2-α** and **B) 2-β** (solid black line) formed by the respective reactions of **1-α** and **1-β** (1 mM) in Milli-Q H$_2$O at 25 °C with 3 eq. of CAN, upon addition of 75 eq. of CAN (dotted red line) and after CAN consumption (dashed purple line). **Bottom**) Time courses for the reaction of **B) 1-α** and **D) 1-β** with 75 eq. CAN monitoring, [Ce^{IV}] (right axis, dotted blue line), and O$_2$ evolution (left axis, solid black line). Kinetic traces for [Ce^{IV}] were monitored at 450 nm. Δ[O$_2$] (TON) was monitored by a pressure transducer and quantified by GC-TCD.

Formation of **2-α** was further confirmed by CSI-HRMS (Figure 2A, Supplementary Fig. 3) and ^{1}H-NMR spectroscopy (see Supplementary Fig. 4-5). Importantly, the CSI-HRMS spectra of **2-α** showed an intense peak at m/z = 545.110 ± 0.003 that can be assigned to {[Fe^{IV}(O)(mcp)](CF$_3$SO$_3$)}$^+$ on the basis of its m/z value and isotope distribution pattern. Consistently, the peak moved to 547.117 ± 0.003 when **2-α** was generated in H$_2$^{18}O, due to the incorporation of ^{18}O into the oxo ligand. In addition, a second strong signal at m/z = 413.162 ± 0.003 was observed, which shifts to 417.172 ± 0.003 when H$_2$^{18}O was used. Therefore, the peak was assigned to the [Fe^{IV}(O)(OH)(mcp)]$^+$

ion (Supplementary Fig.3). These ions correspond to the respective loss of H_2O and CF_3SO_3H from the parent $\{[Fe^{IV}(O)(OH_2)(mcp)](CF_3SO_3)\}^+$ ion, thus identifying **2-α** as $[Fe^{IV}(O)(OH_2)(mcp)]^{2+}$. **2-α** could be also prepared by reacting $[Fe^{II}(Cl)_2(mcp)]$ with CAN (3 eq.), providing further evidence for water and not a triflate ion as the sixth ligand. In addition, support for a terminal oxo ligand in **2-α** was obtained by rR spectroscopy (λ_{exc} = 413.1 nm, -8 ºC, in 1:1 H_2O:CH_3CN), where a resonance enhanced feature was observed at 822 cm^{-1}. This feature downshifted by 40 cm^{-1} with the use of $H_2^{18}O$ (Figure 4, Top panel), consistent with its assignment to the Fe=O stretch of **2-α**. [23,24]

Decay of **2-α** ($\tau_{1/2}$ = 20 min at 25 ºC) did not result in O_2 evolution, showing that it cannot be the WO species. In fact, further reaction of **2-α** with CAN was necessary to generate the WO species. In order to investigate the nature of the latter, the reaction of **2-α** with an excess of CAN was monitored simultaneously by UV-Vis spectroscopy, manometry and CSI-HRMS (Figure 3, Supplementary Fig. 6). UV-Vis spectroscopy and CSI-HRMS were used to monitor the time-dependent evolution of the oxoiron(IV) species, as well as the consumption of Ce^{IV}, while O_2 evolution within the same time period was determined by manometry and GC-TCD.

Reaction of CAN (75 equiv) with **2-α** resulted in O_2 evolution concomitant with Ce^{IV} consumption. After all Ce^{IV} was consumed, O_2 evolution stopped and 18.4 TON of O_2 (Figure 1B, Supplementary Fig.6) were formed. Therefore, 98% of the added CAN was converted productively to O_2, (maximum TON = 18.75 based on the initial Ce^{IV} with $n(Ce^{IV})/n(O_2)$ = 4). At this point, 30% of the initial amount of **2-α** remained in solution, as judged by its absorbance at λ = 769 nm (Supplementary Fig. 6D). The CSI-HRMS spectrum of the solution showed intense peaks at m/z = 414.1696 and 739.0270, values that are within experimental error of the exact masses for $[Fe^{III}(mcp)(OH)_2]^+$ and $[(mcp)Fe(O)(OH)Ce(NO_3)_3]^+$ species, respectively; associated isotope distribution patterns are also consistent with these formulations. The addition of a second aliquot of CAN (75 equiv) restarted O_2 evolution, producing an additional 11 TON of O_2 until Ce^{IV} depletion ceased and complete disappearance of the 769 nm band (**2-α**) was observed (Supplementary Fig.7).

The reaction of **2-α** with CAN (75 equiv) elicited the immediate appearance of a broad absorption band in the 500-650 nm range and a hypsochromic shift of the near-IR feature of **2-α** (Figure 1A, Supplementary Fig.6B). These changes were not observed upon addition of TfOH acid, $Ce^{III}(NO_3)_3$ or $Sc(OTf)_3$ to **2-α**. Interestingly, the new chromophore gradually diminished in intensity concomitant with Ce^{IV} consumption, and the near-IR band of **2-α** re-emerged (albeit with a reduced intensity because of partial decomposition) (Figure 1A and Supplementary Fig.6). These observations provide evidence for the accumulation of a novel reaction intermediate, **3-α**.

The formation of **3-α** was further corroborated by a kinetic analysis of the reaction of **2-α** with CAN at 25 ºC and pH = 1. The initial rates of Ce^{IV} consumption and O_2 evolution by **1-α** (0.1 mM) showed a saturation behavior with respect to $[Ce^{IV}]$. In addition, the reaction rate exhibited a linear dependence on **2-α** (10 μM-1 mM), and in $[Ce^{IV}]$ at $[Ce^{IV}]$ in the 1.25 – 12.5 mM range, with a reaction order close to one for both reagents at large Ce/Fe ratios (under pseudo-first order conditions). At $[Ce^{IV}] > 12.5$ mM, reaction rates exhibited saturation, becoming independent of $[Ce^{IV}]$ (see Supplementary Fig.8-13). This kinetic behavior indicates a pre-equilibrium binding of Ce^{IV} to **2-α** leading to the accumulation of an intermediate, namely **3-α**, the evolution of which represents the rate determining step of the reaction. We assessed the viability of this notion by analyzing the reaction between Ce^{IV} and **2-α** to form **3-α** in 1:1 v:v CH_3CN:H_2O solution at -8 ºC, a temperature at which O_2 evolution and Ce^{IV} consumption basically ceased. We found that the formation of **3-α** is very fast and reversible, with an equilibrium constant K_{eq} of 210($\pm$20) that could be estimated from the titration data (See Supplementary Fig. 14). Notably, analogous kinetic observations have been made in WO mediated by $[Fe^{II}(CF_3SO_3)_2(^{Me,X}Pytacn)]$ (^{Me,X}Pytacn = 1-(2'-pyridylmethyl)-4,7-dimethyl-1,4,7-triazacyclononane, X = H, Cl, CO_2Et, NO_2), suggesting the possibility of a common pathway for WO by these two non-heme iron WO catalysts.[5]

Like **1-α**, the topological isomer **1-β** reacted with CAN (3 eq.) to form the $S = 1$ β-$[Fe^{IV}(O)(OH_2)(mcp)]^{2+}$ (**2-β**, λ_{max} = 753 nm, ε = 280 M^{-1} cm^{-1}) as judged by UV-Vis, CSI-HRMS and ^{1}H-NMR (See Supplementary Fig. 1, right, Supplementary Fig. 3 - 5). However, in contrast to **2-α**, the reaction of **2-β** with CAN (75 equiv) did not result in a significant decrease in the concentration of CAN or O_2 evolution (Figure 1D). Moreover, the formation of a putative **3-β** was not observed. Given the structural similarity between **2-α** and **2-β**, the failure of the latter to elicit water oxidation, together with the kinetic similarities between **2-α** and the catalytically active $[Fe^{II}(CF_3SO_3)_2(^{Me,X}Pytacn)]$ complexes,[5] strongly suggests that the formation of **3-α** is required for WO to proceed.
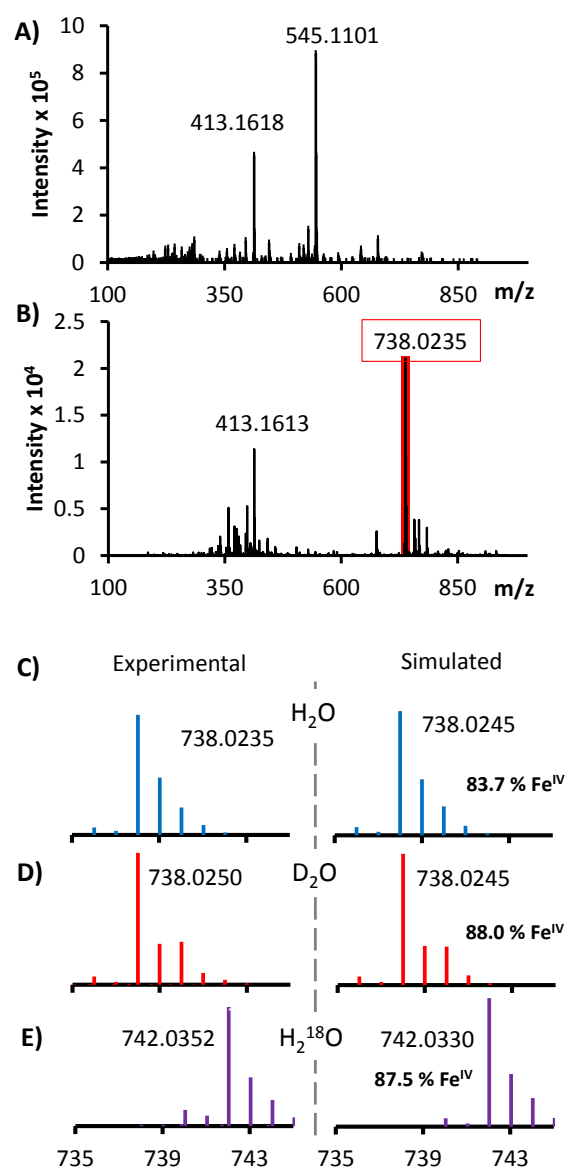
Figure 2. **A)** CSI-HRMS spectrum of **2-α,** recorded immediately after the oxidation of **1-α** (1 mM) by CAN (3 mM).

B) CSI-HRMS spectrum obtained during the WO reaction, upon the addition of 75 eq of CAN to **2-α. C-E)** CSI-HRMS features associated with **3-α** obtained in H_2O, D_2O and $H_2^{18}O$ as solvent. Spectra were recorded by setting the nebulizer and dry gas temperature of the cryospray instrument to 25 °C.

Characterization of intermediate 3-α. CSI-HRMS experiments shed some light on the nature of **3-α** that was formed in the reaction of **2-α** with Ce^{IV} under catalytic conditions ([Fe] = 1 mM; [CAN] = 75 mM, Figure 2). The addition of CAN caused the disappearance of the peak at m/z = 545.110 corresponding to **2-α** (Figure 2B) and the

appearance of a new peak at m/z 738.0235 and designated as **M₃,** which was not observed when **1-β** was treated with excess of CAN (Supplementary Fig.15).

The composition of **M₃** was deduced with the aid of isotopic labeling. When $H_2^{18}O$ was used as solvent, **M₃** upshifted by 4 units (Figure 2E). As the oxygen atoms of the nitrates do not undergo fast exchange with $H_2^{18}O$ (see Supplementary Fig. 18), this upshift suggests that **M₃** must contain two oxygen atoms capable of facile exchange with water. On the other hand, experiments with D_2O showed that **M₃** does not have exchangeable protons (Figure 2D). Furthermore, the isotopic distribution pattern of **M₃** could only be correctly simulated by taking into account the natural abundance isotopes of one Fe and one Ce atom. Specifically, the ^{54}Fe isotope (5.8 % relative to ^{56}Fe) is responsible for the **M₃** − 2 peak, while the ^{142}Ce isotope (11.1 % relative to ^{140}Ce) contributes significantly to the **M₃** + 2 peak. Taken together, these results allow **M₃** to be formulated as $\{[Fe^{IV}(O)_2(mcp)Ce^{IV}(NO_3)_3]\}^+$ (calc. m/z 738.0245, found m/z 738.0235) (For further details see Supplementary Section 1.2.3). This formulation requires the replacement of one hydrogen atom from the $[Fe^{IV}(O)(OH)(mcp)]^+$ ion (m/z 413.1616) by the $[Ce^{IV}(NO_3)_3]^+$ moiety to give rise to **M₃**.

Collision induced dissociation (CID) MS/MS experiments at different collision energies (CE) were performed for **M₃** (m/z = 738.0). At relative low energies (12 eV) the CID fragmentation of **M₃** led to the loss of a neutral NO_3 (m/z = 676.0). Only at CE higher than 24 eV did the parent peak at 738.0 disappear, but the m/z 676.0 ion (corresponding to neutral loss of NO_3 from **M₃**) persisted at even higher collision energies (up to 39 eV). These results indicate the robustness of the $\{Fe^{IV}\text{-}O\text{-}Ce^{IV}\}$ moiety in **M₃** in the gas phase (Supplementary Fig. 17).

Decisively, Figure 2 shows that the decay of **M₃** (monitored by CSI-HRMS) parallels the decrease in the intensity of the 615 nm chromophore attributed to **3-α**. Such a correlation indicates that **M₃** in fact corresponds to **3-α**. Taken together, the spectroscopic results and the kinetic model that arises from analysing Ce^{IV} consumption and O_2 evolution establish **3-α** as the last detectable and catalytically competent intermediate in water oxidation.

The molecular structure derived from the MS analysis indicates that **3-α** corresponds to **M₃**, but the ion may also contain additional water ligands bound at Ce(IV) in the solution state that would be readily lost in the gas phase. This proposal is supported by the fact that Ce(IV) forms kinetically labile and dynamic complexes with a coordination number of 8 to 9. Furthermore, recent Ce(IV) speciation and quantum dynamic studies have shown a fast ligand exchange at the coordination sphere of Ce(IV).[25, 26, 27]
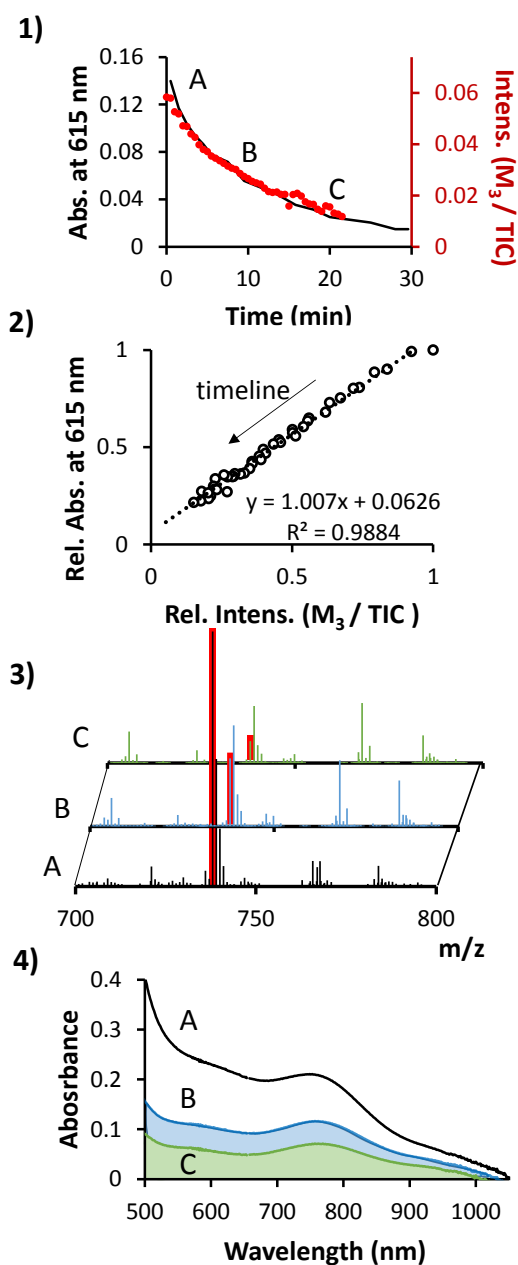
Figure 3. 1) Time course for the decay of the 615-nm chromophore (line, left axis) and the M_3 MS peak intensity (dots, right axis) during the reaction of **1-α** (1 mM) with CAN (75 mM) at 25 °C. 2) Correlation between the relative absorbance (Abs^t/Abs^0) at 615 nm and ion count $[(M_3/TIC)^t/(M_3/TIC)^0]$ of M_3. (t: time of measurement;. TIC: total ion count). 3 & 4) Mass and visible spectra observed at 10 s (A), 10 min (B) and 20 min (C) after the addition of CAN (75 eq) to **2-α** (1 mM in Milli-Q water, 25°C).
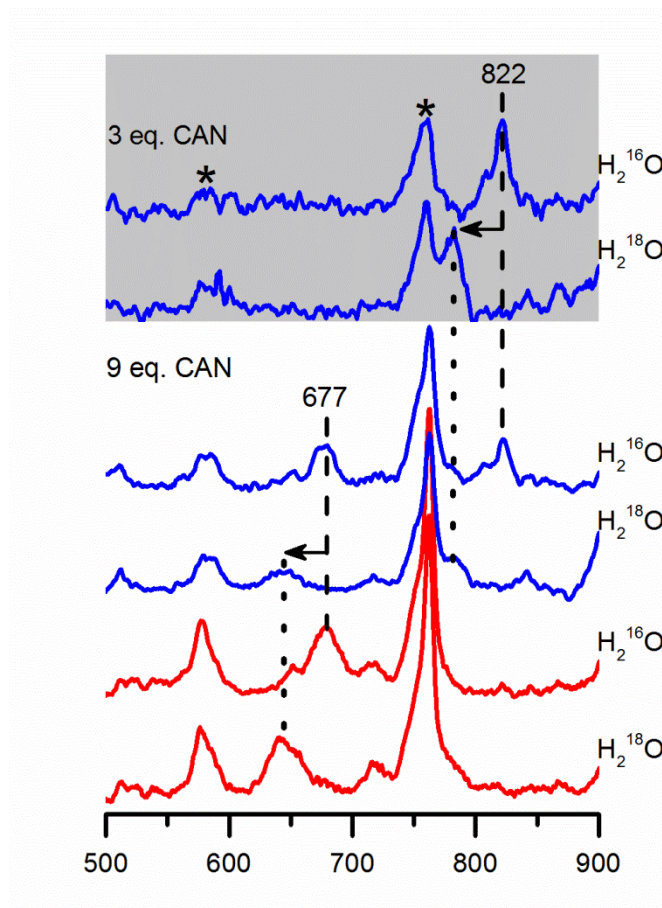
Figure 4. Top panel: rR spectra of **2-α** (λ_{ex} 413.1 nm, 100 mW) prepared upon addition of 3 eq. CAN to a solution of **1-α** (5 mM) in 1:1 H_2O:MeCN. Bottom panel: rR spectra of **3-α** prepared upon addition of 9 eq. CAN to a solution of **1-α** in 1:1 H_2O:MeCN. Blue: λ_{ex} = 413.1 nm, 100 mW, [Fe] = 5 mM. Red: λ_{ex} = 514.5 nm, 100 mW, [Fe] = 8 mM. All spectra were collected from liquid solutions maintained at -8 °C. Asterisks denote features arising from CAN. The intensity of the MeCN solvent peak at 922 cm^{-1} was used to normalize the intensities of the peaks among the various spectra.

More detailed insight into the nature of the iron-cerium adduct was provided by rR spectroscopy of liquid samples maintained at -8 °C. As shown in Figure 4, the rR spectrum (λ_{ex} = 413.1 nm, Figure 4, top panel) of **2-α** prepared with 3 equiv. of Ce^{IV} exhibits a feature at 822 cm^{-1} that downshifts to 782 cm^{-1} upon replacing $H_2^{16}O$ by $H_2^{18}O$, consistent with its assignment to the $\nu_{Fe=O}$ of **2-α**. Near-UV excitation was required to observe this feature as **2-α** has insignificant absorbance in the visible region, as found for other non-heme oxoiron(IV) complexes.[23,24]

Interestingly, the rR spectra of **3-α** obtained with the same excitation wavelength (λ_{ex} = 413.1 nm, Figure 4, bottom panel) also show the 822 cm^{-1} vibration and its downshift to 782 cm^{-1} upon $H_2^{18}O$ substitution. This feature

may arise from either **2-α** or **3-α** or both species. To clarify, we compared the intensities of the 822-cm[-1] peaks for the **2-α** (3-CAN) and **3-α** (9-CAN) samples relative to the adjacent 762-cm[-1] nitrate feature as an internal standard, after taking into account that the 9-CAN sample has three times the amount of nitrate as the 3-CAN sample, the two samples are found to have 822-cm[-1] peaks of comparable intensity. Given an association constant of 210(20) M[-1] for the interaction of **2-α** with CAN from UV-Vis titration experiments, it is expected that **3-α** would account for 85% of the iron in the Raman samples. Therefore the 822 cm^{-1} $\nu_{Fe=O}$ vibration observed in the 9-CAN samples must arise mainly from **3-α**.

Notably, a second feature of similar intensity appears at 677 cm^{-1} with 413.1 nm excitation in the sample of **3-α** (Figure 4, bottom panel). This lower-frequency feature persists when **3-α** is probed with 514.5 nm excitation, a wavelength at which only **3-α** has an absorption feature, but the 822-cm[-1] vibration is not observed, consistent with the absorption features associated with the $Fe^{IV}=O$ unit.[26,27] With either excitation wavelength, the 677 cm^{-1} peak downshifts to 643 cm^{-1} upon replacing $H_2^{16}O$ by $H_2^{18}O$, but is not affected when the experiment was carried out in D_2O (Supplementary Fig 20-21). The 34 cm^{-1} downshift is consistent with a diatomic Fe–O vibration, but the lower frequency indicates a weaker Fe–O bond that is also resonance-enhanced with 514.5 nm excitation upon Ce-adduct formation. Fe–O modes in this frequency range have previously been reported for complexes with $Fe^{III}(\mu\text{-}O)_2Fe^{IV}$ (666 cm^{-1})[28,29] and $Fe^{IV}_2(\mu\text{-}O)_2$ (674 cm^{-1})[30] cores, respectively, suggesting the possibility of forming an analogous $Fe^{IV}(\mu\text{-}O)_2Ce^{IV}$ core, which would be consistent with the elemental composition of **3-α** determined by CSI-HRMS. To test whether this feature could arise from an $Fe^{IV}(\mu\text{-}O)_2Ce^{IV}$ diamond core, rR experiments on **3-α** were performed in a 1:1 $H_2^{16}O$:$H_2^{18}O$ solvent mixture. Under these conditions, the rR spectrum exclusively shows peaks at 677 and 643 cm^{-1}, with no peak found at an intermediate frequency that could be associated with a mixed-labeled diamond core (See Supplementary Fig. 19-20).[31] The $H_2^{16}O$:$H_2^{18}O$ experiment thus excludes formation of an $Fe^{IV}(\mu\text{-}O)_2Ce^{IV}$ core. We have also considered the possibility that the 677 cm^{-1} vibration may correspond to the Fe–OH–Ce mode of an $O=Fe^{IV}$–OH–Ce^{IV} core, as earlier postulated.[5] However, two points argue against this possibility: a) the lack of a D_2O effect on the 677-cm[-1] vibration[32] and b) more importantly, the fact that Fe–OH–Fe vibrations are typically found in the range of 400-500 cm^{-1},[32,33] much lower than observed for **3-α**. Consideration of the above points together with its mass spectral formulation leads us to favour an $O=Fe^{IV}$–O–Ce^{IV} core for **3-α**. An analogous Fe^{IV}–O–Sc^{III} unit has been characterized crystallographically by Fukuzumi and Nam,[34] but unfortunately there is no Raman data reported for comparison.

Identification of **3-α** with an O=Fe^{IV}–O–Ce^{IV} core as the key reaction intermediate in WO reactions introduces unconsidered mechanistic scenarios for the oxidation of water by Ce^{IV} (Figure 5). Most obviously, Ce^{IV} appears not to behave simply as an outer-sphere oxidant, but instead forms an inner-sphere Fe^{IV}(μ-O)Ce^{IV} intermediate that is crucial for the reaction to proceed. Therefore, Ce^{IV}-driven Fe-based WO activity not only requires the presence of two *cis*-labile sites but also a structure of the iron complex that allows formation of the Fe^{IV}(μ-O)Ce^{IV} intermediate. In this regard, the contrasting reactivities of **1-α** and **1-β** may arise from differences in their steric or electronic properties. A possible rationale comes from the differences in the nature of the donor *trans* to the *cis*-labile sites of the *α* and *β* isomers. While the *α* isomer has two tertiary amines *trans* to the labile positions, the *β* isomer has one tertiary amine and one pyridine. From our earlier survey of non-heme iron WO catalysts, the more active complexes are similar to **1-α** with two tertiary amines *trans* to the two labile sites, whereas **1-β**, like the [Fe^{II}(tpa)(OTf)$_2$] complex (tpa = tris(2-pyridylmethyl)amine), has lower WO activity.[4] On the other hand, close inspection of the crystallographic data for **1-β**[19] shows that the N-Me groups point toward the *cis*-labile sites in such a way that might inhibit for formation of oxo-bridged dinuclear species (Supplementary Fig.22). Although examination of simple *β*-[(mcp)Fe^{IV}(μ-O)Ce^{IV}(NO$_3$)$_3$]$^+$ models seems to discard this possibility, a survey of the literature reveals that **1-α** can form a number of oxo-bridged diferric complexes that have been crystallographically characterized, but dimeric species derived from **1-β** are at present not known.[35]
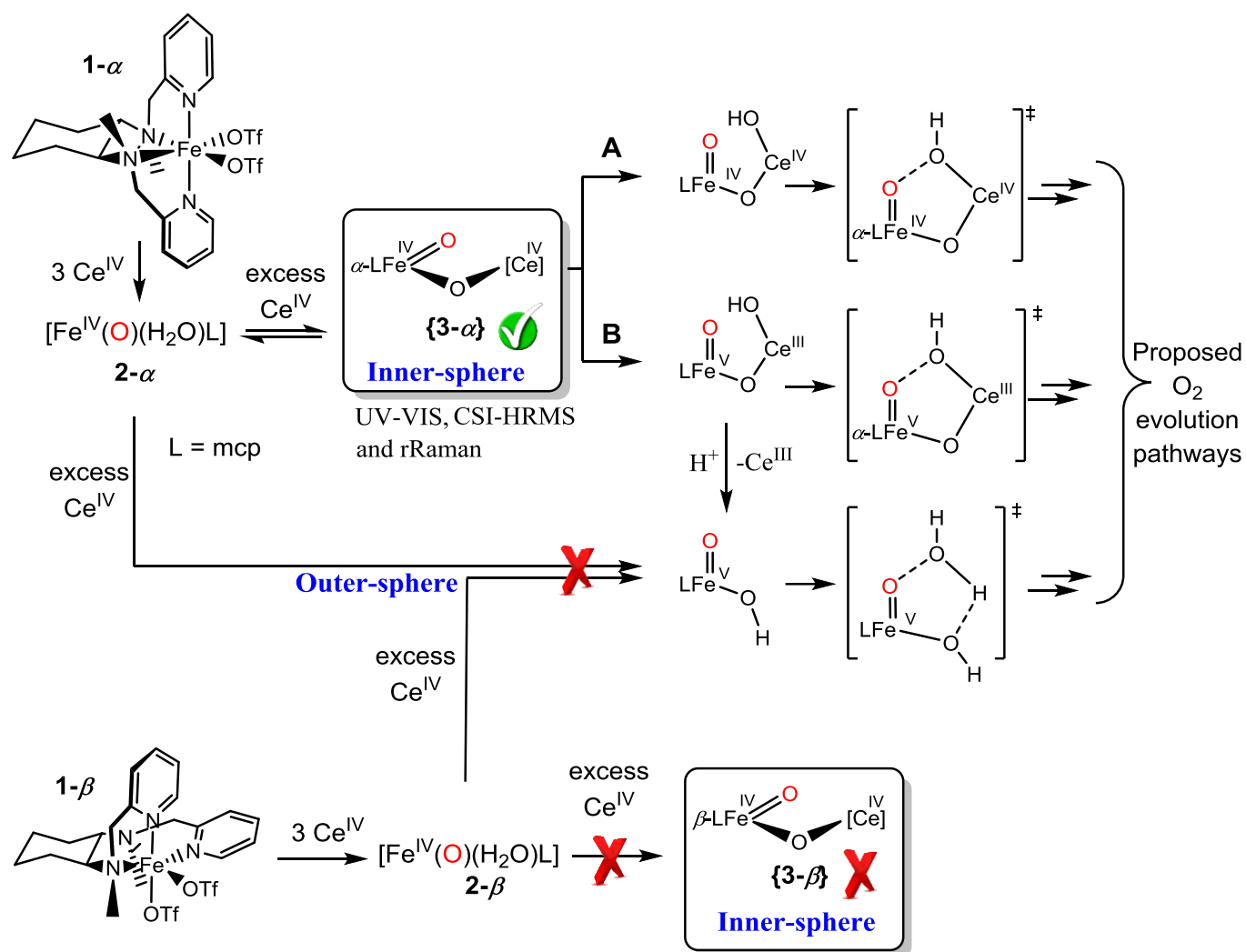
Figure 5. Reactivity differences between topological isomers α - β.

O-O bond formation pathway. How intermediate **3-α** evolves further to produce O_2 remains unclear. Two different pathways are plausible: an oxo/oxyl radical coupling mechanism to form the O-O bond (Path **A**, Figure 5)[12] and the alternative hypothesis entailing electron transfer from Fe^{IV} to Ce^{IV} to generate a highly electrophilic {$Fe^V(O)(\mu\text{-}O)Ce^{III}$} oxidant (Figure 5, path **B**). Water binding to the Ce^{III} would position it well for electrophilic attack by the $Fe^V{=}O$ moiety to form the O–O bond. This pathway is analogous to that proposed for **1**-catalyzed C-H and C=C oxidations with Ce^{IV} as oxidant.[36] Also supporting the notion of a highly electrophilic oxidant are the observed effects of substituents on the pyridine of the supporting ligand of a related catalyst on WOC efficacy, where more electron withdrawing substituents on the pyridine ligand enhance both TON and TOF for water oxidation.[5] Nevertheless, at this point it is not possible to discard the other scenario unequivocally.

The [Fe^{IV}(O)(μ-O)Ce^{IV}] intermediate we have characterized resembles the corresponding Mn^{V}(O)(μ-O)Ca^{II}(OH$_2$) unit proposed in some mechanistic models for the OEC (Figure 6),[37, 38, 39] making **3-α** an iron-based functional OEC model. In fact, the resemblance becomes stronger with electron transfer from Fe^{IV} to Ce^{IV} to generate an [Fe^{V}(O)(μ-O)Ce^{III}] oxidant. The strong similarities between iron and manganese chemistry in biologically relevant oxidation reactions suggest that this analogy should not be unexpected. Also relevant is the fact that Ce^{III} can replace Ca^{II} in biomolecules or act as an antagonist in pharmacology.[40, 41, 42] For example, it has been found that lanthanides, Ce in particular, are essential for the growth of *Methylacidiphilum fumariolicum* SoIV,[40] while Ca^{II} can be replaced by Ce^{III} in the pyrroloquinoline quinone (PQQ)-dependent methanol dehydrogenanse (MDH) enzymes to elicit superior catalytic properties.[40, 41]
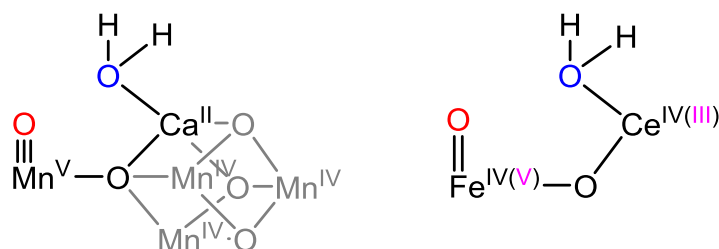

Figure 6. Analogy between a proposed OEC intermediate and the iron-cerium adduct **3-α**.

The mechanisms for O-O bond formation currently being considered for the OEC can be grouped in two main paths: a) a nucleophilic attack of a water molecule to a Mn^{V}≡O (or a Mn^{IV}-oxyl, Mn^{IV}=O·) unit, and b) an oxo/oxyl radical coupling mechanism.[39, 43, 44] Remarkable mechanistic insight in the O-O bond formation reaction has been obtained from studies of Mn[37, 38, 45] and Co[46, 47, 48, 49] tetrametallic cubane model complexes. Up to now these cubane OEC models generally support the oxo/oxyl radical coupling mechanism to form the O–O bond. However, there are no catalytically active WO models that include in their structure a Lewis acid to mimic the role of Ca^{II} in PSII,[37, 38, 45, 50, 51] despite the fact that a Lewis acid (Ca^{II}, but also Sr^{II})[52, 53] has been proven to be absolutely required for the operation of the OEC. Given their obvious interest, the absence of heterodimetallic complexes that are active in water oxidation may reflect the extraordinary difficulty in accessing well-defined models where both a first row transition metal center and a Lewis acid work together in water solution.[49] The success of our effort to trap and characterize **3-α** as having an [O=Fe^{IV}-O-Ce^{IV}] core that resembles the fundamental Mn^{V}(O)(μ-O)Ca(OH$_2$)$_2$ structural motif of the OEC unit is therefore remarkable from an inorganic synthesis perspective. More importantly, the identification of an

[O=Fe^{IV}-O-Ce^{IV}] core that is active in water oxidation provides a model compound to study the formation of the O-O bond in detail.

In conclusion, this work provides experimental evidence and characterization of an Fe^{IV}–O–Ce^{IV} species as the last detectable intermediate in Fe-catalyzed WO reactions. Although Ru–O–Ce intermediates have been proposed in water oxidation reactions by different research groups,[54, 55, 56, 57] to the best of our knowledge this is the first direct experimental characterization of a heterodimetallic core in a synthetic WO catalyst. Furthermore, the Fe^{IV}–O–Ce^{IV} active species we have described in this work can be construed as the closest structural and functional model for the essential heteodimetallic Mn^{V}–O–Ca^{II} center involved in the water oxidation event in PSII.

Methods

Materials. Reagents were purchased from commercial sources and used as received, without any further purification. Cerium(IV) ammonium nitrate (CAN) (≥99.99%) and trifluoromethanesulfonic acid (ReagentPlus grade ≥99%) were purchased from Sigma-Aldrich®. Solvents were purchased from SDS and Scharlab, purified and dried by passing through an activated alumina purification system (MBraun SPS-800) and stored in an anaerobic glovebox under N$_2$. Complexes **1-α**(*1*) and **1-β**(*2*) were prepared as previously described. Water (18.2 MΩ·cm) was purified with a Milli-Q Millipore Gradient AIS system.

Physical Methods. UV-VIS-NIR spectra were recorded on an Agilent 8453 diode array spectrophotometer (190-1100 nm range) in 1-cm quartz cells. A cryostat from Unisoku Scientific Instruments was used for temperature control. The amount of gas generated was measured with a differential pressure transducer sensor (Honeywell-ASCX15DN, ±15 psi). Each reaction had its own reference reaction, which was connected to the other port of the sensor. Further details of the equipment are available elsewhere.[4, 5]

High resolution mass spectra (HRMS) were recorded on a Bruker MicrOTOF-Q II^{TM} instrument with ESI or Cryospray ionization sources at Serveis Tècnics of the University of Girona. Samples were introduced into the mass spectrometer ion source by direct infusion using a syringe pump and were externally calibrated using sodium formate. The instrument was operated in the positive ion mode.

Resonance Raman Spectroscopy: Resonance Raman (rR) spectra were collected via excitation with Kr$^+$ and Ar$^+$ lasers (Spectra-Physics BeamLok 2060-RM) and an Acton AM-506M3 monochromator equipped with a Princeton Instruments ACTON PyLON LN/CCD-1340 x 400 detector. Low-temperature spectra in H$_2$O:CH$_3$CN solution mixtures were obtained at 265 K using a 90° backscattering geometry. Raman frequencies were calibrated to indene prior to data collection. Rayleigh scattering was attenuated using a holographic notch filter (Kaiser Optical Systems) for each excitation wavelength. The monochromator slit width was set for a band pass of 4 cm^{-1} for all spectra. All spectra were collected using a laser excitation power of 100 mW. The plotted spectra are averages of 96 scans with collection times of 20 s. All spectra were intensity-corrected to the 922 cm^{-1} peak of the CH$_3$CN solvent.

Supporting Online Material

Experiments of catalytic water oxidation reactions, pressure monitored O$_2$ traces and kinetic studies. Characterization details of **3-α.**

Author Contributions

J.Ll.-F. and M.C. devised the initial concept for the work and designed the experiments. Z.C. carried out the WO experiments and trapped the intermediate; L.G. performed the CSI-HRMS studies and analysed the data. S.K obtained the resonance Raman spectra and analysed the data together with L.Q. Z.C., L.Q., M.C. and J.Ll.-F. wrote the manuscript.

Competing Financial Interests: The authors have no competing interests.

References

1.   Gunay, A., Theopold, K. H. C−H Bond Activations by Metal Oxo Compounds. *Chem Rev* **110**, 1060-1081 (2010).

2.   Shaik, S., Hirao, H., Kumar, D. Reactivity of High-Valent Iron–Oxo Species in Enzymes and Synthetic Reagents: A Tale of Many States. *Acc Chem Res* **40**, 532-542 (2007).

3.   Liu, X., Wang, F. Transition metal complexes that catalyze oxygen formation from water: 1979–2010. *Coord Chem Rev* **256**, 1115-1136 (2012).

4.   Lloret-Fillol, J., Codolà, Z., Garcia-Bosch, I., Gómez, L., Pla, J. J., Costas, M. Efficient water oxidation catalysts based on readily available iron coordination complexes. *Nat Chem* **3**, 807-813 (2011).

5.   Codolà, Z., Garcia-Bosch, I., Acuña-Parés, F., Prat, I., Luis, J. M., Costas, M.,Lloret-Fillol, J. Electronic Effects on Single-Site Iron Catalysts for Water Oxidation. *Chem Eur J* **19**, 8042-8047 (2013).

6.   Ellis, W. C., McDaniel, N. D., Bernhard, S., Collins, T. J. Fast Water Oxidation Using Iron. *J Am Chem Soc* **132**, 10990-10991 (2010).

7.   Hoffert, W. A., Mock, M. T., Appel, A. M., Yang, J. Y. Incorporation of Hydrogen-Bonding Functionalities into the Second Coordination Sphere of Iron-Based Water-Oxidation Catalysts. *Eur J Inorg Chem* 3846–3857 (2013).

8.   Wiechen, M., Berends, H.-M., Kurz, P. Water oxidation catalysed by manganese compounds: from complexes to 'biomimetic rocks'. *Dalton Trans* **41**, 21-31 (2012).

9.   Cao, R., Lai, W., Du, P. Catalytic water oxidation at single metal sites. *Energy Environ Sci* **5**, 8134-8157 (2012).

10.   Yagi, M., Kaneko, M. Molecular Catalysts for Water Oxidation. *Chem Rev* **101**, 21-36 (2000).

11.   Nocera, D. G. The Artificial Leaf. *Acc Chem Res* **45**, 767-776 (2012).

12.   Kundu, S., Matito, E., Walleck, S., Pfaff, F. F., Heims, F., Rábay, B.*, et al.* O–O Bond Formation Mediated by a Hexanuclear Iron Complex Supported on a Stannoxane Core. *Chem Eur J* **18**, 2787-2791 (2012).

13.   Kodera, M., Kawahara, Y., Hitomi, Y., Nomura, T., Ogura, T., Kobayashi, Y. Reversible O–O Bond Scission of Peroxodiiron(III) to High-Spin Oxodiiron(IV) in Dioxygen Activation of a Diiron Center with a Bis-tpa Dinucleating Ligand as a Soluble Methane Monooxygenase Model. *J Am Chem Soc* **134**, 13236-13239 (2012).

14.   Ferguson-Miller, S., Babcock, G. T. Heme/Copper Terminal Oxidases. *Chem Rev* **96**, 2889-2908 (1996).

15.   Company, A., Lloret-Fillol, J., Costas, M. Small Molecule Models for Nonporphyrinic Iron and Manganese Oxygenases. In: Reedijk J, Poeppelmeier K (eds). *Comprehensive Inorganic Chemistry II (Second Edition)*. Elsevier: Amsterdam, 487-564, (2013).

16.   Hong, D., Mandal, S., Yamada, Y., Lee, Y.-M., Nam, W., Llobet, A., Fukuzumi, S. Water Oxidation Catalysis with Nonheme Iron Complexes under Acidic and Basic Conditions: Homogeneous or Heterogeneous? *Inorg Chem* **52**, 9522-9531 (2013).

17.   Chen, G., Chen, L., Ng, S.-M., Man, W.-L., Lau, T.-C. Chemical and Visible-Light-Driven Water Oxidation by Iron Complexes at pH 7–9: Evidence for Dual-Active Intermediates in Iron-Catalyzed Water Oxidation. *Angew Chem Int Ed* **52**, 1789-1791 (2013).

18.   Knof, U., von Zelewsky, A. Predetermined Chirality at Metal Centers. *Angew Chem Int Ed* **38**, 302-322 (1999).

19.   Costas, M., Que, L. Jr Ligand topology tuning of iron-catalyzed hydrocarbon oxidations. *Angew Chem Int Ed* **41**, 2179-2181 (2002).

20.   Costas, M., Tipton, A. K., Chen, K., Jo, D.-H., Que, L. Jr. Modeling Rieske Dioxygenases: The First Example of Iron-Catalyzed Asymmetric cis-Dihydroxylation of Olefins. *J Am Chem Soc* **123**, 6722-6723 (2001).

21.   Hong, S., Lee, Y.-M., Cho, K.-B., Sundaravel, K., Cho, J., Kim, M. J.*, et al.* Ligand Topology Effect on the Reactivity of a Mononuclear Nonheme Iron(IV)-Oxo Complex in Oxygenation Reactions. *J Am Chem Soc* **133**, 11876-11879 (2011).

22.   Acuña-Parés, F., Codolà, Z., Costas, M., M. Luis, J., Lloret-Fillol J., Unraveling the Mechanism of Water Oxidation Catalyzed by Nonheme Iron Complexes *Chem. Eur. J.* DOI: 10.1002/chem.201304367, (2014).

23.   Jackson, T. A., Rohde, J.-U., Seo, M. S., Sastri, C. V., De Hont, R., Stubna, A.*, et al.* Axial Ligand Effects on the Geometric and Electronic Structures of Nonheme Oxoiron(IV) Complexes. *J Am Chem Soc* **130**, 12394-12407 (2008).

24.   Wang, D., Ray, K., Collins, M. J., Farquhar, E. R., Frisch, J. R., Gomez, L., Jackson, T. A., Kerscher, M., Waleska, A., Comba, P., Costas, M., Que, L., Jr. Nonheme oxoiron(IV) complexes of pentadentate N5 ligands: spectroscopy, electrochemistry, and oxidative reactivity. *Chem. Sci.,* **4**, 282-291 (2013).

25.   Ikeda-Ohno, A., Hennig, C., Weiss, S., Yaita, T., Bernhard, G., Hydrolysis of Tetravalent Cerium for a Simple Route to Nanocrystalline Cerium Dioxide: An In Situ Spectroscopic Study of Nanocrystal Evolution. *Chem. Eur. J.,* **19**, 7348-7360 (2013)

26.   Lutz, O. M. D., Hofer, T. S., Randolf, B. R., Weiss, A. K. H., Rode, B. M., A QMCF-MD Investigation of the Structure and Dynamics of Ce4+ in Aqueous Solution. *Inorg. Chem.*, **51**, 6746-6752 (2012)

27.   Piro, N. A., Robinson, J. R., Walsh, P. J., Schelter, E. J., The electrochemical behavior of cerium(III/IV) complexes: Thermodynamics, kinetics and applications in synthesis. *Coord. Chem. Rev.*, **260**, 21-36 (2014)

28. Wilkinson, E. C., Dong, Y., Zang, Y., Fujii, H., Fraczkiewicz, R., Fraczkiewicz, G., Czernuszewicz, R. S., Que, L.. Raman Signature of the Fe_2O_2 "Diamond" Core. *J Am Chem Soc* **120**, 955-962 (1998).

29. Skulan, A. J., Hanson, M. A., Hsu, H.-f., Que, L. Jr., Solomon, E. I. Spectroscopic Study of $[Fe_2O_2(5\text{-}Et_3\text{-}TPA)_2]^{3+}$: Nature of the Fe_2O_2 Diamond Core and Its Possible Relevance to High-Valent Binuclear Non-Heme Enzyme Intermediates. *J Am Chem Soc* **125**, 7344-7356 (2003).

30. Xue, G., Fiedler, A. T., Martinho, M., Münck, E., Que, L. Jr. Insights into the P-to-Q conversion in the catalytic cycle of methane monooxygenase from a synthetic model system. *Proc Natl Acad Sci U S A* **105**, 20615-20620 (2008).

31. Que, L. Jr, Tolman, W. B. Bis(μ-oxo)dimetal "Diamond" Cores in Copper and Iron Complexes Relevant to Biocatalysis. *Angew Chem Int Ed* **41**, 1114-1137 (2002).

32. Zheng, H., Zang, Y., Dong, Y., Young, V. G., Que, L., Jr. Complexes with $Fe^{III}_2(\mu\text{-}O)(\mu\text{-}OH)$, $Fe^{III}_2(\mu\text{-}O)_2$, and $[Fe^{III}_3(\mu_2\text{-}O)_3]$ Cores: Structures, Spectroscopy, and Core Interconversions, *J. Am. Chem. Soc.*, **121**, 2226-2235 (1999)

33. Cranswick, M. A., Meier, K. K., Shan, X., Stubna, A., Kaizer, J., Mehn, M. P., Münck, E., Que, L., Jr. Protonation of a Peroxodiiron(III) Complex and Conversion to a Diiron(III/IV) Intermediate: Implications for Proton-Assisted O–O Bond Cleavage in Nonheme Diiron Enzymes, *Inorg. Chem.*, **51**, 10417-10426 (2012)

34. Fukuzumi, S., Morimoto, Y., Kotani, H., Naumov, P., Lee, Y.-M., Nam, W. Crystal structure of a metal ion-bound oxoiron(IV) complex and implications for biological electron transfer. *Nat Chem* **2**, 756-759 (2010).

35. Stubna, A., Jo, D.-H., Costas, M., Brenessel, W. W., Andres, H., Bominaar, E. L.*, et al.* A Structural and Mössbauer Study of Complexes with $Fe_2(\mu\text{-}O(H))_2$ Cores: Stepwise Oxidation from $Fe^{II}(\mu\text{-}OH)_2Fe^{II}$ through $Fe^{II}(\mu\text{-}OH)_2Fe^{III}$ to $Fe^{III}(\mu\text{-}O)(\mu\text{-}OH)Fe^{III}$. *Inorg Chem* **43**, 3067-3079 (2004).

36. Garcia-Bosch, I., Codolà, Z., Prat, I., Ribas, X., Lloret-Fillol, J., Costas, M. Iron-Catalyzed C-H Hydroxylation and Olefin cis-Dihydroxylation Using a Single-Electron Oxidant and Water as the Oxygen-Atom Source. *Chem Eur J* **18**, 13269-13273 (2012).

37. Kanady, J. S., Tsui, E. Y., Day, M. W., Agapie, T. A Synthetic Model of the Mn_3Ca Subsite of the Oxygen-Evolving Complex in Photosystem II. *Science* **333**, 733-736 (2011).

38. Tsui, E. Y., Tran, R., Yano, J., Agapie, T. Redox-inactive metals modulate the reduction potential in heterometallic manganese-oxido clusters. *Nat Chem* **5**, 293-299 (2013).

39. Cox, N., Pantazis, D. A., Neese, F., Lubitz, W. Biological Water Oxidation. *Acc Chem Res* **46**, 1588-1596 (2013).

40. Pol, A., Barends, T. R. M., Dietl, A., Khadem, A. F., Eygensteyn, J., Jetten, M. S. M.*, et al.* Rare earth metals are essential for methanotrophic life in volcanic mudpots. *Environ Microbiol* **16**, 255-264 (2014).

41. Jakupec, M. A., Unfried, P., Keppler, B. K. Pharmacological properties of cerium compounds. *Reviews of Physiology, Biochemistry and Pharmacology*, vol. 153. Springer Berlin Heidelberg, 2005, pp 101-111.

42. Nakagawa, T., Mitsui, R., Tani, A., Sasa, K., Tashiro, S., Iwama, T.*, et al.* A Catalytic Role of XoxF1 as La^{3+}-Dependent Methanol Dehydrogenase in *Methylobacterium extorquens* **AM1**. *PLoS ONE* **7**, e50480 (2012).

43. Rapatskiy, L., Cox, N., Savitsky, A., Ames, W. M., Sander, J., Nowaczyk, M. M.*, et al.* Detection of the Water-Binding Sites of the Oxygen-Evolving Complex of Photosystem II Using W-Band [17]O Electron–Electron Double Resonance-Detected NMR Spectroscopy. *J Am Chem Soc* **134**, 16619-16634 (2012).

44. Siegbahn, P. E. M. Water oxidation mechanism in photosystem II, including oxidations, proton release pathways, O—O bond formation and O_2 release. *Biochimica et Biophysica Acta (BBA) - Bioenergetics* **1827**, 1003-1019 (2013).

45. Dismukes, G. C., Brimblecombe, R., Felton, G. A. N., Pryadun, R. S., Sheats, J. E., Spiccia, L.*, et al.* Development of Bioinspired Mn_4O_4−Cubane Water Oxidation Catalysts: Lessons from Photosynthesis. *Acc Chem Res* **42**, 1935-1943 (2009).

46.   Symes, M. D., Surendranath, Y., Lutterman, D. A., Nocera, D. G. Bidirectional and Unidirectional PCET in a Molecular Model of a Cobalt-Based Oxygen-Evolving Catalyst. *J Am Chem Soc* **133**, 5174-5177 (2011).

47.   McCool, N. S., Robinson, D. M., Sheats, J. E., Dismukes, G. C. A Co_4O_4 "Cubane" Water Oxidation Catalyst Inspired by Photosynthesis. *J Am Chem Soc* **133**, 11446-11449 (2011).

48.   Berardi, S., La Ganga, G., Natali, M., Bazzan, I., Puntoriero, F., Sartorel, A.*, et al.* Photocatalytic Water Oxidation: Tuning Light-Induced Electron Transfer by Molecular Co_4O_4 Cores. *J Am Chem Soc* **134**, 11104-11107 (2012).

49.   Evangelisti, F., Güttinger, R., Moré, R., Luber, S., Patzke, G. R. Closer to Photosystem II: A Co_4O_4 Cubane Catalyst with Flexible Ligand Architecture. *J Am Chem Soc 135*, 18734-18737 (2013).

50.   Leeladee, P., Baglia, R. A., Prokop, K. A., Latifi, R., de Visser, S. P., Goldberg, D. P. Valence Tautomerism in a High-Valent Manganese–Oxo Porphyrinoid Complex Induced by a Lewis Acid. *J Am Chem Soc* **134**, 10397-10400 (2012).

51.   Lacy, D. C., Park, Y. J., Ziller, J. W., Yano, J., Borovik, A. S. Assembly and Properties of Heterobimetallic $Co^{II/III}$-Ca^{II} Complexes with Aquo and Hydroxo Ligands. *J Am Chem Soc* **134**, 17526-17535 (2012).

52.   Ono, T.-a., Inoue, Y. Discrete extraction of the Ca atom functional for O_2 evolution in higher plant photosystem II by a simple low pH treatment. *FEBS Lett* **227**, 147-152 (1988).

53.   Boussac, A., Rutherford, A. W. Nature of the inhibition of the oxygen-evolving enzyme of photosystem II induced by sodium chloride washing and reversed by the addition of calcium(2+) or strontium(2+). *Biochemistry* **27**, 3476-3483 (1988).

54.   Murakami, M., Hong, D. C., Suenobu, T., Yamaguchi, S., Ogura, T., Fukuzumi, S. Catalytic Mechanism of Water Oxidation with Single-Site Ruthenium–Heteropolytungstate Complexes. *J Am Chem Soc* **133**, 11605-11613 (2011).

55.   Yoshida, M., Masaoka, S., Abe, J., Sakai, K. Catalysis of Mononuclear Aquaruthenium Complexes in Oxygen Evolution from Water: A New Radical Coupling Path using Hydroxocerium(IV) Species. *Chem Asian J.* **5**, 2369-2378 (2010).

56.   Kimoto, A., Yamauchi, K., Yoshida, M., Masaoka, S., Sakai, K. Kinetics and DFT studies on water oxidation by Ce^{4+} catalyzed by $[Ru(terpy)(bpy)(OH_2)]^{2+}$. *Chem Commun* **48**, 239-241 (2012).

57.   Derek J. Wasylenko , Chelladurai Ganesamoorthy , Matthew A. Henderson , Bryan D. Koivisto , Hans D. Osthoff , and Curtis P. Berlinguette Electronic Modification of the $[Ru^{II}(tpy)(bpy)(OH_2)]^{2+}$ Scaffold: Effects on Catalytic Water Oxidation *J. Am. Chem. Soc.* **45**, 16094–16106, (2010).

CHAPTER VII.

RESULTS AND DISCUSSION

VII.   RESULTS AND DISCUSSION

Artificial photosynthesis is regarded as a promising solution towards the finding of a definitive "green fuel" to feed the world's energy demands. Nowadays, its development is mainly focused on providing a sustainable system to accomplish the photooxidation of water to obtain protons and electrons, and the reduction of H^+ or CO_2 into higher-energy products hopefully using the electrons obtained in the first oxidation step. The oxidation of water has become a *hot topic* in science during the last 10 years because it's the most abundant resource in the Earth that can be used as a primary source of protons and electrons for the production of molecules where energy is stored in the form of chemical bonds (NADPH, ATP, H_2, CH_3OH, HCO_2H…). Moreover, oxidation of water is regarded as one of the most energy demanding step of the photosynthesis, and the development of a cheap, benign and highly active catalyst to obtain protons and electrons effectively is a very attractive goal for science.

To reproduce the structure of the active center and the reactions that lead to the oxidation of water taking place during photosynthesis has proven extremely challenging. Artificial approaches based on discrete model complexes have arisen as very promising tools towards the elucidation of the mechanistic basis of the enzymatic reaction. The identification of the minimum structural requirements that enables this challenging reactivity will provide crucial information for the development of simple and powerful catalysts.

In this thesis we focused our attention on the study of two different metals for creating catalysts for water oxidation. Iridium, which is a well-established robust and efficient metal center for the water oxidation, is studied being part of a family of carbene-type compounds with the aim to find some keys to unravel mechanistic details and structural preferences. Then, first row transition metals are employed for preparing coordination compounds with well-known oxidative robust ligands. Iron complexes of this kind have been previously studied in C-H and C=C oxidation reactions, and in this thesis their competence as catalysts for water oxidation is studied. The complexes are shown to mediate water oxidation reactions with excellent efficiency. Mechanistic studies and characterization of intermediates have been pursued, with the final aim of understanding the requirements for the design and improvement of iron-based catalysts. The characterization of a novel Fe-Ce dimeric species described herein can be construed as the closest structural and functional model for the essential heterodimetallic Mn^V–O–Ca^{II} center involved in the water oxidation event in PSII.

VII.1.   Highly Effective Water Oxidation Catalysis with Iridium Complexes through the Use of NaIO₄

Iridium is well-known to form active and robust WOCs within both homogeneous and heterogeneous phases. However, the highly oxidative environment where the water oxidation takes place makes not straightforward to distinguish between both situations.[1-3] Interested on understanding and improving basic details for the catalytic water oxidation, we decided to investigate a series of $Cp*Ir(NHC)X_2$ (X = I, Cl or CF_3SO_3 (OTf) and NHC = N-heterocyclic carbene-type ligand) complexes, looking for alternatives to avoid or to diminish the oxidative degradation of the ligand and nanoparticle (NP) formation. Initially the WO activity of compounds **1X** (X = Cl, I, OTf) and **2I** (**See Figure VII.1.**) was evaluated using the common cerium ammonium nitrate (CAN) as sacrificial mono-electronic oxidant (SO). Evolution of dioxygen was observed within the range of the most active Cp* based iridium WOCs reported (TON = 7000, TOF = 0.42 s⁻¹). However, those compounds are poorly recyclable and after loading a new batch of oxidant a clear depletion of the activity was observed, indicating a massive degradation of the catalyst (**Figure VII.2, left**).

To avoid the harsh environment imposed by CAN (pH < 1, E° = 1.75 V)[4] and maintain the catalysis for longer periods, we decided to use $NaIO_4$ as an alternative milder sacrificial oxidant. Under these conditions TOF (0.3 s⁻¹) remained constant during the reaction until the whole consumption of the SO. A second batch of periodate fully reactivates the catalytic activity, retaining the O_2 production rate (**Figure VII.2, right**). Remarkably, the catalyst was also found stable at higher temperatures (40ºC). **1Cl**, the best among the compounds studied herein, experimented a 10-fold increase of the TOF (TOF_{40} = 4.7s⁻¹, TOF_{25} = 0.3) and TON close to half a million was recorded. To the best of our knowledge, this is the largest TON ever reported for a chemical-driven WO, and is within the range of the PSII (TOF = 100 - 400 s⁻¹, but D1 protein is replaced every 30 – 60 min).[5,6]
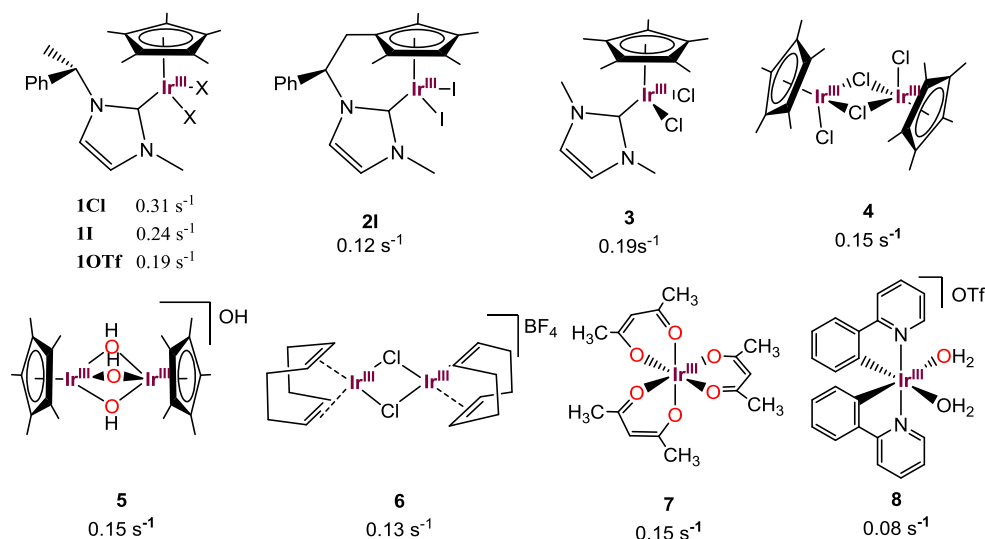
Figure VII.1. Catalysts studied in this work for the WO employing $NaIO_4$ as SO. TOF_{max} (moles O_2 produced per moles of complex, per second), calculated at the initial stage of the reaction, were included for comparison.
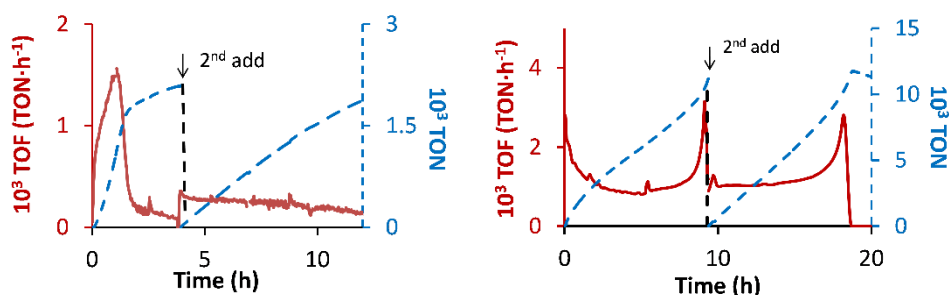
Figure VII.2. Effect of stepwise reaction when CAN (left) or $NaIO_4$ (right) were used as sacrificial oxidants. TON is represented in the right axes and dotted lines in blue and TOF in the left axis and solid lines in red. Conditions: Left) To **1Cl** (15 μM) in water (5 mL) CAN was added (200 mM) at time zero; O_2 evolved with a TOF_{max} of 1530 h^{-1}. At t = 3.9 h, a second CAN addition (200 mM) produced a low but constant rate of O_2 formation (TOF ~ 300 h^{-1}). Right) Equivalent experiment but with $NaIO_4$ (250 mM of $NaIO_4$ to a solution of 10 μM of **1Cl** in water, 5 mL) as oxidant showed high constant TOF (~1100 h^{-1}). The same behavior was observed during the second run.

The different behavior observed with these two oxidants is consistent with previous reports where it was described that the use of CAN leads to the formation of active NP which are deactivated by an agglomeration process.[1] It was also reported that the use of chelating ligands slowed down the NP formation but affects negatively the TOF.[7] Besides, Macchioni and coworkers found that Cp* suffers an important oxidative damage during the initial state of the catalysis.[2,8,9] To investigate the role of the organic fragment, we initially studied the effect of linking the Cp* group to the carbene moiety, expecting for an extra stability of the ligand. However the influence observed was the opposite. After expanding the screening to other common iridium salts and similar organometallic complexes with the aim to understand the role

169

of both Cp* and carbene moiety in the active species (**Figure VII.1**) we concluded that the group attached at the N atom of the carbene could be taking part in the catalytic species, or in the formation of the real catalyst, affecting to a reasonable extent the WO activity.

Interested on the high performance observed when $NaIO_4$ was used as SO, a mechanistic study was carried out with **1Cl**. Kinetics pointed towards a bimolecular process (first order on Ir catalyst and first order on $[IO_4^-]$, **Figure VII.3**). However, when periodate was used in high concentrations (50-300 mM) the order on the oxidant decreased to 0 and the reaction became oxidant-independent. This may explain the apparently constant TOF observed during the course of the catalysis. In other words, due to the very high [SO/cat] ratio used (initially $2.5 \cdot 10^4$) the reaction is in the [0th order vs IO_4^-] phase and the rate of O_2 production is not affected by the consumption of the oxidant.

It is important to notice that water cannot be strictly necessary for the O_2 evolution if an IO_4^- - IO_4^- coupling reaction takes place. This scenario should be maintained in organic solvents, such as MeCN. Nevertheless, employing the organic-soluble $tBuIO_4$, no traces of oxygen were detected. Using $NaIO_4$, the addition of increasing amounts of water to MeCN only restores the activity in some extent (3:1 H_2O:MeCN v/v restores 12% of the activity). This data points towards a mechanism where water is involved.
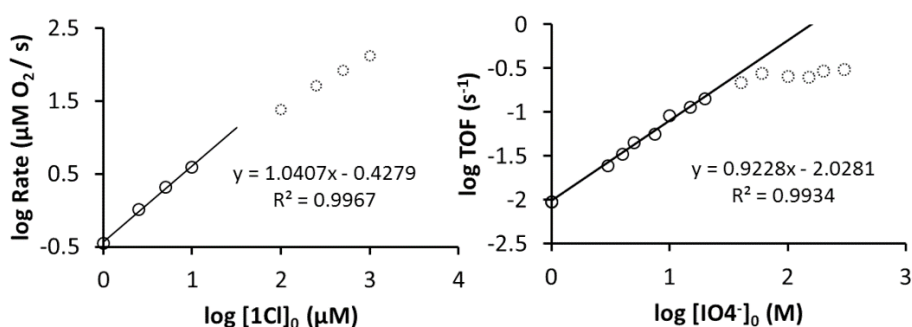
Figure VII.3. Left) Log-log plot for oxygen evolution rates (µM/s) versus initial concentration of **1Cl** (1–1000 µM) and right) log-log plot of TOF versus initial concentration of $[IO_4^-]$ (1 – 300 mM) ($[\mathbf{1Cl}]_0 = 10$ µM).

Spectroscopic analysis (UV-Vis, NMR, DLS) and CSI-HRMS were conducted in order to gain insight into the nature of the catalytic species. According to UV-Vis, the addition of SO lead to the formation of a new species absorbing at 435 nm, which in turn evolves to a blue colored species with an absorption band at 580 nm, and an small shoulder at 405 nm. The initial lag of O_2 evolution observed during these transformation was attributed to the formation of the real catalyst. O_2 was monitored in parallel. For a freshly prepared sample of Ir^{III} the O_2 yield was 80% in the first run (40 eq. $NaIO_4$), while for a recycled catalyst, the O_2 production was quantitative. Therefore, 20% of the oxidant (8 eq.) is consumed during the formation of the active species.

In consonance, ^{1}H-NMR and HRMS signals arising from the complex vanished after the addition of few equivalents of oxidant (10 eq.), indicating that the reaction was initiated by a fast decomposition of the complex. Decomposition byproducts such as HCO_2H, CH_3CO_2H and $PhCOCH_3$ were detected by ^{1}HNMR, in good agreement with the decomposition analysis reported by Macchioni and coworkers, where the Cp* moiety of a Cp*-functionalized iridium complex was oxidized by CAN.[8,9] However DLS did not show a clear evolution of NP, such as observed when using CAN as SO (NP > 10 nm).

Further UV-Vis studies coupled with manometry showed a strong connection between the absorption band at 405 nm and the O_2 production. The depletion of this chromophore and the rising of the 580 nm signature were strictly connected with the consumption of the SO and pressure stabilization. This process was completely reversible (see 5 consecutive runs in **Figure VII.4**). Therefore, the 580 nm signal was assigned to the resting state of the reaction (probably Ir^{IV})[10] and the 405 nm chromophore to the active species (tentatively assigned to Ir^V or Ir^{VI}). The interconversion between the two species could be triggered by the addition of oxidant or a reducing agent ($NaIO_4$ and EtOH respectively), being a fully-reversible process.

The resting state of the $IrCl_3$-catalyzed WO absorbed at 600 nm. This shift can be related to the lack of organic ligand. However, the oxidized band raised at 405 nm, thus indicating that the formation of this species does not require the presence of organic fragments. Unfortunately, further characterization of the nature of those species cannot be obtained and is not straightforward to ensure the homogeneity of the process. However the experimental observations suggest that under the presence of $NaIO_4$, the catalyst could be molecular in nature. Although active species may not contain complete organic ligands, water, hydroxides, oxides or oxidized organic fragments can coordinate forming the structure of the true WOC.[11] In fact, a recent study carried ou by Crabtree and coworkers suggested that under the presence of $NaIO_4$, the Cp* moiety of the iridium complex $[Ir^{III}(Cp^*)(pyr\text{-}CMe_2O)(Cl)_2]$ suffered a complete oxidative damage, while the chelate ligand was maintained intact.[10] By means of TEM-EDX, XPS, ^{17}O-NMR, rR and DFT, the active specie was characterized as $[Ir^{IV}(pyr\text{-}CMe_2O)(OH_2)(\mu\text{-}O)_2]$ (see **General Introduction I.4.2.4**). Macchioni and coworkers very recently characterized some intermediates during the oxidative damage of the Cp* moiety (see **General introduction I.4.2.2)** and, in agreement with Crabtree *et al.* suggested that the catalytic activity was provided by a single molecular catalyst, resulting from these transformations.[2]
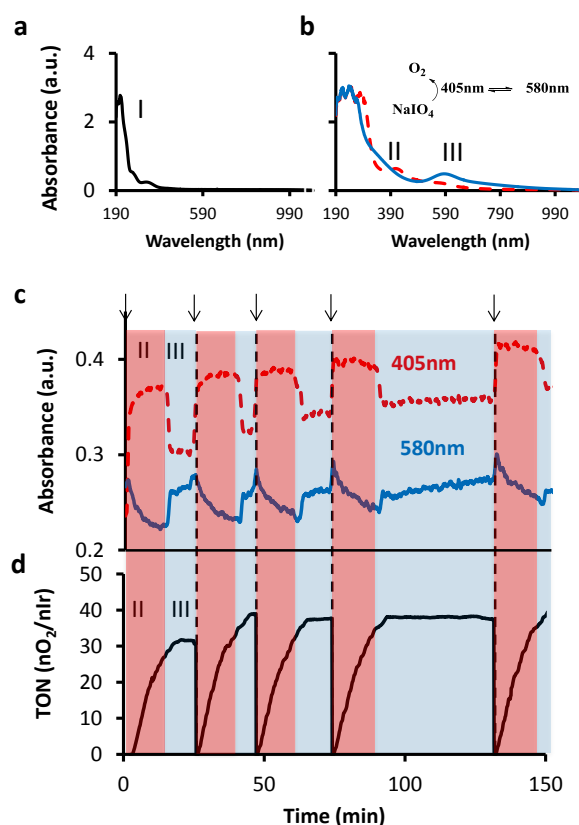
Figure VII.4. The oxygen evolution and the UV-Vis spectrum were monitored in a single experiment. **a** and **b**) UV-Vis spectra in different WO states **I**) 0.5 mM of **1Cl** in H$_2$O (solid spectra), **II**) 0.5 mM of **1Cl** in H$_2$O immediately after the addition of 40 eq. of NaIO$_4$ (t = 60 s) (dotted spectra) and **III**) 0.5 mM of **1Cl** in H$_2$O with 40 eq. of NaIO$_4$ after no more oxygen evolution (solid spectra). **c**) Time-traces followed at 405 nm and 580 nm of a 0.25 mM solution of **1Cl** during several NaIO$_4$ additions. **d**) The oxygen evolution was monitored at the same time (TON$_{max}$ = 40). Every new addition of NaIO$_4$ (80 eq.) the TON was set up to 0. The background and the dilution effect were corrected in the absorbance traces

VII.2. Efficient water oxidation catalysts based on readily available iron coordination complexes

From **Chapter III** and related reports[1,3,10-12] its currently known that iridium complexes are precatalysts for both Ce^{IV} and NaIO$_4$-driven water oxidation reactions. Therefore, the improvement of the efficiency following a rational synthetic catalyst design is complicated due to the uncontrolled structural rearrangement suffered by the complex to yield the true catalytic species. Besides, the low abundance of this metal in the Earth-crust makes unpractical the development of a global Ir-based artificial photosystem. So we decided to lead our research towards the investigation of WOCs based on more abundant and sustainable metals.

Inspired by the excellent catalytic activity of biomimetic non-heme iron coordination complexes in challenging C-H and C=C oxidation reactions, we studied the activity of a series of

these complexes as potential water oxidation catalysts, finding that the family of iron complexes based on neutral tetradentate aminopyridine ligands exhibits a significant catalytic efficiency and lifetime. Turnover numbers > 350 and > 1000 were obtained using CAN (pH 0.8, E^o = 1.75 V)[4] and sodium periodate (pH 2, E^o = IO_4^- / IO_3^- = 1.60 V),[4] respectively. These are among the highest turnover numbers per metal center described so far for any homogeneous water oxidation reaction based on 1st row transition metals.

Typical structures studied were based on a metal (II) center coordinated with an organic tetradentate or pentadentate amine framework (**Figure VII.5**), with one or two labile sites. Those ligands have in common a high chemical robustness against oxidation, as well as a high basicity, allowing the stabilization of metals in high oxidation states.[13-16] This ability is understood as one of the key factors to catalyze with high efficiencies and selectivities stereospecific alkane hydroxylation, alkene cis-dihydroxylation and olefin epoxidation.[16-23] Therefore, these systems were thought to be good candidates to explore water oxidation catalysis.
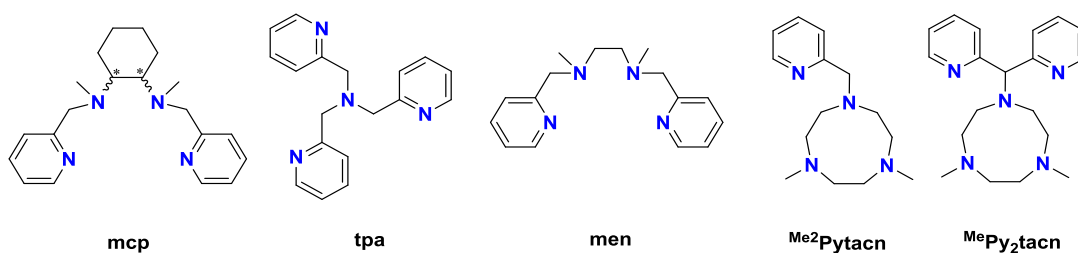
Figure VII.5. Examples of tetradentate and pentadentate ligands used to prepare mononuclear iron (II) complexes to perform selective alkane and olefin oxidation.

The broad accessibility of nitrogen based ligands allowed us to extract preliminary data about the scope, efficiency of the reaction as well as specific mechanistic information depending on the ligand architecture (**Figure VII.6**). Along this line, it was found that iron complexes with tetradentate nitrogen based ligands that leave two exchangeable *cis*-positions were effective water oxidation catalysts (i.e. **1-5Fe**) when using CAN as ultimate oxidant.

173
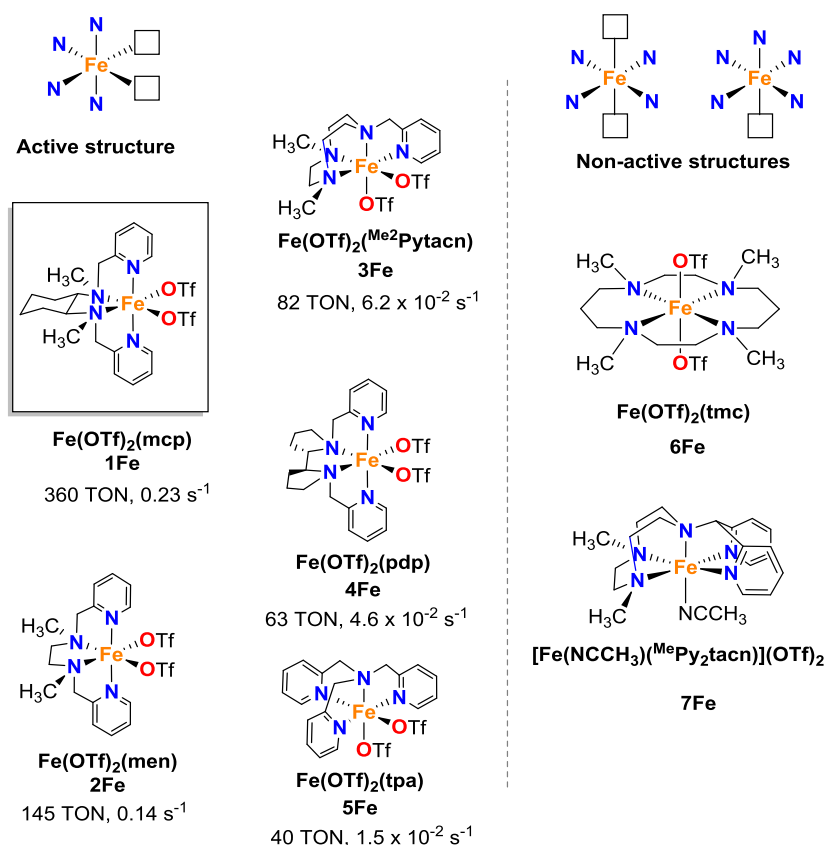
Figure VII.6. Active complexes having neutral nitrogen ligands. No activity was found for complexes with tetradentate ligands leaving *trans* free coordination sites and pentadentate neutral nitrogen ligands. The structure exhibiting the highest activity has been highlighted. Reaction conditions: Catalyst: CAN = 12.5 μM : 125 mM at 25ºC, pH = 0.8.

On the contrary, iron complexes with tetradentate nitrogen ligands leaving two available *trans*-positions (i.e. **6Fe**) or with pentadentate nitrogen ligands (i.e. **7Fe**) as well as other first row transition metal complexes containing the tetradentate ligand Me,HPytacn (MnII, CoII or NiII) do not form significant amounts of O_2 under analogous conditions (**Figure VII.6**). Further screening carried out by Fukuzumi,[24] Sun,[25] Yang[26] *et al.* and in our group (unpublished results) with other *cis*-tetradentate, *trans*-tetradentate, pentadentate and tridentate iron complexes are in agreement with this hypothesis (**Figure VII.7**).
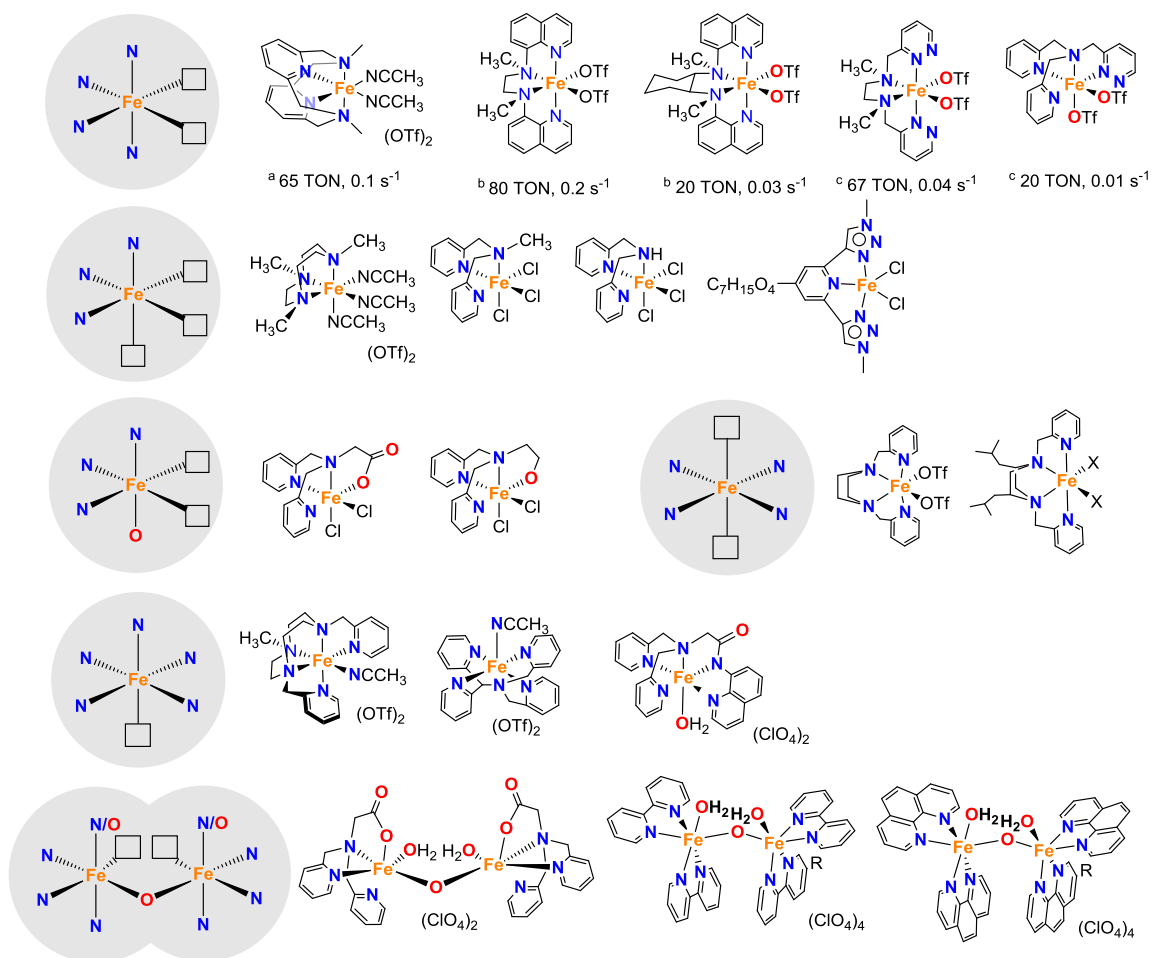
Figure VII.7. Screening of tridentate, *cis*-tetradentate, *trans*-tetradentate, pentadentate and pentadentate dimeric complexes studied as potential catalysts in Ce^{IV}-driven water oxidation. [a]4 µM Fe, 45mM CAN in HOTf (pH 1).[25] [b]12.5 µM Fe cat and 125 mM CAN.[24] [c]100µM Fe cat and 125 mM CAN.[26]

pH-dependent UV-Vis spectroscopy and theoretical studies were carried out to get insight on this behavior and some preliminary conclusions can be extracted from here; i) screened tridentate complexes do not catalyze the water oxidation because $Fe^{IV}=O$ cannot be achieved by those complexes in water, using CAN (unpublished results) ii) the redox potential for the $Fe^{IV/V}$ couple in *trans*-tetradentate and pentadentate complexes (**6Fe** and **7Fe**) is too high (2.07 V and 2.17 V, from DFT calculations) thus Ce^{IV} cannot oxidize the catalyst and form species that could oxidize the water molecule.[27]

Isotopic labeling experiments using $H_2^{18}O$, under catalytic conditions showed a good agreement between the experimental and the theoretical $^{16/18}O_2$ isotopic distribution, and no N_2 formation was detected, discarding the possible oxidation of ammonium ions from CAN. Therefore all the O_2 is exclusively originated from the water oxidation reaction. Moreover, under catalytic conditions (CAN, pH 1) the absence of significant amounts of CO_2, together with absence of nanoparticles (DLS measurements) indicate that no major decomposition of the system

takes place. Indeed, at low pH values $[Fe(OH_2)_6]^{3+}$ is the most stable Fe^{III} speciation in water rather than Fe_2O_3 nanoparticles,[28] and $FeCl_2$, $Fe(OTf)_2$, $FeCl_3$ or $Fe(ClO_4)_3$ do not catalyze the oxidation of water with CAN or $NaIO_4$. Consequently, at low pH values, even if some iron-ligand dissociation occurs from the iron complexes, the resulting $[Fe(OH_2)_6]^{3+}$ ion will not be able to catalyze the water oxidation. Because of that the catalytic activity must be exclusively ascribed to molecular complexes.

Some preliminary information about the possible resting state and catalytic cycle was also proposed in **Chapter IV**. Titration experiments of **3Fe** with CAN (6 eq) showed that $[Fe^{IV}(O)(OH_2)(^{Me,H}Pytacn)]^{2+}$ (**3Fe^{IV}=O**) was formed (λ = 776 nm, ε = 280 $M^{-1}cm^{-1}$, $t_{1/2}$ = 2.4 h), but under these conditions no increase of pressure was detected. Moreover, the analysis of the reaction headspace showed no traces of O_2. The stability of the oxo-iron intermediate and the lack of oxygen production suggests that this intermediate is not the responsible for the O-O bond formation. Further addition of 75 eq of CAN produced concomitant Ce^{IV} consumption and O_2 evolution (**Figure VII.8.**). Stoichiometric O_2 formation versus the consumed Ce^{IV} indicates that the oxidizing equivalents are essentially used into the water oxidation reaction.
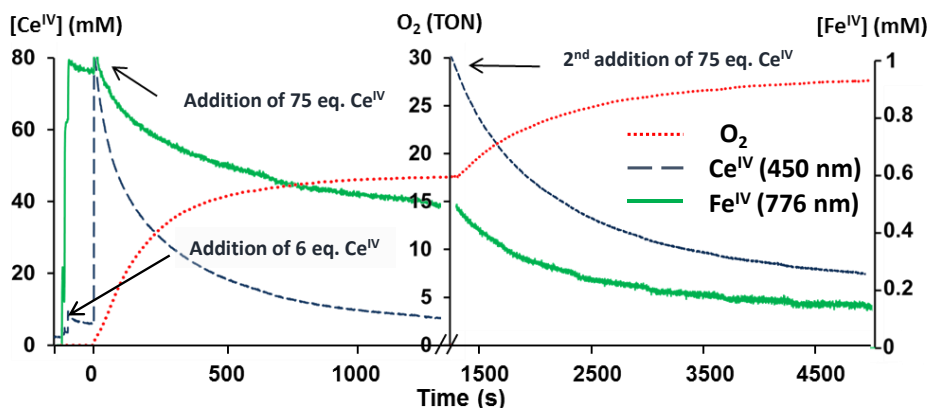
Figure VII.8. Water oxidation reaction monitored by UV-Vis spectroscopy and a pressure sensor for the observation of the Ce^{IV} consumption (blue dashed line), the complex degradation (green) and the oxygen evolution (red dotted line). **3Fe^{IV}=O** was fully formed by addition of CAN (6 eq) over **3Fe** (1 mM in MiliQ water). Oxygen was not detected and the **3Fe^{IV}=O** species were stable for more than 2 hours. A second addition of oxidant (75 eq) allowed the oxygen production.

Kinetic studies showed that the rate of Ce^{IV} consumption was first order on $[Fe^{IV}(O)(OH_2)(^{Me2}Pytacn)]^{2+}$ concentration and first order on Ce^{IV} when CAN was used in low concentrations (**Figure VII.9**). We concluded that $[Fe^{IV}(O)(OH_2)(^{Me2}Pytacn)]^{2+}$ is an intermediate and most probably the resting state. The bimolecular behavior observed points towards the formation of $[Fe^{V}(O)(OH)(^{Me2}Pytacn)]^{2+}$ species responsible for the O-O bond formation in an acid base (AB-type) mechanism. However a change on the initial rate order at high Ce^{IV}

concentration (from 1st order to 0th order above 25 mM of Ce^{IV}, **Figure VII.9, right**) caught our attention for a deeper mechanistic study that is discussed in following chapters.
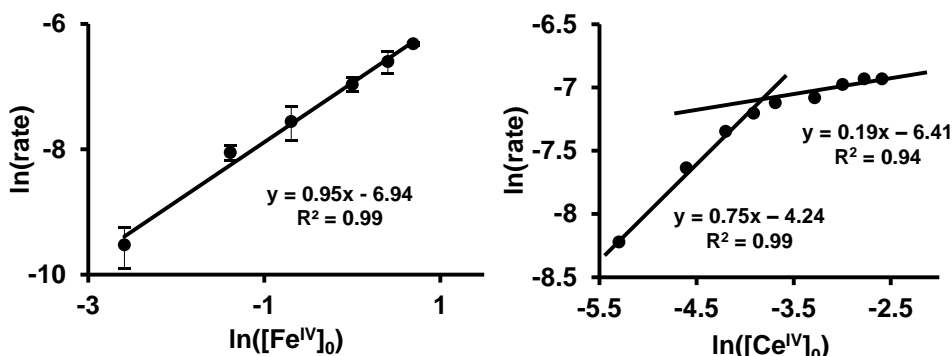
Figure VII.9. Reaction order on $Fe^{IV}=O$ (left, $[Fe^{IV}=O]_0 = 0.075 - 2$ mM, $[Ce^{IV}]_0 = 80$ mM) and Ce^{IV} (right, $[Fe^{IV}=O]_0 = 1$ mM, $[Ce^{IV}]_0 = 5 - 80$ mM) calculated by double-ln plotting the initial rate consumption at 10% of Ce^{IV}.

VII.3.   Electronic Effects on Single-Site Iron Catalysts for Water Oxidation

Two scenarios can explain the saturation behavior observed upon addition of large excess of CAN to **3Fe^{IV}=O** (see VII.2 and **Chapter IV**). i) the rds (rate determining step) is the O-O bond formation and $Fe^V=O$ is partially accumulated when the highest TOF is achieved or ii) a reversible interaction between catalyst and oxidant ($Fe^{IV}=O-Ce$) takes place before the rds and the resting state may change upon use of different catalytic conditions ($Fe^{IV}=O \leftrightarrow Fe^{IV}=OCe$). The second scenario may have some precedent in the interaction between a Lewis acid Sc^{3+} and the oxo-iron(IV) unit in $[Fe^{IV}(O)(tmc)]^{2+}$ (tmc = 1,4,8,11-tetramethyl-1,4,8,11-tetraazacyclotetradecane) [29] and $[Fe^{IV}(O)(N4Py)]^{2+}$ (N4Py = *N,N*-bis(2-pyridylmethyl)-*N*-bis(2-pyridyl)methylamine).[30] To gain further insight, we took advantage of the modular nature of the [^{Me2}Pytacn] ligand and we tune its electronic properties by introducing substituents at the *para* and *ortho* position of the pyridine ring. Interestingly, [Fe(OTf)$_2$(^{X,R}Pytacn)] complexes (**Figure VII.10.** OTf = CF_3SO_3, X = –H, –Cl, –CO$_2$Et, –NO$_2$, R = H) prepared were excellent catalyst for the cerium(IV)-driven water oxidation (WO) with a TOF increase proportional to σ (Hammett sigma constant), indicating that electronic effects have an important influence in the water oxidation (**Figure VII.11.**). This behavior, together with DLS measurements (**Chapter IV**), strongly supports the catalytic activity originated from molecular complexes operating in homogeneous phase.[31]

	X	R	TON	TOF(s^{-1})
3aFe	H	H	82	6.3×10^{-2}
3bFe	Cl	H	102	0.11
3cFe	CO$_2$Et	H	143	0.16
3dFe	NO$_2$	H	180	0.23
3eFe	H	F	25	2.2×10^{-2}
3fFe	H	Me	-	-
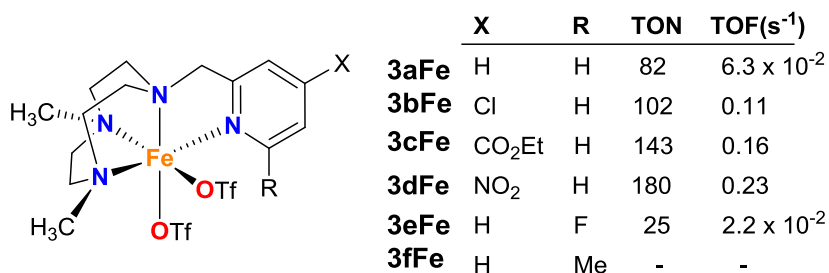
Figure VII.10. Iron complexes with different 4-subtituted pyridines show an increasing activity in water oxidation related to the electrowithdrawing character of the pyridine in the ^{Me2}Pytacn ligand. Reaction conditions for water oxidation: Catalyst : CAN = 12.5 μM : 125 mM at 25ºC, pH = 0.8.
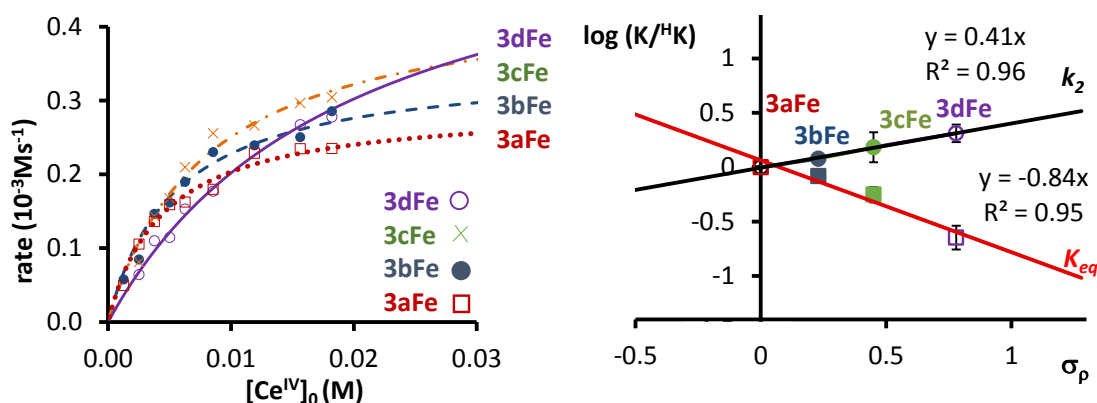
Figure VII.11. Left) Plot of initial rates versus [CAN] for **3a**–**dFe** (0.25 mM). Dots represent k_{obs} (initial rate / [Fe^{IV}]$_0$) in water (25 ºC, pH 1). Dotted lines represent the fitting derived from a saturation kinetics model. Right) Hammett plot for the apparent association (K_{eq}, red line, squares) and rate constants (k_2, black line, circles) against the σ_p Hammett parameters for **3a**–**dFe**.

Titration of [Fe(OTf)$_2$(^{X,R}Pytacn)] complexes with CAN leads to the quantitative formation of [Fe^{IV}(O)(H$_2$O)(^{X,R}Pytacn)]$^{2+}$ species (**3a**–**dFe^{IV}=O**), exhibiting characteristic UV-Vis chromophores between 750 and 800 nm with low absorptivities, indicative of a d-d nature. We realized that further addition of excess of CAN (5 to 75 eq with respect to the iron) produced small but significant changes on the UV-Vis band, including a shift of 8-10 nm to lower wavelengths and an increase of the absorptivity from 10 to 25%, function of the complex, which was not observed by the addition of other additives such as acid, NH$_4$NO$_3$, Ce^{III}(NO$_3$)$_3$ or La^{III}(NO$_3$)$_3$. These changes reverted to the initial Fe^{IV}=O feature once Ce^{IV} was consumed.

The shift in the UV-Vis Fe^{IV}=O chromophores, and the saturation behavior on Ce^{IV} were reproduced for all the complexes studied, albeit with different reaction rates. This saturation behavior is common in enzymatic reactions (E+S↔ES→E+P), so we decided to fit those kinetics using the Michaelis-Menten model, and obtaining K_{eq} and k_2 constants. Comparative analysis of the data shows that the more electro-donating was the ligand, higher was the corresponding K_{eq} but the lower was k_2.

This behavior is in good agreement with the two proposed scenarios:

i) Assuming that Ce^{IV} behaves as a monoelectronic outer sphere oxidant, the transformation of a high valent $Fe^V=O$ from the 1e⁻ oxidation of $Fe^{IV}=O$ is a process favored by donor ligands (K_{eq} increases with $1/\sigma$). However the over-stabilization provided by a more electrodonating substituent could plays against its reactivity, as $Fe^V=O$ becomes less electrophilic, thus lowering the value of k_2 (k_2 increases with σ).

ii) Assuming the scenario that involves formation of a Fe=O-Ce dimer when using excess of CAN, the interaction of two electrophilic moieties ($Fe^{IV}=O$ and Ce^{IV}) is favored by electrodonating groups as the oxo ligand becomes more basic (again, K_{eq} increases with $1/\sigma$). The Fe=O-Ce intermediate is envisioned to proceed by two possible alternative pathways; a) the attack of the water molecule to the $[Fe^{IV}=O-Ce^{IV}]$ or b) the inner-sphere oxidation to $[Fe^V=O-Ce^{III}]$), followed by the attack of the water. Over-stabilization by the electrodonating group will play against oxidative reactivity in both cases (lowering k_2). This trend is actually in contradiction with the $Fe^{IV}=O-(OH)-Ce^{IV}$ interaction proposed by Sakai and coworkers,[32] who proposed that in some cases the O=O bond formation step could take place by the coupling of an oxo-hydroxocerium radical and the M=O moiety. In this scenario, the O_2 production rate is favored by electrodonating groups.

Therefore, it was concluded that further information is needed to discern between the proposed scenarios.
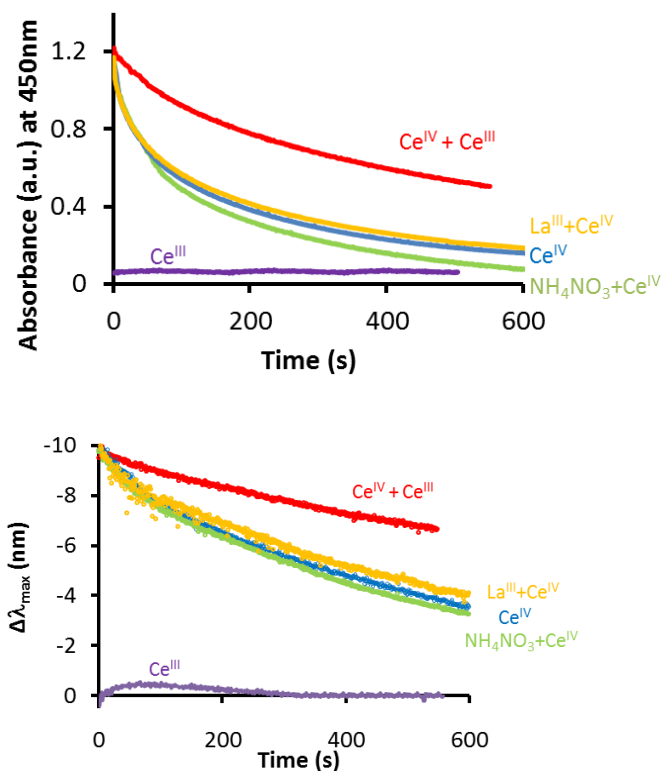
Figure VII.12. Plots of the effect of the ionic strength on the reaction rate of the Ce^{IV} consumption and in the spectral shift over time. Top) traces of the Ce^{IV} absorbance measured at λ value of 450 nm and Bottom) spectral shift evolution of the low energy band (λ_{max} = 776 nm) after the addition of NH_4NO_3 (762 mM, green dots), $Ce(NO_3)_3 \cdot (H_2O)_6$ (127 mM, red dots) and $La(NO_3)_3 \cdot (H_2O)_6$ (127 mM, gold dots) to a solution containing $[Fe^{IV}(O)(H_2O)(^{H,H}Pytacn)]^{2+}$ (1 mM) and CAN (75 mM). These concentrations of reagents yield the same ionic strength, temperature (25ºC) and pH (1) for all the experiments.

To shed some light on the mechanism, we took advantage of the fact that the formation of Fe^V=O from Fe^{IV}=O via an outer sphere electron transfer process is redox-sensitive. By lowering the redox potential (according to the Nernst equation the red-ox potential is dependent on the amount of Ce^{III} and Ce^{IV}) the full formation of the intermediate (Fe^V or $[Fe^{IV}$=O-$Ce^{IV}]$) was not affected (estimated by UV-Vis, **Figure VII.12. Bottom**). Therefore we ruled out the first scenario where Fe^V=O is generated from Fe^{IV}=O by an outer sphere oxidation.

While there are precedents for strong interactions between oxo-iron(IV) species and a Lewis acid (for example Fe=O-Sc^{3+} have been described),[29,30] we favored the dimerization through the aqua ligand (O=Fe^{IV}-OH-Ce^{IV}) because pentadentate oxoiron (IV) complexes, which lack the aqua ligand, do not show any change in the UV-Vis spectrum upon addition of large excess of CAN.

Besides, under the presence of Ce^{III} an inhibition of the catalytic activity was observed (small consumption of Ce^{IV} and negligible O_2 production, **Figure VII.12. Top**). This inhibition could be rationalized by considering the decrease in the redox potential (Nernst equation) and

consequently, we favor the presence of an electron transfer after the formation of the UV-Vis observable specie ($O=Fe^{IV} OH-Ce^{IV} \leftrightarrow O=Fe^{V}-OH-Ce^{III}$).

Kinetics carried out in D_2O showed an apparent lack of KIE (0.9 ± 0.2), indicating that minor reorganization of the O-H bonds occurs in the rate determining step. In excellent agreement with experimental data, DFT suggest that the O-O bond formation event, i.e. the nucleophilic attack of a H_2O molecule to the $Fe^{V}(O)(OH)$, is rate-determining, with a KIE of 0.98 (**Figure VII.13**).
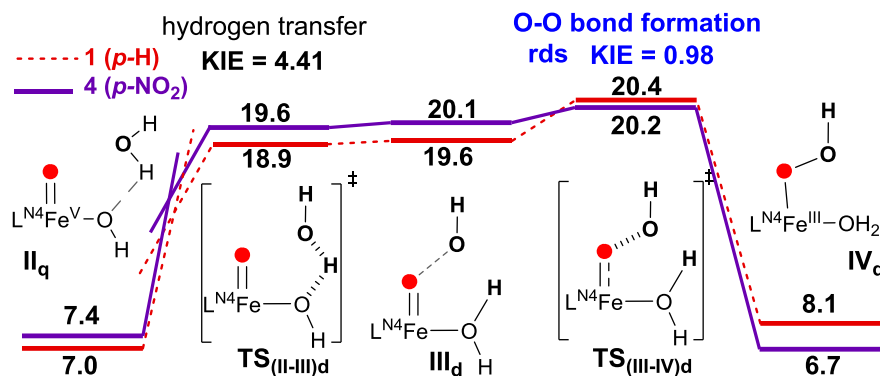
Figure VII.13. DFT modelled O–O bond formation mechanism for **1** and **4**. Values indicate Gibbs energies. Subscripts d and q represent spin state of S = 1/2 and S = 3/2, respectively. All energies are given in kcal·mol⁻¹.

Interestingly, DFT calculations indicates that the *cis*-labile sites of the iron center could be crucial for the O-O bond formation; working in association, H_2O could be properly placed by means of an interaction with the OH ligand, acting as an internal base, to the electrophilic oxo-iron. (**Figure VII.13**). In this line, Yang *et al.* incorporated hydrogen-bonding functionalities into the second coordination sphere of the iron complex (**8Fe and 9Fe**, **Figure VII.14.**) but the small differences that Yang *et al.* observed in the reactivity of the new complexes can also be attributed to electronic effects and more studies are needed to clarify if an external base can aid into the water oxidation activity for this family of iron coordination complexes.[26]

8Fe, x=N   67 TON, 4 x 10⁻² s⁻¹   **9Fe**, x=N   20 TON, 1 x 10⁻² s⁻¹
2Fe, x=CH   72 TON, 6 x 10⁻² s⁻¹   **5Fe**, x=CH   14 TON, 1 x 10⁻² s⁻¹
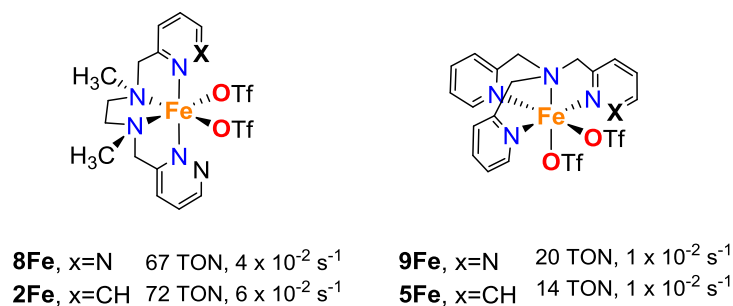
Figure VII.14. Representation of the iron complexes for base-assisted substrate deprotonation (**8Fe, 9Fe**) and comparison of the catalytic water oxidation activity with the previous reported iron complexes (**2Fe, 5Fe**). Reaction conditions for water oxidation: Catalyst : CAN = 100 μM : 125mM at 25ºC, pH = 0.8.

In parallel, our group and others reported experimental evidences of the formation of high valent oxo-iron species by reaction with H_2O_2 as SO.[21,33] Isotopic and product analysis, CSI-HRMS[*] and DFT suggested $Fe^V(O)(OH)$ species evolved from the O-O bond breakage of a $Fe^{III}(OOH)(H_2O)$ as responsible for C-H and C=C oxidations.[16,21,34-37] These species were envisioned to be coincident with those involved in the water oxidation reactions. In order to test this analogy, Ce^{IV}-driven iron-catalyzed stereospecific hydroxylation of alkanes and *cis*-dihydroxylation of olefins was explored and the results confirmed the validity of the proposal (**Figure VII.15**).[38] Oxidant conversions ranging from 7 to 38% using alkanes, and up to 78% using alkenes were detected by GC and GC/MS analysis. The lack of stereoscrambling when tertiary C-H bonds were oxidized suggested that no long living radicals or cations were involved. Selectivity patterns (oxidation is preferentially at the most exposed secondary C-H sites) were found similar to those found for H_2O_2-driven reactions.
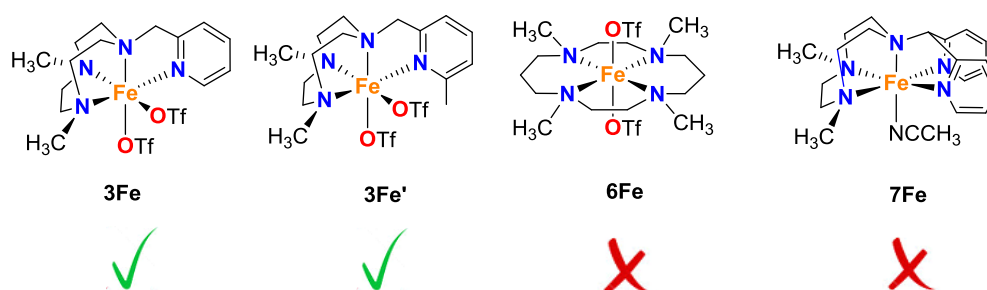
Figure VII.15. Iron complexes used for C-H hydroxylation and olefin *cis*-dihydroxylation.

Reactivity with olefins was also found similar to the H_2O_2-**3Fe** system, being *syn*-diols D1 (**Table VII.1**) the main products arising from a *cis*-dihydroxylation reaction (D/E$_{CAN}$ = 2.6 , D/E$_{H2O2}$ = 2.2). Besides, **3Fe'** led to higher D1 selectivities using both SO (H_2O_2 and CAN), and the oxidation of *trans*-octene by **3Fe** yield the corresponding *syn*-addition diol (D2 in this case) as the main product (D/E$_{CAN}$ = 1.5, D/E$_{H2O2}$ = 2). Labelling studies demonstrates that water was the source of oxygen incorporated into oxidation products.

---

[*]Cryospray Mass spectrometry (CSI-MS) in conjunction with high resolution time-of-flight (TOF) analyzer (dry gas and nebulizer gas temperatures were set at 25 ºC)

Table VII.1. Catalytic oxidation of olefins with CAN. Product yields are based on conversion of substrate.

Substrate	Cat	E1 [%]	E2 [%]	D1 [%]	D2 [%]	H1 [%]	D/E[a]
cis-2-octene	**3Fe**	1	tr.	16	6	6	2.6
trans-2-octene	**3Fe**	-	5	8	18	4	1.5
cis-2-octene	**3Fe'**	1	tr.	10	1	1	6.2

[a] D/E (*cis*-octene) = **D1** / (**E1**+**D2**). D/E (*trans*-octene) = **D2** / (**E2**+**D1**). [b] 0% ee. [c] 45% ee. tr. = trace.

The similar distribution of products obtained for both H_2O_2 or CAN oxidants suggest common active species ([$Fe^V(O)(OH)$]), however generated through different pathways; from Fe^{III} using H_2O_2, and from Fe^{IV} when CAN is the ultimate oxidant. Interestingly, using CAN, the intermediate corresponding to the glycolate complex {[$Fe^{III}(O_2C_8H_{16})(^{Me2}PyTACN)](CF_3SO_3)$}$^+$ was observed by CSI-HRMS after addition of the substrate to a solution of [$Fe^{IV}(O)(OH_2)$]$^{2+}$ species in the presence of excess of Ce^{IV}. In addition, **6Fe** and **7Fe** (**Figure VII.15**) do not produce any oxidation of *cis*-decaline and *cis*-2-octene when treated with Ce^{IV}. Thus, for C-H, C=C oxidations, like for H_2O oxidation, iron complexes containing a tetradentate ligand leaving two *cis*-free sites are required. This observation reinforces the involvement of common intermediates (**Scheme VII.1**).[35]
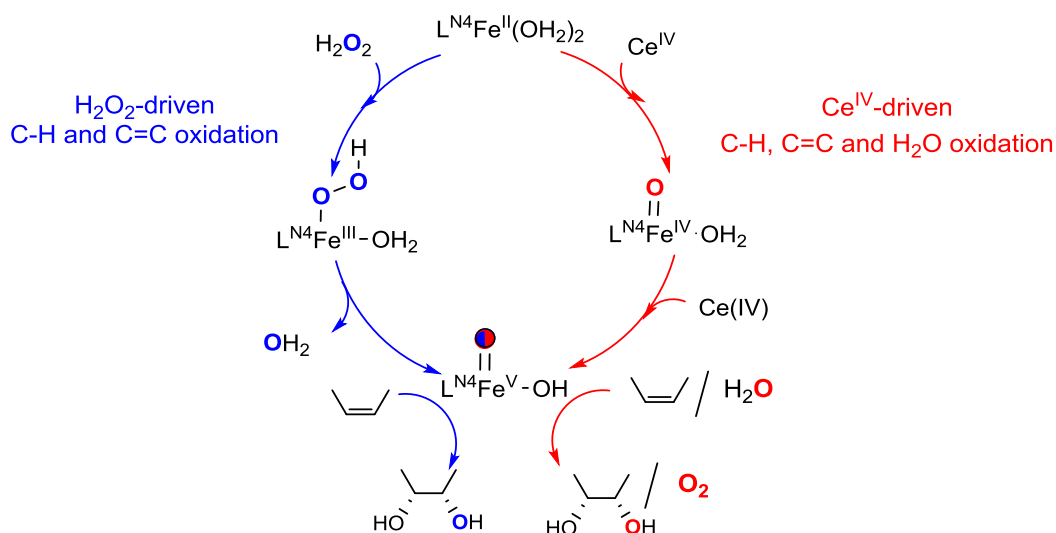
Scheme VII.1. Mechanisms proposed for C-H and C=C oxidations using H_2O_2 (blue path) [35] or CAN (red path) as sacrificial oxidant.[38]

VII.4. Evidence for an Oxygen Evolving Fe–O–Ce Intermediate in Iron-Catalysed Water Oxidation

From our previous studies, based on kinetics (**Chapter IV, V**) and reactivity against organic substrates,[38] we proposed the possible formation and accumulation of a novel intermediate for the specific case of the **3Fe** system when reacting with Ce^{IV}. In those studies the only spectroscopic handle we had available was UV-Vis spectroscopy, which took advantage of the well-established fact that S = 1 oxoiron(IV) species have quite characteristic bands in the near IR region.[33] As the observed changes in these features were small in the presence of a large amount of Ce(IV), we reasoned that the **3Fe^{IV}=O** moiety was likely to be retained in the reaction. The reported crystal structure of a Fe^{IV}=O-Sc^{III} complex[29] served as a precedent for our choice of species **A** (**Figure VII.16**), entailing an interaction between the Fe^{IV}=O and the Ce(IV) ion as the model for the Fe=O-Ce interaction.[38] We subsequently replaced species **A** and switched to species **B** where Ce binds to the hydroxide ligand instead, because we found that **7Fe^{IV}=O**, supported by a pentadentate ligand, did not form this intermediate (**Chapter V**).

Because no new spectroscopic evidences could be obtained for that proposal due to the high instability of this intermediate, we decided to screen other Fe-WOCs.
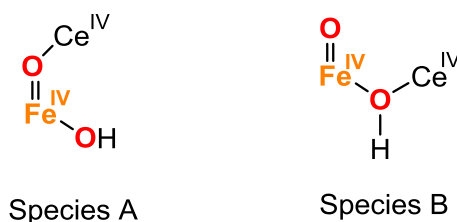
Figure VII.16. Reported proposals for the Fe=O-Ce interaction.

1Fe ([Fe(OTf)$_2$(mcp)], mcp = *N,N′*-dimethyl-*N,N′*-bis(2-pyridylmethyl)-cyclohexane-1,2-diamine) is the most active iron complex for the homogeneous thermal WO in acidic media. Its (O,OH)-bridged dimer ([(Fe(mcp))$_2$(μ-O)(μ-OH)](OTf)$_2$) have a lower reaction rate and a different kinetic behavior,[39] suggesting an AB mechanism for **1Fe** rather than the direct coupling. Moreover, **1Fe** did not produce any significant amounts of O_2 in basic conditions ([Ru(bpy)$_3$]$^{3+}$ as SO), as shown recently by Lau *et al*.[28] However, light-driven WO was observed as **1Fe** was destroyed and iron oxides were formed. These oxides have been demonstrated to be heterogeneous catalysts for the WO. Because the thermodynamically stable speciation of iron at low pH, [Fe(OH$_2$)$_6$]$^{3+}$ (Fe$_2$O$_3$ is active under light-driven conditions), is not active for the WO, the homogeneous O_2 production is supported for **1Fe** under acidic conditions.

1Fe has two topological isomers, α (**1αFe**) and β (**1βFe**), which have shown different reactivity for C-H and C=C bond oxidation.[40,41] This was also observed when the WO activity of

these two compounds was studied in **Chapter VI**, being complex **1βFe** almost unreactive (**1αFe** = 380 TON, **1βFe** = 5 TON). Both complexes were analyzed spectroscopically and spectrometrically to gain insight into the origin of the dramatic differences.

Table VII.2. Water oxidation catalytic activities for α and β

Catalyst	Detection technique	TON O_2[a]	TOF (h^{-1}) [b]	TON CO_2[a]
1αFe	manometry	360 ± 20	0.28 ± 0.02	-
1βFe		8 ± 2	$6.9 \cdot 10^{-3} \pm 3.0 \cdot 10^{-3}$	
1αFe	GC-TCD	380 ± 20	-	0.4 ± 0.2
1βFe		5 ± 2		1.1 ± 0.1

Reactions performed in Milli-Q water at 25 ºC. The catalyst (0.5 mL, 250 μM, final concentration 12.5 μM) was injected through a septum into the reaction vessel containing CAN aqueous solution, (9.5 mL, 131 mM). The initial pH value was 0.8. [a] TON (turnover number) = (n(gas) produced / n(catalyst)) obtained by manometry after 3 h of reaction. [b] TOF (TON·h^{-1}) measured 5 min after the addition of the catalyst.

In both cases, titration of **1Fe**, with CAN (3 eq.) led to the formation of analogous $[Fe^{IV}(O)(OH_2)(mcp)]$ species, (**Fe$_\alpha^{IV}$=O** and **Fe$_\beta^{IV}$=O**) characterized by UV-Vis (λ_{max} = 769nm, ε = 270 $M^{-1}cm^{-1}$, **Fe$_\alpha^{IV}$=O**; λ_{max} =778 nm, ε = 280 $M^{-1}cm^{-1}$ **Fe$_\beta^{IV}$=O**), CSI-HRMS (545.110 m/z, $[Fe^{IV}(O)(mcp)(CF_3SO_3)]^+$ and 547.117 m/z, $[Fe^{IV}(^{18}O)(mcp)(CF_3SO_3)]^+$) and ^{1}H-NMR (see **Chapter VI**). The different spectroscopy for the two complexes supports the retention of the topology in solution. rRaman of the **Fe$_\alpha^{IV}$=O** showed a peak at 822 cm^{-1} which downshifted by 40 cm^{-1} when using $H_2^{18}O$, in consistence with the assignment to the Fe=O stretch.

Decay of **Fe$_\alpha^{IV}$=O** did not result into O_2 evolution, showing that it cannot be the WO active species. In order to investigate the nature of the catalyst we monitored by UV-Vis and manometry (**Figure VII.17**) the addition of 75 eq. of CAN to a solution of **Fe$_\alpha^{IV}$=O** which resulted in O_2 evolution concomitant with Ce^{IV} consumption (**Figure VII.17B**). The formation of a new species (**Iα**) showed a broad absorption band in the 500-650 nm range and a hypsochromic shift of the Fe^{IV}=O feature (**Figure VII.17A**, **dotted red line**), similar to the intermediate observed for **3Fe** with CAN **(Chapter V).** Formation of this novel intermediate was only detected when **1αFe** was the catalyst (not for **1βFe, Figure VII.17 C**) and by the addition of CAN (not observed with TfOH acid, $Ce^{III}(NO_3)_3$ or $Sc(OTf)_3$). Altogether strongly suggest that the formation of **Iα** is required for the WO.
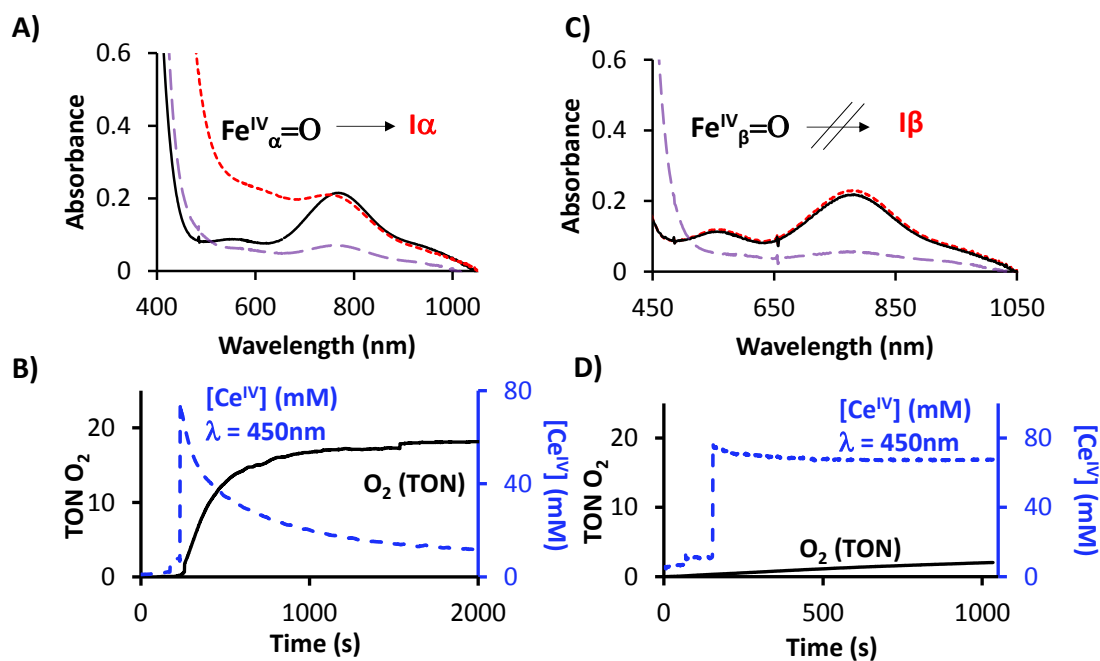
Figure VII.17. Top) UV-Vis spectra of A) $\mathbf{Fe_\alpha^{IV}=O}$ and B) $\mathbf{Fe_\beta^{IV}=O}$ (solid black line) formed by the respective reactions of **1αFe** and **1βFe** (1 mM) in Milli-Q H2O at 25 °C with 3 eq. of CAN, upon addition of 75 eq. of CAN (dotted red line) and after CAN consumption (dashed purple line). Bottom) Time courses for the reaction of B) **1αFe** and D) **1βFe** with 75 eq. CAN monitoring, $[Ce^{IV}]$ (right axis, dotted blue line), and O_2 evolution (left axis, solid black line). Kinetic traces for $[Ce^{IV}]$ were monitored at 450 nm. $\Delta[O_2]$ (TON) was monitored by a pressure transducer and quantified by GC-TCD.

Kinetic analysis of the O_2 evolution and Ce^{IV} consumption initial rates shows a saturation behavior with respect to $[Ce^{IV}]$ (**Figure VII.18, left**), while a linear dependence on $\mathbf{Fe_\alpha^{IV}=O}$, similar to the behavior observed for **3Fe** (**Chapter V**). Again, this kinetic behavior indicates a pre-equilibrium binding of Ce^{IV} to $\mathbf{Fe_\alpha^{IV}=O}$ leading to the accumulation of an intermediate, **Iα**, the evolution of which is rate determining. Titration experiments provide a $K_{eq} = 200 \pm 20$ ($\mathbf{Fe_\alpha^{IV}=O} \leftrightarrow \mathbf{I\alpha}$). This value was obtained at - 8°C in 1:1 v/v MeCN:H₂O, where no O_2 evolution alters a clean transformation (**Figure VII.18, right**).
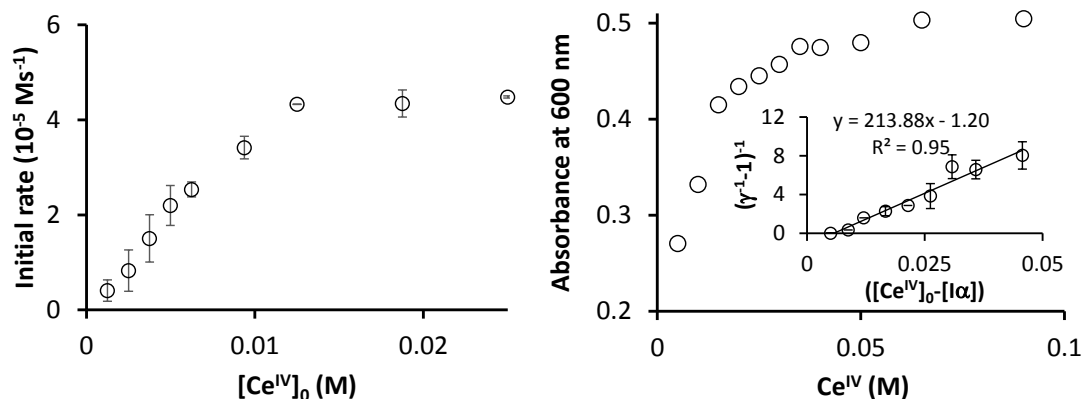
Figure VII.18. Left, initial rates of Ce^{IV} consumption versus $[Ce^{IV}]_0$, in H_2O pH = 1 at 25 °C: $[Fe_\alpha^{IV}=O]_0$ = 0.1 mM; $[Ce^{IV}]_0$ = 1.25 – 18.75 mM. Right, titration of [2-α] (5.0 mM) with CAN (15-100 mM) at pH 1 in H_2O:MeCN (1:1 v/v) at -8 °C (265 K). Inset) Plot of $(\gamma^{-1}-1)^{-1}$ vs $([Ce^{IV}]_0-$ [3-α]) to determine the Ce^{IV} binding constant to $Fe_\alpha^{IV}=O$ to form $I\alpha$ (K_{eq} = [$I\alpha$] / [$Fe_\alpha^{IV}=O$] [Ce^{IV}]). γ = [$I\alpha$] / [$Fe_\alpha^{IV}=O$]. Every CAN addition was carried out on freshly prepared samples of Fe^{II} to completely avoid decomposition of the intermediates. Absorbance values were obtained from the averages of 2-3 experiments. The absorbance was measured in the range of 0-10 s after the addition of Ce^{IV}.

CSI-HRMS and rR (resonance Raman) shed some light in the nature of $I\alpha$ (**Figure VII.19**). By the addition of 75 eq. of CAN to **1αFe** (in H_2O, D_2O and $H_2{}^{18}O$), a peak corresponding to $\{[Fe^{IV}(O)_2(mcp)Ce^{IV}(NO_3)_3]\}^+$ (**M_1**) was observed by CSI-HRMS (**Figure VII.19A-D**). Its composition was deduced from the labelling experiments because on the contrary to the oxo ligands, oxygen atoms of NO_3 do not undergo fast exchange with ^{18}O from water. Moreover, the resistance of the **M_1** ion to high collision energies (MS/MS) indicates a high robustness of the species **M_1**.

From these experiments, several observations indicate that **M_1** corresponds to **$I\alpha$**;

i) The **M_1** peak as well as the changes in the UV-Vis were not observed for **1βFe**, which is not catalytically competent for the water oxidation.

ii) The strong resistance against collision energy of **M_1** is in agreement with a large K_{eq} value, as actually found by UV-Vis.

iii) A parallel decrease in the intensity was observed for the UV-Vis chromophore (**$I\alpha$**) and the **M_1** in CSI-HRMS (**Figure VII.20**).
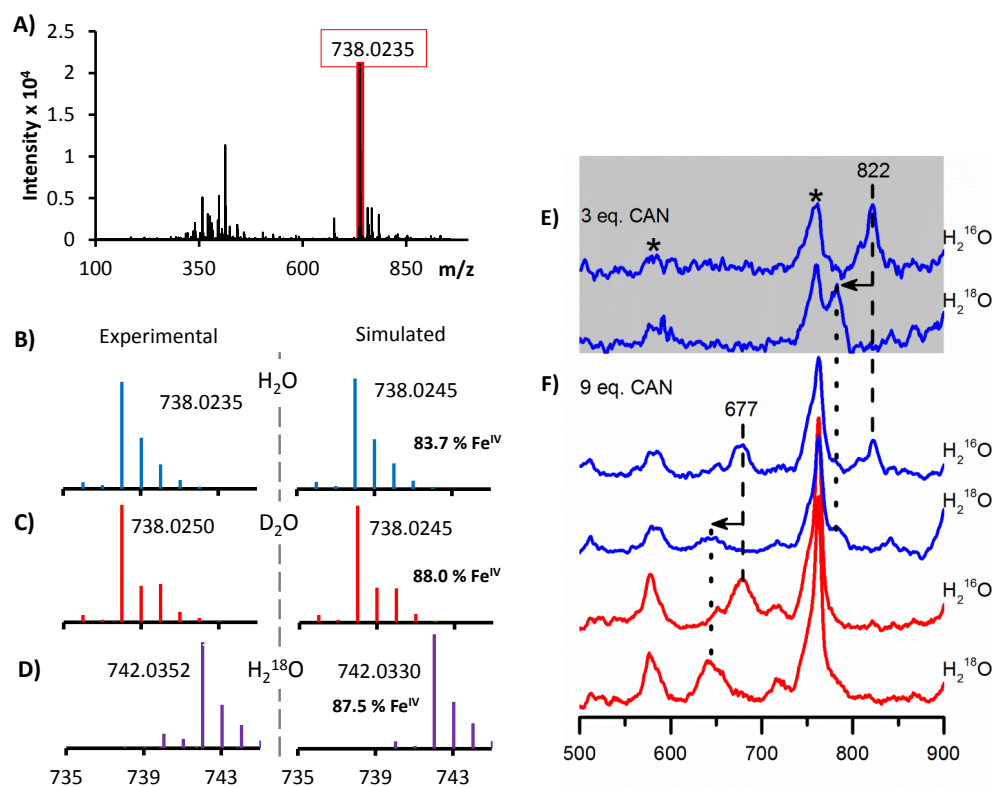
Figure VII.19. A) CSI-HRMS spectrum obtained during the WO reaction, upon the addition of 75 eq of CAN to **Fe$_\alpha^{IV}$=O**. **B-D)** CSI-HRMS features associated with **Iα** obtained in H_2O, D_2O and $H_2^{18}O$ as solvent. Spectra were recorded by setting the nebulizer and dry gas temperature of the cryospray instrument to 25 ºC. **E)** rR spectra of **Fe$_\alpha^{IV}$=O** (λ_{ex} 413.1 nm, 100 mW) prepared upon addition of 3 eq. CAN to a solution of **1αFe** (5 mM) in 1:1 H_2O:MeCN. **F)** rR spectra of **Iα** prepared upon addition of 9 eq. CAN to a solution of **1αFe** in 1:1 H_2O:MeCN. Blue: λ_{ex} = 413.1 nm, 100 mW, [Fe] = 5 mM. Red: λ_{ex} = 514.5 nm, 100 mW, [Fe] = 8 mM. All spectra were collected from liquid solutions maintained at -8 °C. Asterisks denote features arising from CAN. The intensity of the MeCN solvent peak at 922 cm^{-1} was used to normalize the intensities of the peaks among the various spectra.
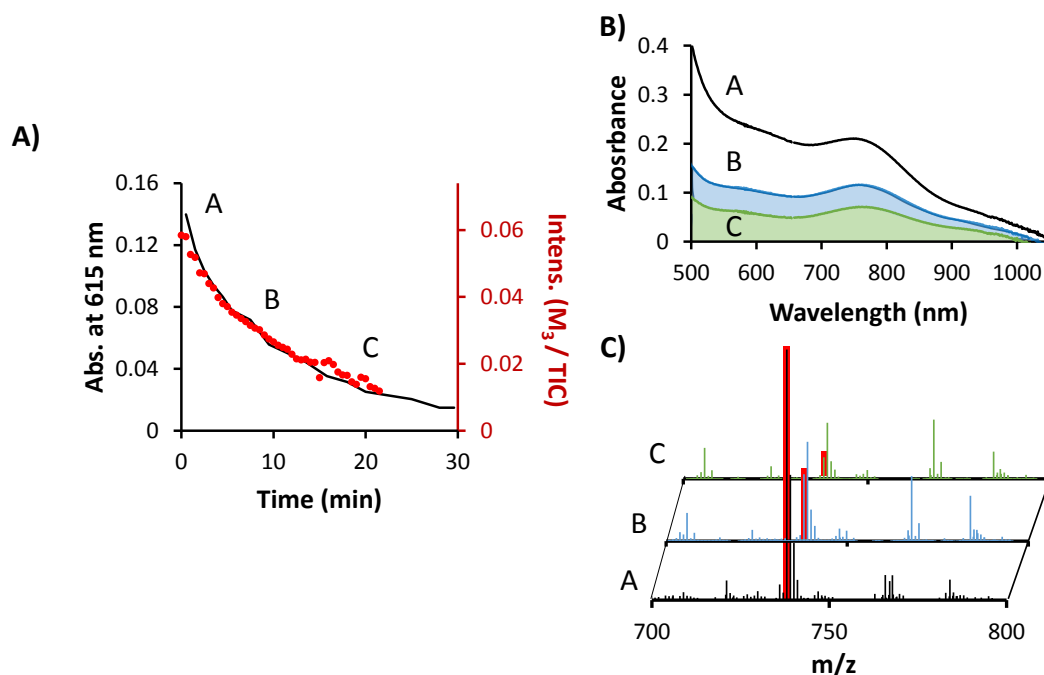
Figure VII.20 A) Time course for the decay of the 615-nm chromophore (line, left axis) and the **M₁** MS peak intensity (dots, right axis) during the reaction of **1αFe** (1 mM) with CAN (75 mM) at 25 ℃. B & C) Mass (**M₁** highlighted in red) and visible spectra observed at 10 s (A), 10 min (B) and 20 min (C) after the addition of CAN (75 eq) to **1αFe** (1 mM in Milli-Q water, 25℃).

More detailed insight into the nature of **Iα** was obtained by rRaman (**Figure VII.19**, right). The excess of CAN exhibit two signals at 822 and 677 cm^{-1}. The first signal was assigned to a Fe=O vibration. Since the energy of this feature is the same as in **Fe$_\alpha$^{IV}=O** it was considered if this could be arising from residual amounts of this compound. However, titration experiments by UV-Vis (**Figure VII.18, right**) indicated than less than 15% **Fe$_\alpha$^{IV}=O** remained in solution under these conditions, suggesting that the feature mainly arises from a Fe=O unit in **Iα**. The second feature, located at 677 cm^{-1} had similar intensity and was indicative of a weaker Fe-O bond. Using H$_2$^{18}O the peak downshifted to 643cm^{-1}. However it was not affected by D$_2$O, as would be expected for the previously postulated **O=Fe^{IV}-(OH)-Ce^{IV}** species (**Figure VII.16 B**, see **Chapter V**). The possibility that the low energy vibrational feature could be indicative of a diamond core Fe^{IV}(μ-O)$_2$Ce^{IV} was ruled out by using a H$_2$^{16}O:H$_2$^{18}O solvent mixture. Under these conditions, two peaks with relative 1:1 intensity and not three with relative intensity 1:2:1 were observed (the intermediate frequency arises from a mixed-labeled core that is statistically the most abundant). Altogether, the data obtained by CSI-HRMS and rR lead as to favor an **O=Fe^{IV}-O-Ce^{IV}** core for **Iα**.

The observed role of Ce^{IV}, not behaving as a simpler outer sphere oxidant, introduces unconsidered mechanisms for the water oxidation catalyzed by Fe. The interaction between both

metals may explain the contrasting reactivities found between **1αFe** and **1βFe**, which in fact are different in their electronic (ligands in *trans* to the *cis*-labile sites are different and can directly affect the stability of high-valent intermediates or even the dimerization) and steric properties (different topology).

At this point, the evolution of the mechanism from **Iα** still remains unclear. C-H and C=C oxidations with Ce^{IV} as oxidant[38] and UV-Vis experiments with $Ce^{III/IV}$ mixtures (**Chapter V**) suggest that $[Fe^{V}(O)(\mu\text{-}O)Ce^{III}]$, formed by the intramolecular electron transfer from Ce^{IV} to Fe^{IV}, and not $[Fe^{IV}(O)(\mu\text{-}O)Ce^{IV}]$ species is involved in the WO reaction mechanism as the active species. Subsequently, $[Fe^{V}(O)(\mu\text{-}O)Ce^{III}]$ can hydrolyze to $[Fe^{V}(O)(OH)]$ species which finally carry out the water oxidation reaction in analogy to the mechanism early proposed,[38] or Ce^{III} may help in the water oxidation by approximating the water molecule to the $Fe^{V}=O$ in a Lewis-acid assisted acid base mechanism (**Scheme VII.2**).
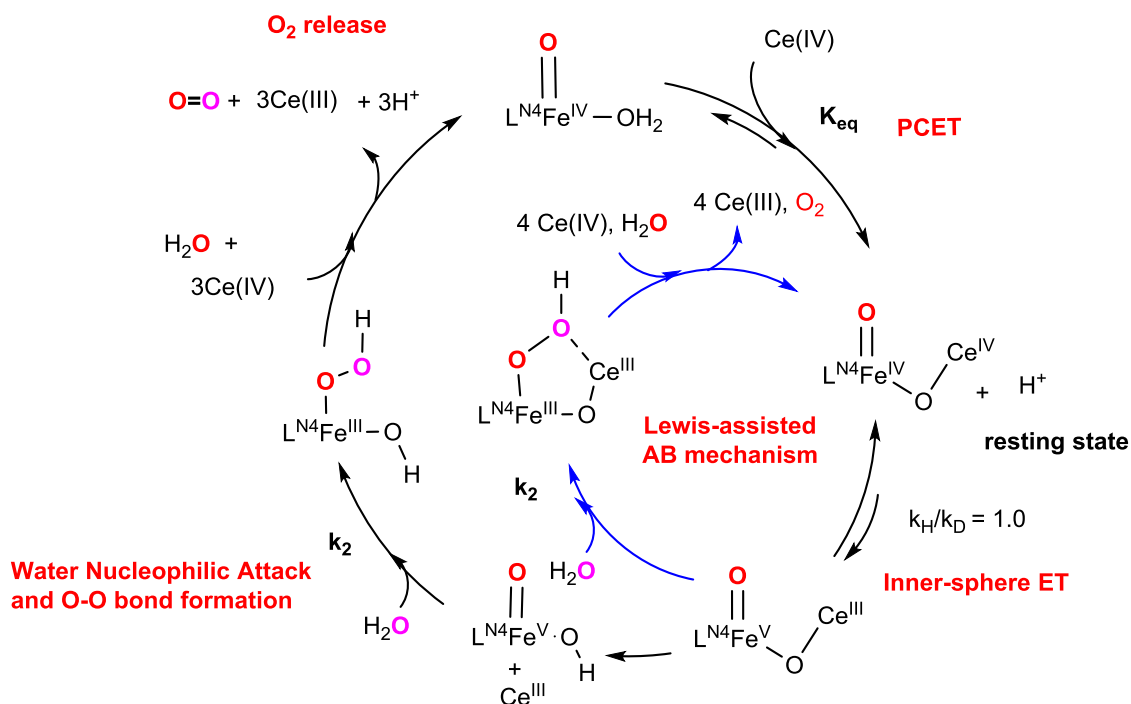
Scheme VII.2. Mechanistic proposals for the iron catalyzed Ce^{IV}-driven water oxidation. The inner cycle (in blue) describes the Lewis-assisted acid base mechanism. The external cycle describes the acid base mechanism through $Fe^{V}(O)(OH)$, on which Ce^{III} is liberated after the inner electron transfer reaction (black). Theoretically, the OH ligand could assist the water oxidation.

The $[Fe^{V}(O)(\mu\text{-}O)Ce^{III}]$ active species proposed resembles the S_4-state (Kok cycle) of the oxygen evolving complex proposed in some mechanistic models as $Mn^{V}(O)(\mu\text{-}O)Ca^{II}(OH_2)$.

Interestingly, Jian-Ren Shen and coworkers found that Ca^{2+} could be substituted by Sr^{2+} in PSII from *Thermosynechococcus vulcanu* retaining half of the TOF. This decrease was probably due to an elongation between the terminal H_2O (substrate) and the Sc^{2+}.[42]

The strong similarities between biological reactivity of iron and manganese, the resemblance to the fundamental $Mn^V(O)(\mu\text{-O})Ca(OH_2)$ structural motif of the OEC (**Figure VII.21**), and its reactivity for the water oxidation makes $Fe^{IV}(O)(\mu\text{-O})Ce^{IV}$ a model compound to study the formation of the O-O bond in detail.
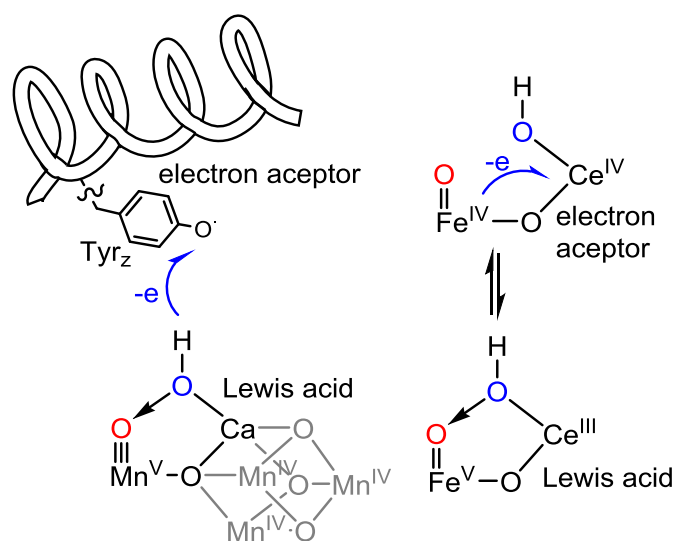
Figure VII.21. Parallels between the OEC and the iron–cerium complex.

VII.5. Catalyst improvements arising from mechanistic studies

VII.5.1 Enhancing the water oxidation activity of iron catalysts by identification and modification of structural weaknesses

Decomposition paths of iron complexes under water oxidation conditions are studied. Identification of decay paths allows rational design of more robust, long living catalysts, which yield the largest TON of O_2 production for any first row transition metal.

Oxo-iron species α-$[Fe^{IV}(O)(H_2O)(mcp)]^{2+}$, (**$Fe_\alpha^{IV}$=O**, 1mM, pH = 1, 25°C) generated by oxidizing **1αFe** with CAN (3 eq.) is unstable, as proven by UV-Vis spectroscopy (λ = 769 nm, ε = 270 $M^{-1}cm^{-1}$, $t_{1/2}$ = 0.15 h, **Figure VII.22**). Any traces of O_2, CO_2 (in the gas phase, measured by GC-TCD and manometry) or H_2O_2 (in solution, titration by peroxotitanyl method)[43] were detected as byproducts of the fast fading of the Fe^{IV}=O chromophore. Hence the water

nucleophilic attack or the O-O bond formation by interaction of two units of $Fe^{IV}=O$ were discarded. Instead, single-electron reduced species such as mononuclear Fe^{III} species or typical oxo-bridged diferric dimers, together with partial ligand fragmentation, were observed by CSI-HRMS (**Figure VII.22C**).
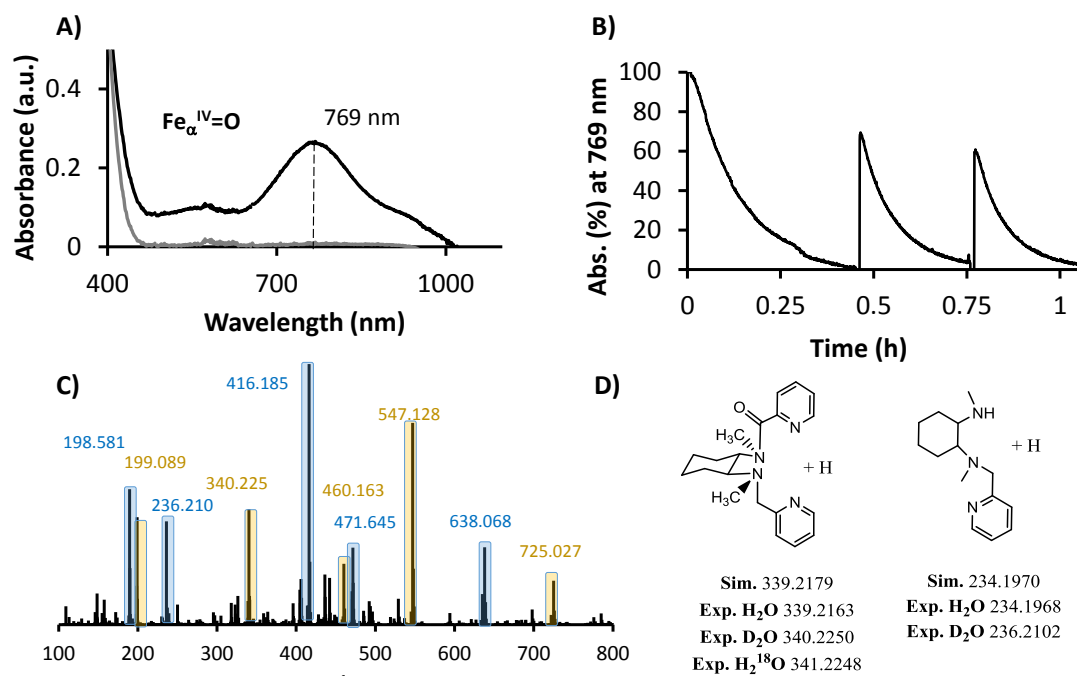
Figure VII.22. A) Formation of $Fe_\alpha^{IV}=O$ from **1αFe** (1mM) by the addition of 3 eq. of CAN in HOTf (final pH = 1, 25°C) and B) recyclability of the $Fe^{IV}=O$ chromophore (monitored at 769 nm) by the addition of 1 eq. of CAN (x 3 times). C) CSI-HRMS recorded 1.5 hour after of the addition of CAN (3 eq., 50 μL) to **1αFe** (4.5 mM, 0.5 mL) in D_2O. D) Ligand fragmentation observed by CSI-HRMS.

Indeed, after its full decay (ca. 0.4 h, judged by UV-Vis, **Figure VII.22B**), $Fe_\alpha^{IV}=O$ could be recovered up to 70% by adding just one equivalent of CAN. The non-complete restoration of the initial intensity of the $Fe^{IV}=O$ chromophore could be due to a lack of redox potential (on the second addition of CAN, 2 eq Ce^{III} remains in solution), a partial irreversible decomposition of the complexes, in agreement with the fragments observed by CSI-HRMS, or even to the partial hydrolysis. After one day in solution, recovery of $Fe_\alpha^{IV}=O$ by further addition of CAN was no longer possible and hydrolytic ligand dissociation became obvious in the mass spectrum. Quantification of the ligand extracted by ^{1}H-NMR (addition of NH_3 to a depletion 3mM of $Fe_\alpha^{IV}=O$ and extraction in $CDCl_3$) indicated that 80% of the ligand remains intact. Therefore the redox limitation and hydrolysis (in short terms) have a minor effects. In agreement, under excess of Ce^{IV} (75 equiv), ligand oxidative degradation becomes more important and only 50% of the entire ligand was recovered at the end of the reaction.

Trying to avoid the self-degradation and improve the catalyst activity we glimpsed two possible alternatives. The first one is based on supporting the complex and catalyze the water oxidation heterogeneously. In fact, this was reported by Klepser and Barlett.[44] These authors anchored **1Fe** containing 4-PO$_3$Et$_2$ substituted pyridines to a WO$_3$ photoanode with the aim to remove the sacrificial oxidants and carry out the water oxidation under photochemical conditions. The thin-film deposited on WO$_3$ showed an improved photochemical performance of 60% when compared to the non-modified anode. However the nature of the catalytic species remains unclear.

The second option was the detection of the structural weaknesses and the subsequent modification of the complex structure to avoid the most exposed sites.

Towards the second option, a deep analysis of the ligand fragments observed by CSI-HRMS spectrum after reaction of the catalyst with few equivalents (3-6 eq) of CAN was useful to identify the sites where oxidative degradation of the ligand takes place more easily. The most intense peaks in the CSI-HRMS analysis (4.5 mM of **Fe$_\alpha^{IV}$=O** in D$_2$O) corresponded to [C$_{20}$H$_{26}$N$_4$O]+D$^+$ and [C$_{14}$H$_{22}$N$_3$D]+D$^+$ (236.2102 and 340.2250 m/z). By labeling experiments, these peaks have been found to belong to the oxidative breakage of a pyridylmethyl arm through the benzylic methylene site (**Figure VII.22**).

Considering that oxidative degradation at this site most likely reflects an initial C-H oxidation, its deuteration is considered as a simple strategy to improve the stability of the catalysts without modifying the topology or the electronic effects, parameters which can drastically effect in the water oxidation (**Chapter V, VI**). Indeed, a simple deuteration of the pseudo-benzylic CH$_2$ sites was found to strengthen the complex relevantly. Half-life time of the deuterated compound (**1Fe^{IV}=O-D$_4$**) was enhanced 18-fold, from 0.15 h to 2.8 h. The WO was consequently affected by this slight modification of the ligand, as the lifetime of the catalysts is improved. While TOF$_{max}$ remained almost equal for both compounds, demonstrating that no change in the reaction mechanism takes place through this modification, TON was enhanced to~1000 TON because of the longer lifetime of the catalyst. These experiments demonstrate that methylene groups are a susceptible weakness on the ligand structure, and the protection of this methylene sites with another oxidatively more robust groups (for example F or CH$_3$) may be crucial to further increase the WO activity.

Table VII.3. Water oxidation catalytic activities for 1Fe and 1FeD$_4$

Catalyst	Detection technique	TON O$_2$[a]	TOF (h^{-1}) [b]	TON CO$_2$[a]
1Fe	manometry	360 ± 20	0.28 ± 0.02	-
1Fe-D$_4$		929 ± 48	0.24 ± 0.02	
1Fe	GC-TCD	380 ± 20	-	0.4 ± 0.2
1Fe-D$_4$		1049 ± 54		0.3 ± 0.3

Reactions performed in Milli-Q water at 25 ºC. The catalyst (0.5 mL, 250 μM, final concentration 12.5 μM) was injected through a septum into the reaction vessel containing CAN aqueous solution, (9.5 mL, 131 mM). The initial pH value was 0.8. [a] TON (turnover number) = (n(gas) produced / n(catalyst)) obtained by manometry after 3 h of reaction. [b] TOF (TON·h^{-1}) measured 5 min after the addition of the catalyst.

VII.5.2 A new *N*-pentadentate iron (II) complex as an active homogeneous catalyst for water oxidation

Based on kinetic and theoretical studies we proposed that the intermediates responsible for the O-O bond formation in iron complexes based on neutral tetradentate ligands (L^{N4}) with two *cis*-labile sites are high valent oxo-iron species such as [L^{N4}Fe^V(O)(OH)]$^{2+}$ (L^{N4} = ^{Me2}Pytacn, mcp, men, tpa and pdp), while species in the oxidation state (IV) are resting during the catalyzed reaction.

In contrast to the iron complexes with L^{N4} ligands, iron complexes with stronger chelating ligands such as neutral pentadentate nitrogen (L^{N5}) are not active in WO, under the same catalytic conditions. These differences in reactivity have been attributed to the impossibility of the later complexes to stabilize the oxidation state V at the metal center.[27] This can be rationalized by considering the number of accessible labile coordination sites that can led to a proton-electron-transfer processes. One oxo group can stabilize the [L^{N5}Fe^V=O]$^{3+}$ while an oxo and hydroxy groups (3 negative charges) form the [L^{N4}Fe^V(O)(OH)]$^{2+}$ WO active species.[27]

With this consideration in mind we designed a new iron complex with a pentadentate anionic ligand, to surpass the inactivity towards WO of the reported [L^{N5}Fe^V=O] complexes (**Figure VII.23**).

10Fe

[Fe^{III}(dpaq)(H$_2$O)]$^{2+}$

11Fe

[Fe^{II}(OTf)(AQ^{Me2}tacn)]

L = solvent ligand
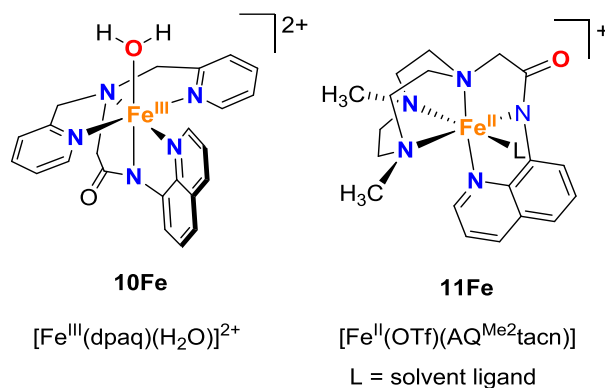
Figure VII.23. Iron complexes based on *N*-(quinolin-8-yl)acetamidyl fragment. Left) iron(III) complex [Fe^{III}(dpaq)(H$_2$O)]$^{2+}$ reported by Kodera *et al*. Right) New iron(II) complex based on the tacn moiety. L stands for a solvent molecule.

We get inspired by the dpaq ligand that Kodera and coworkers recently reported (**Figure VII.23. 10Fe**).[45] This ligand is formally a derivate of the well-known tpa ligand (ligand of **5Fe**)

where one of the pyridine arms has been replaced by a N-(quinolin-8-yl)acetamidyl (AQ) anionic fragment. Remarkably, the derived iron(III) metal complex was found very active and selective in C-H oxidation which is usually taken as a sign of that the ligand can stabilize high oxidation states. On the other hand, iron (II) amidate complexes are very rare although interesting since they can serve as mimics of Bleomycin.[46] In this line, we synthesized the 1-(N-(quinolin-8-yl)acetamidyl)-4,7-dimethyl-1,4,7-triazacyclononane (HAQ^{Me2}tacn) ligand by introducing the N-(quinolin-8-yl)acetamidyl fragment into the highly basic dimethyl-triazacyclononate (^{Me2}tacn) structure. (**Figure VII.23. 11Fe**).

The reaction of the deprotonated ligand, by using one equivalent of NaH, with an stoichiometric amount of Fe^{II}(OTf)$_2$(CH$_3$CN)$_2$ in THF gives a deep red solution corresponding to the [Fe^{II}(AQ^{Me2}tacn)](OTf) complex (**11Fe**). As expected, the deep-red microcrystalline iron compound turned immediately pale green when exposed to air. The ^{1}H-NMR in CD$_3$OD of **11Fe** shows paramagnetic peaks in the 20-190 ppm range, in agreement with the formation of a Fe^{II} S = 1 complex (**Figure VII.24 B**). The high resolution mass spectrometry (CSI-HRMS at 25ºC) analysis in degassed H$_2$O presents mainly the [Fe^{II}(AQ^{Me2}tacn)]$^+$ ion (calc. for C$_{19}$H$_{26}$FeN$_5$O 396.1487 m/z, found 396.1496 m/z) (**Figure VII.24 A**). X-ray diffraction analysis of a mono-crystal shows an octahedral distorted complex with the five nitrogen atoms of the AQ^{Me2}tacn ligand bonded to the iron(II) center. The coordination sphere is completed by an amidate oxygen atom belonging from an adjacent iron complex forming a polymeric structure in solid state (**Figure VII.25**). Bond distances between the N atoms of the AQ anionic fragment and the Fe center are significantly shorter than the found for the aliphatic nitrogens (Fe-Namidate ~ 2.1 Å vs Fe-Ntacn ~2.2-2.3 Å). A closer look to the structure reveals an unexpected short distance for the Fe1-O1 (2.157 (4) Å) and similar for N1-C1 and C1-O1 distances (1.309(6) Å and 1.271(6) Å, respectively) suggesting an important charge delocalization though the N1-C1-O1 moiety (**Figure VII.25**).
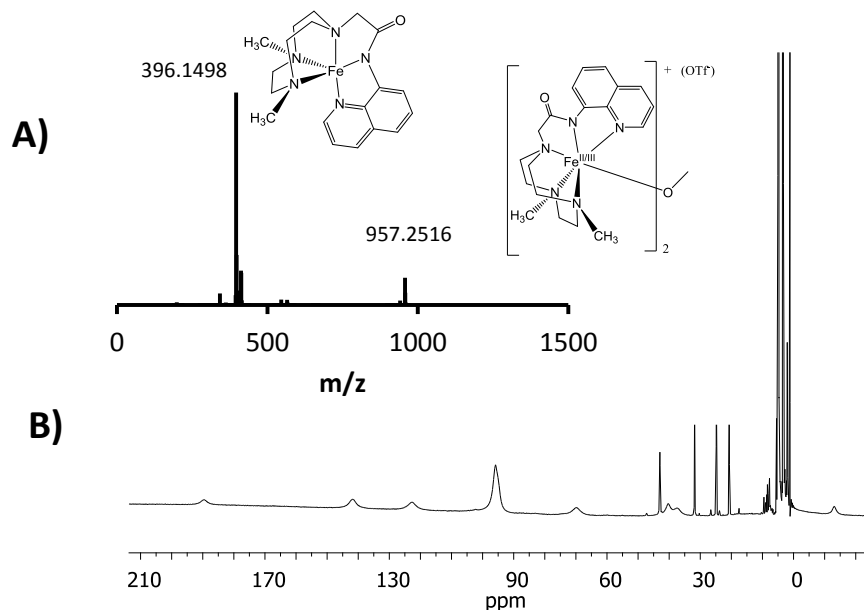
Figure VII.24. A) CSI-HRMS (298K) of complex **11Fe** (1mM) dissolved in 2 mL of degassed MilliQ water. B) Paramagnetic ^{1}H-NMR (400 MHz) of complex **11Fe** (6mg in 0.5 mL CD$_3$OD).
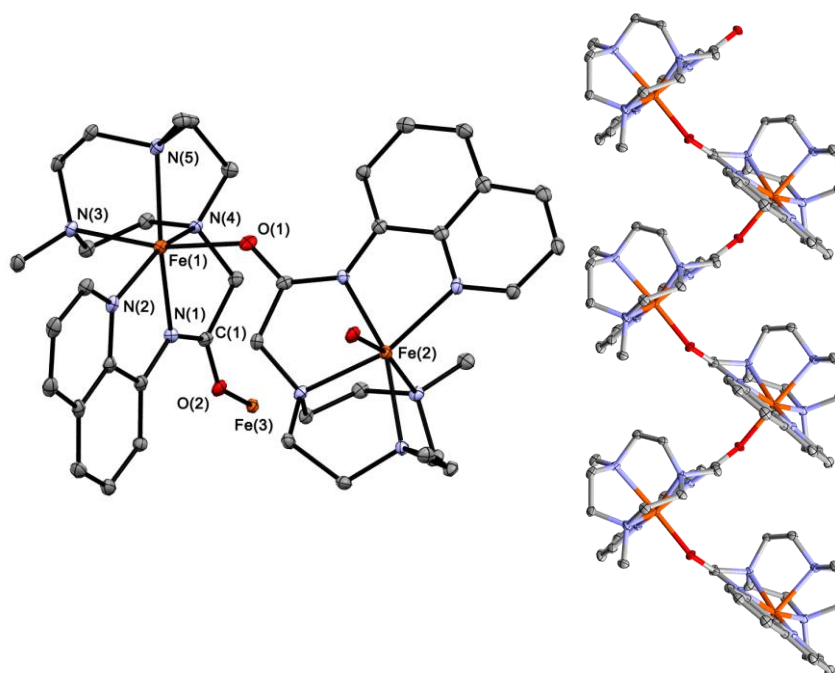
Figure VII.25. Left) Ortep structure with ellipsoids set at the 50% probability level of (1)2 from the X-ray diffraction analysis. Hydrogen atoms have been omitted for clarity. Relevant distances (Å) and bond angles (°) for 1: Fe(1)−N(1), 2.102(4); Fe(1)−N(2), 2.173(4); Fe(1)−N(3), 2.301(4); Fe(1)−N(4), 2.182(4); Fe(1)−N(6), 2.124(5); Fe(1)−O(1), 2.157(4); C(1)−N(1), 1.309(6); C(1)−O(1), 1.271(6); N(1)-Fe(1)-N(6), 76.92(17); N(1)-Fe(1)-O(1), 96.48(16); N(6)-Fe(1)-O(1), 99.96(15); N(6)-Fe(1)-N(2), 151.79(16); N(1)-Fe(1)-N(4), 158.59(15); O(1)-Fe(1)-N(3), 167.43(14). Right) Illustration of the polymeric nature of complex 1 in solid state.

The catalytic WO ability of complex **11Fe** was studied evaluating the O_2 formation when exposing to a chemical oxidant such as CAN or $NaIO_4$. Reactions were performed by dissolving the iron complex in water and immediately injected into a solution containing the oxidant. The total amount of gas produced was monitored by manometry until raising a plateau. Likewise, the time dependence formation of O_2 and CO_2 was monitored and quantified by gas chromatography (GC-TCD) and mass spectrometry by means of gas sampling from the reaction headspace. Excellent agreement between the manometry and GC-TCD analysis showed that the O_2 formation is higher in the case of using low catalyst concentration and $NaIO_4$ as oxidant, but always with very low amounts of CO_2 (**Figure VII.26 and Table VII.4**). It is important to notice that no induction time in the O_2 detection nor generation of CO_2 was observed. Indeed, this suggests that the WO occur in homogeneous phase (**Figures VII.26-27**).

As previously reported, the use of $NaIO_4$ (milder oxidant) produce an increase of the TON[39] by 5-fold but unexpectedly we also observed a TOF growth by more than 3-fold (**Table VII.4.**). To rationalize this observation we should take into account the experimental conditions imposed by the oxidant (pH 1 and 4.5 for CAN and $NaIO_4$, respectively). The TON and TOF values at different pH when using $NaIO_4$ as oxidant indicates pH 3 as the optimal value. At pH 1, similar TON and TOF were recorded for both CAN (2.8, 6.8 h^{-1}) and $NaIO_4$, (4.7, 8.5 h^{-1}), pointing that hydrolysis could be a major deactivation pathway. The addition of base did not benefit the oxygen production.
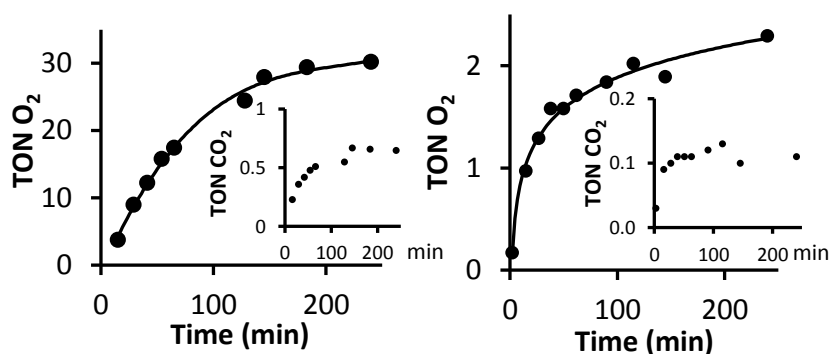
Figure VII.26. O_2 and CO_2 on-line monitoring by GC-TCD during the reaction of **11Fe** (0.1 mM) with left) $NaIO_4$ (250 mM) and right) CAN (125 mM)

Table VII.4. WO catalytic activities found for the anionic complex **11Fe**.

Oxidant	[Cat] (μM)	TON O$_2$[c]	TOF O$_2$[d]	TON O$_2$[e]	TON CO$_2$[e]
CAN[a]	50	2.8 ±0.1	8 ±1	2.4 ±0.3	0.3 ±0.1
	100	2.2 ±0.1	7 ±2	2.0 ±0.2	0.2 ±0.0
NaIO$_4$[b] pH=4.5	**12.5**	**76 ±4**	**40 ±5**	**77 ±4**	1.6 ±0.2
	50	40 ±2	25 ±3	42 ±1	0.9 ±0.1
	100	28 ±2	18 ±2	27 ±1	0.9 ±0.1

Reactions performed in Milli-Q water at 25 ºC. Values from the average of 3 experiments [a] CAN aq. solution (9.5 mL, 125 mM), initial pH = 0.8. [b] NaIO$_4$ aq. solution (9.5 mL, 250 mM), initial pH = 4.5. [c] TON (turnover number) = (n(O$_2$) produced / n(catalyst)) measured by manometry. [d] TOF (TON·h^{-1}) measured after 5 min of the catalyst addition. [e] Values measured by GC-TCD at the end of the reaction.

Titration experiments of **11Fe** with Ce^{IV} shows that after addition of 1eq equivalent of CAN a new band in the UV-Vis at 670 nm (ε = 600 M^{-1}cm^{-1}, **Figure 27A**) and new prominent peaks in the CSI-HRMS corresponding to [Fe^{III}(AQ^{Me2}tacn)(OH)]$^+$ (calc. for C$_{19}$H$_{27}$FeN$_5$O$_2$ 413.1514 m/z, found 413.1520 m/z) appears. CSI-HRMS recorded immediately after the addition of 5 eq. of CAN to **11Fe**, shows a dominant peak corresponding to the [Fe^{IV}(AQ^{Me2}tacn)(O)]$^+$ intermediate (calc. for C$_{19}$H$_{26}$FeN$_5$O 412.1436 m/z, found 412.1445 m/z) (**Figure 27B**). Small amounts of free ligand were also observed, but no trace of Fe^{II} peaks were recorded in these conditions. The addition of 1 eq of NaIO$_4$ (0.5mM) was enough to detect the same peak at 412 m/z, related to a **11Fe^{IV}=O** intermediate, may indicating a relationship with the active specie during WO (**Figure 27C**). This species was clearly dominant upon addition of excess of oxidant (20 eq., **Figure 27D**) and this time almost no free ligand was detected, suggesting that the amidate is coordinated during the catalysis. Therefore, amidate-based pentadentate iron complexes are able to carry out the oxidation of water.
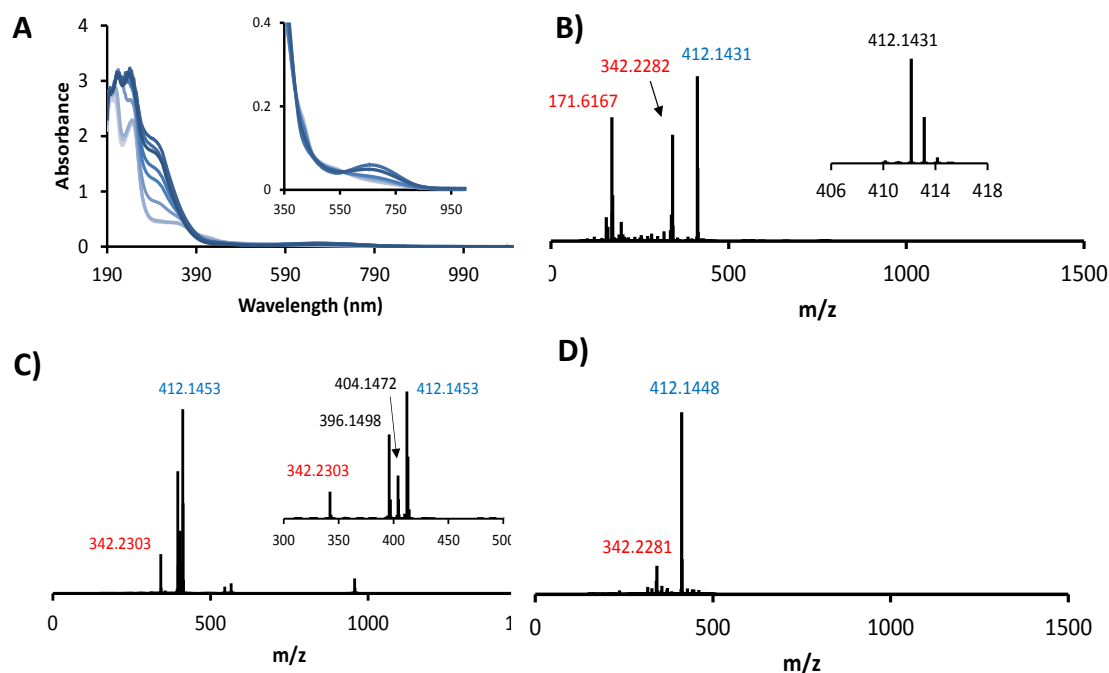
Figure VII.27. A) Evolution of the UV-Vis spectrum of complex **11Fe** (0.1mM in water) after the addition of CAN (0.1mM, 1 eq). Inset, magnification of the 350-1000 nm region. **B**) CSI-HRMS spectrum after the addition of 5 eq of CAN to **11Fe** (1mM, degassed MilliQ H_2O). **C**) CSI-HRMS spectrum after the addition of 1 eq of $NaIO_4$ to **11Fe** (1mM, degassed MilliQ H_2O). **D**) CSI-HRMS spectrum after the addition of 20 eq of $NaIO_4$ to **11Fe** (0.5mM, degassed MilliQ H_2O).

To shed some light on the potential catalytic species we calculate the DFT-redox potentials at B3LYP/6-31G*//cc-pVTZ level including dispersion, solvent and spin contamination corrections. Oxidation of **11Fe** by 1e⁻ ($E^{II/III}$ = 0.26 V vs SHE) was found to be more favorable than a PCET process (0.35 V at pH = 3). Subsequent 1e⁻ oxidation could yield $[Fe^{IV}(AQ^{Me2}tacn)(OH_2)]^{3+}$ ($E^{III/IV}$ = 1.36 V) or via PCET process $[Fe^{IV}(AQ^{Me2}tacn)(OH)]^{2+}$ (1.2 V at pH 3). Under catalytic conditions further deprotonation of $[Fe^{IV}(AQ^{Me2}tacn)(OH)]^{2+}$ could take place to form $[Fe^{IV}(AQ^{Me2}tacn)(O)]^{+}$. More interestingly, further oxidation to give $[Fe^{V}(AQ^{Me2}tacn)(O)]^{2+}$ is less favorable than the ligand oxidation to form $[Fe^{IV}(AQ^{Me2}tacn)^{\bullet}(O)]^{2+}$ ($E^{IV/IV\bullet}$ = 1.24 V), in which the spin density shows a **Fe^{IV}=O** complex with the AQ⁻ fragment oxidized by one electron to AQ⁻. The radical is mainly centered at amidate but also delocalized in the aromatic system (**Figure VII.28**). This behavior resembles to the Fe^{IV}=O porphyrin radical cation (compound I) of the P450.[47] Further oxidation of the systems seems unviable judged by the calculated redox ($E^{IV\bullet/V\bullet}$ = 2.16V). In turn, these results suggest that $[Fe^{IV}(AQ^{Me2}tacn)^{\bullet}(O)]^{2+}$ is the species with higher oxidation state that can be formed when a large excess of CAN or $NaIO_4$ is present in solution.
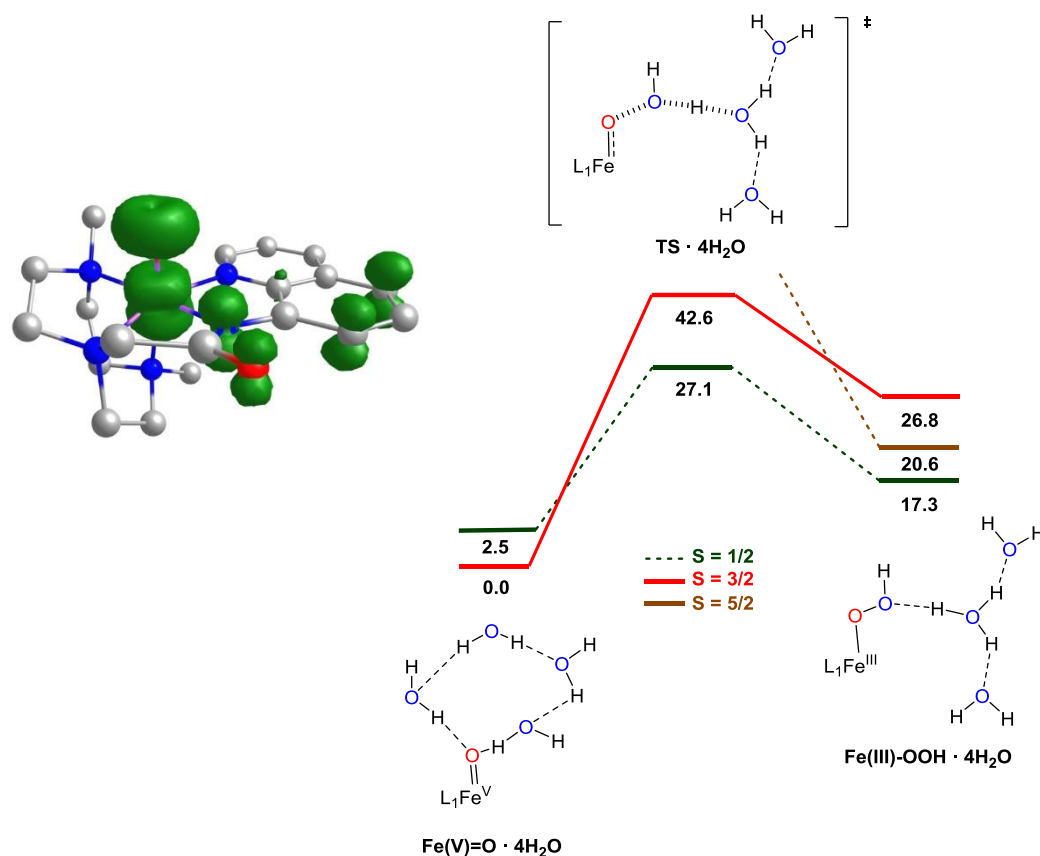
Figure VII.28. Left) Illustration of the spin density of complex [Fe^{IV}(AQ^{Me2}tacn)·(O)]$^{+2}$. Right) O-O bond formation free energy profiles found for [Fe^{IV}(AQtacn)·(O)]$^{2+}$ in the S = 1/2, 3/2 and 5/2 spin states. Gibbs energy values are given in kcal·mol^{-1}.

The computed AB mechanism for complex [Fe^{IV}(AQ^{Me2}tacn)·(O)]$^{2+}$ gives a Gibbs energy barrier of 23.0 kcal·mol^{-1} (**Figure VII.28**). This energy value is higher by 4.1 kcal·mol^{-1} than the reported for [Fe^V(^{Me2}Pytacn)(O)(OH)]$^{2+}$ intermediate (**3Fe^V=O**, $\Delta G^{\neq}$ = 18.9 kcal·mol^{-1}) and then consistent with their differences in initial TOF values (8-40 h^{-1} and 222 h^{-1} respectively).[27,48] On the other hand, the presence of an internal base in [Fe^V(^{Me2}Pytacn)(O)(OH)]$^{2+}$ (the OH ligand) produce a reduction of the Gibbs energy barrier by 7.4 kcal·mol^{-1} when the AB mechanism is assisted by the hydroxyl ligand.[27,48] Intents to model an internal base assisted AB mechanism assisted by the amidate group bonded to the iron center as an internal base produced in all the cases higher energetic pathways.

In summary, complex **11Fe** is the first reported non-heme iron pentacoordinate complex active for thermal WO. The negative charge and non-redox nature of the pentadentate amidate ligand may be key to reduce the redox potential to form the active WO species and should be considered in future iron catalyst design for water oxidation. This results open the door for the quest of more robust WOC based in iron based on anionic pentadentate ligands.

The lack of induction time and apparent absence of CO_2 at the begging of the reaction suggest that the catalytic species are molecular. DFT studies indicates that $[Fe^{IV}(AQ^{Me2}tacn)^{\bullet}(O)]^{2+}$ rather than $[Fe^{V}(AQ^{Me2}tacn)(O)]^{2+}$ is the active catalytic species. Computational modelling of the O-O bond formation supports the external AB mechanism through the **11Fe^{IV}=O$^{\bullet}$** intermediate. Regarding that the Fe^{II} amidate complex **11Fe** is a rare iron complex and can be seen as a model for the anti-cancer drug Bleomycin, further studies will be carried out in our group.

VII.6. References

1   Junge, H., Marquet, N., Kammer, A., Denurra, S., Bauer, M., Wohlrab, S., Gärtner, F. *et al. Chem. Eur. J* **2012,** 18, 12749-12758

2   Zuccaccia, C., Bellachioma, G., Bortolini, O., Bucci, A., Savini, A. , Macchioni, A. *Chem. Eur. J.* **2014,** 20, 3446-3456

3   Grotjahn, D. B., Brown, D. B., Martin, J. K., Marelius, D. C., Abadjian, M.-C., Tran, H. N., Kalyuzhny, G. *et al. J. Am. Chem. Soc.* **2011,** 133, 19024-19027

4   Parent, A. R., Crabtree, R. H. , Brudvig, G. W. *Chem. Soc. Rev.* **2013,** 42, 2247-2252

5   Duan, L., Bozoglian, F., Mandal, S., Stewart, B., Privalov, T., Llobet, A. , Sun, L. *Nat Chem* **2012,** 4, 418-423

6   Betley, T. A., Surendranath, Y., Childress, M. V., Alliger, G. E., Fu, R., Cummins, C. C. , Nocera, D. G. *Phil. Trans. R. Soc. B* **2008,** 363, 1293-1303

7   Savini, A., Bellachioma, G., Bolaño, S., Rocchigiani, L., Zuccaccia, C., Zuccaccia, D. , Macchioni, A. *ChemSusChem* **2012,** 5, 1415-1419

8   Savini, A., Belanzoni, P., Bellachioma, G., Zuccaccia, C., Zuccaccia, D. , Macchioni, A. *Green Chem.* **2011,** 13, 3360-3374

9   Zuccaccia, C., Bellachioma, G., Bolaño, S., Rocchigiani, L., Savini, A. , Macchioni, A. *Eur. J. Inorg. Chem.* **2012,** 2012, 1462-1468

10   Hintermair, U., Sheehan, S. W., Parent, A. R., Ess, D. H., Richens, D. T., Vaccaro, P. H., Brudvig, G. W. *et al. J. Am. Chem. Soc.* **2013,** 135, 10837-10851

11   Hong, D., Murakami, M., Yamada, Y. , Fukuzumi, S. *Energy Environ. Sci.* **2012,** 5, 5708-5716

12   Hintermair, U., Hashmi, S. M., Elimelech, M. , Crabtree, R. H. *J. Am. Chem. Soc.* **2012,** 134, 9785-9795

13   Yin, Q., Tan, J. M., Besson, C., Geletii, Y. V., Musaev, D. G., Kuznetsov, A. E., Luo, Z. *et al. Science* **2010,** 328, 342-345

14   Company, A., Prat, I., Frisch, J. R., Mas-Ballesté, D. R., Güell, M., Juhász, G., Ribas, X. *et al. Chem. Eur. J* **2011,** 17, 1622-1634

15   Garcia-Bosch, I., Company, A., Fontrodona, X., Ribas, X. , Costas, M. *Org. Lett.* **2008,** 10, 2095-2098

16   Company, A., Gómez, L., Güell, M., Ribas, X., Luis, J. M., Que, L. , Costas, M. *J. Am. Chem. Soc.* **2007,** 129, 15766-15767

17   Kim, C., Chen, K., Kim, J. , Que, L. *J. Am. Chem. Soc.* **1997,** 119, 5964-5965

18   Costas, M. , Que, J. L. *Angew. Chem. Int. Ed.* **2002,** 41, 2179-2181

19   Chen, K. , Que, J. L. *Angew. Chem. Int. Ed.* **1999,** 38, 2227-2229

20   White, M. C., Doyle, A. G. , Jacobsen, E. N. *J. Am. Chem. Soc.* **2001,** 123, 7194-7195

21   Company, A., Gómez, L., Fontrodona, X., Ribas, X. , Costas, M. *Chem. Eur. J* **2008,** 14, 5727-5731

22   Chen, K., Costas, M. , Que, J. L. *J. Chem. Soc., Dalton Trans.* **2002,** 672-679

23   Cussó, O., Garcia-Bosch, I., Ribas, X., Lloret-Fillol, J. , Costas, M. *J. Am. Chem. Soc.* **2013,** 135, 14871-14878

24   Hong, D., Mandal, S., Yamada, Y., Lee, Y.-M., Nam, W., Llobet, A. , Fukuzumi, S. *Inorg. Chem.* **2013,** 52, 9522-9531

25   Zhang, B., Li, F., Yu, F., Cui, H., Zhou, X., Li, H., Wang, Y. *et al. Asian J. Chem.* **2014,** DOI: 10.1002/asia.201400066

26   Hoffert, W. A., Mock, M. T., Appel, A. M. , Yang, J. Y. *Eur. J. Inorg. Chem.* **2013,** 2013, 3846-3857

27   Acuña-Parés, F., Codolà, Z., Costas, M., Luis, J. M. , Lloret-Fillol, J. *Chem. Eur. J.* **2014,** 20, 5696-5707

28   Chen, G., Chen, L., Ng, S.-M., Man, W.-L. , Lau, T.-C. *Angew. Chem. Int. Ed.* **2013,** 52, 1789-1791

29   Fukuzumi, S., Morimoto, Y., Kotani, H., Naumov, P., Lee, Y.-M. , Nam, W. *Nat Chem* **2010,** 2, 756-759

30   Morimoto, Y., Kotani, H., Park, J., Lee, Y.-M., Nam, W. , Fukuzumi, S. *J. Am. Chem. Soc.* **2010,** 133, 403-405

31   Kim, K. , Lippard, S. J. *J. Am. Chem. Soc.* **1996,** 118, 4914-4915

32   Yoshida, M., Masaoka, S., Abe, J. , Sakai, K. *Chem. Asian J.* **2010,** 5, 2369-2378

33   McDonald, A. R. , Que Jr, L. *Coord. Chem. Rev.* **2013,** 257, 414-428

34   Company, A., Feng, Y., Güell, M., Ribas, X., Luis, J. M., Que, L., Jr. , Costas, M. *Chem. Eur. J.* **2009,** 15, 3359-3362

35   Prat, I., Mathieson, J. S., Güell, M., Ribas, X., Luis, J. M., Cronin, L. , Costas, M. *Nat. Chem.* **2011,** 3, 788 - 793

36   Bassan, A., Blomberg, M. R. A., Siegbahn, P. E. M. , Que, L., Jr. *J. Am. Chem. Soc.* **2002,** 124, 11056-11063

37   Quinonero, D., Morokuma, K., Musaev, D. G., Mas-Balleste, R. , Que, L., Jr. *J. Am. Chem. Soc.* **2005,** 127, 6548-6549

38   Garcia-Bosch, I., Codolà, Z., Prat, I., Ribas, X., Lloret-Fillol, J. , Costas, M. *Chem. Eur. J* **2012,** 18, 13269-13273

39   Fillol, J. L., Codolà, Z., Garcia-Bosch, I., Gómez, L., Pla, J. J. , Costas, M. *Nat. Chem.* **2011,** 3, 807-813

40   Costas, M. , Que Jr., L. *Angew. Chem. Int. Ed.* **2002,** 12, 2179-2181

41   Hong, S., Lee, Y.-M., Cho, K.-B., Sundaravel, K., Cho, J., Kim, M. J., Shin, W. *et al. J. Am. Chem. Soc.* **2011,** 133, 11876-11879

42   Koua, F. H. M., Umena, Y., Kawakami, K. , Shen, J.-R. *Proc. Natl. Acad. Sci.* **2013,** 110, 3889-3894

43   Garcia-Bosch, I., Company, A., Frisch, J. R., Torrent-Sucarrat, M., Cardellach, M., Gamba, I., Güell, M. *et al. Angew. Chem. Int. Ed.* **2010,** 49, 2406-2409

44   Klepser, B. M. , Bartlett, B. M. *J. Am. Chem. Soc.* **2014,** 136, 1694-1697

45   Hitomi, Y., Arakawa, K., Funabiki, T. , Kodera, M. *Angew. Chem. Int. Ed.* **2012,** 51, 3448-3452

46   Lehmann, T. E., Ming, L.-J., Rosen, M. E. , Que, L. *Biochemistry* **1997,** 36, 2807-2816

47   Shaik, S., Kumar, D., de Visser, S. P., Altun, A. , Thiel, W. *Chem. Rev.* **2005,** 105, 2279-2328

48   Codolà, Z., Garcia-Bosch, I., Acuña-Parés, F., Prat, I., Luis, J. M., Costas, M. , Lloret-Fillol, J. *Chem. Eur. J* **2013,** 19, 8042-8047

CHAPTER VIII.

GENERAL CONCLUSIONS

VIII. GENERAL CONCLUSIONS

In **Chapter III**, Ir-catalyzed water oxidation with three distinct Cp* carbene iridium complexes, as well as IrCl$_3$ and other benchmark iridium organometallic compounds have been studied employing NaIO$_4$ as chemical oxidant. Extraordinary TON (400000) and TOF (3 s^{-1}) have been achieved with compound **1Cl** without noticeable degradation of the oxidation activity. Novel understanding into the nature of the active species has been obtained by ^{1}H-NMR, CSI-HRMS, and UV-Vis experiments. While a fast decomposition of the organometallic iridium complexes takes place initially, DLS analysis of the catalytic reactions show that nanoparticles are not noticeable using NaIO$_4$, unlike in the Ce^{IV}-driven water oxidation. A transient species absorbing at λ_{max} = 405 nm has been found strictly connected with the O$_2$ evolution. Its depletion was accompanied by the formation of a new band at λ_{max}~ 580 nm, which has been previously reported to belong to the active species. The sum of our observations, along with recent findings by others, strongly suggests that the nature of the active species is strongly dependent in the experimental conditions. The real catalyst is suggested to be molecular in nature, although they may do not contain complete organic ligands, which leaves water, hydroxide, oxide groups and oxidized ligands as the only ligand candidates.

In **Chapter IV**, highly water soluble catalysts based on abundant and environmentally benign iron-based coordination complexes has been found active for the water oxidation, with the highest values reported per atom for any first row transition metal system described to date under homogeneous conditions. Ligand availability, modularity and versatility of this type of coordination complexes open up to systematically study a large number of structures. This must allow pinpointing key structural and electronic features of the iron complexes to sustain efficient water oxidation, and eventually will lead to superior catalysts. This study also allowed us to establish that the presence of two *cis-* free coordination sites is a structural key aspect for the catalytic activity. Complexes leaving one or two *trans*-free coordination sites were not found catalytically competent. DLS supported the homogeneity of the process and preliminary investigations suggested that WO takes place on a highly electrophilic [Fe^V(O)(OH)(L^{N4})]$^{2+}$ species, arising from the 1e$^-$ oxidation of a Fe^{IV}(O) intermediate, characterized as the resting state of the catalytic cycle by UV-Vis spectroscopy and ESI-MS spectrometry.

In **Chapter V**, the systematic tuning of the electronic effects on **3Fe** ([Fe(OTf)$_2$(^{Me2}Pytacn)]) have been found to impact directly on the WO activity, strongly supporting that the catalytic activity originates from molecular complexes operating in a homogeneous phase, in agreement with DLS from Chapter IV. Towards a better mechanistic understanding, careful spectroscopic analyses (UV-Vis) and kinetic studies suggest that excess of CAN triggers the formation of a novel [Fe^{IV}(O)(OH)Ce^{IV}] intermediate before the generation of the active species, which is probably [Fe^{V}(O)(OH)(L^{N4})]$^{2+}$ towards an unusual inner-sphere oxidation. Besides, DFT calculations have been employed to characterize the O-O bond formation pathway.

In **Chapter VI**, the characterization by CSI-HRMS, UV-Vis and rRaman of the [Fe(OTf)$_2$(mcp)] (**1Fe**) dimeric intermediate between Fe^{IV}(O) and Ce^{IV} is achieved. The transient species has been reformulated as a heterobimetallic oxo-bridged iron-cerium complex ([Fe^{IV}(O)(μ-O)Ce^{IV}]) and is the last detectable intermediate in Fe-catalyzed WO reactions. This intermediate is the first direct experimental characterization of a heterodimetallic core in a synthetic WO catalyst. Furthermore, the Fe^{IV}–O–Ce^{IV} species described can be construed as the closest structural and functional model for the essential heterodimetallic Mn^{V}–O–Ca^{II} center involved in the water oxidation event in PSII.

In **Chapter VII.5.1**, towards the understanding of the low stability of the [Fe(O)(OH$_2$)(mcp)] (**1Fe^{IV}=O**) intermediate, a deep analysis by HRMS have pointed methylene groups of the complex as susceptible sites to oxidation. The simple substitution of the weak C-H bonds by C-D have led to an impressive enhancement of both the half-life time of the **Fe^{IV}=O** intermediate and the catalytic activity.

In **Chapter VII.5.2,** the first non-heme iron pentacoordinate complex for the thermal WO is presented (**11Fe**). The negative charge and non-redox nature of the pentadentate amidate ligand seems to be key to reduce the redox potential to form the active WO species, opening the door for the quest of more robust WOC based in iron based on anionic pentadentate ligands. DFT studies indicates that [Fe^{IV}(AQ^{Me2}tacn)$^{\bullet}$(O)]$^{2+}$ is the active catalytic species and the O-O bond formation takes place towards an AB mechanism.

ANNEX

CHEMISTRY

A EUROPEAN JOURNAL

Supporting Information

Highly Effective Water Oxidation Catalysis with Iridium Complexes through the Use of NaIO$_4$

Zoel Codolà,[a] João M. S. Cardoso,[b] Beatriz Royo,[b] Miquel Costas,[a] and Julio Lloret-Fillol*[a]

chem_201204568_sm_miscellaneous_information.pdf

High efficient Iridium Catalyst Water Oxidation with NaIO$_4$

Zoel Codolà,[a] João M. S. Cardoso,[b] Beatriz Royo[b] Miquel Costas,[a]

and Julio Lloret Fillol*,[a]

[a]Departament de Química, Universitat de Girona, Campus de Montilivi,

17071 Girona (Spain)

[b] Instituto de Tecnología Química e Biológica, Universidade Nova de Lisboa

Avenida da República, EAN, 2780-157 Oeiras, Portugal.

*To whom correspondence should be addressed. e-mail: Julio.lloret@udg.edu,

Contents:

SI.1 – Experimental Section

SI.1.1 General Methods

Physical Methods. UV-VIS-NIR spectra were recorded on an Agilent 8453 diode array spectrophotometer (190-1100 nm range) in 1 cm quartz cells. A cryostat from Unisoku Scientific Instruments was used for the temperature control. The amount of gas generated was measured with a differential pressure transducer sensor (Honeywell-ASCX15DN, ±15 psi). Each reaction had their reference reaction which was connected to the other port of the sensor. Electrospray ionization mass spectrometry (ESI-MS) experiments were performed on a Bruker Daltonics Esquire 3000 Spectrometer, by introducing samples directly into the ESI-source using a syringe pump, without any further dilution. Details of the experiments are described in the corresponding section.

SI.1.2 Characterization of the Ir complexes
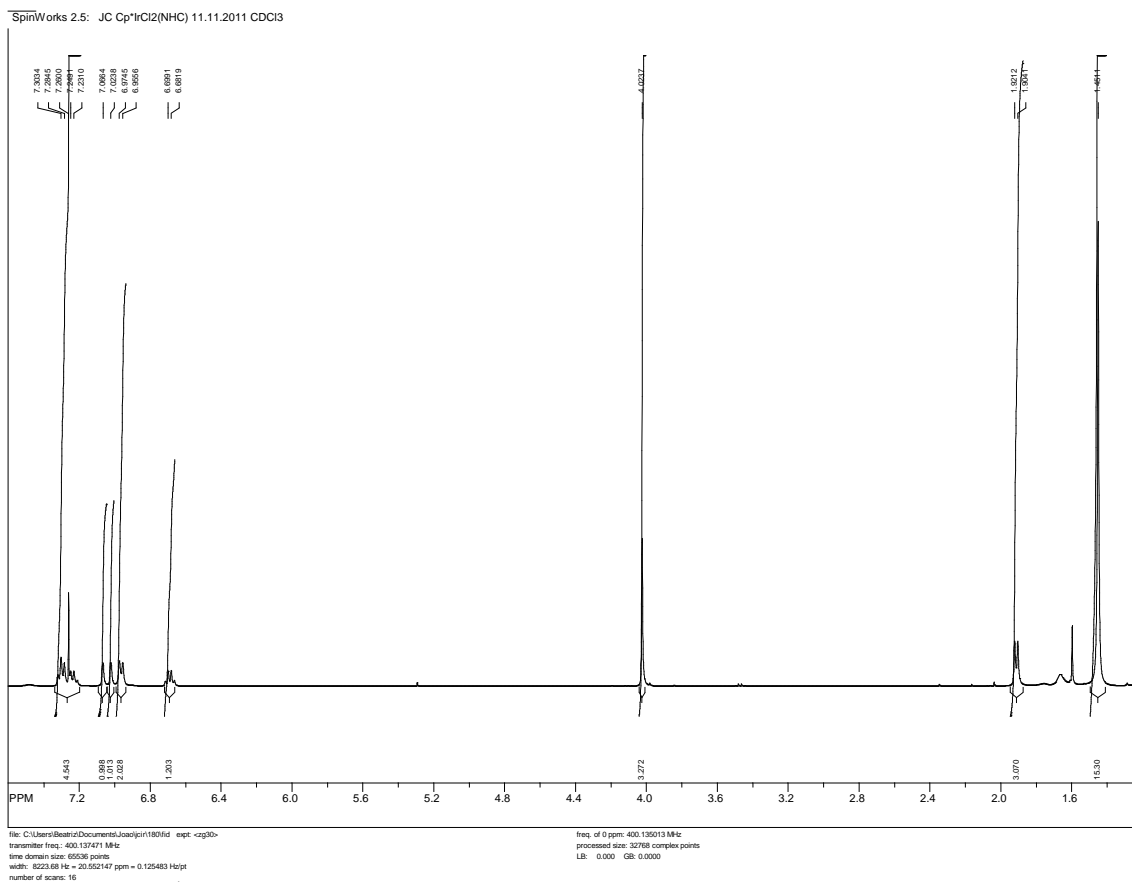
Figure SI.1. ^{1}H-NMR spectra of complex **1Cl** in CDCl$_3$
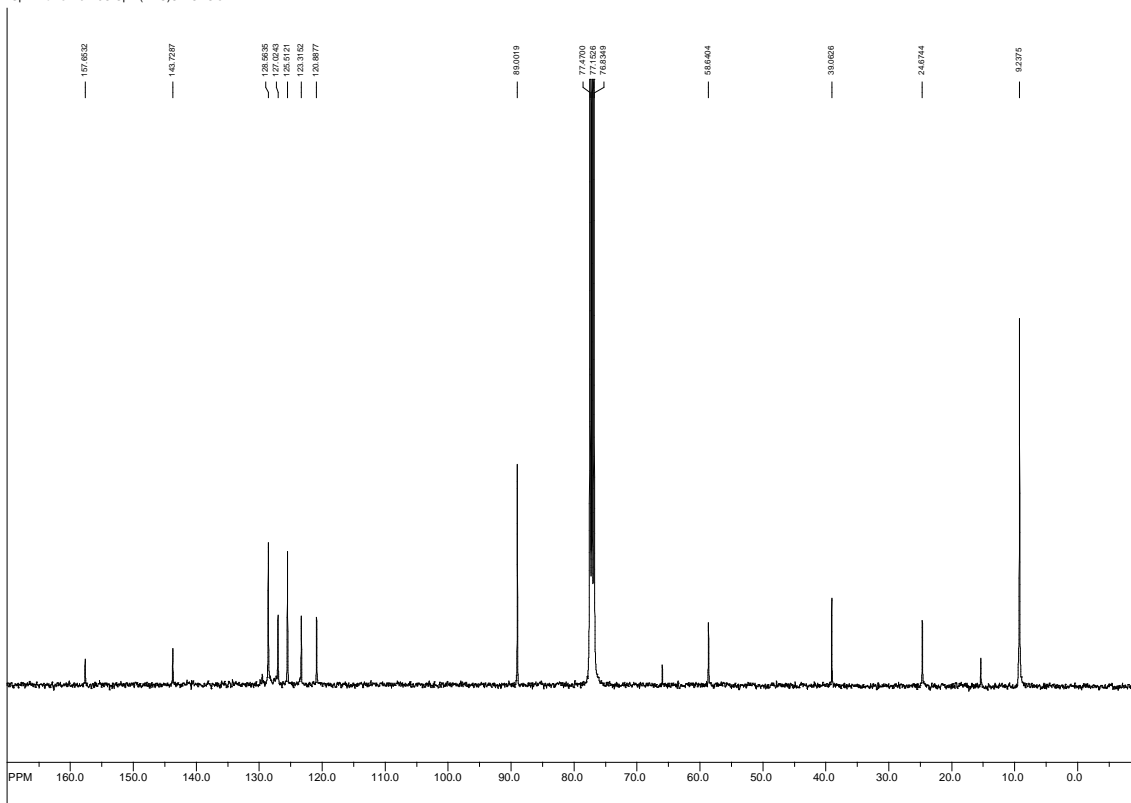
2

Figure SI.2. ^{13}C-NMR spectra of complex **1Cl** in CDCl$_3$
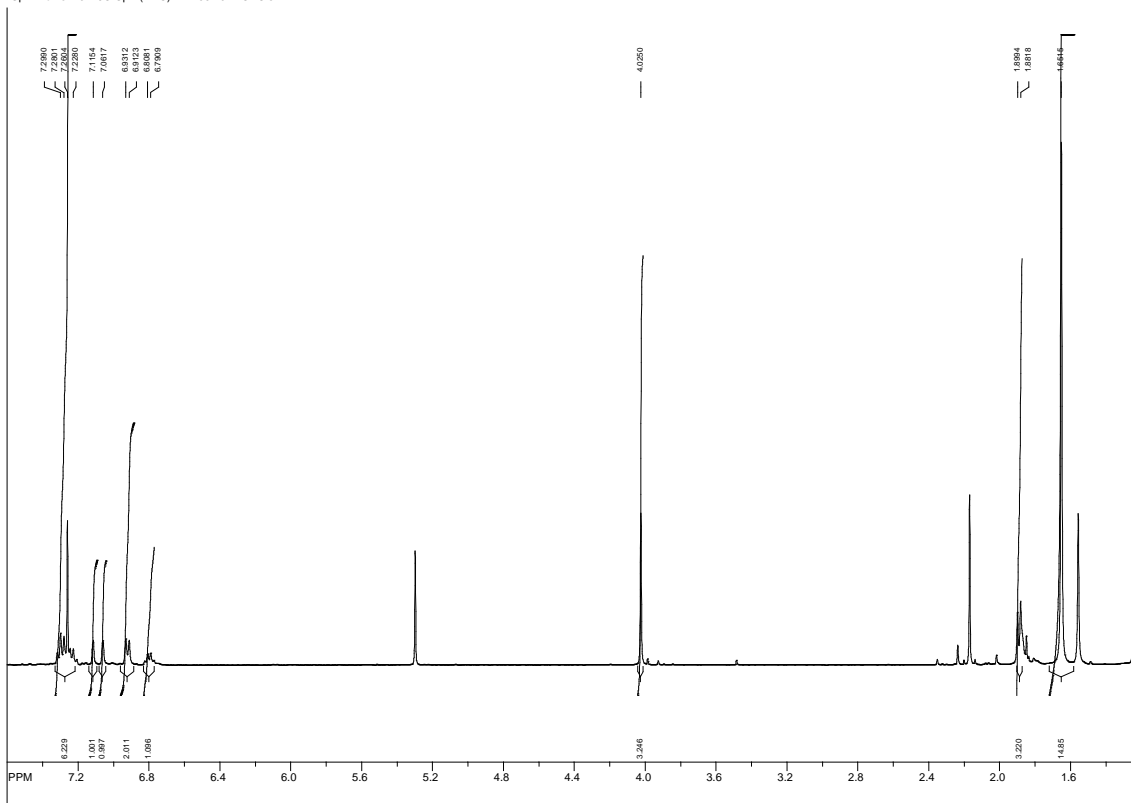
Figure SI.3. ^{1}H-NMR spectra of complex **1I** in CDCl$_3$

152.7288
143.6732
128.5321
127.0781
125.5804
123.1396
121.3365
90.1461
77.4774
77.1600
76.8424
61.1936
43.7418
25.0597
10.6897

| PPM | 160.0 | 150.0 | 140.0 | 130.0 | 120.0 | 110.0 | 100.0 | 90.0 | 80.0 | 70.0 | 60.0 | 50.0 | 40.0 | 30.0 | 20.0 | 10.0 | 0.0 |
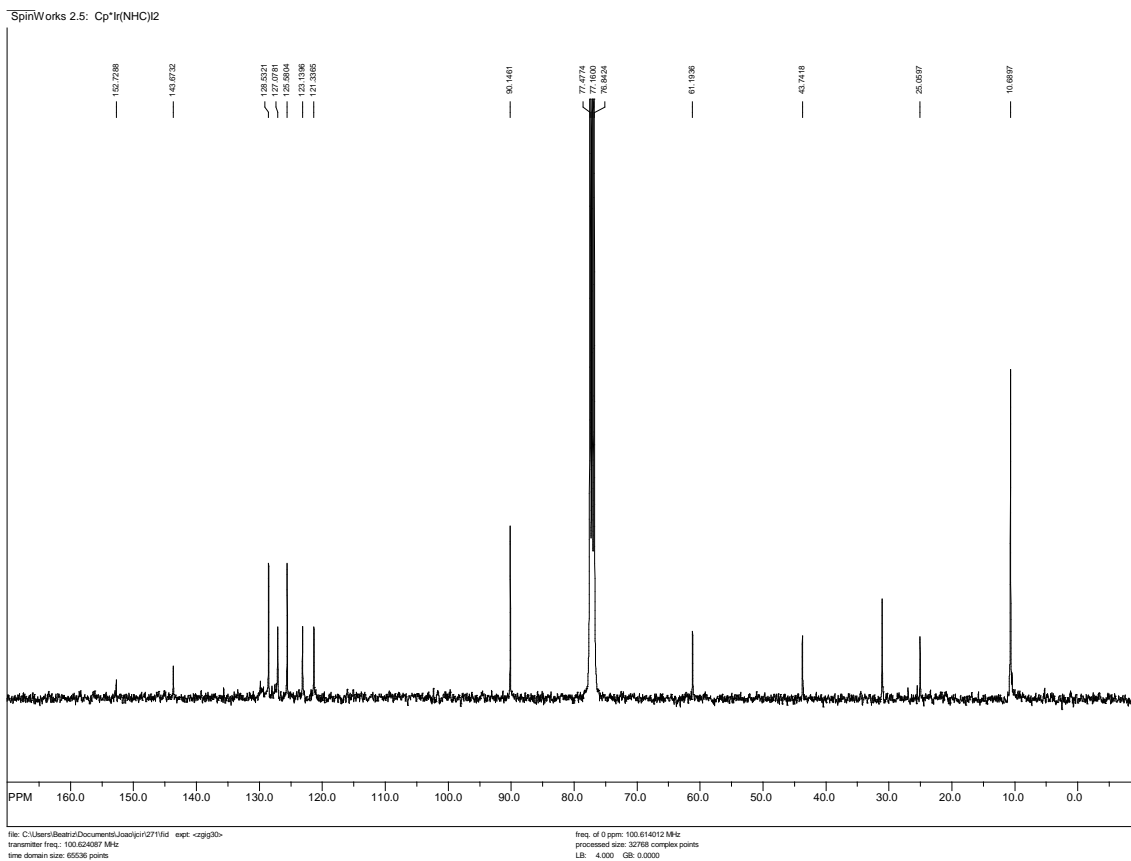
Figure SI.4. ^{13}C-NMR spectra of complex **1I** in CDCl$_3$
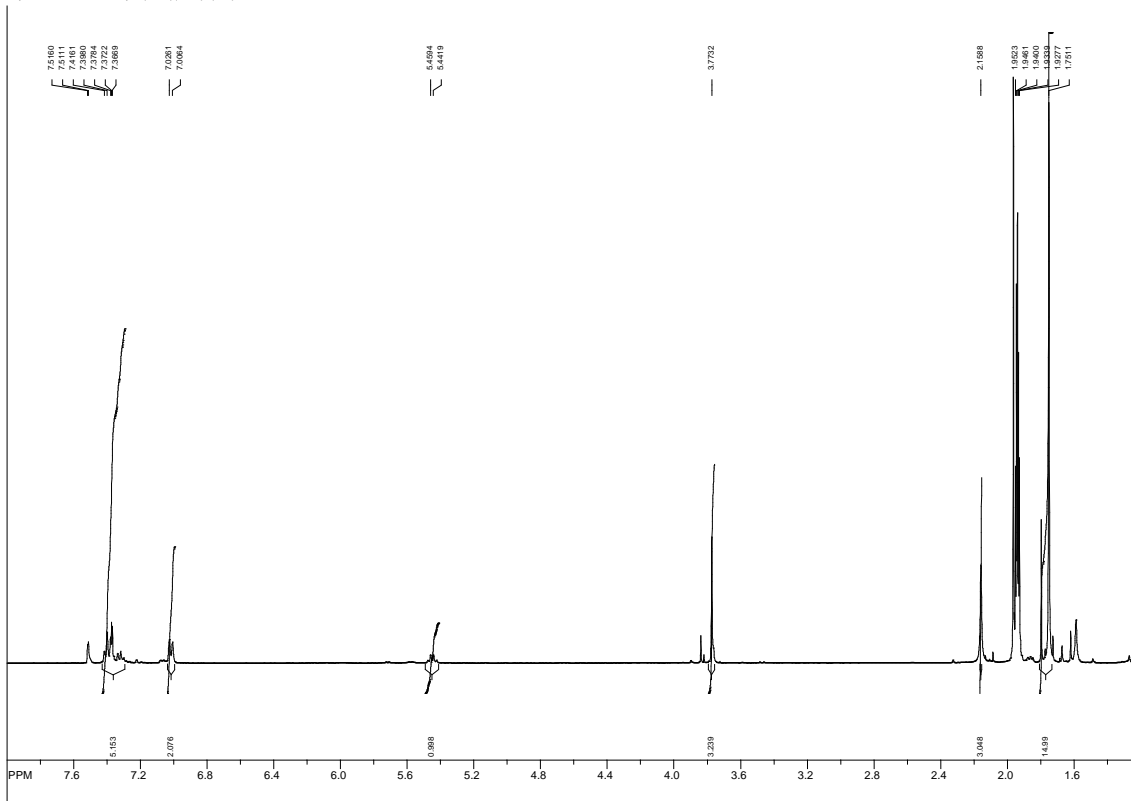
Figure SI.5. ^{1}H-NMR spectra of complex **1OTf** in CD$_3$CN
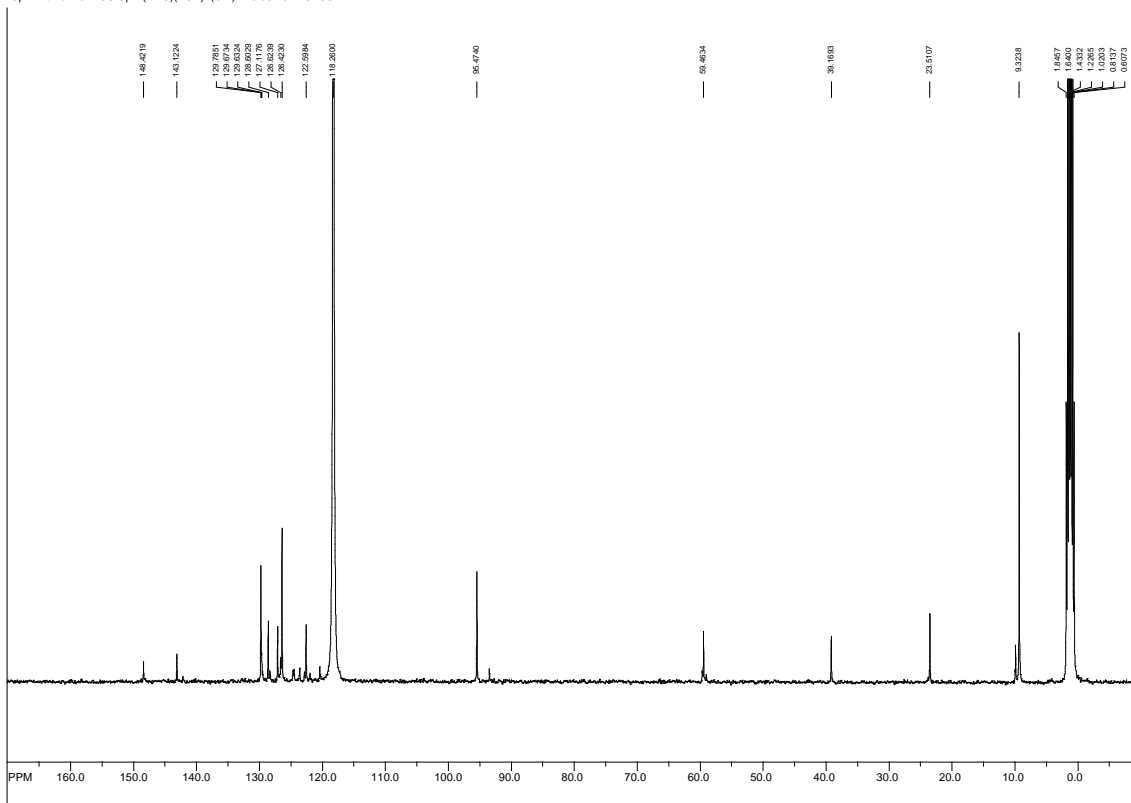
6

Figure SI.6. ^{13}C-NMR spectra of complex **1OTf** in CD$_3$CN

Peak labels: 148.4219, 143.1224, 129.7851, 129.6734, 128.6324, 128.6029, 127.1176, 126.6239, 126.4230, 122.5984, 118.2600, 95.4740, 59.4634, 39.1693, 23.5107, 9.3238, 1.8457, 1.6400, 1.4332, 1.2265, 1.0203, 0.8137, 0.6073

7

SI.2 – Catalytic water oxidation reactions

SI.2.1 On-line monitoring experiments of oxygen formation

- Cerium (IV) Ammonium Nitrate (CAN) as sacrificial oxidant.
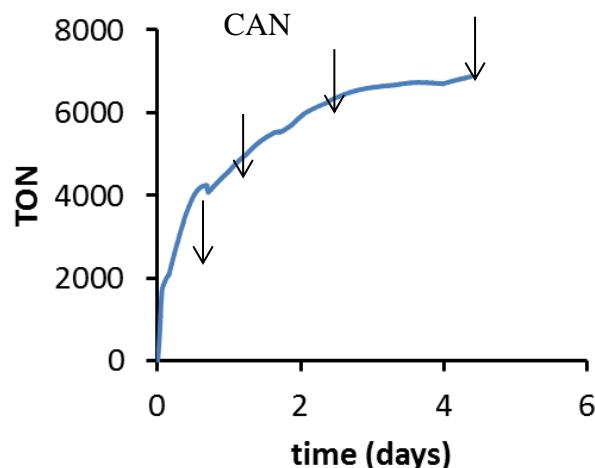
Figure SI.7. O_2 evolution in TON ($n(O_2)/n(Ir^{III})$) versus time. To **1Cl** (15 μM) suspended in water (5 mL) CAN (200 mM) was added during the time in subsequent additions.

- NaIO$_4$ as sacrificial oxidant
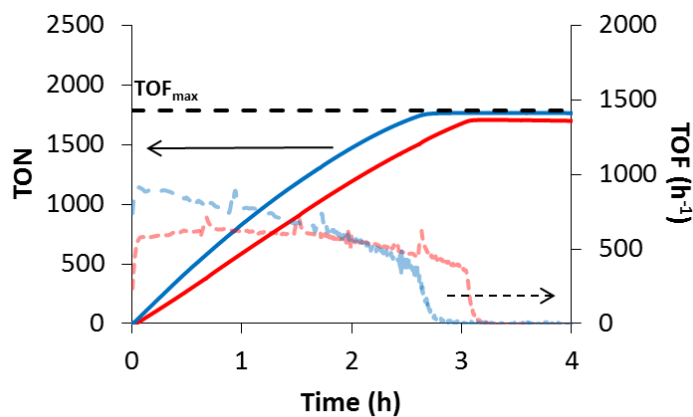
Figure SI.8. Comparison between TON ($n(O_2)/n(Ir^{III})$, left axis) and TOF (TON·h^{-1}, right axis) for a reaction of **1Cl** (70 μM) used as suspended solid (red line) or used as stock solution (blue line) when using NaIO$_4$ (40 eq., 250 mM) as oxidant in MiliQ water (5 mL) at 25 ºC. Dotted line represents the maximum theoretical turnover number.
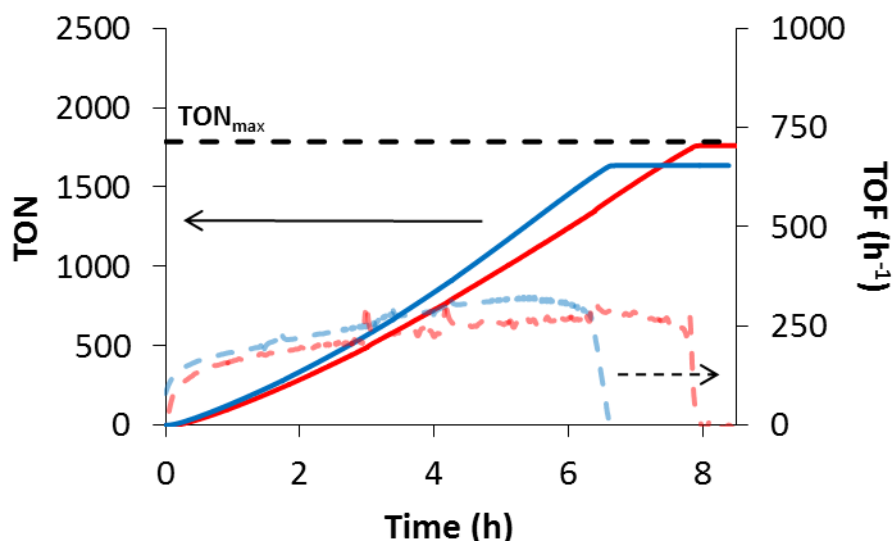
Figure SI.9. Comparison between TON ($n(O_2)/n(Ir^{III})$, left axis) and TOF (TON·h^{-1}, right axis) for a reaction of **IrCl$_3$** (70 μM) used as suspended solid (red line) or used as stock solution (blue line) when using NaIO$_4$ (40 eq., 250 mM) as oxidant in MiliQ water (5 mL) at 25 ºC. Dotted line represents the maximum theoretical turnover number.

Table SI.1. Catalytic activity for **IrCl$_3$** and **1Cl** used as suspended solids or as previously prepared stock solutions.

Complex / SO	Phase	TOF$_{max}$	TON
IrCl$_3$ / NaIO$_4$	stock[a]	340 ± 30	1650 ± 20
	solid[b]	300 ± 5	1750 ± 15
1Cl / NaIO$_4$	stock[a]	890 ± 10	1770 ± 10
	solid[b]	610 ± 25	1730 ± 45

[a] suspended solid sampler: [Ir^{III}] (final concentration = 70 μM) was added directly into an aqueous solution of NaIO$_4$ (250 mM, 5 mL). [b] stock solution preparation: [Ir^{III}] (700 μM) was added into the reaction containing an aqueous solution of NaIO$_4$ (40 eq in 1 mL) under vigorous stirring. After all iridium compound was dissolved (aprox. 10 min), an aliquot of 0.5 mL was added into the reaction containing an aqueous solution of NaIO$_4$ (250 mM of NaIO$_4$ and 70 μM of [Ir^{III}] in 5 mL of H$_2$O).

9
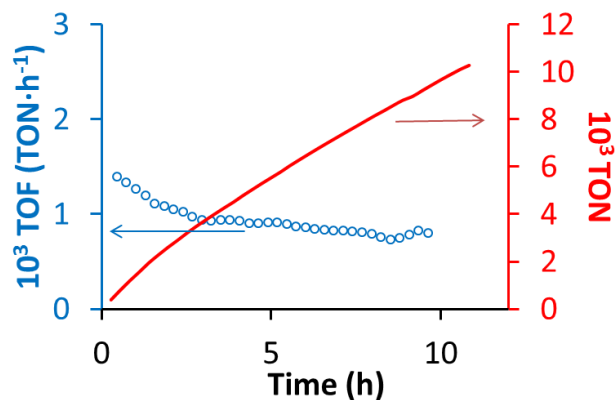
Figure SI.10. TON ($n(O_2)/n(Ir^{III})$, right axis) and TOF ($TON·h^{-1}$, left axis) time monitoring for catalytic water oxidation reaction with complex **1Cl** (10 μM) and NaIO$_4$ (250 mM) at 25 ºC.
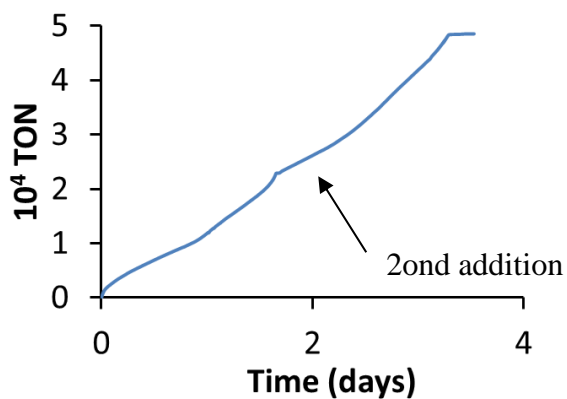
Figure SI.11. Plot of O$_2$ evolution versus time for a double addition of NaIO$_4$ (500 mM + 500 mM) to a 2 mL of a stock solution of **1Cl** (10 μM).
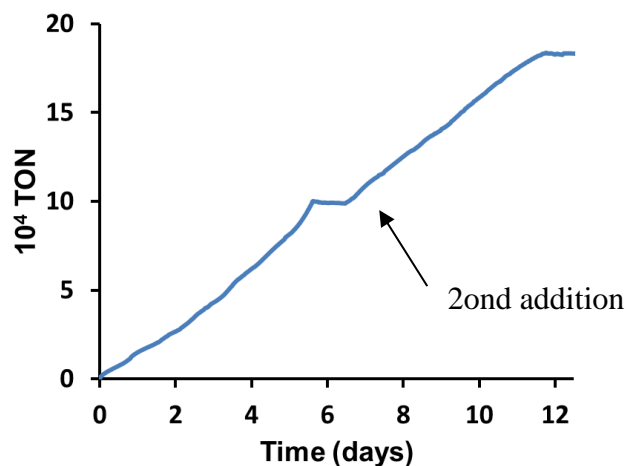
Figure SI.12. Plot of O$_2$ evolution versus time for a double addition of NaIO$_4$ (500 mM + 500 mM) to a 2 mL of a stock solution of **1Cl** (2.5 μM).

10
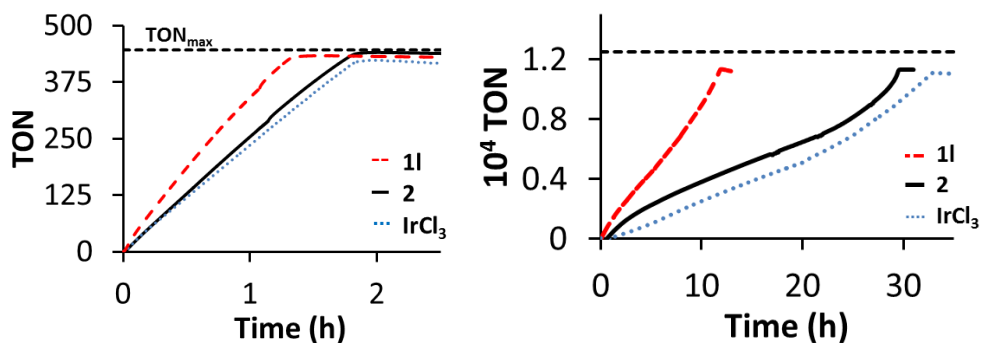
Figure SI.13. Oxygen evolution, in TON, versus time plots found when $NaIO_4$ (Left: 62.5 mM; Right: 250 mM) was used as sacrificial oxidant and compounds **1I**, **2** and **IrCl₃** as stock solutions (Left: 70 μM; Right: 10 μM) in 5 mL of MiliQ water (pH ~ 5) at 25 °C. Dotted line represents the maximum theoretical turnover number (446 for the left plot and 12500 for the right plot).

SI.2.2 Kinetic studies

The required amount of iridium complex to carry out the kinetic experiments was used from a previously prepared stock solution. Stock solutions were prepared by using a known amount of iridium complex and 40 eq. of $NaIO_4$. The solution was maintained stirring until the band at 580 nm appears in the UV-Vis spectrum indicating the total consumption of the oxidant. Then the corresponding amount of iridium complex (stock solution) was injected through a septa to a 15 mL (total volume) glass vial containing 4.5 mL of the $NaIO_4$ at the desired concentration and fix temperature. The oxygen production was recorded with a differential pressure transducer, by comparison with a reference to minimize noises and the total O_2 content was confirmed by GC-TCD analysis of an aliquot of the headspace.
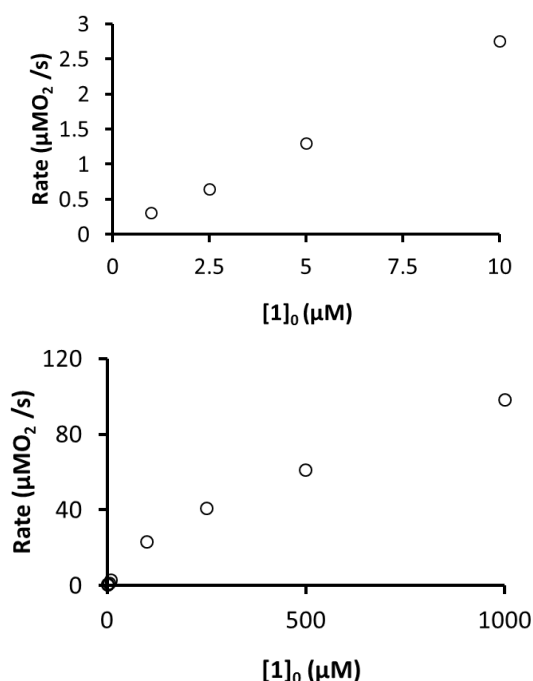
Figure SI.14. Initial rates (10% O_2 formation) of oxygen evolution (O_2 µM/s,) versus initial concentration of **1Cl** at low (left: 1-10 µM) and high (right: 1-1000 µM) range of concentrations using $NaIO_4$ as oxidant ($[NaIO_4]_0$ = 250 mM).
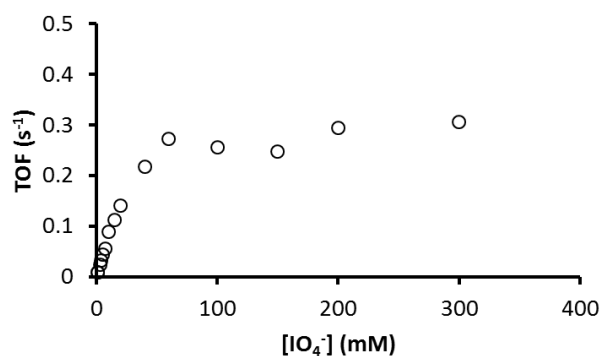
SI.3 – Study of the active catalytic species

SI.3.1 – UV-Vis Study
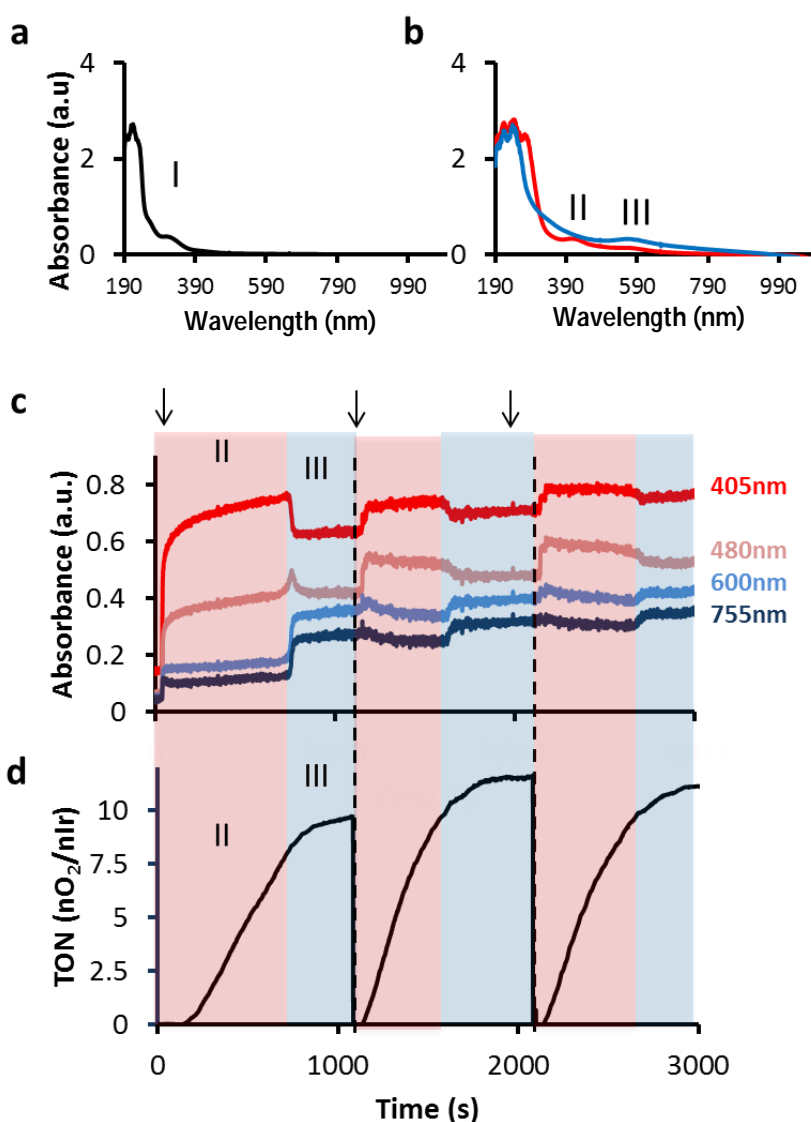
Figure 16. Oxygen evolution and UV-Vis spectrum monitored for a single
experiment of $IrCl_3$ with $NaIO_4$ in catalytic conditions. **a and b**) UV-Vis spectra in
different WO states **I**) 0.5 mM of **IrCl$_3$** in H_2O (black spectra), **II**) 0.5 mM of
IrCl$_3$ in H_2O immediately after the addition of 20 eq. of $NaIO_4$ (red spectra) and
III) 0.5 mM of **IrCl$_3$** in H_2O with 20 eq. of $NaIO_4$ after no more oxygen evolve

13

(blue spectra). **c)** Time-traces followed at 405, 480, 600 and 755 nm during several NaIO$_4$ additions. **d)** Parallel monitor of oxygen formation (TON$_{max}$ = 10). After every new addition of NaIO$_4$ (20 eq.) the TON value was set up to 0. The absorbance was background and dilution corrected.
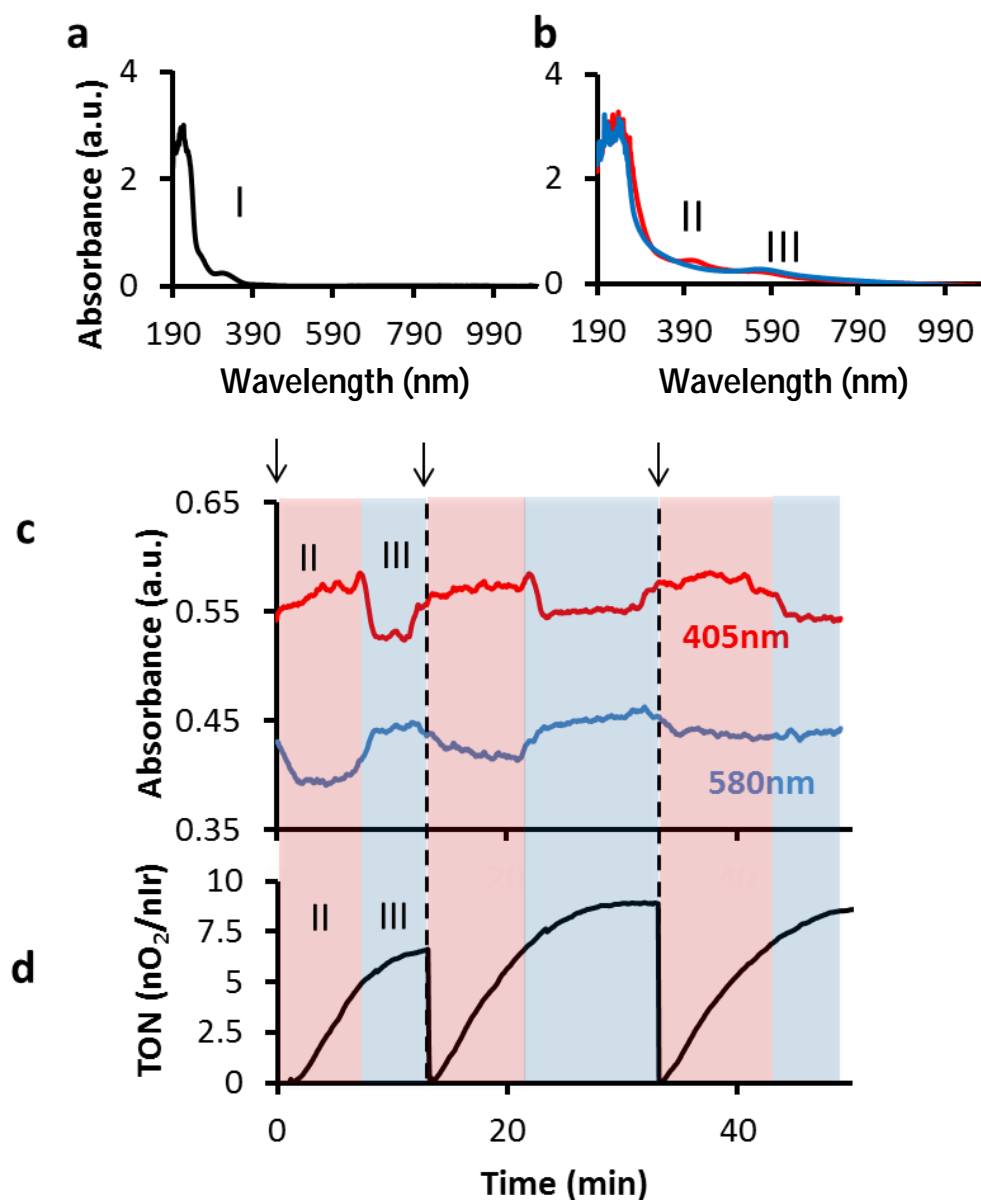
Figure 17. Oxygen evolution and UV-Vis spectrum monitored in a single experiment of a catalytic reaction of **1OTf** with NaIO$_4$. **a and b)** UV-Vis spectra in the different WO states **I)** 0.25 mM of **1OTf** in H$_2$O (black spectra), **II)** 0.25 mM of **1OTf** in H$_2$O immediately after the addition of 20 eq. of NaIO$_4$ (red spectra) and **III)** 0.25 mM of **1OTf** in H$_2$O with 20 eq. of NaIO$_4$ after no more oxygen evolve (blue spectra). **c)** Time-traces followed at 405 and 580 nm of a 0.25 mM solution of **1OTf** during several NaIO$_4$ additions. **d)** Parallel monitor of

14

oxygen formation ($TON_{max} = 10$). After every new addition of NaIO$_4$ (20 eq.) the TON value was set up to 0. The absorbance was background and dilution corrected.

Figure SI.18. Spectrum 1) UV-Vis spectrum of **1Cl** during O$_2$ evolution in a reaction of **1Cl** (0.5 mM) with 20 eq. of NaIO$_4$. Spectrum 2) After addition of 100 µL of EtOH to spectrum 1. Spectrum 3) after 1 h from the addition of 1 mL of EtOH to spectrum 1.
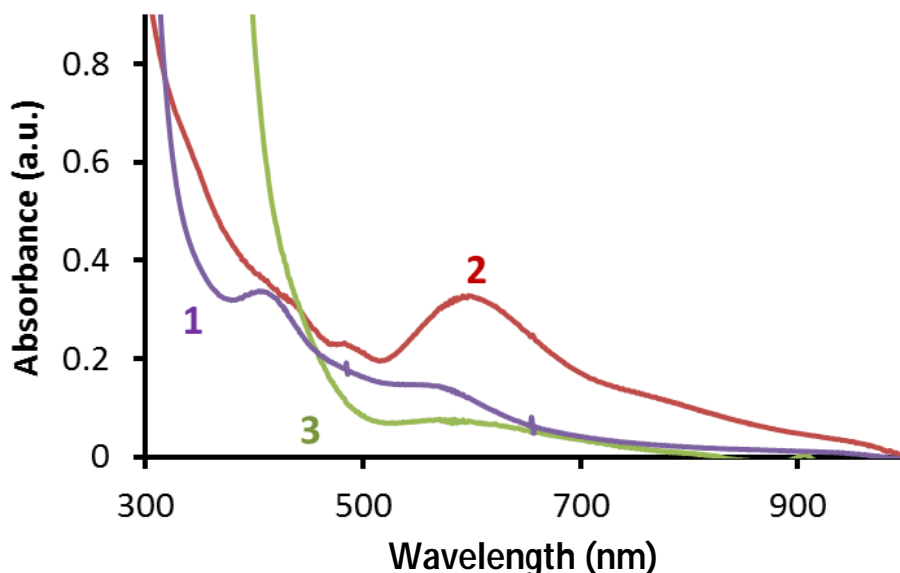
Figure SI.19. Spectrum 1) UV-Vis spectrum of **IrCl$_3$** during O$_2$ evolution in a reaction of **1Cl** (0.5 mM) with 20 eq. of NaIO$_4$. Spectrum 2) after addition of 100 µL of EtOH to spectrum 1. Spectrum 3) after 5 h from the addition of 1 mL of EtOH to spectrum 1.

15

SI.3.2 – ¹H-NMR study
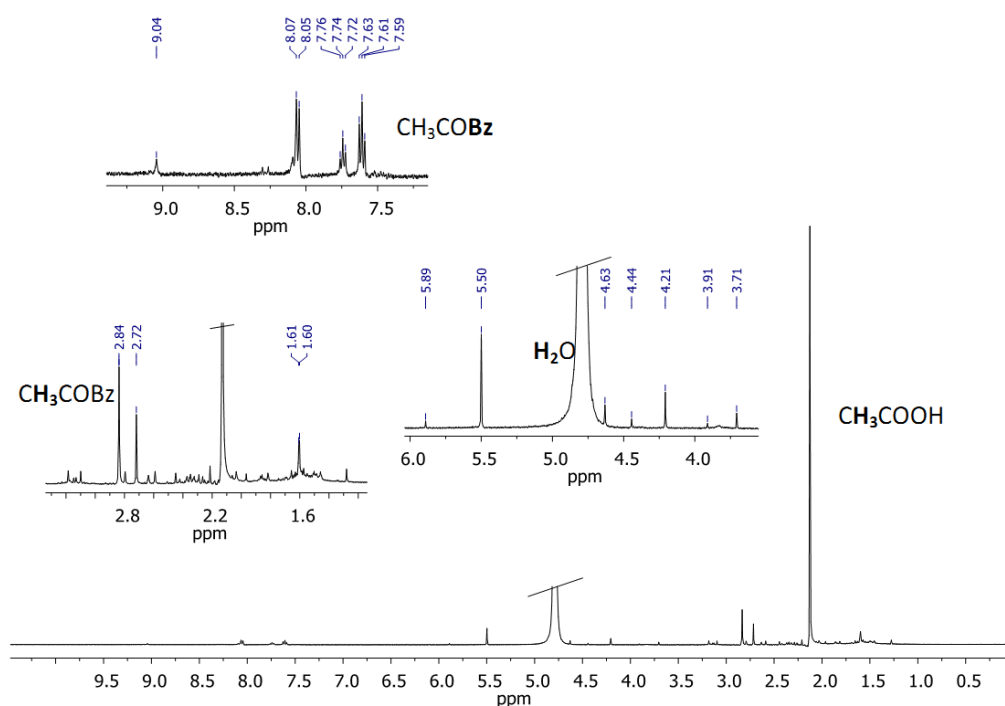
Figure SI.20. ¹H-NMR of **1Cl** in D_2O (3.4 mmol in 1 mL) after 1 h from the addition of 40 eq of $NaIO_4$.
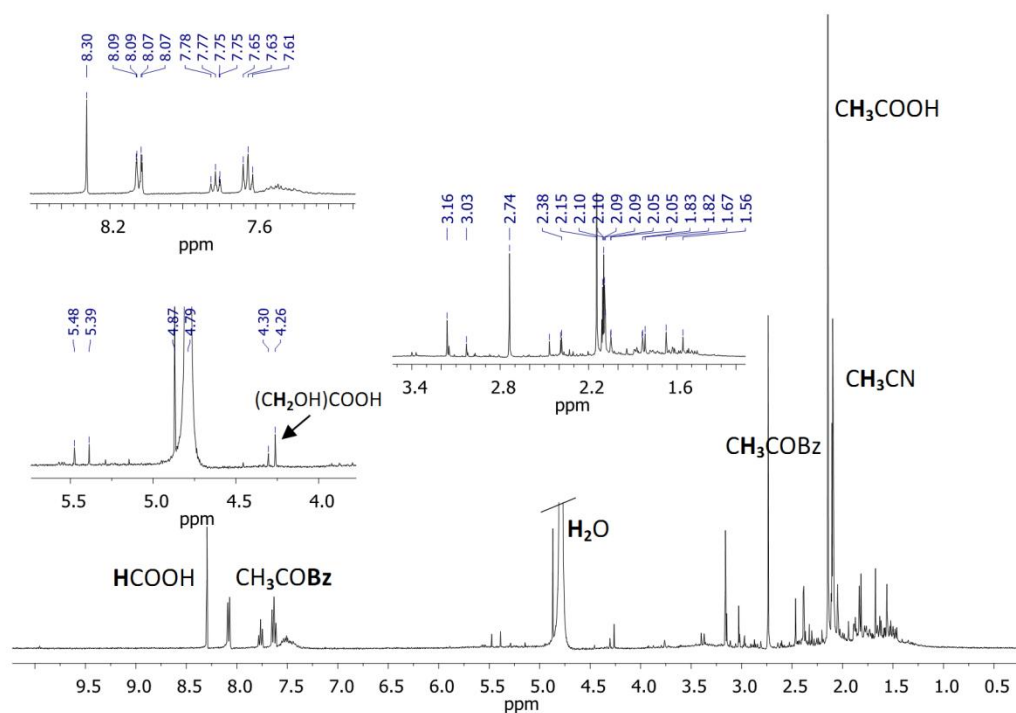
Figure SI.21. ¹H-NMR of **1Cl** in D_2O:CD_3CN (3.4 mmol in 0.45:0.05 mL) immediately after the consumption of 30 eq of $NaIO_4$.
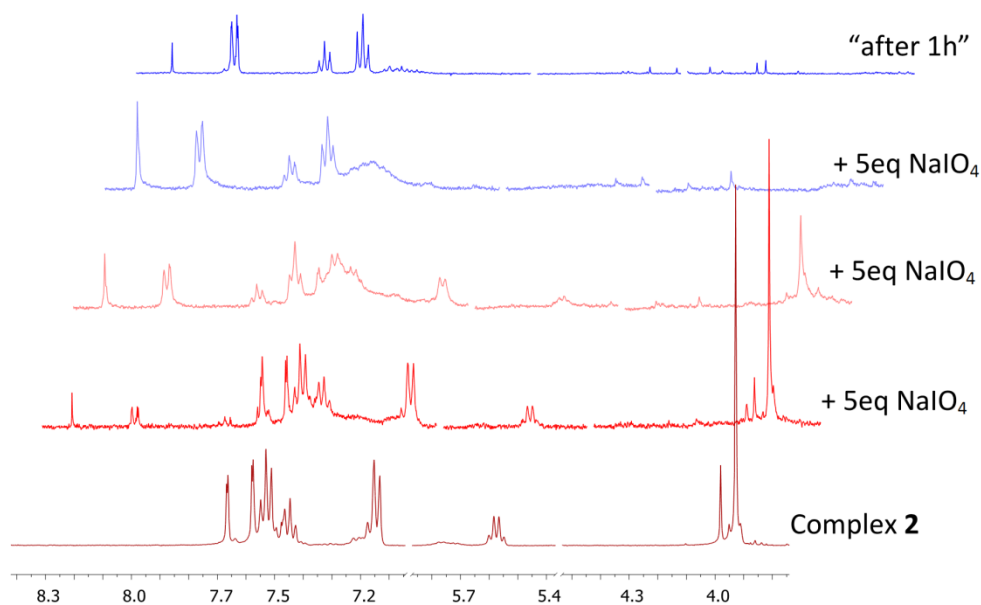
Figure SI.22. ^{1}H-NMR after addition of increasing amounts of NaIO$_4$ to complex **1Cl** in D$_2$O:CD$_3$CN (3.4 mmol in 0.45:0.05 mL). The spectrum at the top was recorder 30 min after the addition of the last 5 eq of NaIO$_4$.
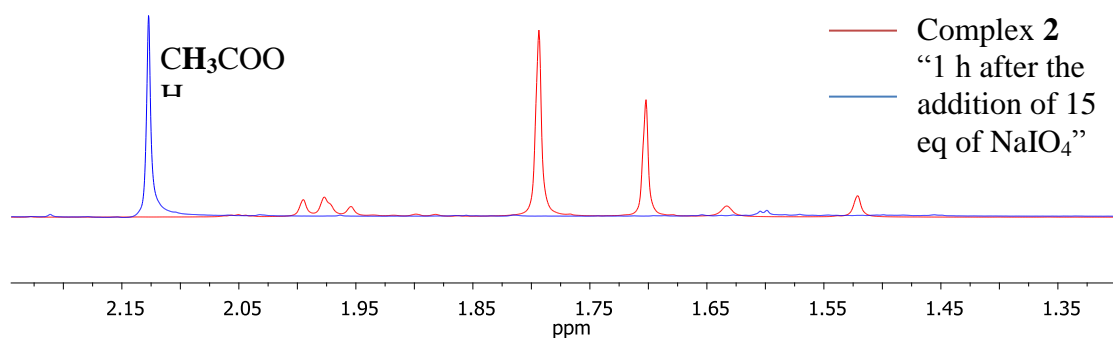
Figure SI.23. ^{1}H-NMR signals of the aliphatic region for complex **1Cl** dissolved in D$_2$O:CD$_3$CN (0.45:0.05) (red spectrum) and after 30 min of the addition of 15 eq of NaIO$_4$ (blue spectrum).
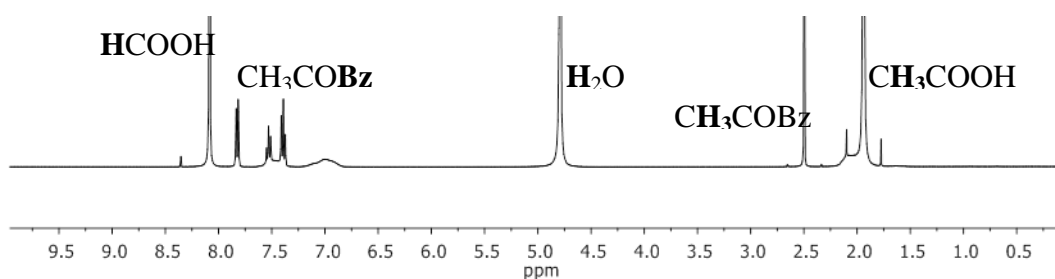
Figure SI.24. ^{1}H-NMR of a acetophenone, formic and acetic acid mixture in D$_2$O.

17
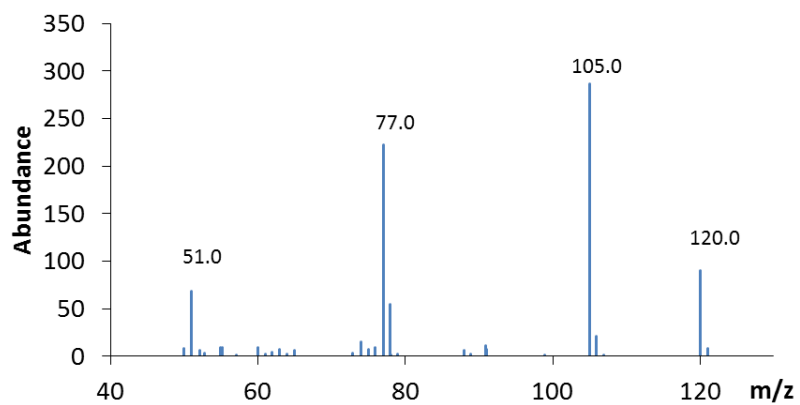
Figure SI.25. GC-MS mass spectrum of an Et_2O extraction after 30 min of reaction of **1Cl** and $NaIO_4$ (15 eq.) in $D_2O:CD_3CN$ (0.45:0.05). The molecular peak at m/z = 120.0 and the other fragments observed are characteristic peaks for acetophenone.

SI.3.3 – ESI-HRMS-TOF
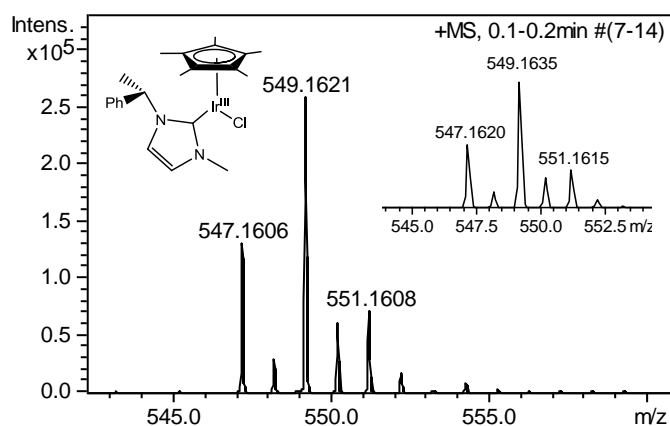
Figure SI.26. Magnification of the ESI-HRMS-TOF mass spectrum of complex **1Cl** where it is shows the molecular peak corresponding to the mass of [**1Cl** − **HCl**]$^+$ and its simulated spectra ($C_{22}H_{29}IrN_2Cl$, inset).
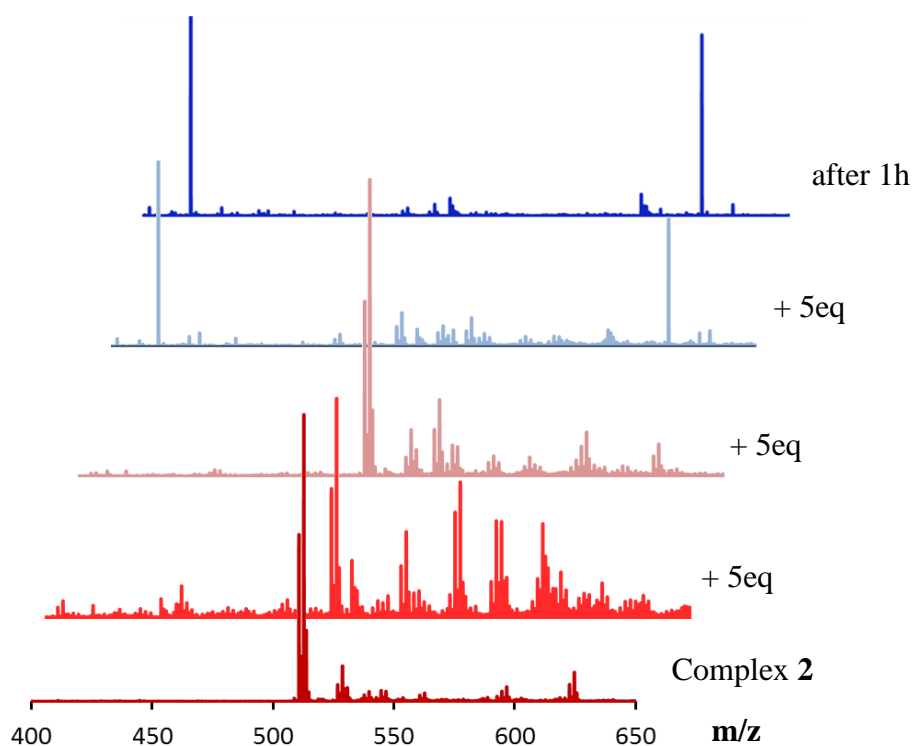
Figure SI.27. ESI-HRMS-TOF recorded after stepwise NaIO$_4$ additions (5 eq). The spectrum at the top was recorder 30 min after the addition of the last 5 eq of NaIO$_4$.
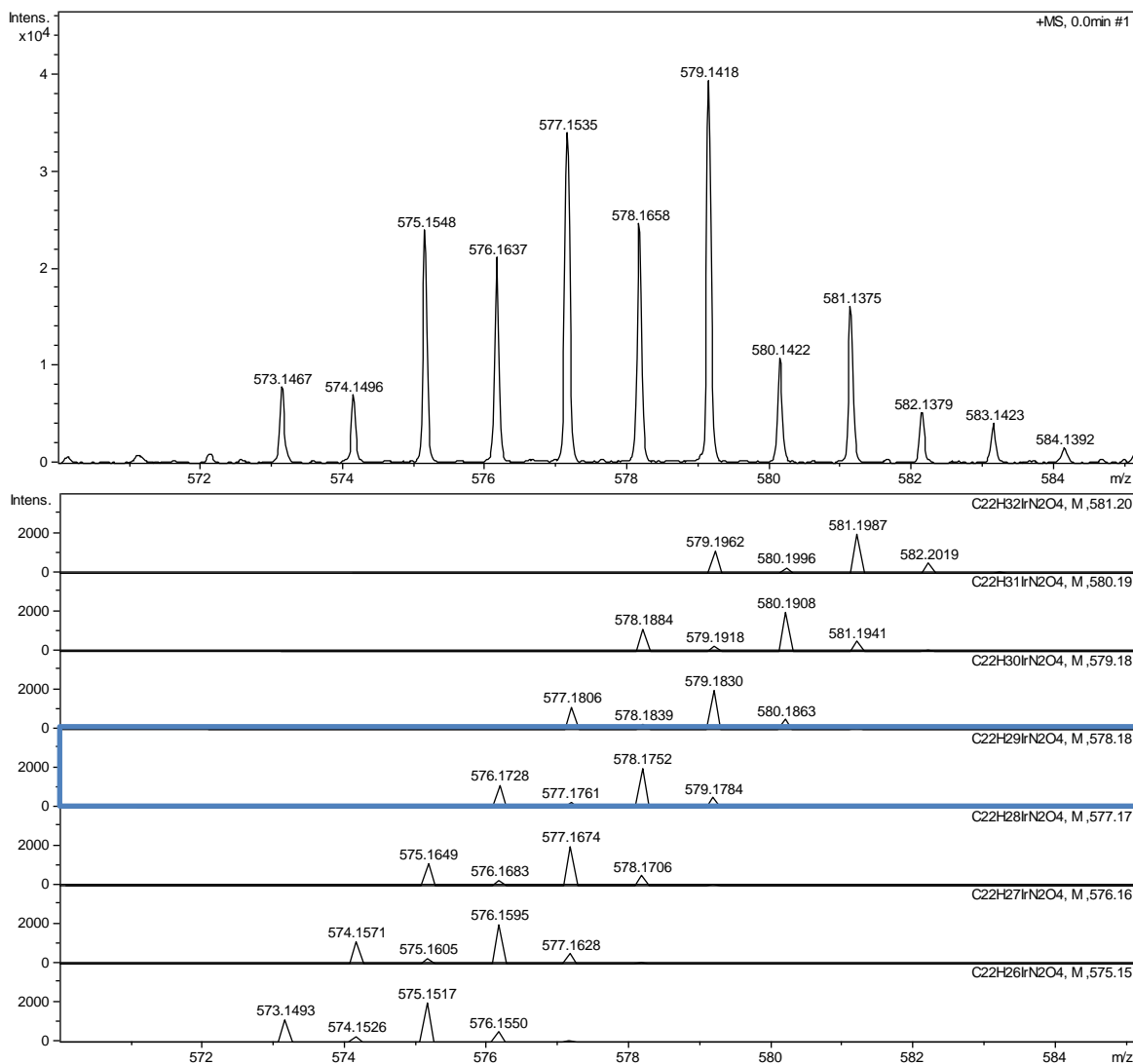
Figure SI.28. Top), ESI-HRMS-TOF of **1Cl** in H_2O recorded immediately after the addition of 5 eq of $NaIO_4$ and bottom), simulated patterns for $[C_{22}H_{29}IrN_2 + 4 \cdot O]^+$ (highlighted) and the corresponding losing or gaining of hydrogen atoms.
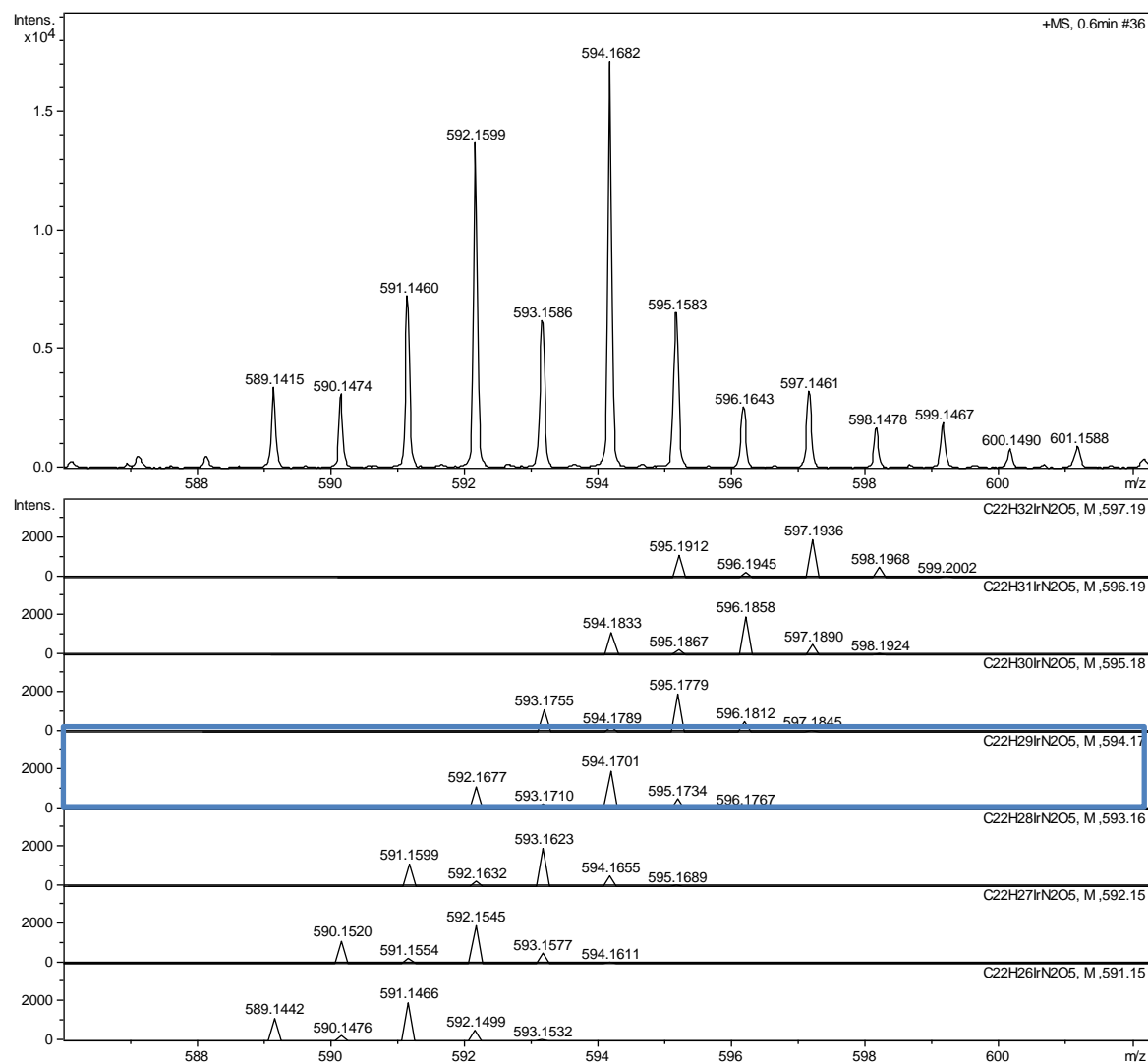
Figure SI.29. Top), HRMS-TOF of **1Cl** in H$_2$O recorded immediately after the addition of 5 eq of NaIO$_4$ and bottom), simulated patterns for [C$_{22}$H$_{29}$IrN$_2$ + 5·O]$^+$ (highlighted) and the corresponding losing or gaining of hydrogen atoms.

SI.3.4 – DLS

Dynamic Light Scattering (DLS) experiments were performed on a Zetasizer Nano ZS; Malvern Instruments (particle size distribution from 0.6 to 6000 nm and detection limit of 0.1 ppm). Dynamic Light Scattering (DLS) was carried out to investigate the possible formation of nanoparticles in solution. All the experiments were performed filtering (syringe, 0.22 μm) the samples to remove dust particles.
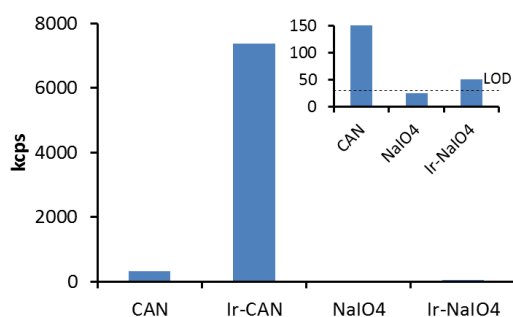
Figure SI.30. Light scattering intensity values (kcps = kcounts per second) for **1Cl** (0.2 mM) with sacrificial oxidants (12.5 mM) and their corresponding blanks (12.5 mM). Limit of detection (LOD) is about 30 kcps.
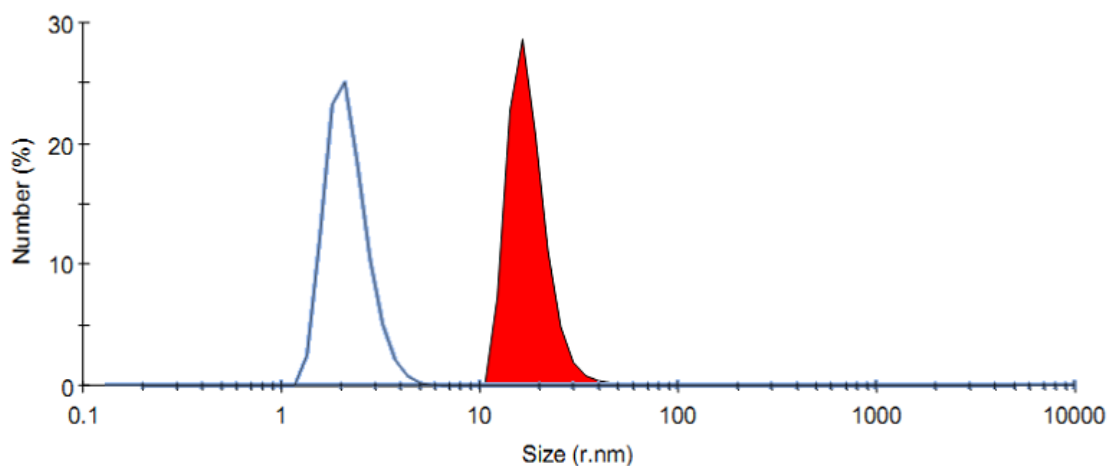
Figure SI.31. Size distribution by number of nanoparticles for an aqueous solution of CAN (12.5 mM, blue line) and **1Cl** (0.2 mM, red filled plot) with 12.5 mM of CAN after the consumption of the sacrificial oxidant (red plot).
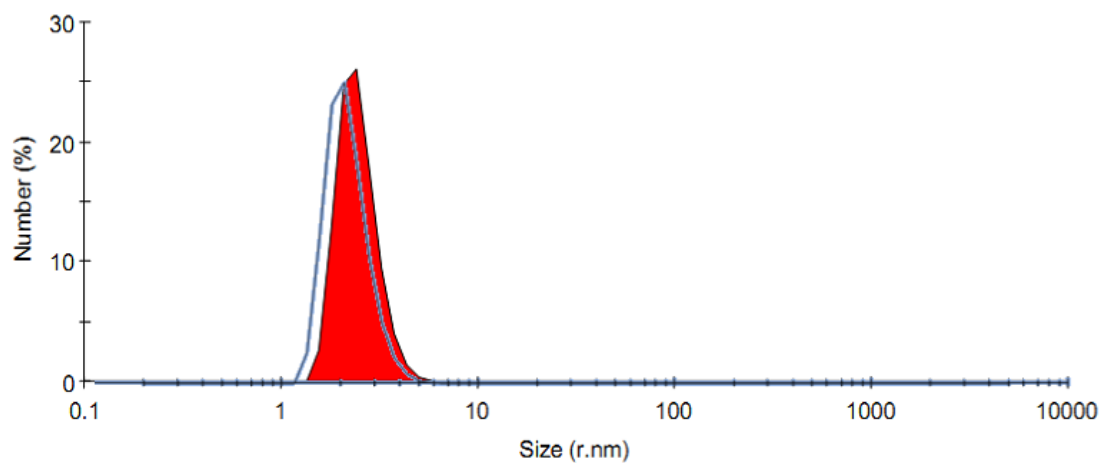
Figure SI.32. Size distribution by number of nanoparticles for an aqueous solution of NaIO$_4$ (12.5 mM, blue line) and **1Cl** (stock solution, 0.2 mM, red filled plot) with 12.5 mM of NaIO$_4$ after the consumption of the sacrificial oxidant (red plot).
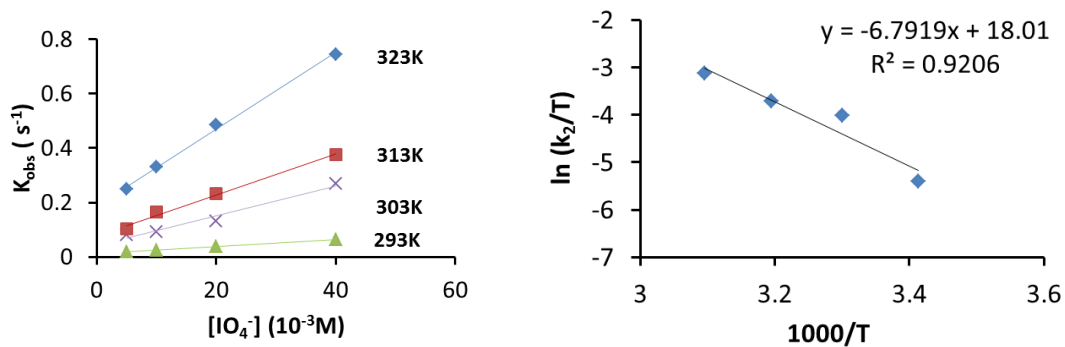
Figure SI.33. Left) k_{obs} obtained from the initial rates at 10 % of oxygen formation for **1Cl** ($[1Cl]_0$ = 50 μM) at different temperatures and NaIO$_4$ concentrations (5 – 40 mM) . Right) Eyring plot calculated for **1Cl** from the k_{obs} at temperatures between 293 K and 323 K.

24

Efficient Water Oxidation Catalysts Based on Readily Available

Iron Coordination Complexes

Julio Lloret Fillol,[a,*] Zoel Codolà,[a] Isaac Garcia-Bosch,[a] Laura Gómez,[a] Juan José Pla,[a]

and Miquel Costas [a,*]

[a]*Departament de Química, Universitat de Girona, Campus de Montilivi, 17071 Girona (Spain)*

*To whom correspondence should be addressed. Email:
Julio.lloret@udg.edu; Miquel.costas@udg.edu.

Contents:

SI.1 – Catalytic water oxidation results

SI.2 – Experimental Section

SI.3 – References

SI.1 – Catalytic water oxidation results

Table SI.1. Metal salts precursor screening of catalytic water oxidation.

Catalysts	[Cat] μM	Oxidant	[mM]	TON[a]	TOF[b]
$Mn(OTf)_2$	37.5	CAN or $NaIO_4$	[125]	-	-
$Co(OTf)_2$	37.5	CAN or $NaIO_4$	[125]	-	-
$Co(BF_4)_2$	37.5	CAN or $NaIO_4$	[125]	-	-
$CoCl_2$	37.5	CAN or $NaIO_4$	[125]	-	-
$[Ni(OTf)_2]$	37.5	CAN or $NaIO_4$	[125]	-	-
$NiCl_2$	37.5	CAN or $NaIO_4$	[125]	-	-
$[Fe(OTf)_2]$	37.5	CAN or $NaIO_4$	[125]	-	-
$FeCl_2$	37.5	CAN or $NaIO_4$	[125]	-	-
$FeCl_3$	37.5	CAN or $NaIO_4$	[125]	-	-
$[Fe(OTf)_2]$ + 2·bpy	37.5	CAN or $NaIO_4$	[125]	-	-
$[Fe(OTf)_2]$ + 3·bpy	37.5	CAN or $NaIO_4$	[125]	-	-

All the reactions were performed in water at 25 °C [a] Turnover number maximum, TON = (mol of O_2/mol of cat.). [b] Turnover frequency under initial rate (TON·h^{-1}). The sensitivity of O_2 analytics allows quantifying the gas formed when the O_2 volume are higher than **50** microL which imply errors higher than 20%. Therefore could not be discarded that small among of O_2 were produce by complexes **1Co**, **1Mn**, **6Fe** and/or **7Fe**. However, these small O_2 amounts are negligible respect to other catalysts studied in this work.

Table SI.2. [Fe(OTf)$_2$(^{Me2}Pytacn)] complexes and conditions for screening of catalytic water oxidation.

Catalysts		[Cat] µM	Oxidant	[mM]	TON[a]	TOF[b]
[Fe(OTf)$_2$(^{Me2}Pytacn)]	(**1Fe**)	37.5	CAN	[50]	52	167
[Fe(OTf)$_2$(^{Me2}Pytacn)]	(**1Fe**)	37.5	CAN	[75]	57	241
[Fe(OTf)$_2$(^{Me2}Pytacn)]	(**1Fe**)	37.5	CAN	[100]	51	295
[Fe(OTf)$_2$(^{Me2}Pytacn)]	(**1Fe**)	37.5	CAN	[125]	70	436
[Fe(OTf)$_2$(^{Me2}Pytacn)]	(**1Fe**)	37.5	CAN	[150]	64	392
[Fe(OTf)$_2$(^{Me2}Pytacn)]	(**1Fe**)	37.5	CAN	[175]	60	328
[Fe(OTf)$_2$(^{Me2}Pytacn)]	(**1Fe**)	37.5	CAN	[200]	58	234
[Fe(OTf)$_2$(^{Me2}Pytacn)]	(**1Fe**)	37.5	NaIO$_4$	[125]	49	18
[Fe(OTf)$_2$(^{Me2}Pytacn)]	(**1Fe**)	50	CAN	[125]	58	460
[Fe(OTf)$_2$(^{Me2}Pytacn)]	(**1Fe**)	12.5	CAN	[125]	82	222

All the reactions were performed in water at 25 ºC [a] Turnover number maximum, TON = (mol of O$_2$/mol of cat.). [b] Turnover frequency under initial rate (TON·h^{-1}). TON and TOF values were averaged of several reactions with usual errors below 10%.

The increase of the CAN concentration, at the fixed iron concentration, leads to a significant TON and TOF increase with a maximum TON peak at [CAN] = 125 mM (TON: 70 and TOF: 436 h^{-1}). A further increase of oxidant concentration produces a slight drop of TON and TOF, which may be due to ligand oxidation and therefore catalyst degradation. A further increase of the activity per catalyst was also observed upon lowering its concentration, rising up to more than 85 TON for 12.2 µM.

SI.2 – Experimental Section

SI.2.1 Experiments of water oxidation reactions

Parallel Pressure Transducer Hardware

The parallel pressure transducer hardware is composed by 8 differential pressure transducers (Honeywell-ASCX15DN, ±15 psi) connected to a hardware data-acquisition system (base on Atmega microcontroller) controlled by a home-developed software program.

The differential pressure transducer Honeywell-ASCX15DN is a 100 microseconds response, signal-conditioned (high level span, 4.5 V) output, calibrated and temperature compensated (0 °C to 70 °C) sensor. The differential sensor has two sensing ports that can be used for differential pressure measurements. The pressure calibrated devices to within ± 0.5 matm was offset and span calibrated *via* software with a high precision pressure transducer (PX409-030GUSB, 0.08% Accuracy). Each of the 8 differential pressure transducers (Honeywell-ASCX15DN, ±15 psi) produce a voltage outputs direct with the pressure difference between the two measuring ports.

The voltage outputs were digitalized with a resolution of 0.25 matm from 0 to 175 matm and 1 matm from 176 to 1000 matm using an Atmega microcontroller with an independent voltage auto-calibration. Firmware Atmega microcontroller and control software were home-developed.

The sensitivity of O_2 analytics allows quantifying the gas formed when the O_2 volume are higher than **50** microL. Therefore, it could not be discarded that small amounts of O_2 were produced by complexes **1Co**, **1Mn**, **6Fe** and/or **7Fe**. However, these small O_2 amounts are negligible with respect to other catalysts studied in this work.

Honeywell-ASCX15DN
pressure transducer
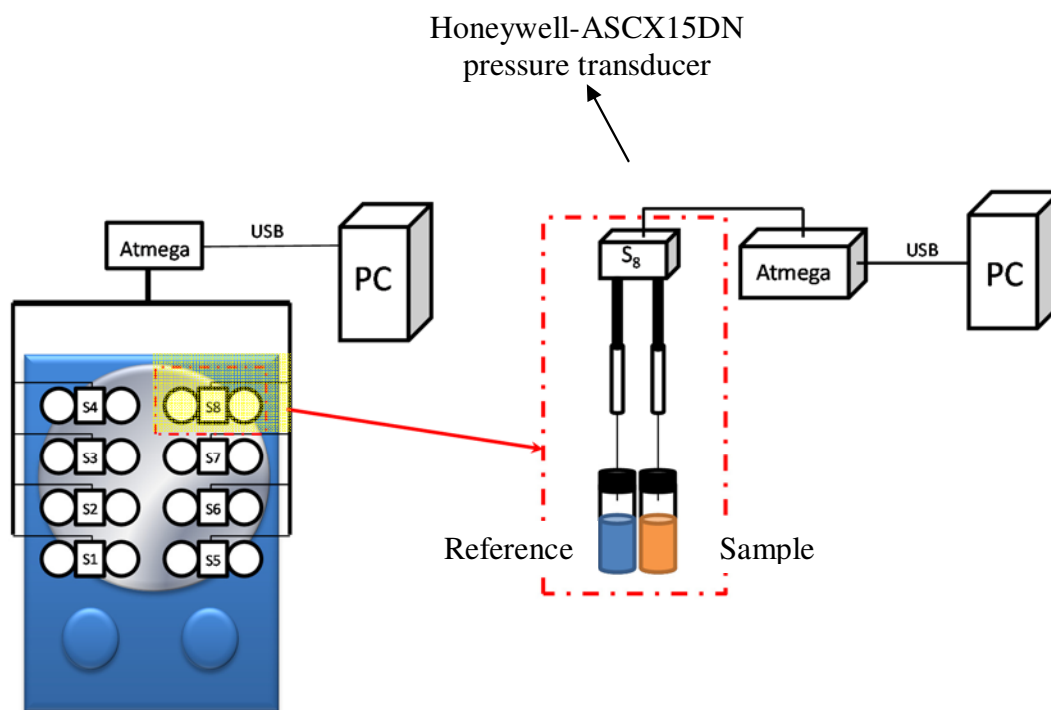
Figure SI.1. Scheme of the parallel pressure transducer hardware.

Air sample analyzed by GC-TCD

Normalization Report   Page 1 of 1

Method Name: C:\EZChrom Elite\Enterprise\Projects\Default\Method\H2O2_55.met
Data: C:\EZChrom Elite\Enterprise\Projects\Default\Data\Zoel\3-2-2011 6-59-10 PM aire
User: System
Acquired: 3/2/2011 6:59:31 PM
Printed: 5/3/2011 10:34:35 AM

3/2/2011 6:59:31 PM C:\EZChrom
Elite\Enterprise\Projects\Default\Method\H2O2_55.met
  C:\EZChrom Elite\Enterprise\Projects\Default\Data\Zoel\3-2-2011 6-59-10 PM aire
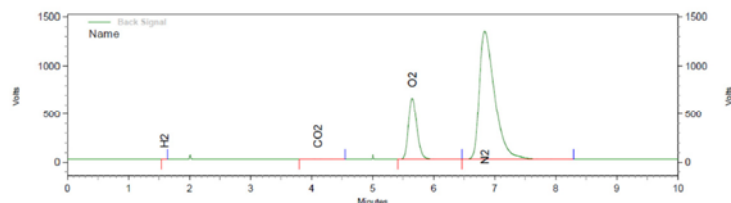
Back Signal
Results

Pk #	Name	Retention Time	Area	Area Percent	Concentration
1	H2	1.590	1343	0.001	
2	CO2	4.100	321647	0.143	
3	O2	5.647	47032557	20.929	
4	N2	6.837	177363620	78.927	
Totals			224719167	100.000	100.000

Normalization Report   Page 1 of 1

Method Name: C:\EZChrom Elite\Enterprise\Projects\Default\Method\H2O2_55.met
Data: C:\EZChrom Elite\Enterprise\Projects\Default\Data\JLL\2-25-2011 3-50-13 PM aire
User: System
Acquired: 2/25/2011 3:50:44 PM
Printed: 6/3/2011 8:02:44 PM

2/25/2011 3:50:44 PM C:\EZChrom
Elite\Enterprise\Projects\Default\Method\H2O2_55.met
  C:\EZChrom Elite\Enterprise\Projects\Default\Data\JLL\2-25-2011 3-50-13 PM aire
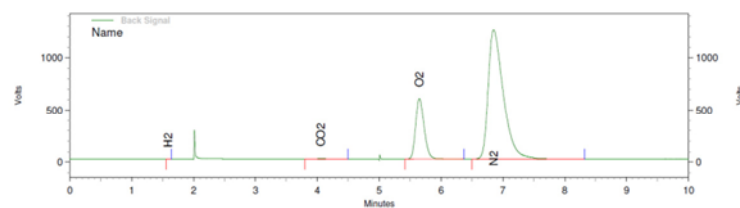
Back Signal
Results

Pk #	Name	Retention Time	Area	Area Percent	Units
1	H2	1.583	924	0.000	
2	CO2	4.060	164452	0.081	%
3	O2	5.650	42516736	20.871	%
4	N2	6.850	161029491	79.048	%
Totals			203711603	100.000	

Reproducibility error of the measurement below 1%

Selected GC-TCD analysis of the gas in the headspace after the pressure reaches a plateau.

1- GC-TCD 0.1 mL headspace gas analyze of a **2OTf** (12.5 μM) with NaIO$_4$ (250 mM) in 5 mL of H$_2$O reaction. (TON: 1304)

Normalization Report

Page 1 of 1

Method Name:	C:\EZChrom Elite\Enterprise\Projects\Default\Method\H2O2_55.met
Data:	C:\EZChrom Elite\Enterprise\Projects\Default\Data\Zoel\3-3-2011 3-57-51 PM ZJ5
User:	System
Acquired:	3/3/2011 3:58:13 PM
Printed:	6/3/2011 7:59:06 PM

3/3/2011 3:58:13 PM C:\EZChrom
Elite\Enterprise\Projects\Default\Method\H2O2_55.met
C:\EZChrom Elite\Enterprise\Projects\Default\Data\Zoel\3-3-2011 3-57-51 PM ZJ5
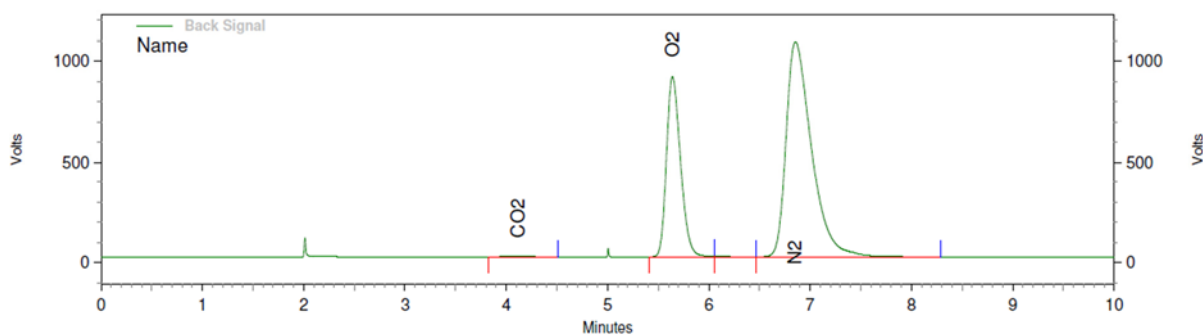
Back Signal Results

Pk #	Name	Retention Time	Area	Area Percent	Units
	H2				
1	CO2	4.110	160991	0.077	%
2	O2	5.640	66100082	31.600	%
4	N2	6.853	142779418	68.256	%

Totals			
		209040491	99.933

2- GC-TCD 0.1 mL headspace gas analyze of a **2OTf** (12.5 µM) with CAN (125 mM) in 10 mL of H_2O reaction. (TON = 360)

Normalization Report

Page 1 of 1

Method Name:	C:\EZChrom Elite\Enterprise\Projects\Default\Method\H2O2_55.met
Data:	C:\EZChrom Elite\Enterprise\Projects\Default\Data\JLL\2-25-2011 4-08-42 PM JLL14
User:	System
Acquired:	2/25/2011 4:09:06 PM
Printed:	6/3/2011 8:01:28 PM

2/25/2011 4:09:06 PM C:\EZChrom
Elite\Enterprise\Projects\Default\Method\H2O2_55.met
 C:\EZChrom Elite\Enterprise\Projects\Default\Data\JLL\2-25-2011 4-08-42 PM JLL14
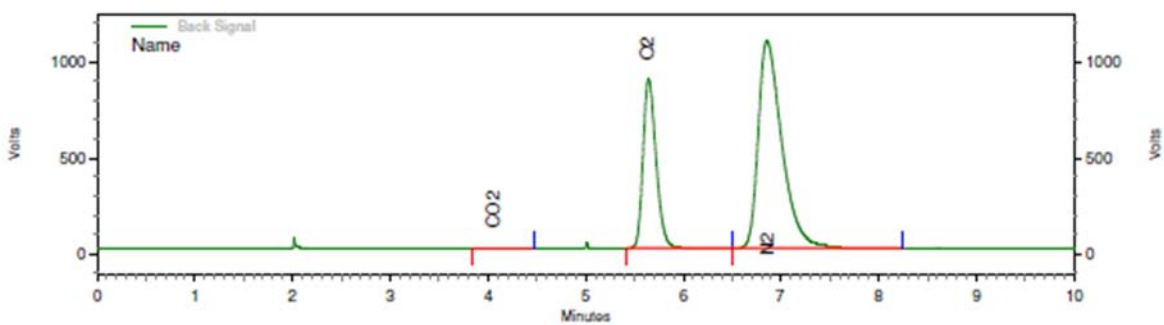
**Back Signal
Results**

Pk #	Name	Retention Time	Area	Area Percent	Units
	H2				
1	CO2	4.053	72398	0.036	%
2	O2	5.643	62488487	30.973	%
3	N2	6.857	139189562	68.991	%
Totals			201750447	100.000	

3- GC-TCD 0.1 mL headspace gas analyze of a **1Fe** (50 μM) with CAN (125 mM)) in 10 mL of H_2O reaction. (TON: 64)

Normalization Report

<div align="right">Page 1 of 1</div>

Method Name:	**C:\EZChrom Elite\Enterprise\Projects\Default\Method\H2O2_55.met**
Data:	**C:\EZChrom Elite\Enterprise\Projects\Default\Data\JLL\2-25-2011 4-32-18 PM JLL13**
User:	**System**
Acquired:	**2/25/2011 4:32:52 PM**
Printed:	**6/3/2011 8:01:52 PM**

2/25/2011 4:32:52 PM C:\EZChrom
Elite\Enterprise\Projects\Default\Method\H2O2_55.met
C:\EZChrom Elite\Enterprise\Projects\Default\Data\JLL\2-25-2011 4-32-18 PM JLL13
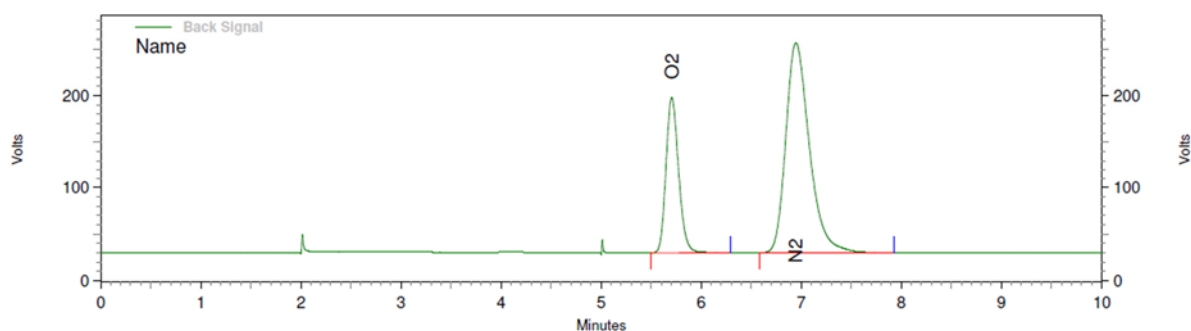
Back Signal
Results

Pk #	Name	Retention Time	Area	Area Percent	Units
	H2				
	CO2				%
1	O2	5.707	11325983	**28.394**	%
2	N2	6.947	28563186	**71.606**	%

Totals				
		39889169	**100.000**	

4- GC-TCD 0.1 mL headspace gas analyze of a **1Fe** (12.5 μM) with CAN (125 mM)) in 10 mL of H_2O reaction. (TON: 84)

Normalization Report

Page 1 of 1

Method Name:	C:\EZChrom Elite\Enterprise\Projects\Default\Method\H2O2_55.met
Data:	C:\EZChrom Elite\Enterprise\Projects\Default\Data\JLL\2-27-2011 1-24-34 PM JLL17
User:	System
Acquired:	2/27/2011 1:24:56 PM
Printed:	6/3/2011 8:49:14 PM

2/27/2011 1:24:56 PM C:\EZChrom
Elite\Enterprise\Projects\Default\Method\H2O2_55.met
C:\EZChrom Elite\Enterprise\Projects\Default\Data\JLL\2-27-2011 1-24-34 PM JLL17

Back Signal Results

Pk #	Name	Retention Time	Area	Area Percent	Units
	H2				
	CO2				%
1	O2	5.690	41427984	**23.498**	%
2	N2	6.917	134877740	**76.502**	%
	Totals		176305724	**100.000**	

Dynamic light scattering (DLS) and real-time visualization and tracking analysis of nanoparticles in solution (NTA).

Following a reviewer suggestion, we carried out different analyses to investigate the possible formation of nanoparticles in solution. Experiments performed include Dynamic Light Scattering (DLS), particle size distribution (from 10 to 1000nm), and particle concentration by real-time visualization and tracking analysis of nanoparticles in a liquid (NTA). All the experiments were performed without filtering the samples to ensure measurement of all particles.

In the DLS experiments, blank samples representative of the catalytic conditions a) H_2O alone, b) CAN (125mM) in water, and C) **1Fe** complex (12.5μM) in water, were compared with analyses of catalytic reactions (CAN (125mM) and **1Fe** complex (12.5μM) after 20 min of the beginning of the reaction, to minimize the presence of nanobubbles. Catalytic reactions had very low concentration of nanoparticles in solution (< 0.1 ppm), that is below the limit of detection (for this instrument, the lowest nanoparticle concentration limit that can be detected for a reliable measurement > 0.1 ppm), and it was not possible to have a reliable size distribution measurement (the range of particle size that can be measured with this DLS instrument is from 0.6 nm to 6000 nm).

NTA experiments are more sensitive in the range of 10 nm to 2000 μm, and measured values of particles/ml were in the same magnitude order 0.76×10^8 particles/ml as the blank experiments (CAN, 125 mM: 0.21×10^8 and **1Fe**, 12.5μM: 0.29×10^8). Therefore we concluded that no significant formation of nanoparticles was detected. Should we take the value of 1×10^8 particles / ml as responsible for the catalytic water oxidation behavior, this value will correspond to an activity of 10^6 s^{-1} TOF. This value is evidently unrealistic since it would be three orders of magnitude higher than that of the OEC (K. N. Ferreira, T. M. Iverson, K. Maghlaoui, J. Barber, S. Iwata, Science 2004, 303, 1831 and A.W. Rutherford, A. Boussac, Science 2004, 303, 1782.)

Therefore, even if nanoparticles are formed in solution, they have no significant effect on the measured catalysis.

SI.2.2 Isotopic labeled water oxidation reactions

SI.2.2.1 Qualitative Isotopic labeled water oxidation

Reactions of water isotopic labeling were conducted under nitrogen.

$H_2^{16}O : H_2^{18}O$ (1:1): A 2 mL vial under N_2 atmosphere was charged with 0.25 mL of $H_2^{18}O$ with [CAN] = 125 mM. Subsequently, 0.25 mL of previously prepared 4 mM **1Fe** in $H_2^{18}O$ was added. After 20 min a gas aliquot was analyzed. N_2 and $^{32}O_2$, $^{34}O_2$ and $^{36}O_2$, 28:50:22, distribution was detected.

$H_2^{16}O$: When replacing $H_2^{18}O$ by $H_2^{16}O$ only N_2 and $^{32}O_2$ was detected.

$H_2^{18}O$: When replacing $H_2^{16}O$ by $H_2^{18}O$ only N_2 and $^{36}O_2$ was detected.
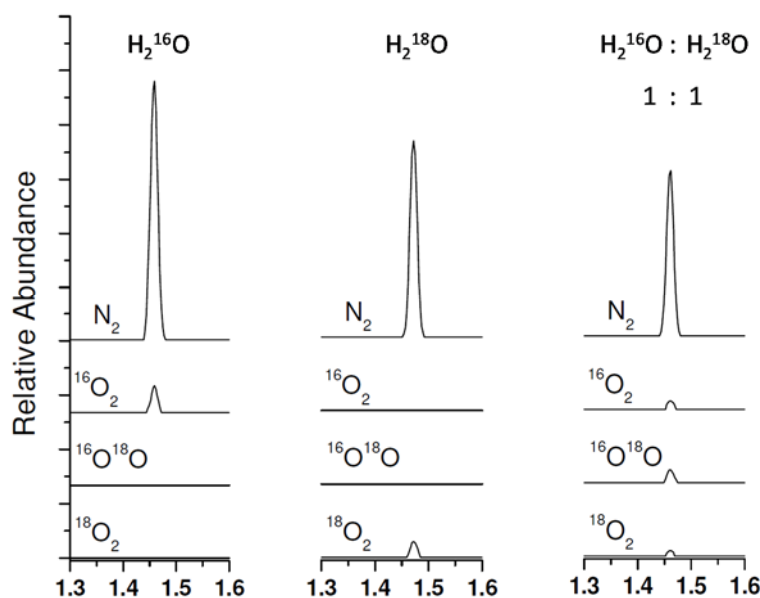
Figure SI.2. Left) GC-MS for the reaction with $H_2^{16}O$. Middle) GC-MS for the reaction with $H_2^{18}O$. Right) GC-MS for the reaction with $H_2^{16}O : H_2^{18}O$ (1:1).

SI.2.2.2 Qualitative Isotopic labeled water oxidation

a) when using cerium (IV) ammonium nitrate as oxidant:

To a Cerium (IV) ammonium nitrate (125mM) dissolved in 4.5 mL of specific $H_2^{18}O/H_2^{16}O$ mixtures (see below) was added a solution of complexes **1Fe** and **2OTf** (40 µM) dissolved in 0.5 mL of the same $H_2^{18}O/H_2^{16}O$ mixture, under N_2 in a 14 mL vial. The isotopic O_2 distribution of gas on the headspace was analyzed after selected times.

1Fe (40 µM)

Theoretical (2.5% $H_2^{18}O$): 95.06% $^{32}O_2$; 4.88% $^{34}O_2$; 0.06% $^{36}O_2$

after 4h, found (2.5% $H_2^{18}O$): 94.93% $^{32}O_2$; 4.99% $^{34}O_2$; 0.08% $^{36}O_2$

1Fe (40 µM)

Theoretical (6% $H_2^{18}O$): 88.36% $^{32}O_2$; 11.28% $^{34}O_2$; 0.36% $^{36}O_2$

after 4h, found (6% $H_2^{18}O$): 88.40% $^{32}O_2$; 11.23% $^{34}O_2$; 0.37% $^{36}O_2$

2OTf (40 µM)

Theoretical (6.5% $H_2^{18}O$): 87.42% $^{32}O_2$; 12.16% $^{34}O_2$; 0.42% $^{36}O_2$

after 1h, found (6.5% $H_2^{18}O$): 87.56% $^{32}O_2$; 12.02% $^{34}O_2$; 0.42% $^{36}O_2$

after 12h, found (6.5% $H_2^{18}O$): 87.64% $^{32}O_2$; 11.94% $^{34}O_2$; 0.41% $^{36}O_2$

b) When using NaIO$_4$ as oxidant:

A solution of complex **2OTf** (40 µM) in 0.5 mL H$_2$^{18}O/H$_2$^{16}O (6.5% H$_2$^{18}O) was added to a solution of NaIO$_4$ (250 mM) in 4.5 mL of H$_2$^{18}O/H$_2$^{16}O (6.5% H$_2$^{18}O), followed by the addition of triflic acid (TfOH, 5µL) under N$_2$ in a 14 mL vial. The isotopic O$_2$ distribution of gas on the headspace was analyzed after selected times. In all cases we obtain good agreement with the theoretical statistic distribution calculated from the water isotopic content.

2OTf (40 µM)

Theoretical (6.5% H$_2$^{18}O): 87.42% ^{32}O$_2$; 12.16% ^{34}O$_2$; 0.42% ^{36}O$_2$

after 2h, found (6.5% H$_2$^{18}O): 87.61% ^{32}O$_2$; 11.98% ^{34}O$_2$; 0.42% ^{36}O$_2$

after 12h, found (6.5% H$_2$^{18}O): 87.27% ^{32}O$_2$; 12.31% ^{34}O$_2$; 0.42% ^{36}O$_2$

after 24h, found (6.5% H$_2$^{18}O): 87.13% ^{32}O$_2$; 12.45% ^{34}O$_2$; 0.42% ^{36}O$_2$

after 44h, found (6.5% H$_2$^{18}O): 86.60% ^{32}O$_2$; 12.96% ^{34}O$_2$; 0.45% ^{36}O$_2$

b) When using NaIO$_4$ as oxidant at short reaction times.

To solid NaIO$_4$ weighted in a 2 mL vial, and placed under N$_2$, a solution of complex **2OTf** (40 µM) in 0.5 mL of H$_2$^{18}O (^{18}O 98%) with TfOH (0.5µL) was added, to generate a final 250mM NaIO$_4$ solution in H$_2$^{18}O. The isotopic O$_2$ distribution in the gas phase of the headspace was monitored by analysis of gas aliquots (0.1 µL) by GC-MS.

The amount of the ^{32}O$_2$ isotopomer due to air contamination was calculated by analyzing the ^{32}O$_2$ amount found in the headspace of a blank reaction prepared under N$_2$. After the ^{32}O$_2$ air contamination subtraction, the ^{32}O$_2$ amount was negligible.

Interestingly $^{36}O_2$ amount was always much higher than $^{34}O_2$. Furthermore, the percentage of $^{36}O_2$ in the oxygen isotopic mixture was changing only slightly during reaction time, from 86% to 90%, being stabilized to 90% after 3 min. (See Figure SI.3). The $^{36}O_2$: $^{34}O_2$ isotopic distribution found corresponds to the ^{18}O incorporation into the oxygen of more than 95% of labeled $H_2^{18}O$, in good agreement with the 98% of labeled $H_2^{18}O$ used (97.5% if ^{16}O of sodium periodate is taken into consideration. Deviation corresponds to a contamination around 15 µL of $H_2^{16}O$).

SI.2.2.3 Study of NaIO$_4$ isotopic oxygen exchange using ESI-MS

O$_2$ Isotopic labeling analysis:

1.- Under a N_2 atmosphere, in a 14 mL vial, a solution of NaIO$_4$ (final concentration 250 mM) in $H_2^{18}O/H_2^{16}O$ (4.5 mL, 6.5% $H_2^{18}O$) was prepared. To this solution it was added a solution of complex **2OTf** (40 µM) in $H_2^{18}O/H_2^{16}O$ (0.5 mL, 6.5% $H_2^{18}O$) also under N_2, followed by the addition of TfOH (5µL) under N_2. After selected times, the isotopic O_2 distribution of gas on the headspace was determined by taking gas aliquots (0.1 µL) that were analyzed by GC-MS. In all cases we obtain good agreement with the theoretical statistic distribution of the isotopic water composition.

2OTf (40 µM)

Theoretical (6.5% $H_2^{18}O$): 87.42% $^{32}O_2$; 12.16% $^{34}O_2$; 0.42% $^{36}O_2$

after 2h**,** found (6.5% $H_2^{18}O$): 87.61% $^{32}O_2$; 11.98% $^{34}O_2$; 0.42% $^{36}O_2$

after 12h, found (6.5% $H_2^{18}O$): 87.27% $^{32}O_2$; 12.31% $^{34}O_2$; 0.42% $^{36}O_2$

after 24h, found (6.5% $H_2^{18}O$): 87.13% $^{32}O_2$; 12.45% $^{34}O_2$; 0.42% $^{36}O_2$

after 44h, found (6.5% $H_2^{18}O$): 86.60% $^{32}O_2$; 12.96% $^{34}O_2$; 0.45% $^{36}O_2$

2.- Under a N_2 atmosphere, in a 2 mL vial, to a NaIO$_4$ (final concentration 250 mM) complex **2OTf** (40 µM) dissolved in 0.5 mL of $H_2^{18}O$ (98% ^{18}O) and TfOH (0.5µL) was added. The isotopic O_2 distribution in the gas phase of the headspace was monitored by analysis of gas aliquots (0.1 µL) by GC-MS.

The amount of the $^{32}O_2$ isotopomer due to air contamination during sampling was calculated by analyzing the $^{32}O_2$ amount found in the headspace of a blank aliquot (0.1 μL) taken from a vial prepared under N_2. After the $^{32}O_2$ air contamination was subtracted, the $^{32}O_2$ amount was negligible.

Interestingly $^{36}O_2$ amount was always much higher that the $^{34}O_2$. Furthermore, the percentage of $^{36}O_2$ in the oxygen isotopic mixture was changing only slightly during the reaction time, from 86% to 90%, being stabilized at 90% after 3 min. (See Figure 3). The $^{36}O_2$: $^{34}O_2$ isotopic distribution found corresponds to a ^{18}O incorporation from $H_2^{18}O$ into O_2 of > 95%.

Study of NaIO$_4$ isotopic oxygen exchange using ESI-MS:

3.- To solid NaIO$_4$ (13.7 mg), a solution of TfOH in $H_2^{18}O$ (98% ^{18}O), (0.1 mL, 1 μL/mL)) was added under a N_2 atmosphere. After complete solubilization of the NaIO$_4$ (less than 30 sec.), an aliquot of the solution was analyzed by ESI-MS. The first ESI-MS spectrum was recorded in less than one minute after addition of the TfOH - $H_2^{18}O$ (98% ^{18}O), (0.1 mL, 1 μL/mL)) solution to the NaIO$_4$.

In figure SI.3 it is represented the ion count for IO$_4^-$ isotopomers, 190.7 ($I^{16}O_4^-$), 192.7 ($I^{16}O_3^{18}O$), 194.7 ($I^{16}O_2^{18}O_2$), 196.7 ($I^{16}O^{18}O_3$), 198.7 ($I^{18}O_4$). As expected, under catalytic conditions the NaIO$_4$ incorporates rapidly ^{18}O from water.[1] The oxygen exchange arrives to equilibrium after about 20 minutes of the dissolution with $H_2^{18}O$.
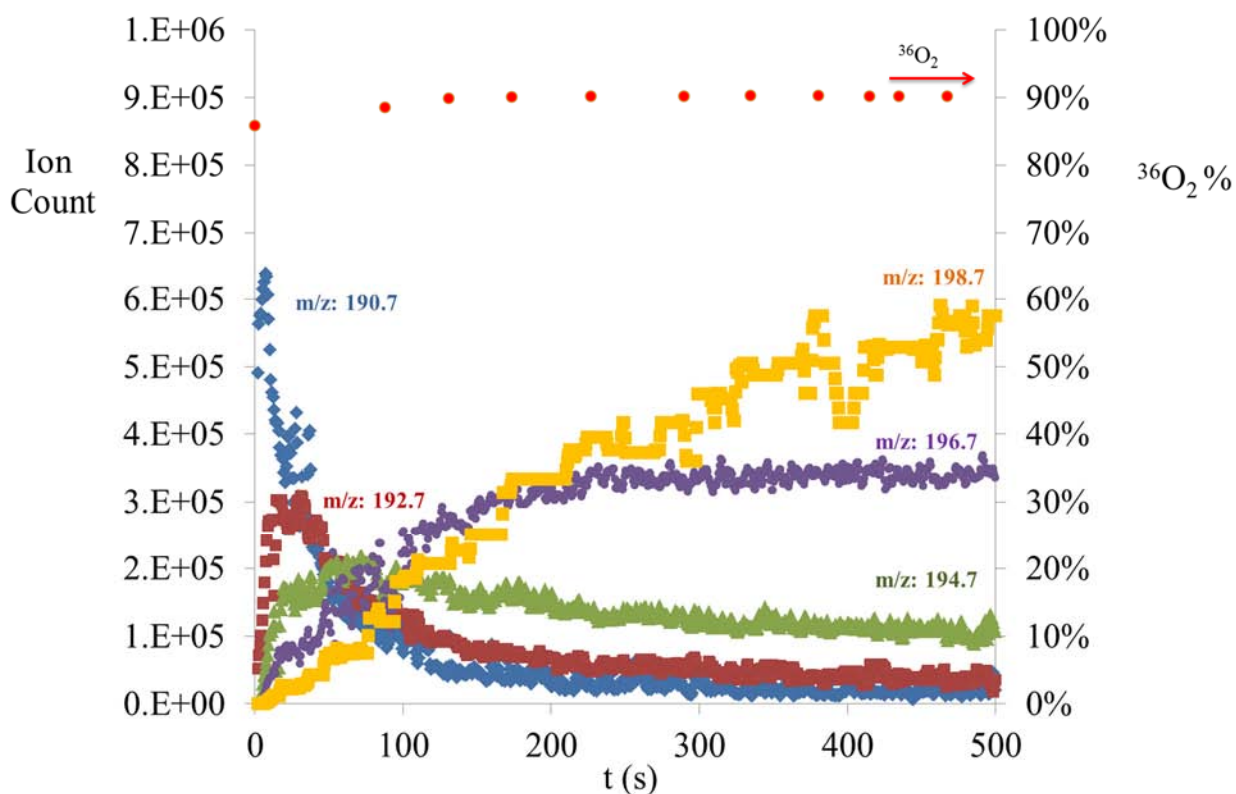
Figure SI.3. m/z ion traces corresponding to the evolution of IO_4^- isotopomers over time, under catalytic conditions, measured by ESI-MS. Axis on the right corresponds to the ion counting for the IO_4^- isotopomers. Axis on the left corresponds to the percentage of ^{36}O measured by GC-MS.

SI.2.3 UV-VIS and ESI-MS characterization of $[Fe^{IV}(O)(H_2O)(^{Me2}Pytacn)]^{2+}$, 1Fe(IV)=O,

in water.
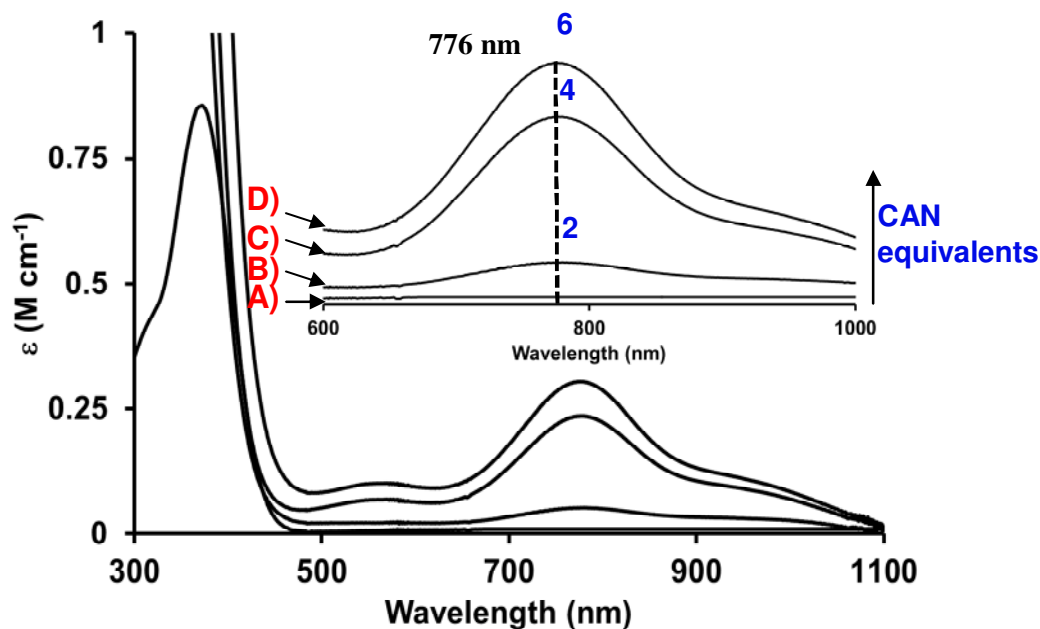
Figure SI.4. A) UV-VIS of compound **1Fe(II)** in water. B) After addition of 2 equivalents of CAN. C) After addition of a total amount 4 equivalents of CAN. D) Full formation of $[Fe^{IV}(O)(H_2O)(^{Me2}Pytacn)]^{2+}$, **1Fe(IV)=O,** when 6 equivalents of CAN were added (λ_{max} = 776 nm, ε = 280 $M^{-1} \cdot cm^{-1}$).
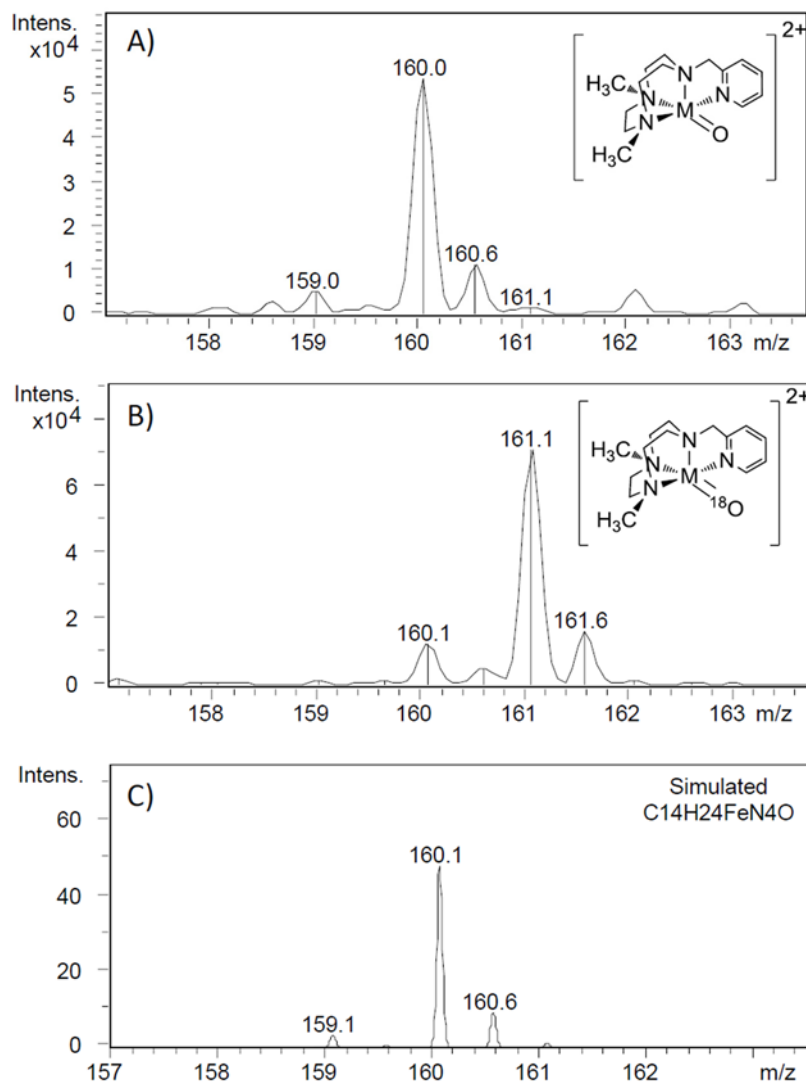
Figure SI.5. Electrospray ionization mass spectrometry (ESI-MS) experiments for complex **1Fe(IV)=O** A) Magnification of the ESI-MS $[Fe^{IV}(O)(^{Me2}Pytacn)]^{2+}$ peak formed by a water solution of $[Fe^{IV}(O)(H_2O)(^{Me2}Pytacn)]^{2+}$ generated using 25 equivalents of CAN in $H_2^{16}O$. The peak and pattern correspond to the molecular ion complex $[Fe^{IV}(O)(^{Me2}Pytacn)]^{2+}$. B) ESI-MS obtained when $H_2^{18}O$ was used instead of $H_2^{16}O$ and using the same experimental procedure that in A. The peak and pattern correspond to the molecular ion complex $[Fe^{IV}(^{18}O)(^{Me2}Pytacn)]^{2+}$. C) Simulated mass spectrum for $[Fe^{IV}(O)(H_2O)(^{Me2}Pytacn)]^{2+}$

SI.2.4 Pressure-Monitored O$_2$ traces
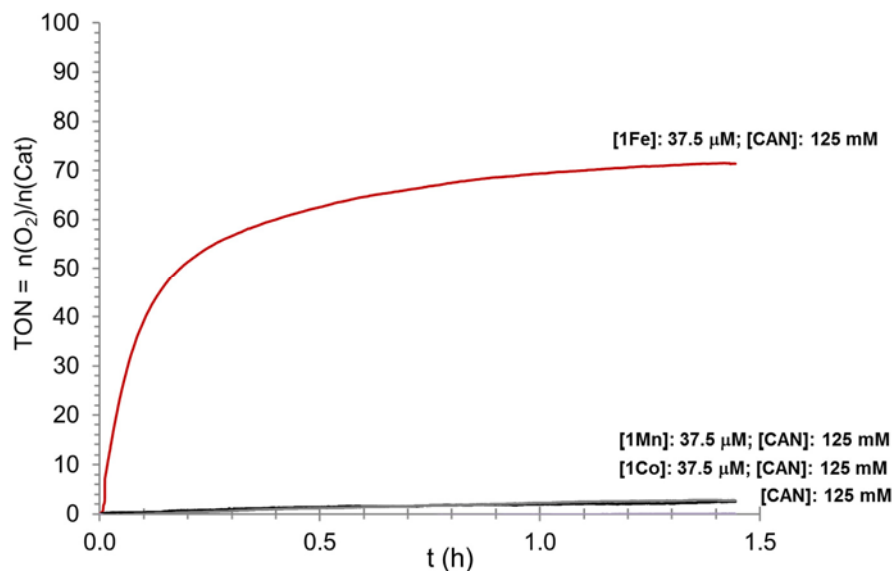
Figure SI.6. Pressure-monitored traces of oxygen formed (TON) as a function of time, measured by a pressure transducer and confirmed by GC. Oxygen traces by reacting 37.5 μM of **1Fe**, **1Co** and **1Mn** complexes with 125 mM of CAN are shown; additionally 37.5 μM of **1Fe** with CAN (75 mM) are also shown. Oxygen trace of 125 mM of CAN without catalysts is also included. Oxygen traces for **1Co**, **1Mn** and CAN perform likewise the system noise.
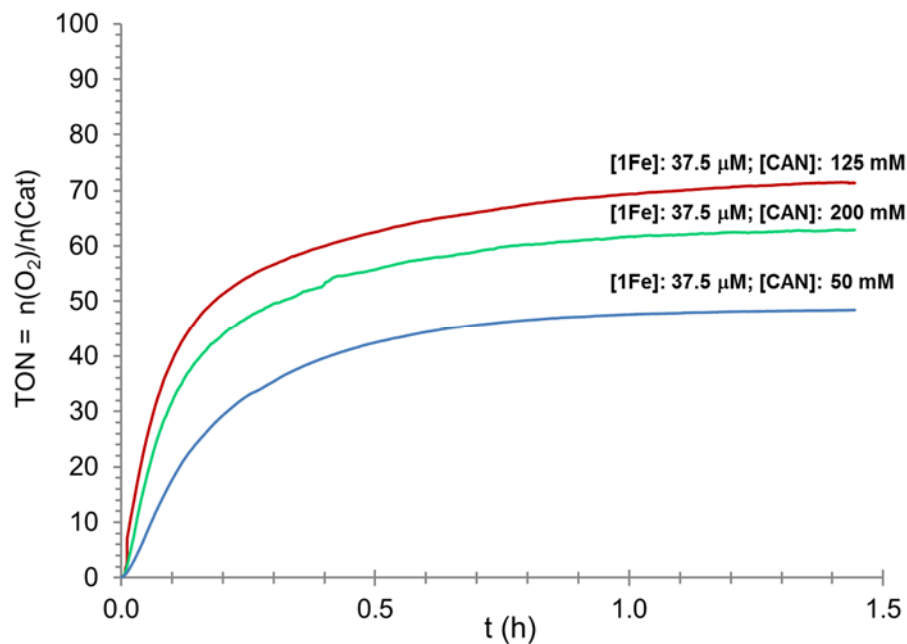
Figure SI.7. Pressure-monitored traces of oxygen formed (TON) as a function of time, measured by a pressure transducer and confirmed by GC. The effect of CAN concentration in the **1Fe** catalytic behavior is shown by comparing the oxygen traces.
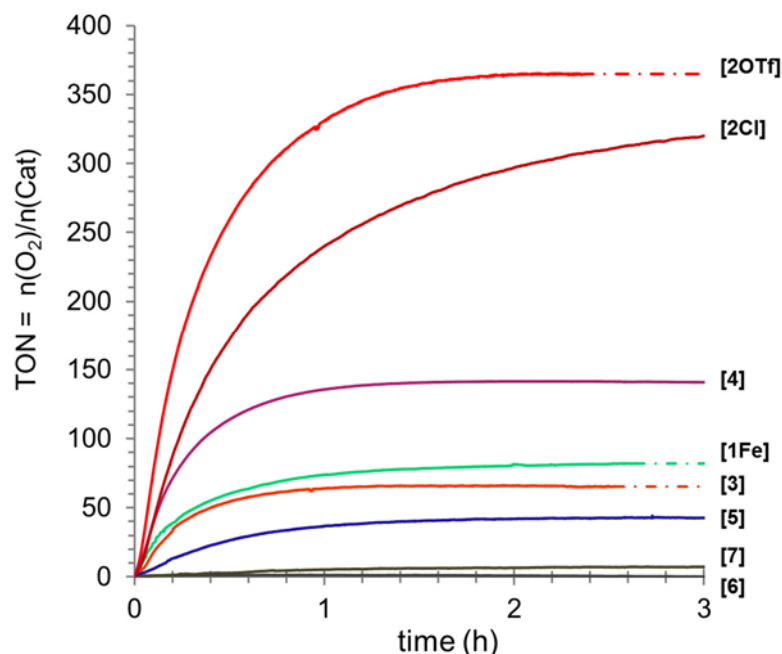
Figure SI.8. Pressure-monitored traces of oxygen formed (TON = n(O_2)/n(iron centers)) as a function of time, measured by a pressure transducer and confirmed by GC. Oxygen traces of studied catalysts under the same reaction conditions (catalyst: 12.5 μM; CAN: 125 mM), in H_2O at 25 ºC.
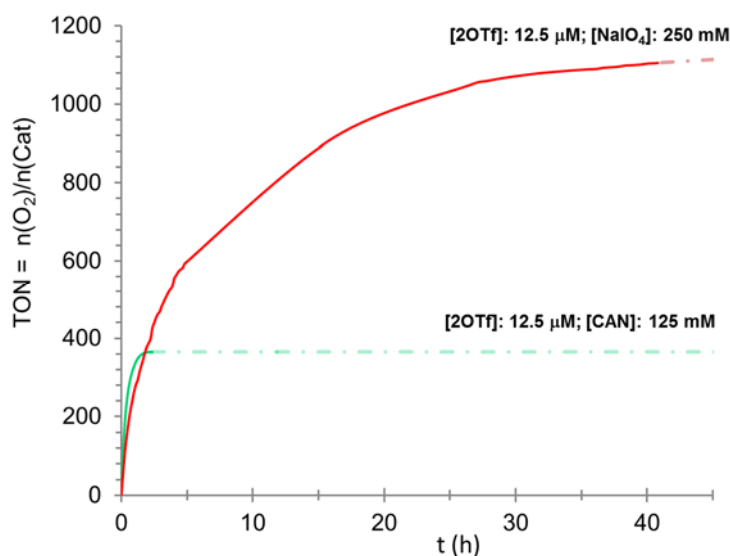
Figure SI.9. Pressure-monitored traces of oxygen formed (TON) as a function of time, measured by a pressure transducer and confirmed by GC. Oxygen traces for catalyst **2OTf** as a function of the oxidant. Reactions performed in H_2O at 25 ºC.
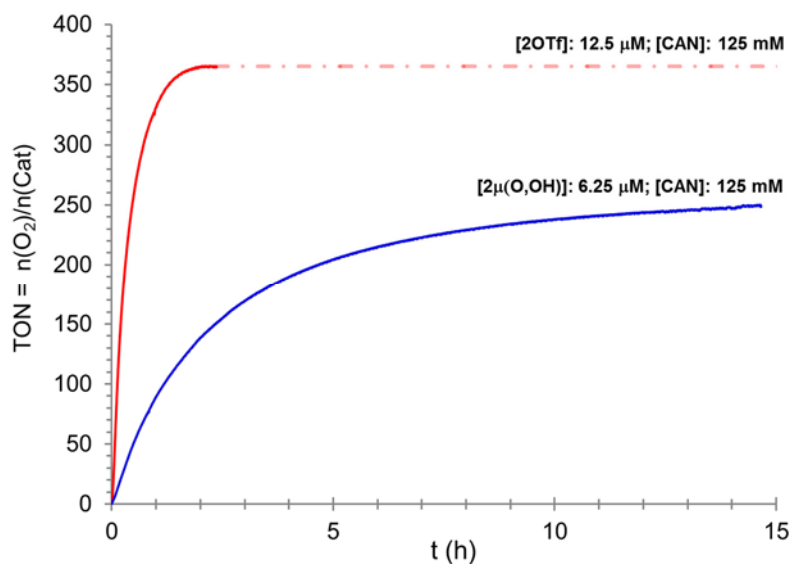
Figure SI.10. Monitored traces of oxygen formed (TON = $n(O_2)/n$(iron centers)) as a function of time, measured by a pressure transducer and confirmed by GC. Oxygen traces for catalyst **2OTf** and dimer **[2μ(O,OH)]** under the same catalytic conditions, in H_2O solution at 25 °C.

SI.2.5 – Kinetic Studies

All the reactions were performed at pH = 1 by adjusting the concentration of protons by adding triflic acid. The required amount of $[Fe^{II}(OTf)_2(^{Me2}Pytacn)]$ complex was dissolved in a quartz UV-Vis cell at 25ºC in 2.7 mL of Milli-Q water. Then, the Fe^{IV}-oxo species $[Fe^{IV}(O)(H_2O)(^{Me2}Pytacn)]^{2+}$ (**$1Fe^{IV}=O$**) was generated by adding 6 equiv. of CAN (≥99.99%) dissolved in 0.3 mL of mili-Q water. The Fe^{IV}-oxo formation was monitored by UV-Vis at 776 nm. After full **$1Fe^{IV}=O$** formation (λ_{max} = 776 nm, ε = 280 $M^{-1} \cdot cm^{-1}$), 0.3 mL of a CAN solution in Milli-Q water was added, obtaining a required concentration of the desired Ce^{IV} [5 – 80 mM]. The Ce^{IV} consumption ((Ce^{IV} consumed) = (Ce^{IV} decay) – (Ce^{IV} self-decay)) was followed by UV-Vis monitoring its UV-Vis band decay at 450 nm. In all cases the O_2 formation was also in parallel monitored using a pressure transducer sensor (as an example, see **Figure SI.11**). Since the reaction solution suffers important changes during the catalytic reactions the initial rate method was applied.
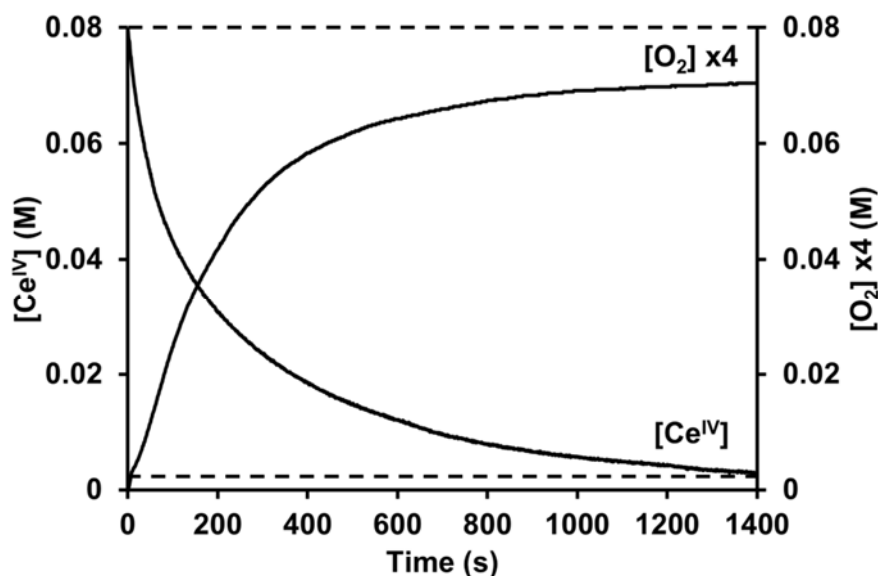
Figure SI.11. Parallel Ce^{IV} decay (at 450 nm) and O_2 evolution monitoring illustrates the 4:1 stoichiometry between Ce(IV) consumed and O_2 formed, in H_2O at 25 ºC ([**$1Fe^{IV}=O$**]$_0$ = 1mM; [Ce^{IV}]$_0$ = 80 mM).

The reaction rates were calculated using the initial rate approximation (10% Ce^{IV} consumed) (**Figure SI.12**). Summary of reaction rates, Ce^{IV} consumption and O_2 yield ($Y(O_2) = n(O_2)/4 \cdot n(Ce^{IV}$ consumed)) are summarized in **Table SI.3**.

Table SI.3. Initial rates for the Ce^{IV} consumption in water oxidation reactions performed by **1Fe^{IV}=O**. Reaction conditions: $[Fe^{IV}] = 0.075 - 2.0$ mM; $[Ce^{IV}] = 5 - 80$ mM; pH = 1.0.

$[Fe^{IV}]_0$ (mM)[a]	$[Ce^{IV}]_0$ mM	Ce^{IV} consumed initial rate (M s^{-1})[b]	$Y(O_2)$[c]	$[Ce^{IV}]_f$ (mM)[d]
0.075	80	$7.3 \times 10^{-5} \pm 1.7 \times 10^{-5}$	>99%	60 ± 7
0.25	80	$3.2 \times 10^{-4} \pm 1.6 \times 10^{-5}$	>99%	42 ± 5
0.5	80	$5.2 \times 10^{-4} \pm 1.6 \times 10^{-4}$	-	27 ± 3
1.0	80	$9.5 \times 10^{-4} \pm 1.6 \times 10^{-4}$	97%	8 ± 2
1.0[e]	80	$9.5 \times 10^{-4} \pm 1.8 \times 10^{-4}$	97%	8 ± 3
1.5	80	$1.4 \times 10^{-3} \pm 3.0 \times 10^{-4}$	89%	7 ± 2
2.0	80	$1.8 \times 10^{-3} \pm 1.4 \times 10^{-4}$	94%	1 ± 1
1.0	5.3	$2.7 \times 10^{-4} \pm 3.3 \times 10^{-5}$	>99%	1 ± 1
1.0	10.7	$4.8 \times 10^{-4} \pm 4.0 \times 10^{-5}$	>99%	1 ± 1
1.0	16	$6.4 \times 10^{-4} \pm 1.4 \times 10^{-5}$	95%	2 ± 1
1.0	21.3	$7.4 \times 10^{-4} \pm 4.1 \times 10^{-5}$	>99%	4 ± 2
1.0	26.6	$8.1 \times 10^{-4} \pm 2.6 \times 10^{-5}$	>99%	2 ± 1
1.0	40	$8.4 \times 10^{-4} \pm 7.5 \times 10^{-6}$	92%	2 ± 1
1.0	53.3	$9.3 \times 10^{-4} \pm 2.7 \times 10^{-5}$	>99%	2 ± 1
1.0	66.6	$9.8 \times 10^{-4} \pm 4.5 \times 10^{-5}$	86%	5 ± 2

All the reactions were performed in water at 25 ºC. [a] **1Fe^{IV}=O** species was generated adding 6 equiv. of CAN. [b] Initial rates were calculated by linear regression after 10% cerium consumption (See Figure SI.13 and Figure SI.17). [c] Yield was calculated by comparing O_2 formed with Ce^{IV} consumed after no more O_2 evolve; ($Y(O_2) = n(O_2)/4 \cdot n(Ce^{IV}$ consumed)). [d] $[Ce^{IV}]_f$: Ce^{IV} concentration after no more O_2 evolve. [e] D$_2$O (99.5%) was used as solvent.

SI.2.5.1 – Reaction order on 1Fe(IV)
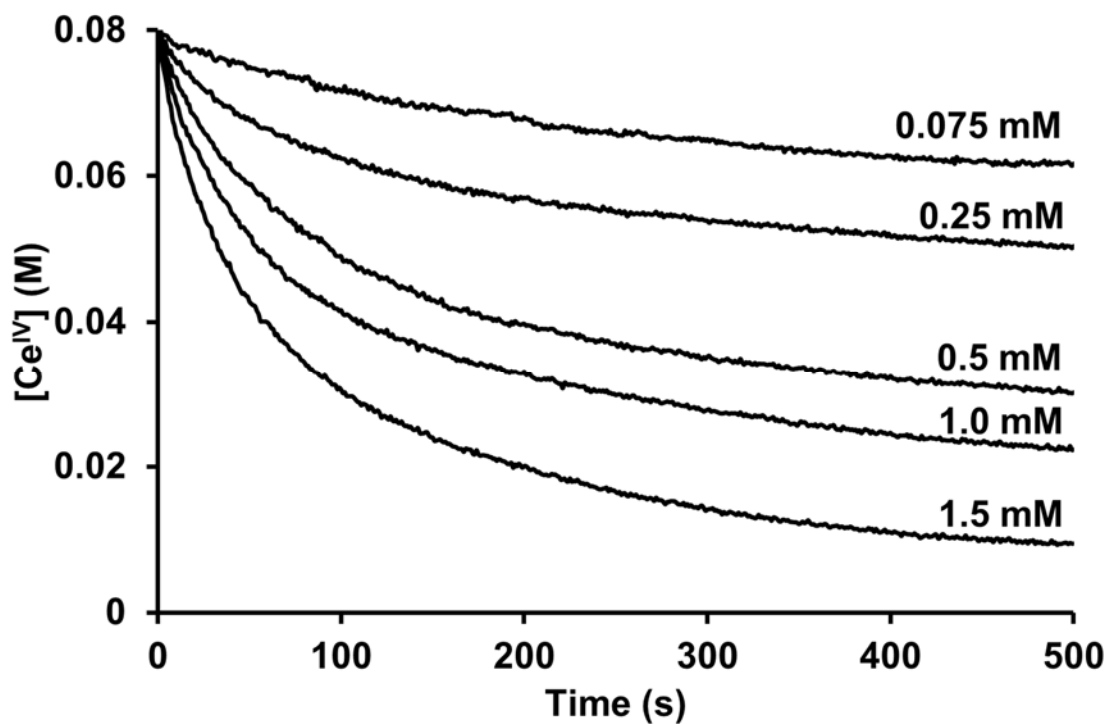
Figure SI.12. Traces of the Ce^{IV} consumed ((Ce^{IV} consumed) = (Ce^{IV} decay) – (Ce^{IV} self-decay)) monitored at 450 nm with different initial **1Fe^{IV}=O** concentrations, in H_2O at 25 ºC: [**1Fe^{IV}=O**] = 0.075 – 2.0 mM; [Ce^{IV}] = 80 mM. Labels on the figure represented the respective initial Fe(IV) concentrations.
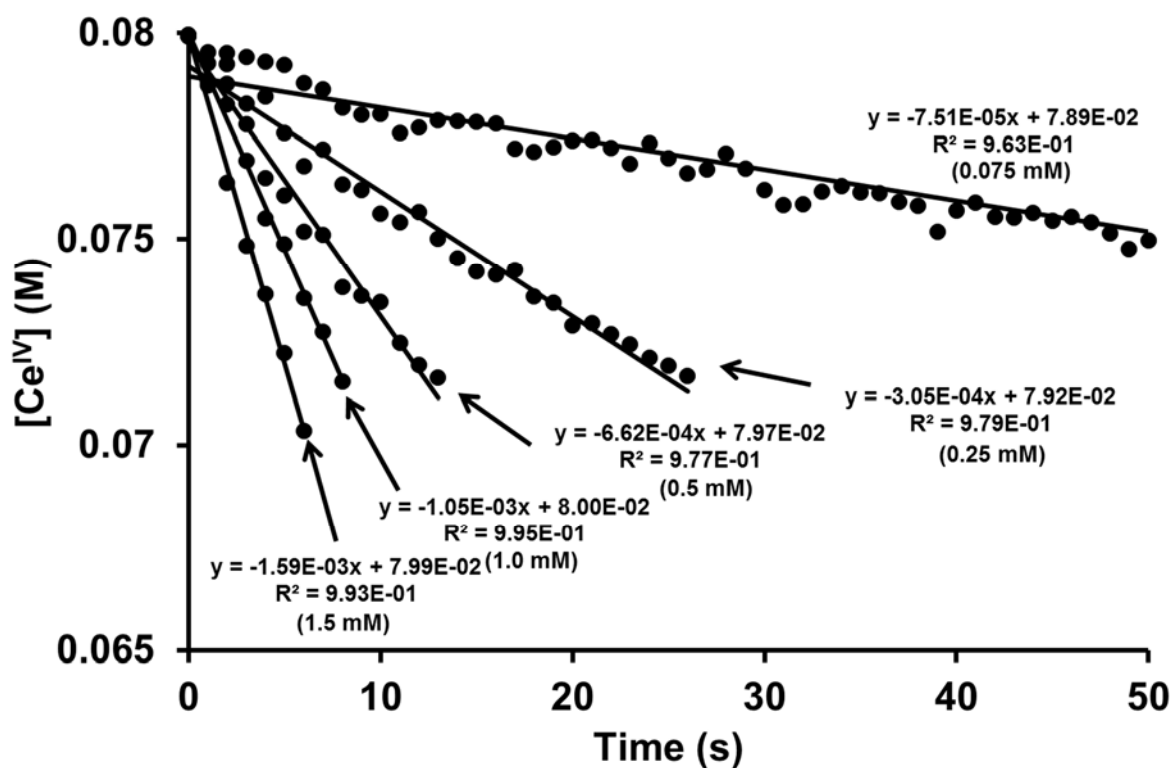
Figure SI.13. Initial rates calculation for the Ce^{IV} consumption $((Ce^{IV}$ consumed$) = (Ce^{IV}$ decay$) - (Ce^{IV}$ self-decay$))$ at different **$1Fe^{IV}=O$** initial concentrations, in H_2O at 25 ºC: [**$1Fe^{IV}=O$**] $= 0.075 - 2.0$ mM; [Ce^{IV}] $= 80$ mM. Between parenthesis are represented the respective initial Fe(IV) concentrations. 10% of Ce^{IV} consumption was used to calculate the initial rates.

y = 8.73E-04x + 6.24E-05
R² = 9.98E-01
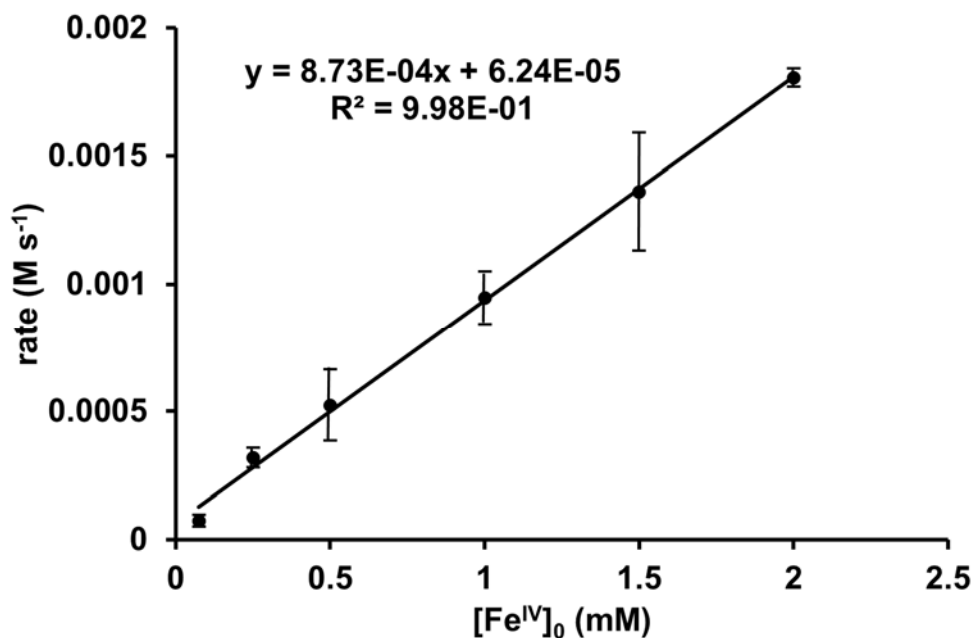
Figure SI.14. Kinetic plot for the initial rate consumption at 10% of Ce^{IV} (80 mM) as a function of the initial concentration of **1Fe^{IV}=O** in H_2O at 25 °C, $[Fe^{IV}]$ = 0.075 – 2.0 mM, $[Ce^{IV}]$ = 80 mM.

y = 0.947x - 6.9389
R² = 0.9908
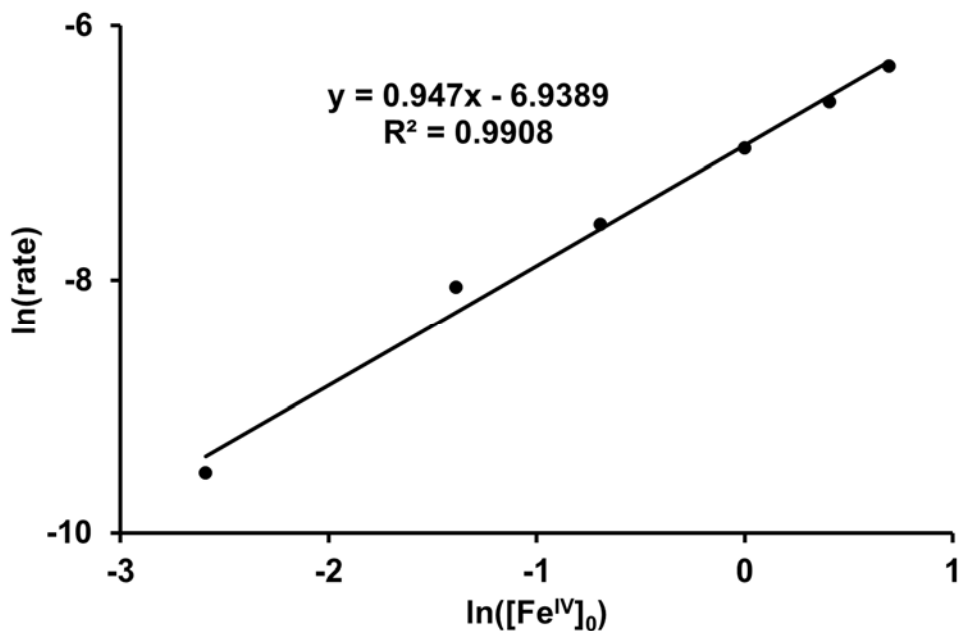
Figure SI.15. Reaction order of **1Fe^{IV}=O** calculated by double-ln plot of initial reaction rates and $[\mathbf{1Fe^{IV}=O}]_0$.

SI.2.5.2 – Reaction order on Ce^{IV}.
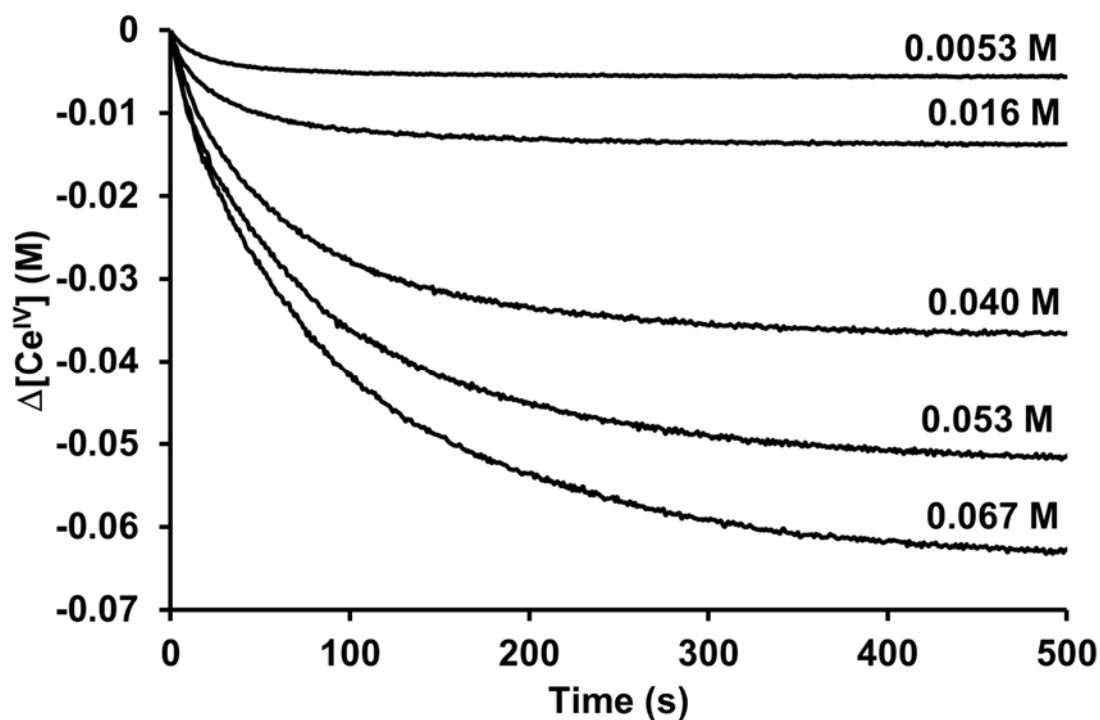
Figure SI.16. Traces of the Ce^{IV} consumed ((Ce^{IV} consumed) = (Ce^{IV} decay) – (Ce^{IV} self-decay)) monitored at 450 nm with different initial Ce^{IV} concentrations, in H$_2$O at 25 ºC: [**1Fe^{IV}=O**] = 1.0 mM; [Ce^{IV}] = 5 - 80 mM. Labels on the figure represented the respective initial Fe(IV) concentrations.
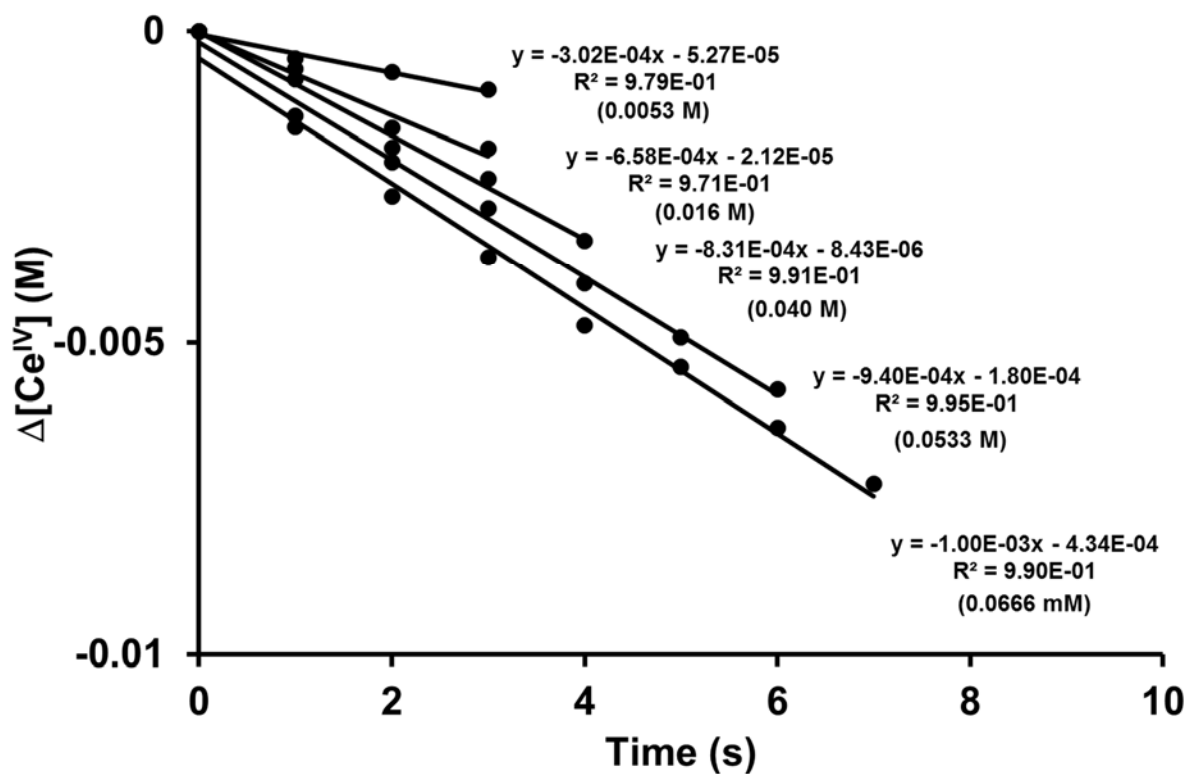
Figure SI.17. Initial rates calculation for the Ce^{IV} consumption consumed ((Ce^{IV} consumed) = (Ce^{IV} decay) – (Ce^{IV} self-decay)) at different $[Ce^{IV}]$ initial concentrations, in H_2O at 25 ºC: $[\mathbf{1Fe^{IV}=O}]$ = 1.0 mM; $[Ce^{IV}]$ = 5 - 80 mM. Between parenthesis are represented the respective initial Ce^{IV} concentrations. 10% of Ce^{IV} consumption was used to calculate the initial rates.
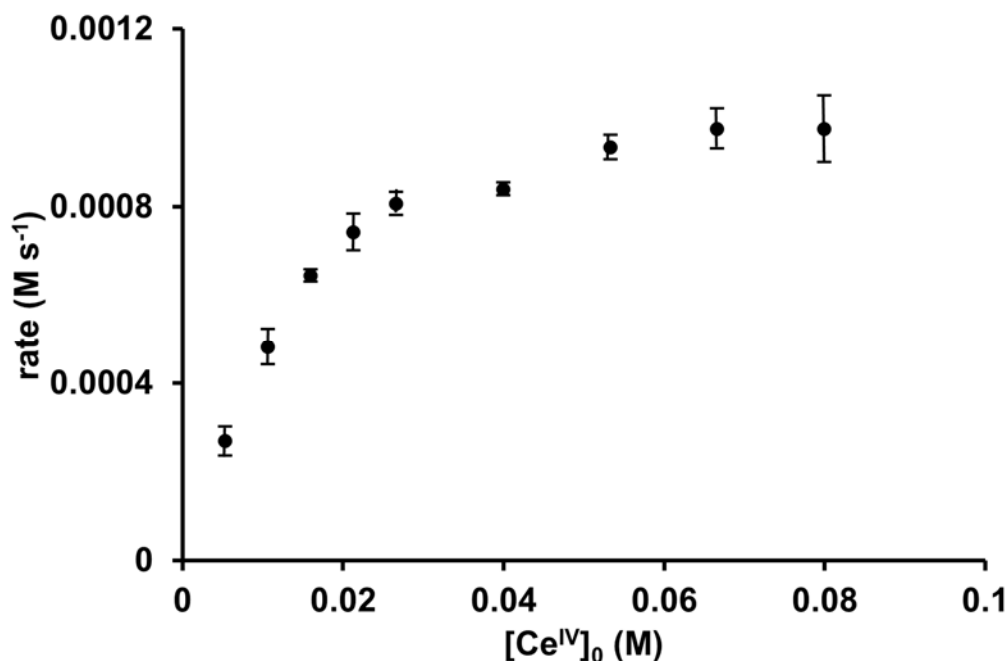
Figure SI.18. Kinetic plot for the initial rate consumption at 10% of Ce^{IV} as function of Ce^{IV} initial concentration, in H_2O at 25 °C: $[\mathbf{1Fe^{IV}=O}]_0 = 1.0$ mM; $[Ce^{IV}]_0 = 5 - 80$ mM.
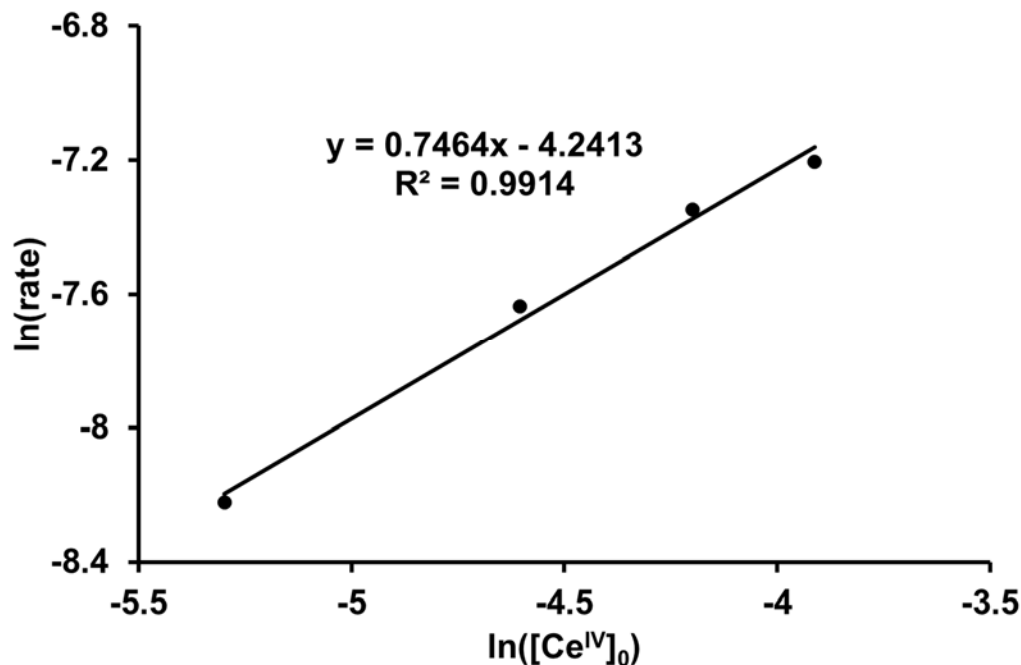
Figure SI.19. Reaction order on Ce^{IV}, calculated by double-ln plot initial rate-$[Ce^{IV}]_0$ at low Ce^{IV} concentrations: $[Ce^{IV}] = 5 - 21.3$ mM. $[\mathbf{1Fe^{IV}=O}]_0 = 1.0$ mM.
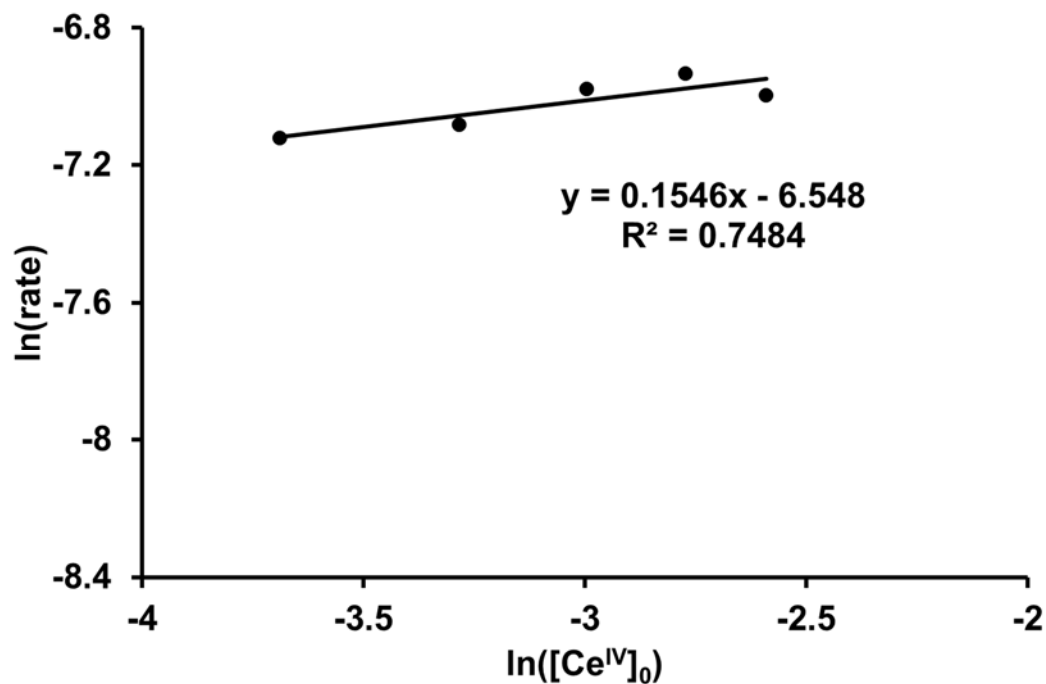
Figure SI.20. Reaction order on Ce^{IV}, calculated by double-ln plot initial rate-$[Ce^{IV}]_0$ at high Ce^{IV} concentrations: $[Ce^{IV}] = 26.6 - 80$ mM. $[\mathbf{1Fe^{IV}{=}O}]_0 = 1.0$ mM.

SI.3 – References.

[1]   F. A. Cotton, G. Wilkinson, C. A. Murillo, M. Bochmann, *Advanced Inorganic Chemistry*, Sixth ed., John Willey & Sons, Inc., **1999**.

CHEMISTRY
A EUROPEAN JOURNAL

Supporting Information

Electronic Effects on Single-Site Iron Catalysts for Water Oxidation

Zoel Codolà, Isaac Garcia-Bosch, Ferran Acuña-Parés, Irene Prat, Josep M. Luis, Miquel Costas,* and Julio Lloret-Fillol*[a]

chem_201301112_sm_miscellaneous_information.pdf

Contents:

SI.1 – Experimental Section

SI.2 – Computational Section

SI.3 – References

SI.4 – CG-TCD analysis

SI.5 – Cartesian Coordiantes.

SI.1 – Experimental Section

Materials. Reagents were purchased from commercial sources and used as received, without any further purification. Cerium(IV) ammonium nitrate (CAN) ≥99.99% trace metals basis and trifluoromethanesulfonic acid ReagentPlus ≥99% were purchased from Sigma-Aldrich®. Solvents were purchased from SDS and Scharlab, purified and dried by passing through an activated alumina purification system (MBraun SPS-800) and stored in an anaerobic glovebox under N2. The preparation of the complexes **1**,[1] **6**[2] and **7**[3] were carried out as previously described. Synthons for the complexes **2**, **3**, **4** and **5** were prepared as previously reported.[4] The coordination to the tacn ligands and the complex formation were done in a similar manner as complex **1**, **6** and **7**. Water (18.2 MΩ•cm) was purified with a Milli-Q Millipore Gradient AIS system.

Physical Methods. UV-VIS-NIR spectra were recorded on an Agilent 8453 diode array spectrophotometer (190-1100nm range) in 1cm quartz cells. A cryostat from Unisoku Scientific Instruments was used for the temperature control. The amount of gas generated was measured with a differential pressure transducer sensor (Honeywell-ASCX15DN, ± 15 psi). Each reaction had their reference reaction which was connected to the other port of the sensor. Further details of the equipment are available elsewhere.[4] Electrospray ionization mass spectrometry (ESI-MS) experiments were performed on a Bruker Daltonics Esquire 3000 Spectrometer, by introducing samples directly into the ESI-source using a syringe pump, without any further dilution. Details of the experiments are described in the corresponding section.

Catalytic gas evolution experiments. A vial containing a CAN (Cerium (IV) ammonium nitrate) aqueous solution (125 mM, 9.5 mL) was connected to one of the pressure transducer sensors, under an air atmosphere. The reaction was initiated by adding a catalysts aqueous solution (250 µM, 0.5 mL) via syringe through septa (final catalyst concentration 12.5 µM and final volume 10 mL, headspace 7.30 ± 0.05 mL). The pH value was found to be 0.7. The oxygen evolution of the reaction was monitored by recording the headspace pressure increase (1 second interval) and calibrate with GC-TCD. The variability of the O_2 yielded was typically less than 10 %.

Gas chromatography identification and quantification of gases. An aliquot of gas captured from the headspace (125 µL) was analyzed with an Agilent 7820A GC System equipped with columns Washed Molecular Sieve 5A, 2m x 1/8" OD,Mesh 60/80 SS and Porapak Q, 4m x 1/8" OD, SS. Mesh: 80/100 SS and a Thermal Conductivity Detector. The O2 amount obtained was calculated by difference between air-O_2 and reaction measured, considering N2 as constant. O_2/N_2 calibration was performed using previously prepared different O_2/N_2 mixtures. Differences with the pressure sensors were less than 10%.

2

Kinetic Studies. The required amount of iron complex was dissolved with 2.7 mL of Mili-Q water in a quartz UV-Vis cell at 25 ºC. Then, the $Fe^{IV}(O)(H_2O)$ intermediate was generated by the addition of 6 eq of CAN dissolved in 0.3mL of Mili-Q water. Once fully formed, a second addition of CAN dissolved in 0.3 mL of a TfOH:H_2O mixture (at pH ~ 0) was added. The amount of TfOH used in each case was adjusted to obtain a final pH of 1. The final concentration of Ce^{IV} was ranged in the experiments from 1.25 to 18.75 mM and the concentration of iron complex from 0.0625 to 1.0 mM. The cerium consumption was monitored at λ of 420 nm. The initial rate method was applied to perform the kinetic study to avoid the consumption of the catalysts during the catalytic reactions. All the kinetic data were treated following the same procedure. Decays of 20% (< 10 seconds) were considered for this study. To this data, the self-decay of a Ce^{IV} blank experiment (same concentration, pH = 1) was subtracted. For the transformation of the absorbance to concentration, blank samples for every Ce^{IV} concentration were linearized and the equation was used as a calibration curve.

SI.1.1 – UV-VIS characterization
SI.1.1.1 The time evolution of the hypsochromic shift during catalysis.
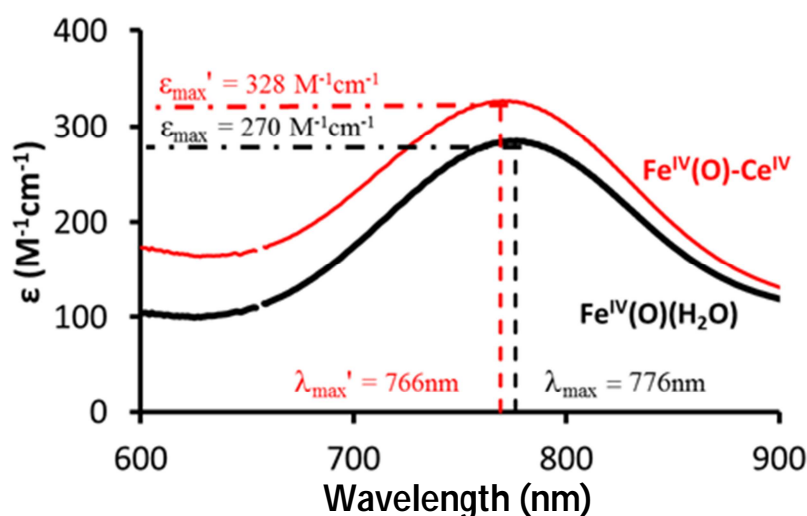
Figure SI.1. UV-Vis spectrum of the iron(IV) oxo band generated by the addition of 6 equivalents of CAN to 1 mM of **1Fe^{IV}(O)(H$_2$O)** (black line, λ_{max} = 776 nm and ε_{max} = 270 M^{-1}·cm^{-1}) and the band after the addition of 25 eq. of CAN corresponding to the formation of a new intermediate, **1Fe^{IV}(O)-Ce^{IV}** (red line, λ_{max} = 766 nm and ε_{max} = 328 M^{-1}·cm^{-1}).

Under UV-Vis monitoring conditions the addition of an excess of Ce^{IV} (studied in the range between 6 to 75 equivalents and pH = 1) produces an instantaneous shift of the characteristic band corresponding to the Fe^{IV}=O bond to lower wavelengths for all complexes. Remarkably, during the catalysis for each complex, the λ_{max} returns gradually to their initial position as the Ce^{IV} is consumed (Figure SI.1 and SI.2). Furthermore, a second addition of Ce^{IV} (valid in the 6 to 75 equivalents range) leads again to the same shift in the UV-Vis band. Subsequently, the initial position of the UV-Vis band was gradually recovered as Ce^{IV} was consumed. These experiments indicate that the cause of the shift in the UV-Vis band is strictly associated with the amount of the Ce^{IV} present in solution. However, water solutions of CAN at pH adjusted with triflic acid to 1 do not exhibit any absorbance at 600-900 nm. In addition, since the pH of the solution was maintained constant at pH = 1 during the consumption of Ce^{IV}, possible modifications in the UV-Vis spectra due to changes in the pH can be ruled out.

Spectral analyses: Hypsochromic shift in λ_{max} and changes in ε_{max} of the low energy UV-Vis band corresponding to [LFe^{IV}(O)(H$_2$O)]$^{2+}$ species during catalysis.

    i.- A hypsochromic shift and an increase in ε_{max} in the band characteristic of the [LFe^{IV}(O)(H$_2$O)]$^{2+}$ species is instantaneously observed for the whole set of complexes when Ce^{IV} (6-75 equivalents range) is added.

ii.- No perturbation of the band is observed when

    ii.a) pH was lowered down to pH = 1 – 0.7. This range of pH corresponds to the value that is reached when CAN is used.

    ii.b) $Ce(NO_3)_3$ was used instead of CAN.

    ii.c) ionic strength was changed by using $La(NO_3)_3$ or NH_4NO_3.

iii.- Water solutions of CAN adjusted with triflic acid to pH = 1 do not exhibit any absorbance between 600 and 900 nm.

iv. Under catalytic conditions the oxygen evolution is inhibited by adding $Ce(NO_3)_3$, but the spectral shift is retained.

Time evolution of the hypsochromic shift during catalysis

i. The hypsochromic shift is time dependent, and the shifted band returns to its initial position when $[Ce^{IV}]$ is consumed during catalysis (**Figures SI.2a** and **SI.2b**). A second addition of Ce^{IV} (6-75 equivalents range) leads again to the same shift in the UV-Vis band (Figure SI.2b). Subsequently, the initial position of the UV-Vis band was gradually recovered as Ce^{IV} was consumed.

ii. Since the pH of the solution is maintained constant at pH = 1 during the consumption of Ce^{IV}, possible modifications in the UV-Vis spectra due to changes in the pH can be ruled out.

In conclusion the UV-VIS shift requires both $[LFe^{IV}(O)(H_2O)]^{2+}$ species and Ce^{IV}, ruling out a hypothetic pH, Ce^{III}, ionic strength effect or combination of pH and Ce^{IV} effect.
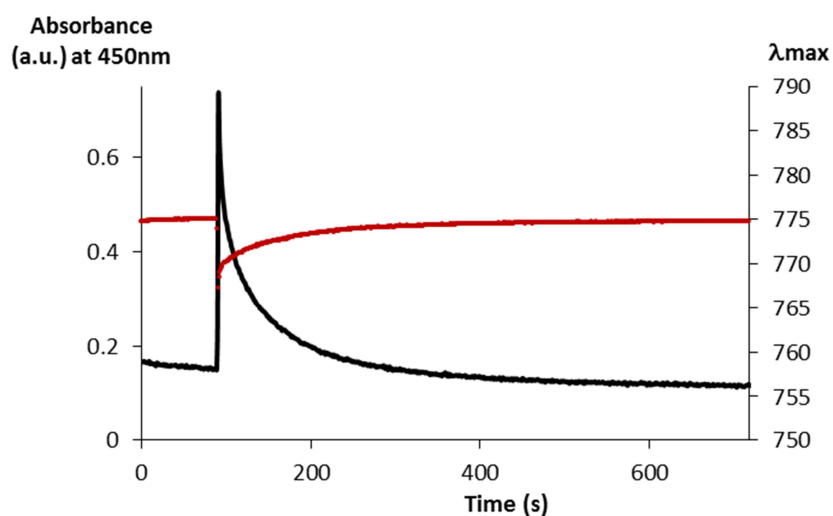
Figure SI.2a. Evolution of the λ_{max} for the UV-Vis band associated to [Fe^{IV}(O)(H$_2$O)(^{H,H}Pytacn)], **1Fe^{IV}=O** (1mM) (red line, right axis) and absorbance for the UV-Vis band at 450 nm corresponding to Ce^{IV} (black line, left axis) when 20 equivalents of CAN are added at t = 100 s, at pH 1 and 25 °C.
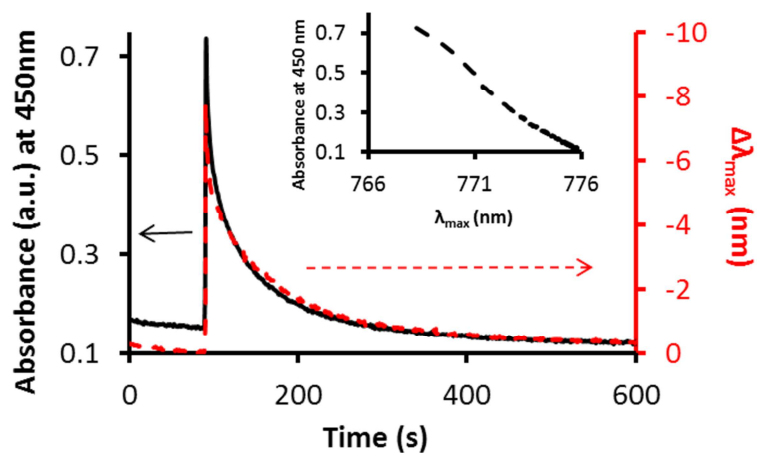
Figure SI.2b. Evolution of the λ_{max} for the UV-Vis band associated to **1Fe^{IV}(O)(H$_2$O)** (1mM) (red dotted line, right axis) and absorbance for the UV-Vis band at 450 nm corresponding to Ce^{IV} (black line, left axis) when 20 equivalents of CAN are added at t = 100 s, at pH 1 and 25 °C. Inset, the linear behaviour of the absorbance vs λ_{max} relates both parameters.

6
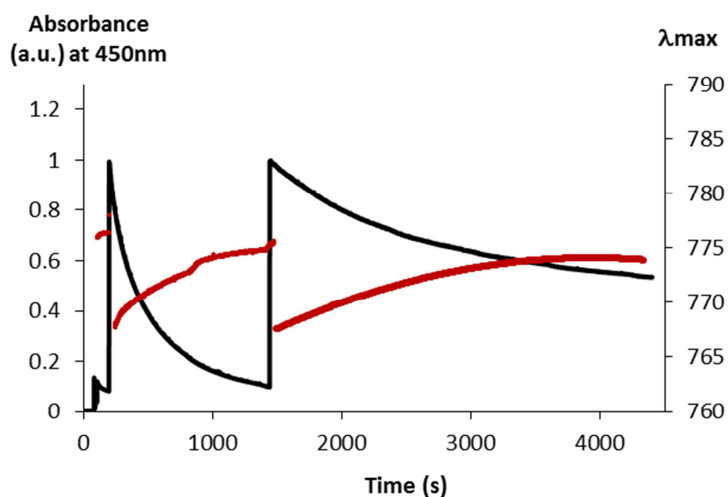
Figure SI.2c. Evolution of the λ_{max} for the UV-Vis band associated to $[Fe^{IV}(O)(H_2O)(^{H,H}Pytacn)]$, **1Fe^{IV}=O** (1mM) (red line, right axis) and absorbance for the UV-Vis band at 450 nm corresponding to Ce^{IV} (black line, left axis) following addition of 75 equivalents of CAN to **1Fe^{IV}=O** (1mM) at t = 100 s, and a second addition of 75 equivalents of CAN at t = 1500 s. (at pH 1 and 25 ºC)

In summary, the saturation of reaction rates at high $[Ce^{IV}]$ together with the hypsochromic shift of λ_{max} most likely indicate a reversible interaction between $[LFe^{IV}(O)(H_2O)]^{2+}$ and Ce^{IV} species preceding the rds.

Calculation of the K_{eq} from the hypsochromic λ_{max} shift.

The hypsochromic shift and absorbance change for the **$[LFe^{IV}(O)(H_2O)]^{2+}$** characteristic band is dependent on Ce^{IV} concentration. By analysing abs_{max} at 766 nm versus $[Ce^{IV}]_0$ concentration for a series of catalytic reactions, the corresponding equilibrium constant could be obtained, with a value of 270 ± 20. This equilibrium constant is in good agreement with the one obtained from the kinetic analysis of the catalytic reactions monitoring Ce^{IV} consumption, $K_{eq} = 230 \pm 20$ (See section below).

Details in the calculation of K_{eq}: As depicted in Figure 3 there is an increase in absorbance at λ of 766 nm provoked by the presence of Ce^{IV}. The Ce^{IV} and Ce^{III} ions do not absorb in the range of 600-800 nm, and we previously discard any other possibility different to a Fe^{IV}-Ce^{IV} interaction. This absorbance change becomes saturated by the increase of Ce^{IV} concentration in solution. The saturation is reached at around 50 eq. of Ce^{IV}, in concordance with the saturation observed for the spectra shift.

This saturation in absorbance can be mathematically treated such as a complexation (or titration) curve, considering that the absorbance change at λ of 766 nm is a result from a reversible reaction of **$[LFe^{IV}(O)(H_2O)]^{2+}$** with Ce^{IV} to form an intermediate I .

7

7
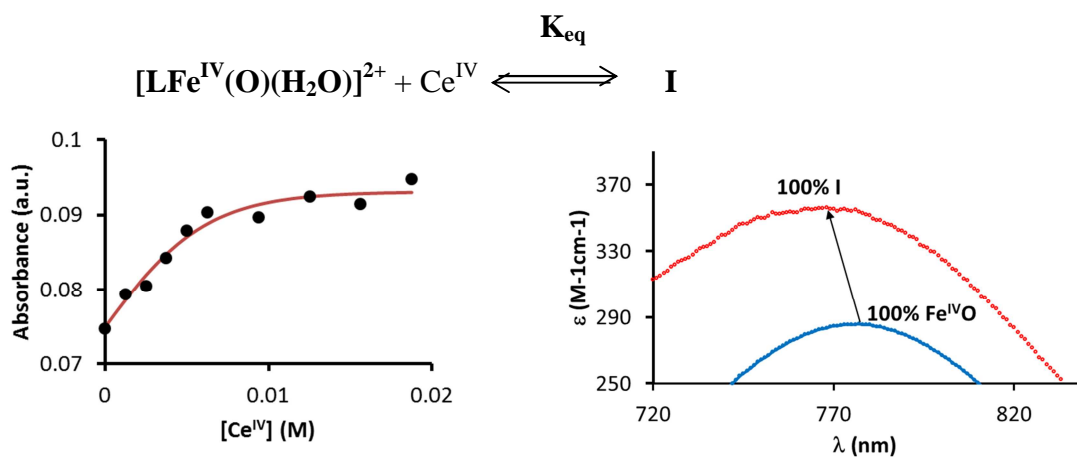
Figure SI.3. Left) Absorbance at λ of 766 nm versus the concentration of Ce^{IV}. Right) Magnification of the UV-Vis spectrum region corresponding to the low energy band of $[LFe^{IV}(O)(H_2O)]^{2+}$. In blue, the band of $[LFe^{IV}(O)(H_2O)]^{2+}$, $[Fe^{IV}O]_o$ and in red the shifted band after the addition of 20 eq. of CAN, reflecting the formation of a new intermediate, I. (at pH 1 and 25 ºC)

We calculated K_{eq} from the analysis of the absorbance (Abs) at the maximum of the band (at 766 nm) at different CAN concentrations. From the $Abs_{titration}$ obtained for the different CAN concentrations the concentration of $[LFe^{IV}(O)(H_2O)]^{2+}$ ($Fe^{IV}O$) and intermediate (I) can be straightforward obtained. The obtained $[Fe^{IV}O]_i$ and Fe^{IV}-Ce^{IV} adduct concentrations are plotted versus the $[Ce^{IV}]$ in the following figure.
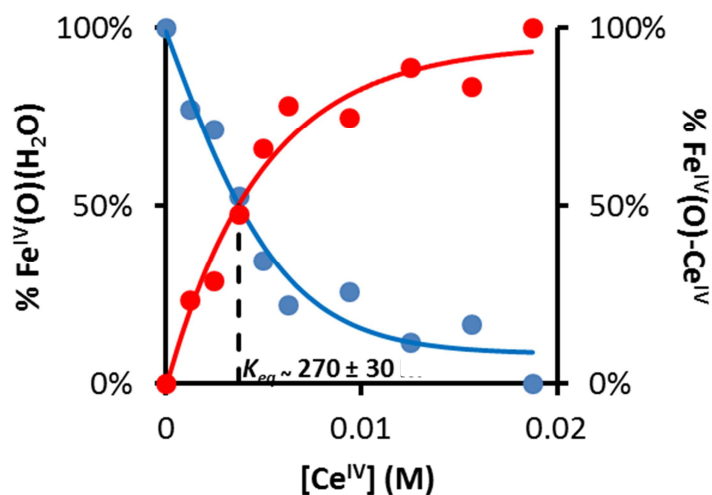
Figure SI.4. Percentage of **1Fe^{IV}(O)(H$_2$O)** and **1-Fe^{IV}(O)–Ce^{IV}** calculated from the absorbance at 766 nm versus concentration of Ce^{IV}. The K_{eq} is calculated at the equivalence point.

Now, from $[Fe^{IV}O]_i$ and $[I]_i$ at known Ce^{IV} concentration the K_{eq} constant can be obtained at the equivalence point as follows.

$$K_{eq} = \frac{[I]_i}{[Fe^{IV}O]_i[Ce^{IV}]} \xrightarrow{[I]_i = [Fe^{IV}O]_i} K_{eq} = \frac{1}{[Ce^{IV}]}$$

The good agreement between the K_{eq} constant calculated from the kinetic analysis (Saturation Model) and from complexation gives an additional consistency to the model.

In Figure SI.5 it is represented the evolution traces for the **1-Fe^{IV}(O)** and the **[I]** obtained from the analysis of the UV-Vis band shift during the time.

9
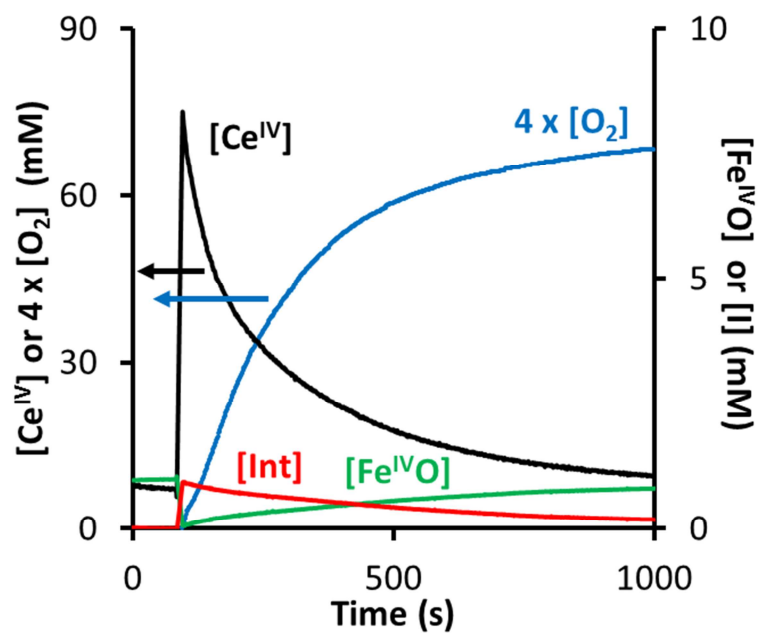
Figure SI.5. Monitoring traces for oxygen evolution (black curve), cerium(IV) consumption (blue curve) and **[1-Fe^{IV}(O)]** (green curve) and **[I]** intermediate (red curve) concentration along the course of the reaction in H$_2$O at 25 ºC and pH 1. At t = 0 s there is in solution 1 mM of **1-Fe^{IV}(O)** previously prepared. At t = **100** s, 75 eq. of Ce^{IV} were added. (at pH 1 and 25 ºC)

4. Effects on the UV-Vis shift and on O_2 evolution rate constant by modification of the Ce^{IV}/Ce^{III} ratio.

Under catalytic conditions, addition of $Ce(NO_3)_3$ inhibits the oxygen evolution, but the spectral shift of the low energy UV-Vis band ($\lambda_{max} \sim 750$ nm) is maintained. On the other hand, addition of $La(NO_3)_3 \cdot (H_2O)_6$ or NH_4NO_3 does not affect the UV-Vis spectral features, nor the O_2 evolution rate. Moreover, the changes in pH do not modify the spectral band in those solutions.

Interpretation of these observations can be done by taking into consideration redox modification. When the Ce^{IV}/Ce^{III} ratio is modified, the redox potential decreases in concordance with the Nernst equation. For instance, a solution containing 1 mM of **$1Fe^{IV}=O$** and 75 mM of CAN, the presence of 127 mM of $Ce(NO_3)_3 \cdot (H_2O)_6$ reduces the redox potential.

Therefore, the reduction of the red-ox potential does not appear to inhibit the initial reversible reaction of **$1Fe^{IV}=O$** and CAN defined by K_{eq}, and which causes the spectral shift. However, this redox reduction inhibits the subsequent reaction, defined by k_2.

These observations are also very conclusive in discarding a reaction mechanism involving initial outer sphere electron transfer from **$1Fe^{IV}=O$** to Ce^{IV} to form a $Fe^V=O$ species, that accumulates $Fe^V=O$ in solution at large Ce^{IV} concentration, and which then undergoes electrophilic attack over the water molecule.
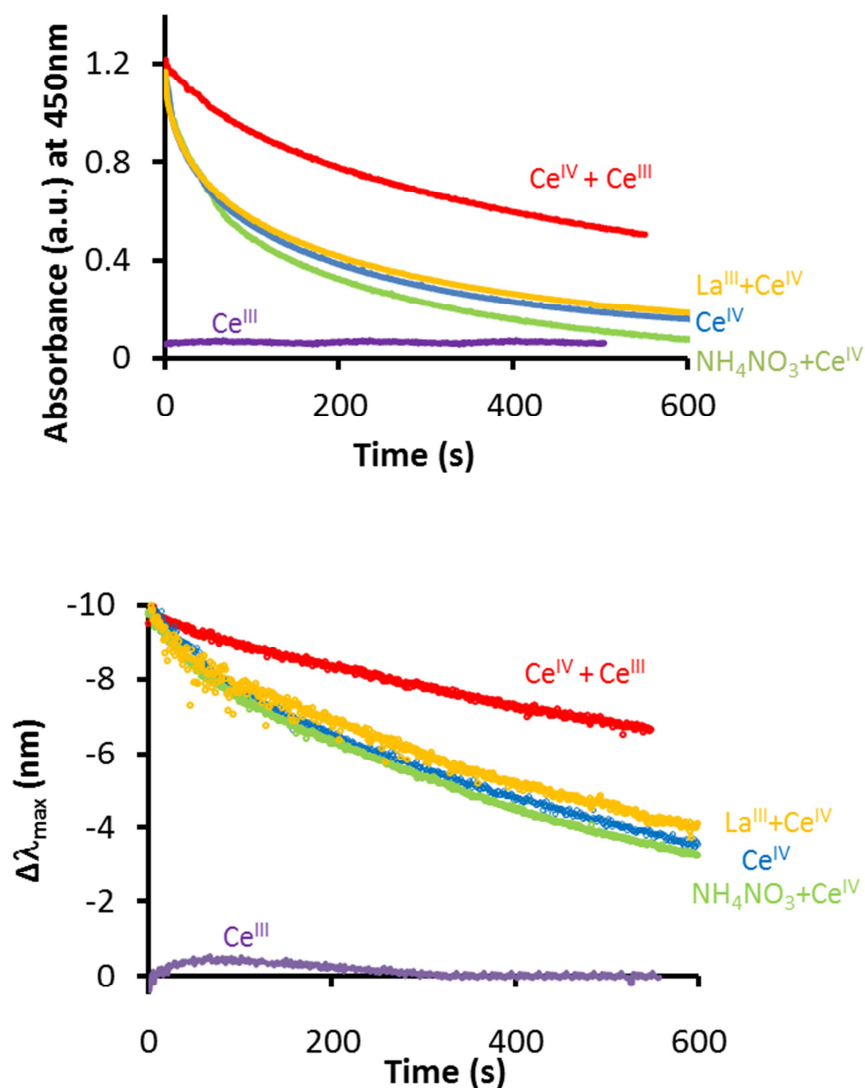
Figure SI.6. Plots of the effect of the ionic strength on the reaction rate of the Ce^{IV} consumption and in the spectral shift over time. Top) traces of the Ce^{IV} absorbance measured at λ value of 450 nm and Bottom) spectral shift evolution of the low energy band (λ_{max} = 776 nm) after the addition of NH_4NO_3 (762 mM, green dots), $Ce(NO_3)_3 \cdot (H_2O)_6$ (127 mM, red dots) and $La(NO_3)_3 \cdot (H_2O)_6$ (127 mM, gold dots) to a solution containing **$1Fe^{IV}(O)(H_2O)$** (1 mM) and CAN (75 mM). These concentrations of reagents yield the same ionic strength, temperature (25ºC) and pH (1) for all the experiments.

SI.1.2. – ESI-MS Characterization

ESI-MS were recorded on an esquire 6000 ESI ion Trap LC/MS (Bruker Daltonics) equipped with an electrospray ion source. The instrument was operated in the positive ESI(+) ion mode. Samples were introduced into the mass spectrometer ion source directly via a KdScientific syringe pump without any further dilution, at 4µL/min. Nitrogen was employed as both a drying and nebulizing gas. Experimental Parameters: Nebulizer 7.89 psi, trap drive 30.0, capillary exit 103 V, dry temp 300 ºC, dry gas 4.99 l/min, skimmer 40 V. Electrospray ionization mass spectrometry (ESI-MS) experiments

for complexes **1**, **2**, **3** and **4**. The experiments were performed adding 1mM of complex into a MiliQ aqueous solution of CAN, 25 mM and immediately the mass spectrum recorded.
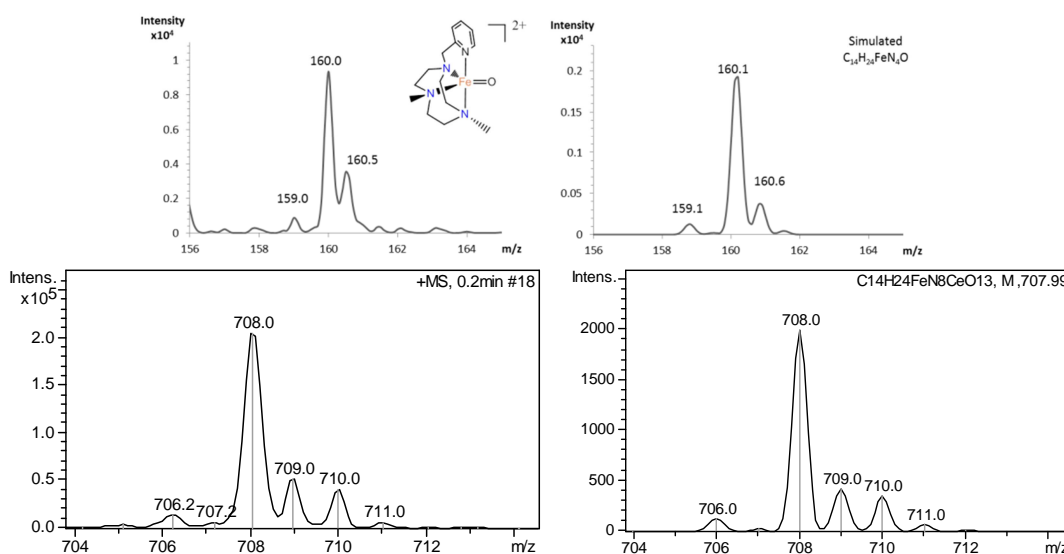
Figure SI.7. Top) magnification of the **1-Fe^{IV}=O** (left) and simulated (right) Bottom) left, magnification of dimer containing 1-Fe^{IV}=O and Ce(NO$_3$)$_4$ and simulated (right)
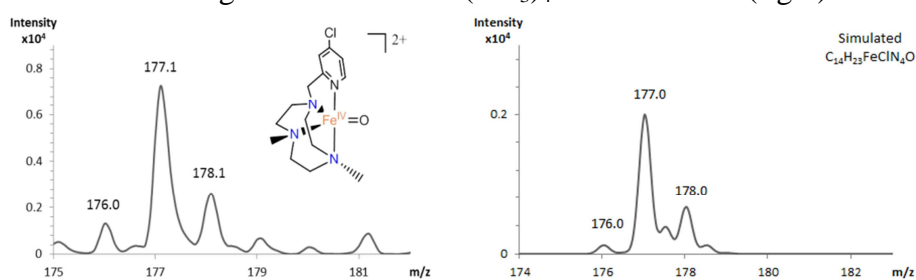
Figure SI.8. Magnification of the **2-Fe^{IV}=O** (left) and simulated (right).
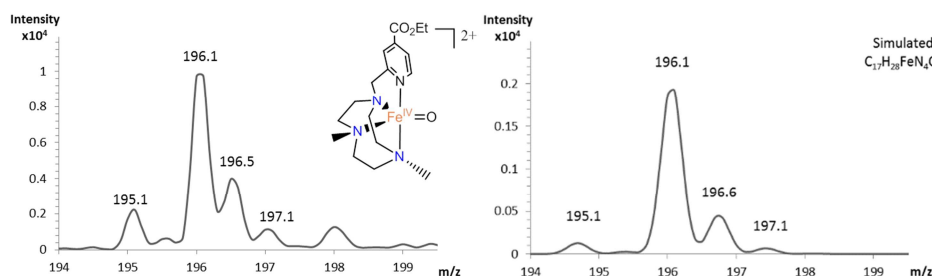
Figure SI.9. Magnification of the **3-Fe^{IV}=O** (left) and simulated (right).
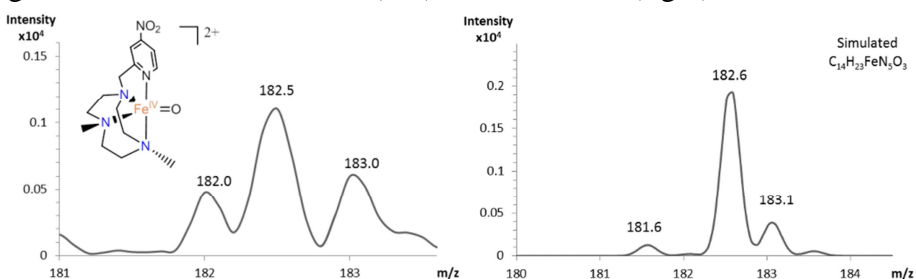
Figure SI.10. Magnification of the **4-Fe^{IV}=O** (left) and simulated (right).

SI.1.3 – Kinetic Studies

The required amount of iron complex was dissolved with 2.7 mL of Mili-Q water in a quartz UV-Vis cell at 25 ºC. Then, the Fe^{IV}(O)(H$_2$O) intermediate was generated by the addition of 6 eq of CAN

13

dissolved in 0.3mL of Mili-Q water. Once fully formed, a second addition of CAN dissolved in 0.3 mL of a TfOH:H_2O mixture (at pH ~ 0) was added. The amount of TfOH used in each case was adjusted to obtain a final pH of 1. The final concentration of Ce^{IV} was ranged in the experiments from 1.25 to 18.75 mM and the concentration of iron complex from 0.0625 to 1.0 mM. The cerium consumption was monitored at λ of 420 nm.

The initial rate method was applied to perform the kinetic study to avoid the consumption of the catalysts during the catalytic reactions. All the kinetic data were treated following the same procedure.

Decays of 20% (<10 seconds) were considered for this study. To this data, the self-decay of a Ce blank experiment (same concentration, pH = 1) was subtracted.

For the transformation of the absorbance to concentration, blank samples for every Ce^{IV} concentration were linearized and the equation was used as a calibration curve.
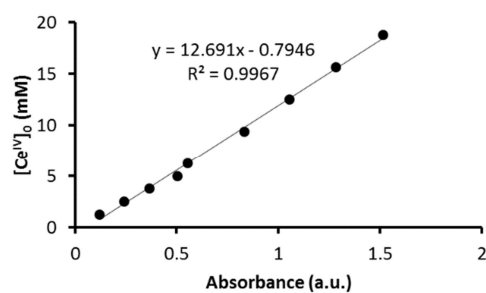
Figure SI.11. Absorbance to concentration equation obtained by fitting Ce^{IV} initial concentration versus the absorbance.

SI 1.3.1 – Reaction rate of cerium decay versus Fe^{IV} and Ce^{IV} concentrations
S.I. 1.3.1.1 Complex 1
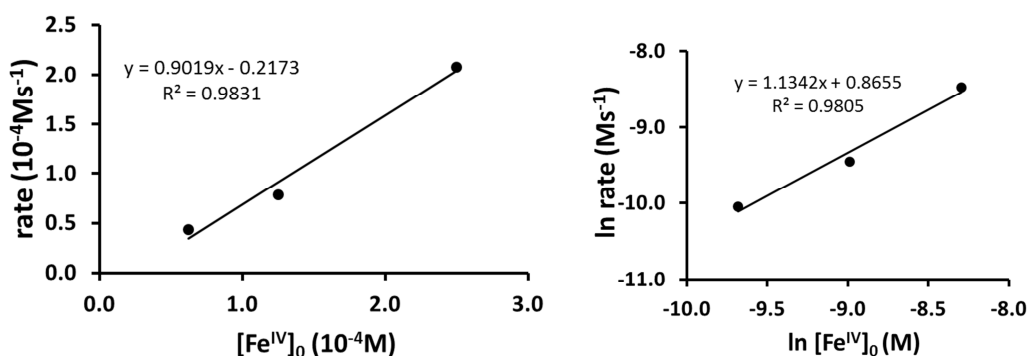
Figure SI.12. (left) Initial rates versus initial concentration of $1Fe^{IV}=O$ in H_2O, pH = 1 at 25 °C, $[Fe^{IV}]$ = 0.0625 – 1.0 mM, $[Ce^{IV}]$ = 18.75 mM. (right) Calculation of the reaction order of $1Fe^{IV}=O$ by plotting the double logarithm.

14
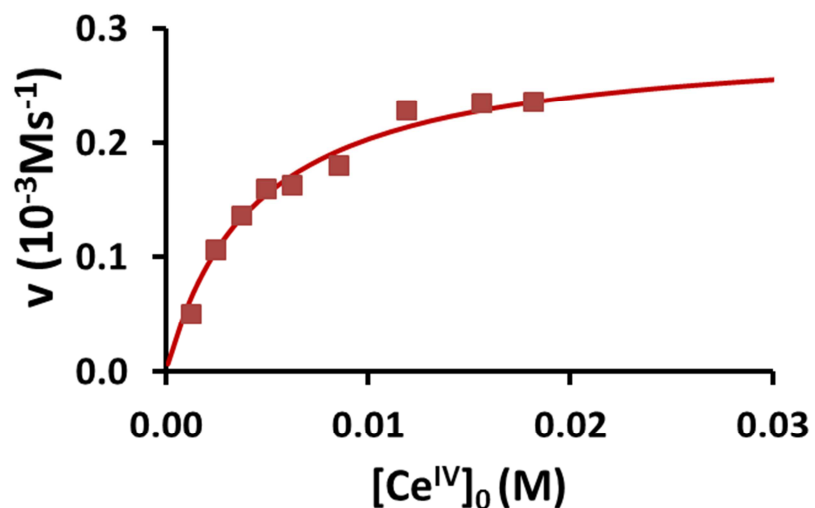
Figure SI.13. Initial rate versus $[Ce^{IV}]_0$, in H_2O pH = 1 at 25 °C: $[\mathbf{1Fe^{IV}=O}]_0 = 0.25$ mM; $[Ce^{IV}]_0 = 1.25 - 18.75$ mM. The line represents the fitting derived from the Michaelis-Menten model.

S.I. 1.3.1.2 Kinetic isotopic effect of complex 1
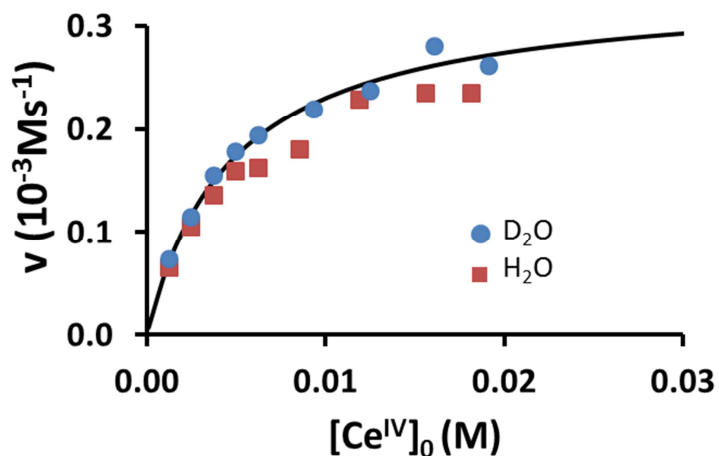
Figure SI.14. Initial rate as function of Ce^{IV} initial concentration, pH = 1 in H_2O (■) and D_2O (●) at 25 °C: $[\mathbf{1Fe^{IV}=O}]_0 = 0.25$ mM; $[Ce^{IV}]_0 = 1.25 - 18.75$ mM. The line represents the fitting derived from the Michaelis-Menten model for D_2O.

15
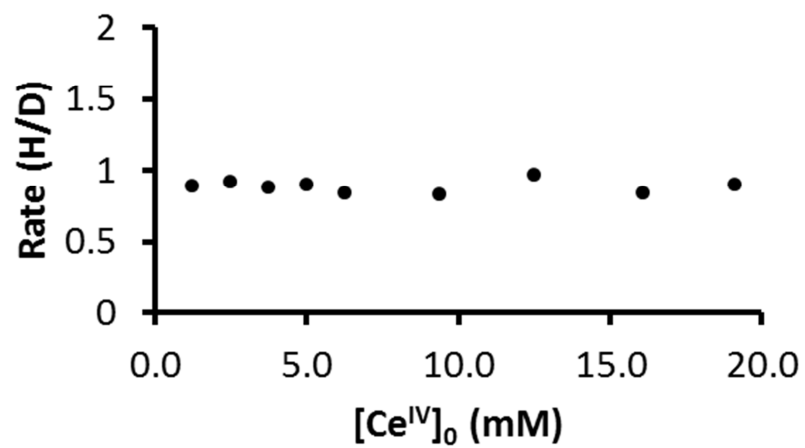
Figure SI.15. Ratio of the initial rate between H_2O and D_2O.

S.I. 1.3.1.3 Complex 2
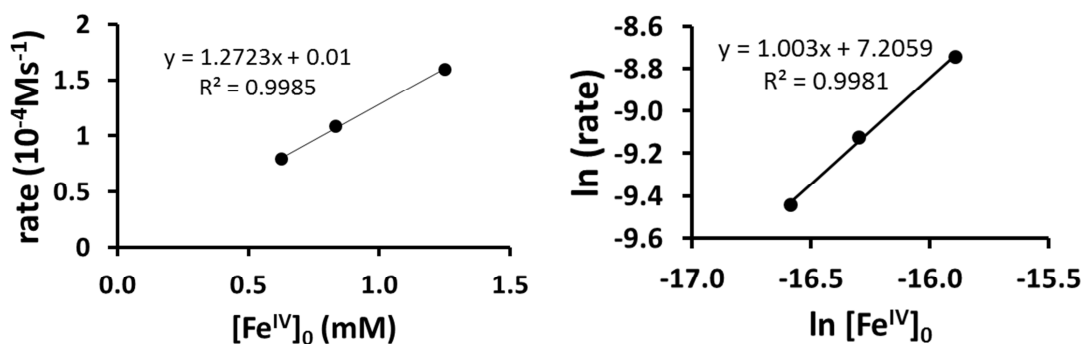
Figure SI.16. (left) Initial rates versus initial concentration of **$2Fe^{IV}=O$** in H_2O, pH =1 at 25 °C, [Fe^{IV}] = 0.0625 – 1.0 mM, [Ce^{IV}] = 18.75 mM. (right) Calculation of the reaction order of **$2Fe^{IV}=O$** by plotting the double logarithm.
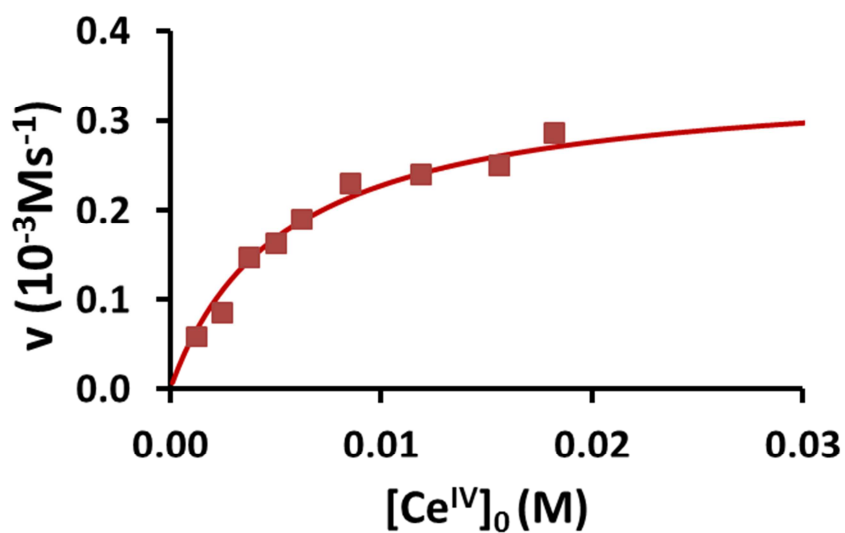
Figure SI.17. Initial rate versus [Ce^{IV}]$_0$, in H_2O, pH = 1 at 25 °C: [**$2Fe^{IV}=O$**]$_0$ = 0.25 mM; [Ce^{IV}]$_0$ = 1.25 – 18.75 mM.. The line represents the fitting derived from the Michaelis-Menten model.

17

S.I. 1.3.1.4 Complex 3
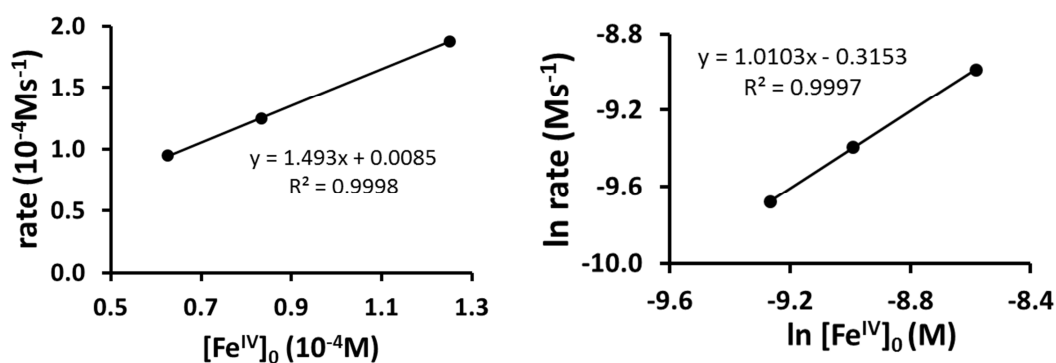
Figure SI.18. (left) Initial rates versus initial concentration of **3Fe^{IV}=O** in H$_2$O, pH =1 at 25 °C, [Fe^{IV}] = 0.0625 – 1.0 mM, [Ce^{IV}] = 18.75 mM. (right) Calculation of the reaction order of **3Fe^{IV}=O** by plotting the double logarithm.
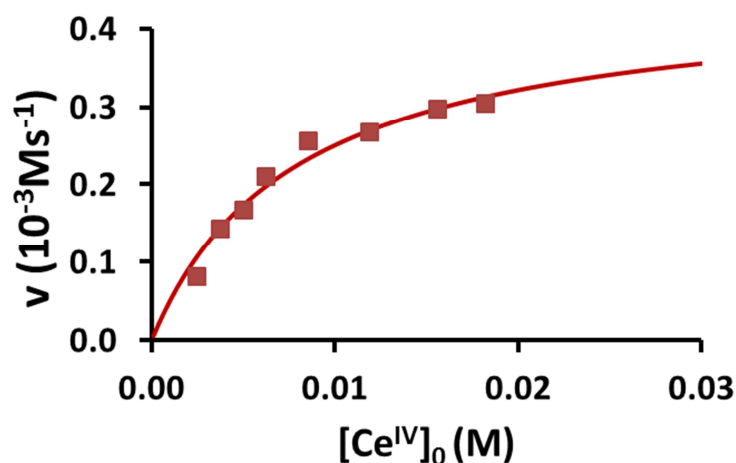
Figure SI.19. Initial rate versus [Ce^{IV}]$_0$, in H$_2$O, pH = 1 at 25 °C: [**3Fe^{IV}=O**]$_0$ = 0.25 mM; [Ce^{IV}]$_0$ = 1.25 – 18.75 mM. The line represents the fitting derived from the Michaelis-Menten model.

18
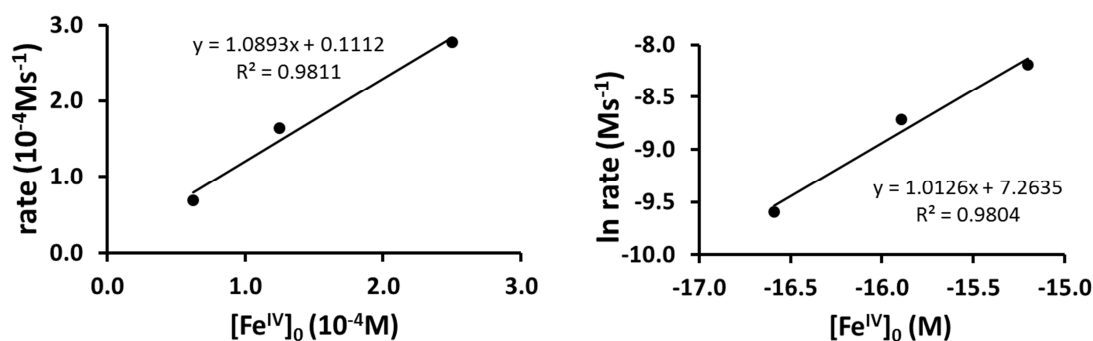
Figure SI.20. (left) Initial rates versus initial concentration of **4Fe^{IV}=O** in H$_2$O, pH =1 at 25 °C, [Fe^{IV}] = 0.0625 – 1.0 mM, [Ce^{IV}] = 18.75 mM. (right) Calculation of the reaction order of **4Fe^{IV}=O** by plotting the double logarithm.
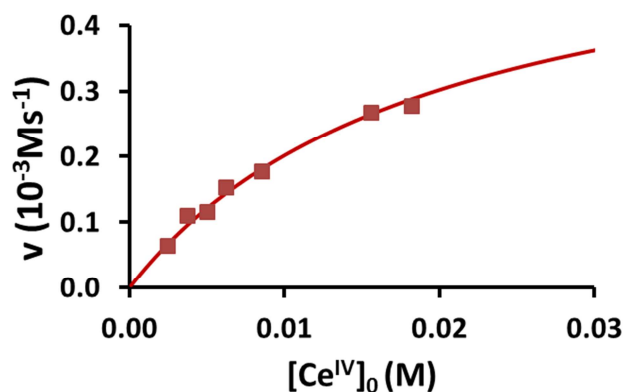
Figure SI.21. Initial rate versus [Ce^{IV}]$_0$, in H$_2$O, pH = 1 at 25 °C: [**4Fe^{IV}=O**]$_0$ = 0.25 mM; [Ce^{IV}]$_0$ = 1.25 – 18.75 mM. The line represents the fitting derived from the Michaelis-Menten model.

19

SI 1.3.2 – Saturation Model

As could be observed in the kinetic data of the Ce^{IV} consumption, saturation is appreciated at higher concentrations. These encourage us to approximate our curves to a Saturation Model and find the rate and equilibrium constants for the proposed mechanism.
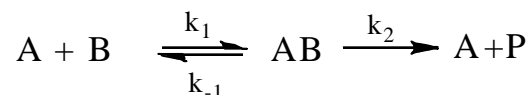
$$A + B \underset{k_{-1}}{\overset{k_1}{\rightleftharpoons}} AB \xrightarrow{k_2} A + P$$

Following the steady state approximation,

$$\frac{d[AB]}{dt} = k_1[A][B] - k_{-1}[AB] - k_2[AB] = 0 \rightarrow [AB] = \frac{k_1[A][B]}{k_{-1} + k_2}$$

Km is defined as,

$$K_m = \frac{k_{-1} + k_2}{k_1}$$

And the total $Fe^{IV}O$ concentration is

$$[A_0] = [A] + [AB] \rightarrow [A] = [A_0] - [AB]$$

So,

$$[AB] = \frac{[A][B]}{K_m} = \frac{([A_0] - [AB])[B]}{K_m} \rightarrow [AB] = \frac{[A]_0[B]}{K_m + [B]}$$

The reaction rate is

$$v_2 = k_2[AB] = k_2 \frac{[A]_0[B]}{K_m + [B]} = \frac{V_{max}[B]}{K_m + [B]}$$

Where

$$V_{max} = k_2 [A]_0$$

The double reciprocal plot (Lineweaver-Burk) is employed for the linearization,

$$\frac{1}{v_2} = \frac{K_m + [B]}{V_{max}[B]} = \frac{K_m}{V_{max}} \cdot \frac{1}{[B]} + \frac{1}{V_{max}}$$

The equilibrium constant (K_{eq}) can be calculate from k_m considering $k_1 > k_{-1} \gg k_2$.[5]

$$K_m = \frac{k_{-1} + k_2}{k_1} = \frac{1}{K_{eq}} + \frac{k_2}{k_1} \approx \frac{1}{K_{eq}}$$

S.I. 1.3.2.1 Complex 1
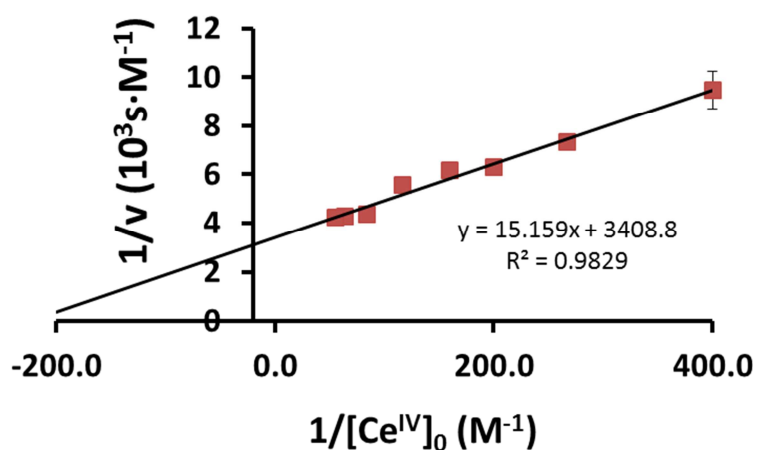
Figure SI.22. Linearization of the saturation model. $[\mathbf{1Fe^{IV}=O}]_0 = 0.25$ mM; $[Ce^{IV}]_0 = 1.25 - 18.75$ mM.

S.I. 1.3.2.2 Complex 2
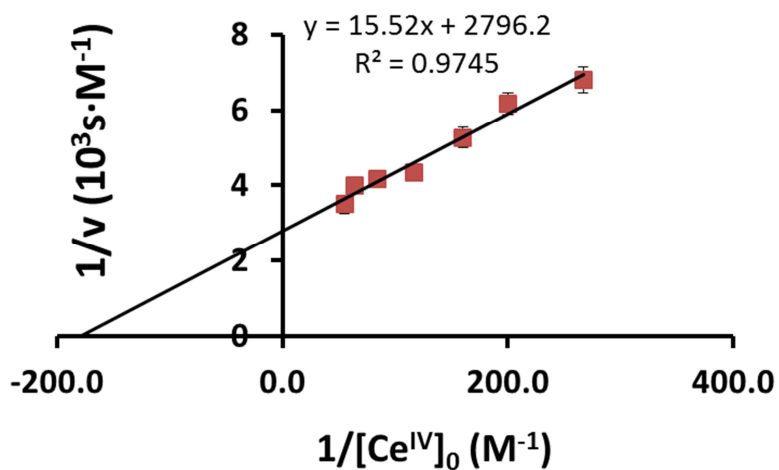
Figure SI.23. Linearization of the saturation model. $[\mathbf{2Fe^{IV}=O}]_0 = 0.25$ mM; $[Ce^{IV}]_0 = 1.25 - 18.75$ mM.

S.I. 1.3.2.3 Complex 3
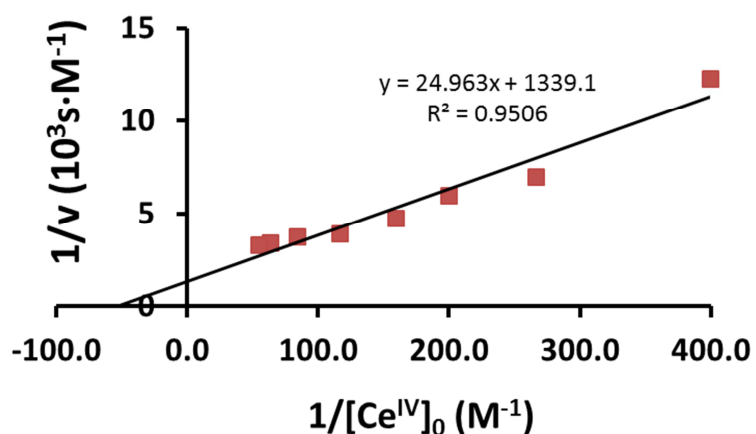
Figure SI.24. Linearization of the saturation model. $[\mathbf{3Fe^{IV}=O}]_0 = 0.25$ mM; $[Ce^{IV}]_0 = 1.25 - 18.75$ mM.

S.I. 1.3.2.4 Complex 4
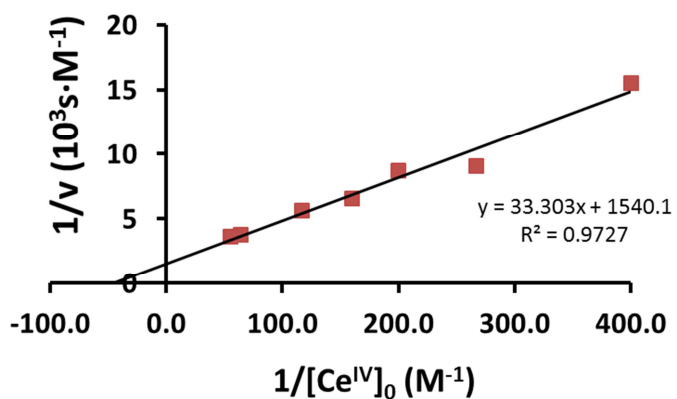
Figure SI.25. Linearization of the saturation model. $[\mathbf{4Fe^{IV}=O}]_0 = 0.25$ mM; $[Ce^{IV}]_0 = 1.25 - 18.75$ mM.
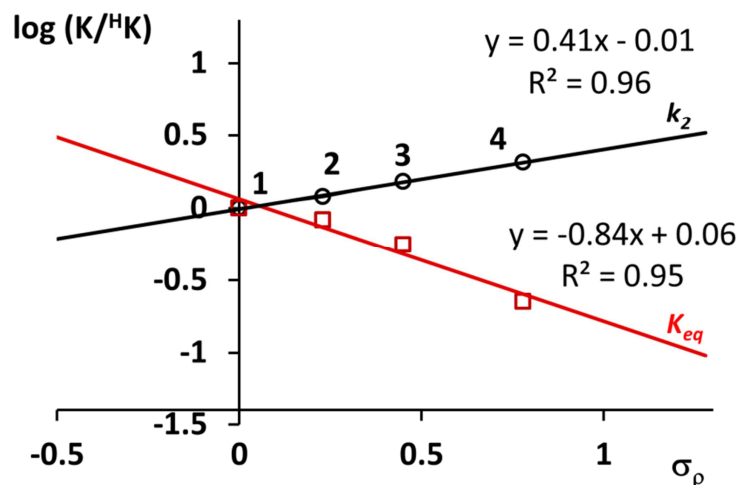
Figure SI.26. Hammett plots for low (0.25 mM of Fe and 1.25-18.75 mM CAN, left) and high concentrations of CAN (1 mM of Fe and 5-75 mM CAN, right) for k_2 (black dots) and k_{eq} (red squares).
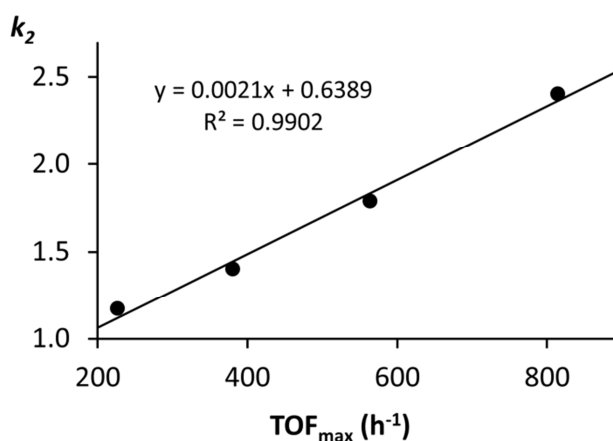
Figure SI.27. Plot of the k_2 obtained from the kinetic experiments versus TOF obtained from the O_2 evolution during the catalytic reactions.

Table SI.1. Summary of the Ce^{IV} and Fe^{IV} reaction order for complexes **1**, **2**, **3** and **4** in H_2O as solvent at 25ºC.

Complex	Ce^{IV} reaction order	Fe^{IV} reaction order
1	0.85/0.89[a]	1.13/0.95[a]
2	0.85	1.00
3	1.01	1.01
4	1.00	1.01

[a] Data previously reported

SI.2 – Computational Section

DFT geometries were optimized at the UB3LYP[6] level in conjunction with the 6-31G(d) basis set[7] for all atoms, including the effect of water solvent with polarizable continuum model PCM-SMD[8] as implemented in the Gaussian 09 program.[9] The final solvent-phase free energies (G_{H2O}) were calculated by the following equation $G_{H2O} = E(6\text{-}31G(d))_{<S^2>coor} + G_{coor\text{-}gas} + G_{solv}$, where $E(6\text{-}31G(d))$ is the spin contamination corrected electronic energy, $G_{coor\text{-}gas}$ are the gas-phase free-energy corrections and G_{solv} is the PCM-SMD water solvent phase correction of the free energy. The spin contamination was corrected by using the following equation:

$$E_{<S^2>coor} = \frac{E_{cont} - a * E_{(S+1)}}{1 - a}$$

$$a = \frac{<S^2_{cont}> - S * (S + 1)}{<S^2_{(S+1)}> - S * (S + 1)}$$

where $E_{<S^2>coor}$ is the spin corrected electronic energy ($E(6\text{-}31g(d))_{<S^2>coor}$), the E_{cont} and $<S^2_{cont}>$ are the energy and total square spin angular momentum respectively, obtained from the structure optimized at the UB3LYP/6-31G(d) and the $E_{(S+1)}$ and $<S^2_{(S+1)}>$ are the energy and total square spin angular momentum of the afterward unpaired spin state (S+1), respectively, computed at the same level and molecular geometries.

Finally, the free energy correction ($G_{coor\text{-}gas}$) was included form a frequency calculation in gas-phase using the optimized solvent-phase geometries. This methodology was used since the gas phase and solvent phase mechanism aresubstantially different. Stationary points were verified by frequency analysis and the connection between transition states and minimums by intrinsic reaction coordinate (IRC) calculations.
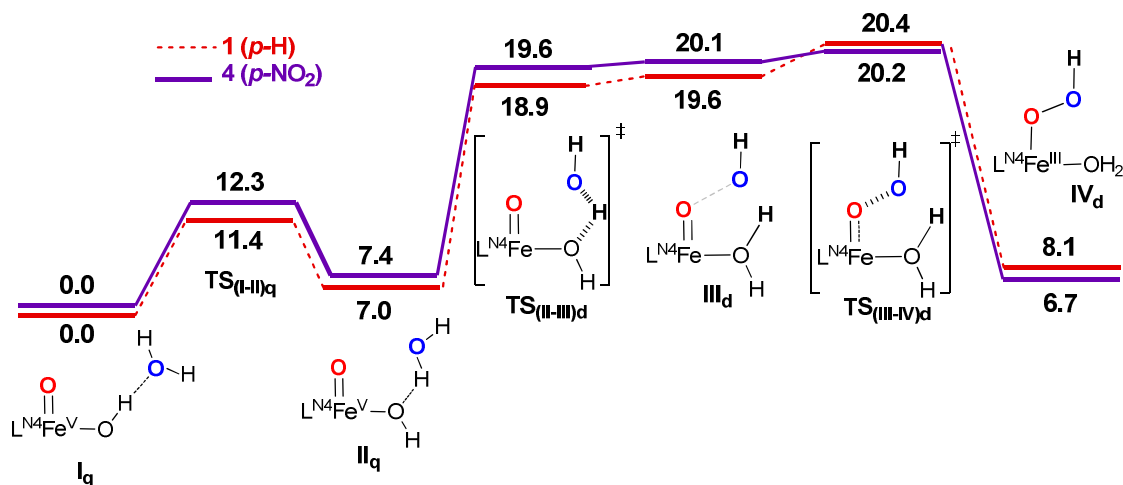
Figure SI.28. DFT calculated mechanism for the O-O bond formation with complexes **1** and **4**. Values indicate Gibbs energies given in kcal·mol^{-1}. Subscripts d and q represent spin state of S = 1/2 and S = 3/2, respectively.
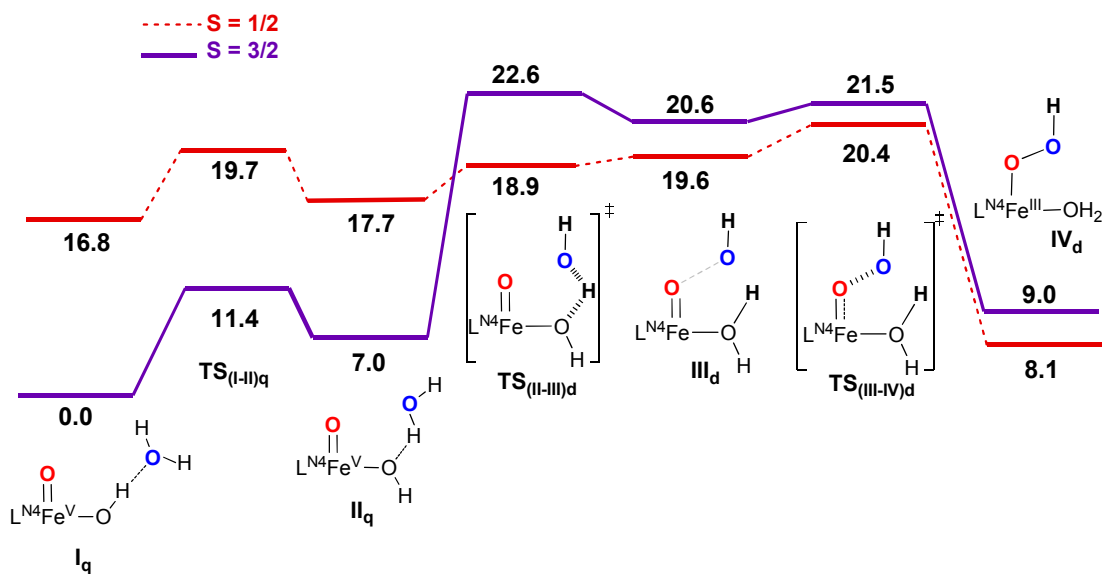
Figure SI.29. DFT calculated spin 1/2 and 3/2 pathways for the O-O bond formation mechanism with complex **1**. Values indicate Gibbs energies given in kcal·mol^{-1}. Subscripts d and q represent spin state of S = 1/2 and S = 3/2, respectively.
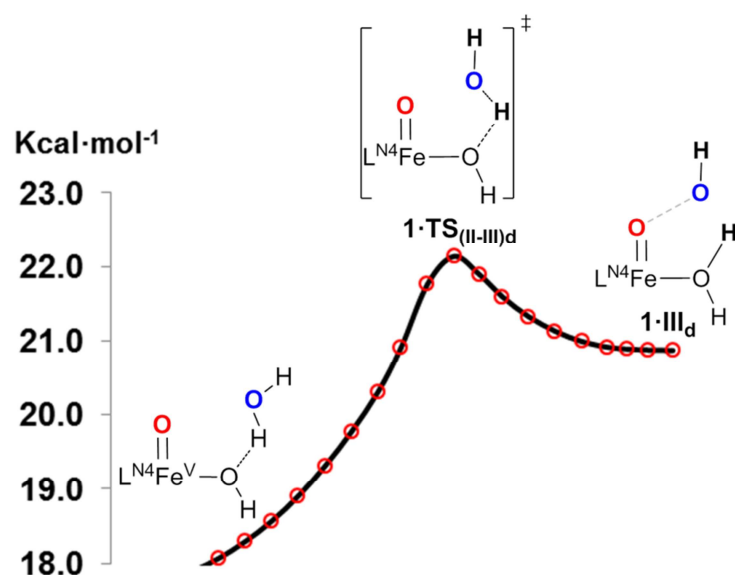
Figure SI.30. Plot of the IRC calculation of the hydrogen transfer transition state **1TS$_{\text{(II-III)d}}$** at UB3LYP/6-31G(d)(PCM-SMD) level, which connects the TS with the respective minimums.
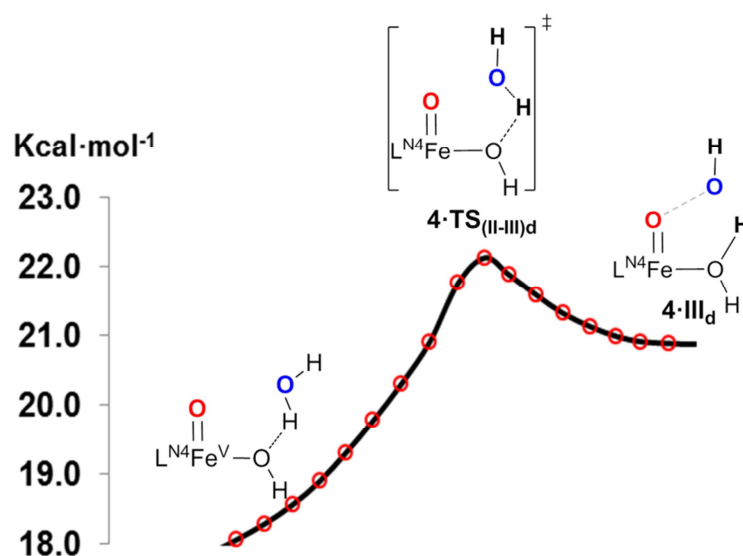
Figure SI.31. Plot of the IRC calculation of the hydrogen transfer transition state **4TS$_{\text{(II-III)d}}$** at B3LYP/6-31G(d)(PCM-SMD) level, which connects the TS with the respective minimums.

26

SI.3 – References

(1) Company, A.; Gómez, L.; Güell, M.; Ribas, X.; Luis, J. M.; Que, L. J.; Costas, M. *J. Am. Chem. Soc.* **2007**, *129*, 15766;

(2) Company, A.; Gomez, L.; Fontrodona, X.; Ribas, X.; Costas, M. *Chem-Eur J* **2008**, *14*, 5727.

(3) Roelfes, G.; Vrajmasu, V.; Chen, K.; Raymond, H. Y. N.; Rohde, J.-U.; Zondervan, C.; la Crois, R. M.; Schudde, E. P.; Lutz, M.; Spek, A. L. Hage, R.; Feringa, B. L.; Münck, E.; Que, Jr. L. *Inorg. Chem.* **2003,** *42*, 2639-2653.

(4) (a) Zhang, C. X.; Kaderli, S.; Costas, M.; Kim, E.-I.; Neuhold, Y. M.; Karlin, K. D.; Zuberbühler, A. D. *Inorg. Chem.* **2003**, *42*, 1807; (b) Kojima, T.; Hayashi, K.-i.; Iizuka, S.-y.; Tani, F.; Naruta, Y.; Kawano, M.; Ohashi, Y.; Hirai, Y.; Ohkubo, K.; Matsuda, Y.; Fukuzumi, S. *Chem. –Eur. J.* **2007**, *13*, 8212; (c) Machkour, A.; Mandon, D.; Lachkar, M.; Welter, R. *Inorg. Chem.* **2004**, *43*, 1545.

(5) James H. Espenson "*Chemical Kinetics and Reaction Mechanism", McGraw-Hill,* **1995**, 70-100

(6) A. D. Becke, *J. Chem. Phys.,* **1993**, *98*, 5648.

(7) a) W. J. Hehre, R. Ditchfield, J. A. Pople, *J. Chem. Phys.* **1972**, *56*, 2257; b) P. C. Hariharan ,J. A. Pople, *Theoret. Chimica Acta* **1973**, *28*, 213; c) M. Suensson, S. Humbel, R. D. J. Froese, T. Matsubara, S. Sieber, K. Morokuma, *J. Phys. Chem.* **1996**, *100*, 19357.

(8) A. V. Marenich, C. J. Cramer, D. G. Truhlar, *J. Phys. Chem. B,* **2009**, *113*, 6378.

(9) Gaussian 09, Revision A.1, M. J. Frisch, G. W. Trucks, H. B. Schlegel, G. E. Scuseria, M. A. Robb, J. R. Cheeseman, G. Scalmani, V. Barone, B. Mennucci, G. A. Petersson, H. Nakatsuji, M. Caricato, X. Li, H. P. Hratchian, A. F. Izmaylov, J. Bloino, G. Zheng, J. L. Sonnenberg, M. Hada, M. Ehara, K. Toyota, R. Fukuda, J. Hasegawa, M. Ishida, T. Nakajima, Y. Honda, O. Kitao, H. Nakai, T. Vreven, J. A. Montgomery, Jr., J. E. Peralta, F. Ogliaro, M. Bearpark, J. J. Heyd, E. Brothers, K. N. Kudin, V. N. Staroverov, R. Kobayashi, J. Normand, K. Raghavachari, A. Rendell, J. C. Burant, S. S. Iyengar, J. Tomasi, M. Cossi, N. Rega, J. M. Millam, M. Klene, J. E. Knox, J. B. Cross, V. Bakken, C. Adamo, J. Jaramillo, R. Gomperts, R. E. Stratmann, O. Yazyev, A. J. Austin, R. Cammi, C. Pomelli, J. W. Ochterski, R. L. Martin, K. Morokuma, V. G. Zakrzewski, G. A. Voth, P. Salvador, J. J. Dannenberg, S. Dapprich, A. D. Daniels, Ö. Farkas, J. B. Foresman, J. V. Ortiz, J. Cioslowski, and D. J. Fox, Gaussian, Inc., Wallingford CT, 2009.

SI.4 –Sample analyzed by GC-TCD

Selected GC-TCD analysis of the gas in the headspace after the pressure reaches a plateau.

1 – GC-TCD 0.125 mL headspace gas analysis of an air sample from the headspace of one of the vials before a water oxidation reaction.

Normalization Report   Page 1 of 1

6/16/2011 4:08:16 PM C:\EZChrom
Elite\Enterprise\Projects\Default\Method\H2O2_55.met
C:\EZChrom Elite\Enterprise\Projects\Default\Data\6-16-2011 4-07-45 PM aire
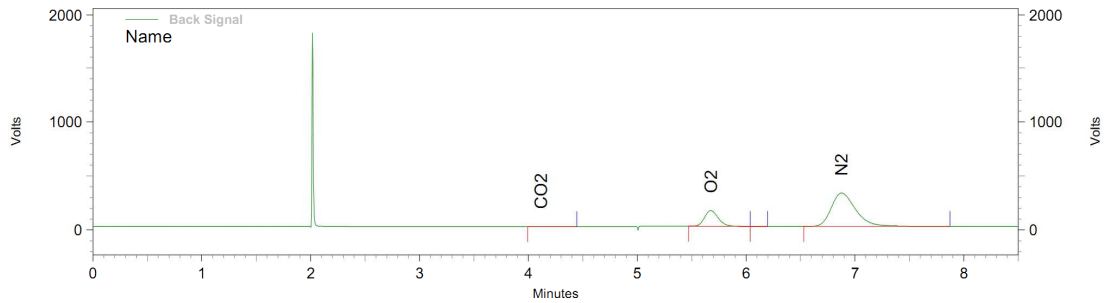
Back Signal Results

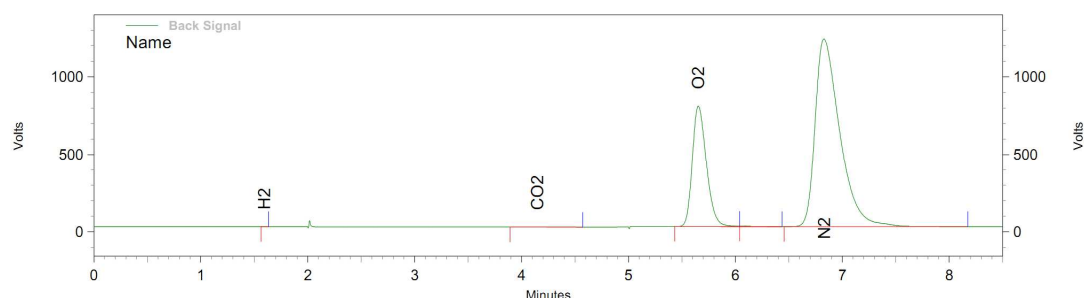| Pk #	Name	Retention Time	Area	Area Percent	Units
	H2				
1	CO2	4.117	18759	0.040	%
2	O2	5.677	9819374	20.923	%
4	N2	6.877	37063762	78.975	%
Totals			46901895	99.938	

2 - GC-TCD 0.125 mL headspace gas analysis after a reaction of **1** (12.5 μM) and CAN (125 mM) in 10 mL of H_2O. TON = 84 (TON of 80 was measured with a differential pressure transducer Honeywell-ASCX15DN).

Normalization Report   Page 1 of 1

Method Name: C:\EZChrom Elite\Enterprise\Projects\Default\Method\H2O2_55.met
Data: C:\EZChrom Elite\Enterprise\Projects\Default\Data\JLL\2-27-2011 1-24-34 PM JLL17
User: System
Acquired: 2/27/2011 1:24:56 PM
Printed: 6/3/2011 8:49:14 PM

2/27/2011 1:24:56 PM C:\EZChrom
Elite\Enterprise\Projects\Default\Method\H2O2_55.met
C:\EZChrom Elite\Enterprise\Projects\Default\Data\JLL\2-27-2011 1-24-34 PM JLL17
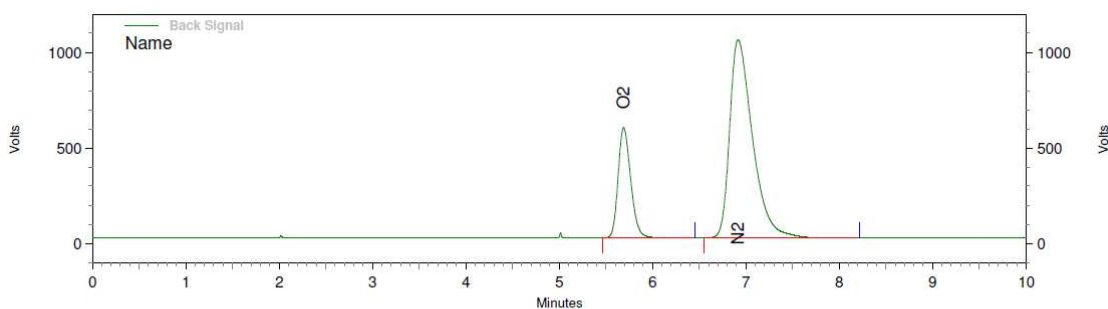
Back Signal Results

Pk #	Name	Retention Time	Area	Area Percent	Units
	H2				
	CO2				%
1	O2	5.690	41427984	**23.498**	%
2	N2	6.917	134877740	**76.502**	%

Totals					
			176305724	**100.000**	

3 - GC-TCD 0.125 mL headspace gas analysis after a reaction of **2** (12.5 μM) and CAN (125 mM) in 10 mL of H$_2$O. TON = 136 (TON of 107 was measured with the pressure sensor).

Normalization Report   Page 1 of 1

Method Name: C:\EZChrom Elite\Enterprise\Projects\Default\Method\N2O2Zoel.met
Data: C:\EZChrom Elite\Enterprise\Projects\Default\Data\6-16-2011 6-41-37 PM zzz260
User: System
Acquired: 6/16/2011 6:42:04 PM
Printed: 6/16/2011 6:50:33 PM

6/16/2011 6:42:04 PM C:\EZChrom
Elite\Enterprise\Projects\Default\Method\N2O2Zoel.met
C:\EZChrom Elite\Enterprise\Projects\Default\Data\6-16-2011 6-41-37 PM zzz260
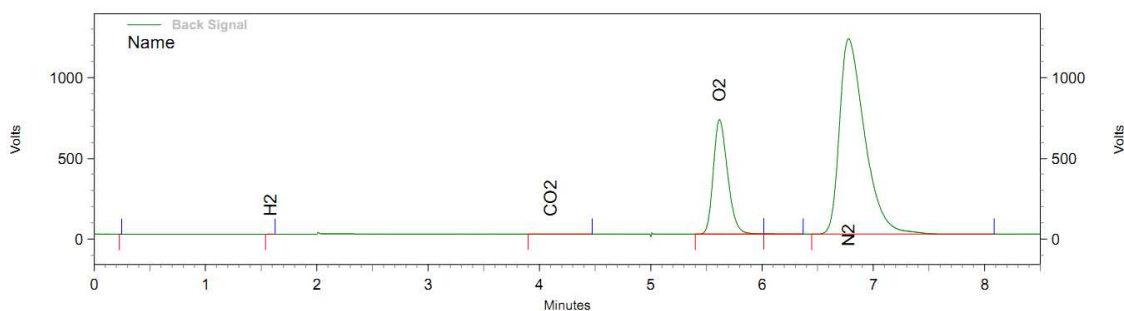
Back Signal Results

Pk #	Name	Retention Time	Area	Area Percent	Units
2	H2	1.583	1451	0.001	
3	CO2	4.100	58747	0.030	%
4	O2	5.617	48818675	24.990	%
6	N2	6.777	146347036	74.913	%

| Totals | | | 195225909 | 99.934 | |

4 - GC-TCD 0.125 mL headspace gas analysis after a reaction of **3** (12.5 μM) and CAN (125 mM) in 10 mL of H_2O. TON = 174 (TON of 141 was measured with the pressure sensor).

Method Name:	**C:\EZChrom Elite\Enterprise\Projects\Default\Method\N2O2Zoel.met**
Data:	**C:\EZChrom Elite\Enterprise\Projects\Default\Data\6-16-2011 5-52-47 PM zzz255**
User:	**System**
Acquired:	**6/16/2011 5:53:14 PM**
Printed:	**6/16/2011 6:01:45 PM**

6/16/2011 5:53:14 PM C:\EZChrom
Elite\Enterprise\Projects\Default\Method\N2O2Zoel.met
 C:\EZChrom Elite\Enterprise\Projects\Default\Data\6-16-2011 5-52-47 PM zzz255
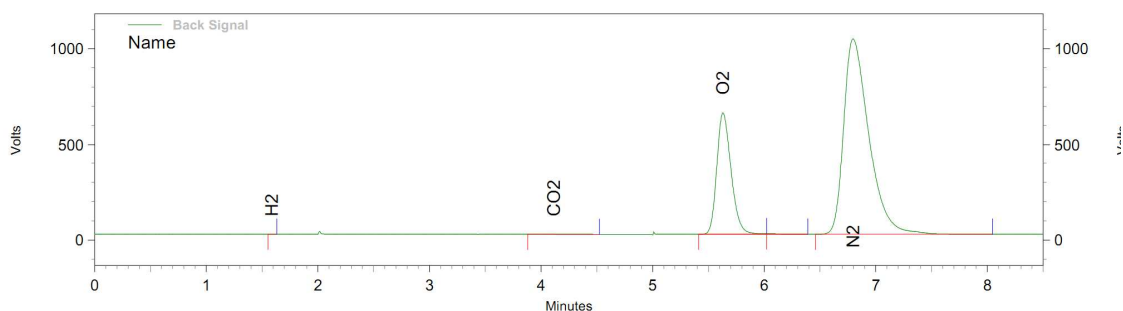
Back Signal Results					
Pk #	*Name*	*Retention Time*	*Area*	**Area Percent**	*Units*
1	H2	1.587	1084	**0.001**	
2	CO2	4.113	80592	**0.048**	%
3	O2	5.630	43319796	**26.041**	%
5	N2	6.797	122833221	**73.840**	%

Totals			166234693	**99.931**	

5 - GC-TCD 0.125 mL headspace gas analysis after a reaction of **4** (12.5 µM) and CAN (125 mM) in 10 mL of H_2O. TON = 203 (TON of 186 was measured with the pressure sensor).

Back Signal Results

Pk #	Name	Retention Time	Area	Area Percent	Units
1	H2	1.593	1351	**0.001**	
2	CO2	4.147	99829	**0.049**	%
3	O2	5.653	54538831	**26.827**	%
5	N2	6.830	148504096	**73.047**	%

Totals					
			203144107	**99.924**	

SI.5 – Cartesian coordinates of B3LYP/6-31G(d)(PCM-SMD) optimized structures.

SI.5.1 Cartesian coordinates of optimized structures in solution:

Energies are given in Hartrees.

$1 \cdot I_q$ (E_{zp} = -2257.601110, G = -2257.384983)

Evidence for an Oxygen Evolving Fe–O–Ce Intermediate

in Iron-Catalysed Water Oxidation

Zoel Codolà,[a] Laura Gómez,[a] Scott T. Kleespies,[b] Lawrence Que, Jr.[b]*

Miquel Costas,[a]* Julio Lloret-Fillol[a]*

[a] Institut de Química Computacional i Catàlisi (IQCC) and Departament de Química, Universitat de Girona, Campus de Montilivi, 17071 Girona (Spain)

[b] Department of Chemistry and Center for Metals in Biocatalysis, University of Minnesota, 207 Pleasant St. S.E., Minneapolis, Minnesota 55455, United States

* To whom correspondence should be addressed. e-mail: Julio.lloret@udg.edu, miquel.costas@udg.edu, larryque@umn.edu

Contents:

SI.1 – Supplementary Discussion

    SI.1.1 Study of the $Fe^{IV}=O$ species

    SI.1.2 Study of the active catalytic species

SI.2 – Supplementary References

SI.1.1 Study of the $Fe^{IV}=O$ species
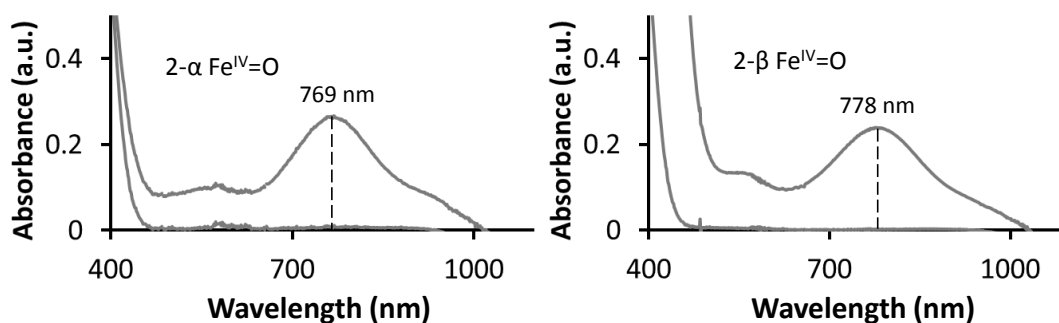
Supplementary Figure 1. UV-Vis spectra for **2-α** (left) and **2-β** (right) formed by reaction of **1-α** and **1-β** with CAN (3 eq), (1 mM in Milli-Q water, at pH 1).
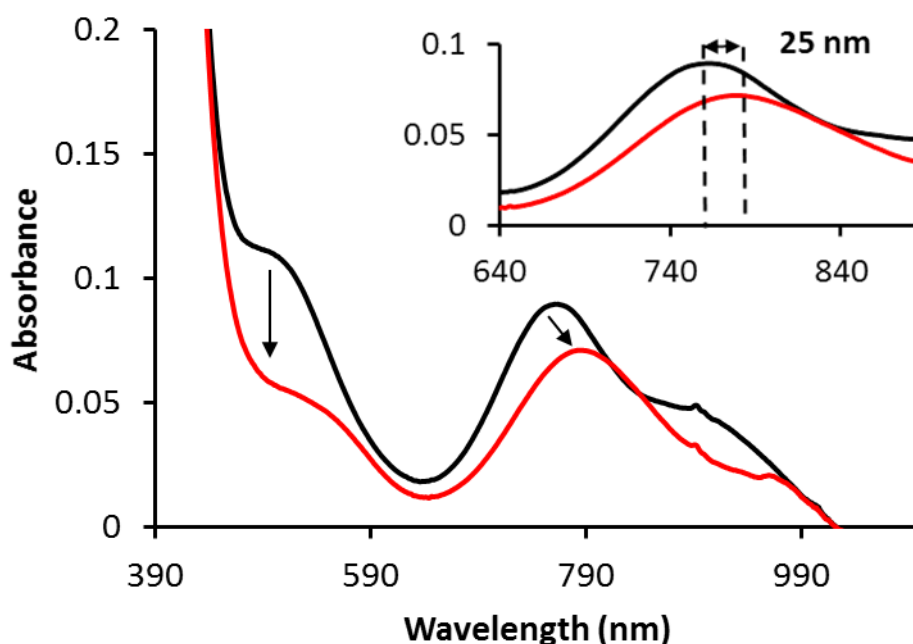
Supplementary Figure 2. β-[$Fe^{IV}(O)(NCCH_3)(mcp)$]$^{2+}$ (**2-β**) (black line, $\lambda_{max} = 753$ nm) was prepared by the addition of 6 eq of CAN to β-[$Fe^{II}(mcp)(OTf)_2$] (1 mM in CH_3CN). β-[$Fe^{IV}(O)(H_2O)(mcp)$]$^{2+}$ (red line, $\lambda_{max} = 778$ nm) was obtained by the addition of 1000 equiv. of water to β-[$Fe^{IV}(O)(NCCH_3)(mcp)$]$^{2+}$. Inset, magnification of the shift observed in the 640 – 900 nm range.
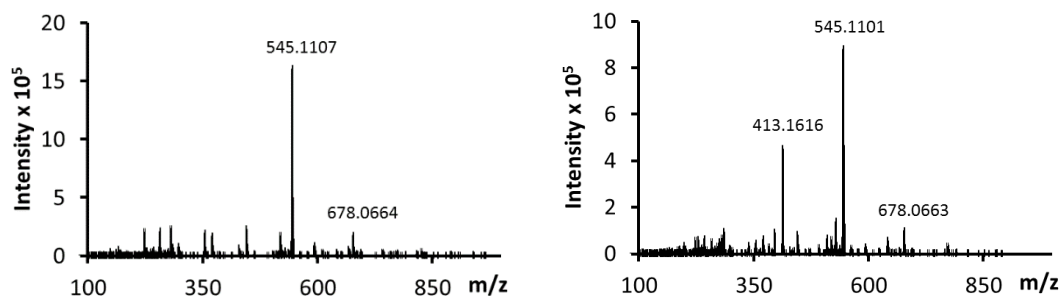
Supplementary Figure 3. CSI-HRMS spectra recorded immediately after the addition of 50 μL of CAN (3 mM in HOTf:H$_2$O 3:10) to 1 mM solutions of **1-*β*** (left) or **1-*α*** (right) in MilliQ water (2 mL).
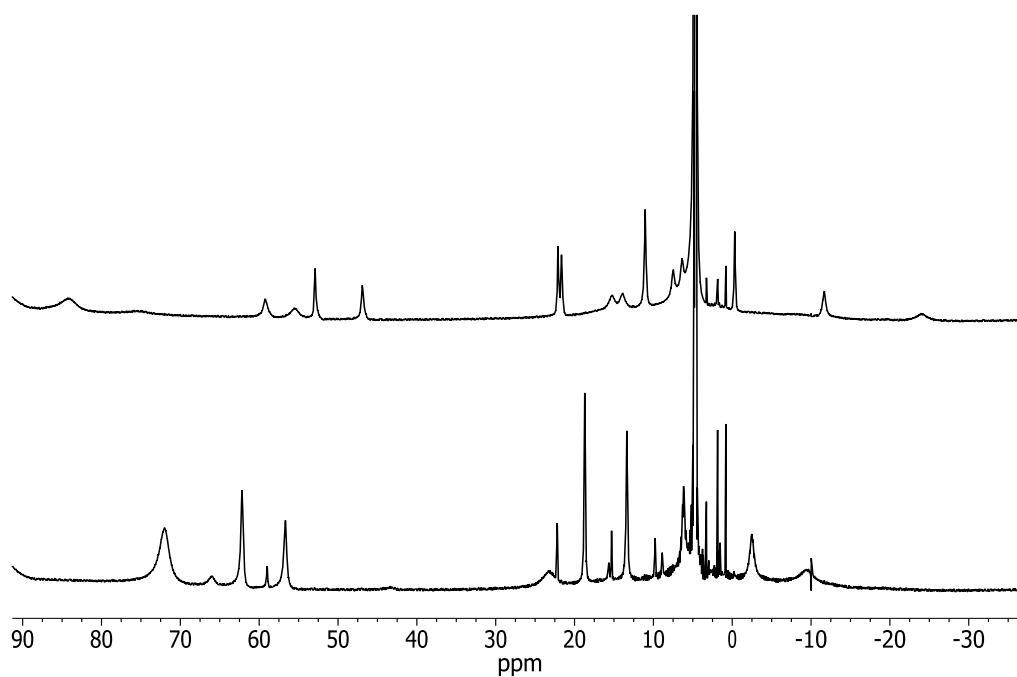
Supplementary Figure 4. ^{1}H-NMR spectra of **1-*β*** (top, 4.5 mM) and **1-*α*** (bottom, 4.5 mM) in D$_2$O at 5 °C.
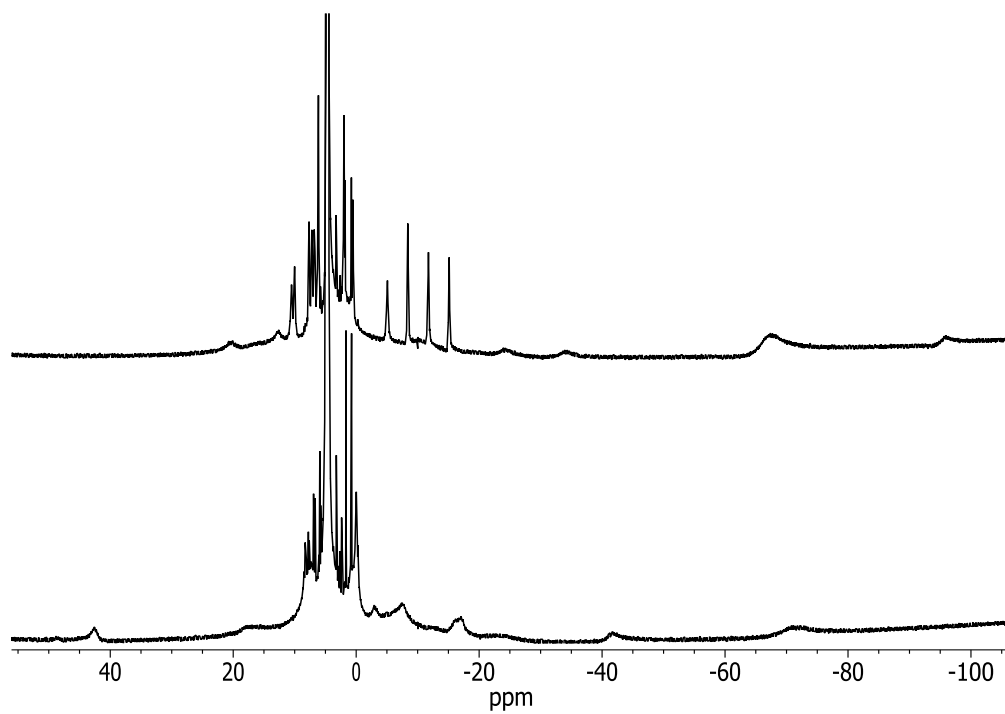
Supplementary Figure 5. ^{1}H-NMR spectra of **2-β** (top, 4.5 mM) and **2-α** (bottom, 4.5 mM) in D$_2$O at 5 ºC generated by adding 3 eq of CAN (50 μL, final pH = 1).
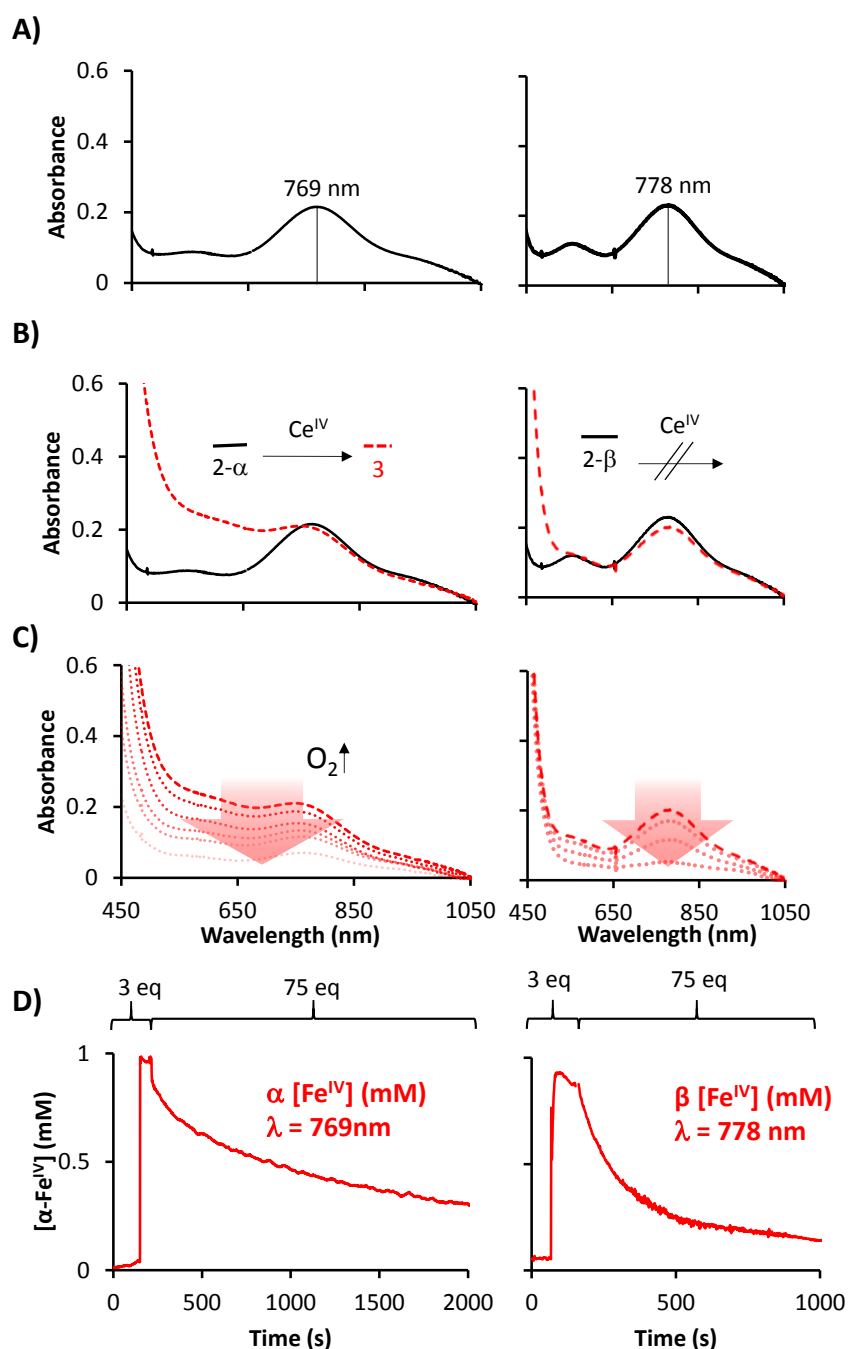
Supplementary Figure 6 A) UV-Vis spectra of **2-α** (left) and **2-β** (right) generated by the addition of 3 equiv. of CAN to an aqueous solution of **1-α** and **1-β**, respectively. **B)** Spectra recorded immediately after the addition of 75 equiv. of CAN to **2-α** (left) and **2-β** (right) and **C)** its time evolution. **D)** Traces of the 769 nm and 778 nm band, corresponding to **2-α** and **2-β,** upon addition of (3 + 75) eq of CAN to **1-α** and **1-β** respectively.
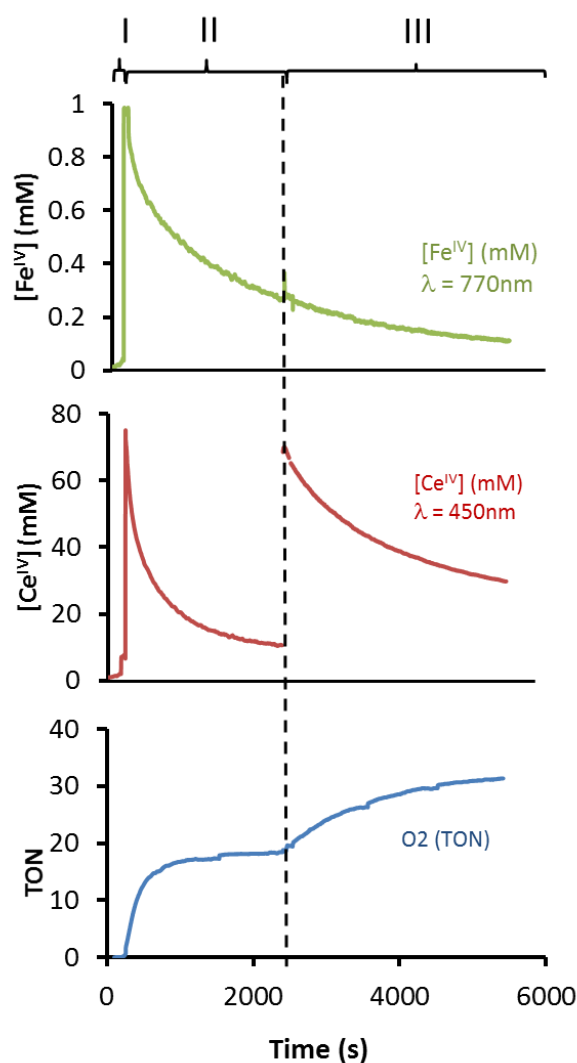
Supplementary Figure 7 Oxygen evolution (blue, bottom), Ce^{IV} consumption (red, middle) and $Fe^{IV}=O$ disappearance (green, top) monitored by a pressure transducer coupled with a UV-Vis spectrometer for **1-α**, (I) on the addition of 3 eq. of Ce^{IV} to fully form the $Fe^{IV}=O$ species and (II), after the addition of 75 eq. of Ce^{IV}. Kinetic traces for [Ce(IV)] and **2-α** were monitored at 450 nm and 769 nm, respectively. $\Delta[O_2]$(TON) was monitored by a pressure transducer. (III) After 2300 s, 75 eq of Ce^{IV} were added to the solution.

SI.1.2.1 Kinetic studies

The required amount of iron complex was dissolved with 2.7 mL of Milli-Q water in a quartz UV-Vis cell at 25 °C. Then, the $Fe^{IV}(O)(H_2O)$ intermediate was generated by the addition of 3 eq of CAN dissolved in 50 µL of diluted TfOH (3:10, TfOH:H_2O). Once fully formed, Milli-Q water (0.25 mL) was added to the solution. A second addition of CAN in 0.3 mL of TfOH:H_2O (at pH ~ 0) was added. This second addition leads to the desired final concentration of Ce^{IV} (ranged from 1.25 to 18.75 mM) and iron complex (0.1 mM) for the kinetic studies at pH = 1. Cerium(IV) consumption was monitored at λ = 420 nm. Oxygen evolution was monitored in parallel by a pressure transducer.

The initial rate method was applied to obtain rate constants in the kinetic studies to avoid interference of the consumption of the catalysts during the catalytic reactions. All the kinetic data were treated following the same procedure. Only data obtained within the first 10 seconds of reaction was used, which corresponds to the decay of 20% of the starting Ce absorbance. From these data, the self-decay of a Ce^{IV} blank experiment (same concentration, pH = 1) was subtracted.

For the transformation of the absorbance to concentration, blank samples for every Ce^{IV} concentration were linearized and the equation was used as a calibration curve.
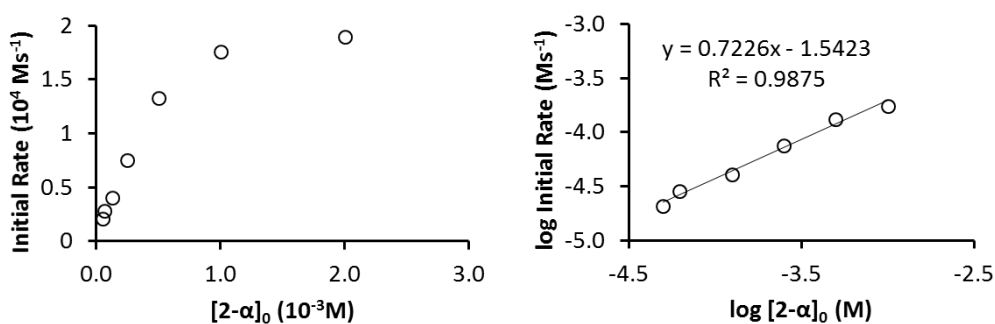
Supplementary Figure 8. Left) Plot of initial rates for Ce^{IV} consumption versus [**2-α**]$_0$ in H_2O at pH = 1 and 25 °C: [**2-α**]$_0$ = 0.05 - 2 mM; [Ce^{IV}]$_0$ = 18.75 mM. Right) Log-log plot in the determination of reaction order for **2-α** (Fe^{IV}=O).
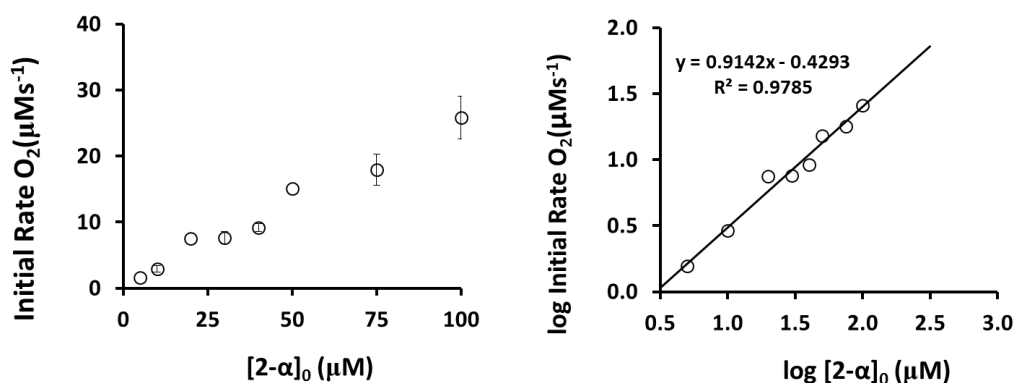
Supplementary Figure 9. Reaction order under optimized catalytic conditions. Left) initial rates of O_2 evolution versus $[2\text{-}\alpha]_0$, in H_2O at pH = 0.8 and 25 ºC: $[2\text{-}\alpha]_0 = 5 - 100$ μM; $[Ce^{IV}]_0 = 125$ mM. Right) Log-log plot in the determination of reaction order for **2-α** (**$Fe^{IV}=O$**).
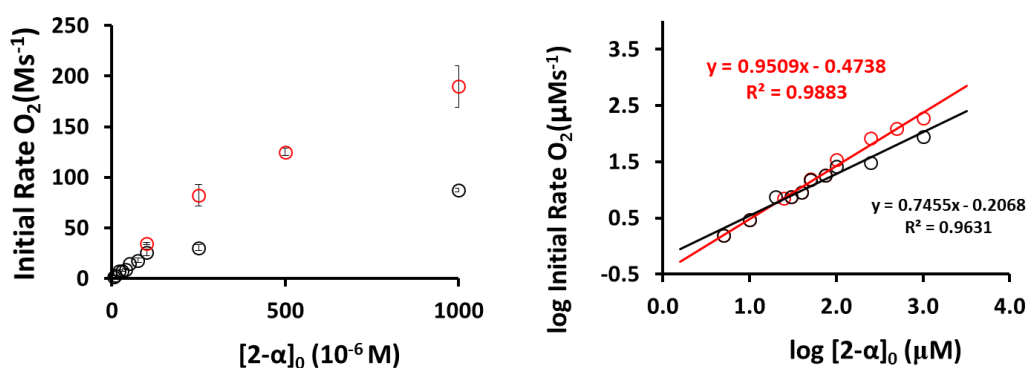
Supplementary Figure 10. Reaction order vs [2-α]. In red $[Ce^{IV}]_0 = 500$ mM, and in black, $[Ce^{IV}]_0 = 125$ mM. Left) In black, initial rates of O_2 evolution versus $[2\text{-}\alpha]_0$, in H_2O at pH = 0.8 and 25 ºC: $[2\text{-}\alpha]_0 = 5 - 1000$ μM; $[Ce^{IV}]_0 = 125$ mM; In red, $[Ce^{IV}]_0 = 500$ mM.(pH 0.6) Right) Log-log plot in the determination of reaction order for **2-α** (**$Fe^{IV}=O$**).
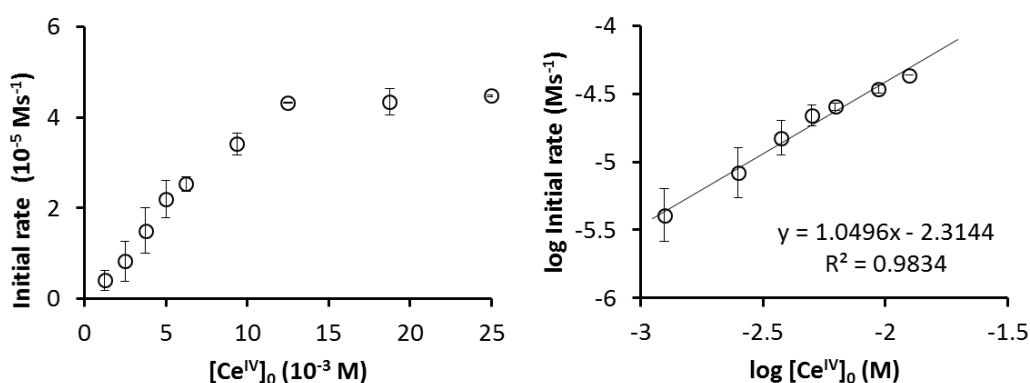
Supplementary Figure 11. Left) initial rates of Ce^{IV} consumption versus $[Ce^{IV}]_0$, in H_2O pH = 1 at 25 ºC: $[2\text{-}\alpha]_0 = 0.1$ mM; $[Ce^{IV}]_0 = 1.25 - 18.75$ mM. Right) Log-log plot in the determination of reaction order for Ce^{IV}.
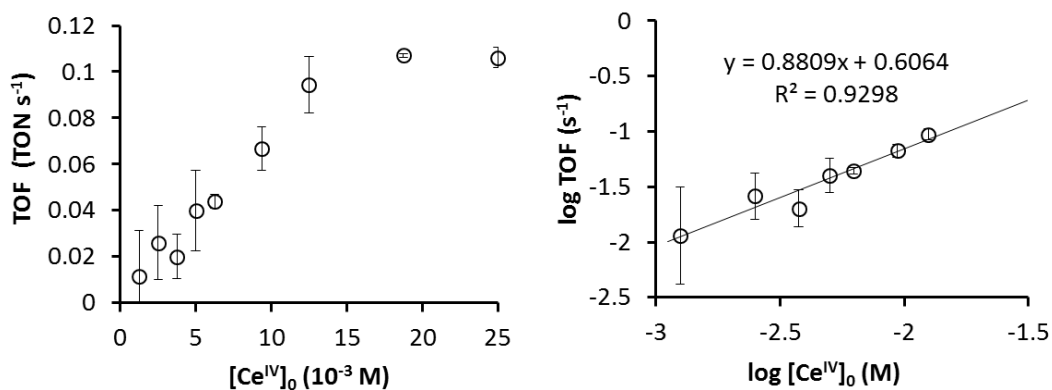
Supplementary Figure 12. Left) initial rates of O_2 evolution versus $[Ce^{IV}]_0$, in H_2O pH = 1 at 25 °C: $[\textbf{2-α}]_0$ = 0.1 mM; $[Ce^{IV}]_0$ = 1.25 − 18.75 mM. Right) Log-log plot in the determination of reaction order for Ce.
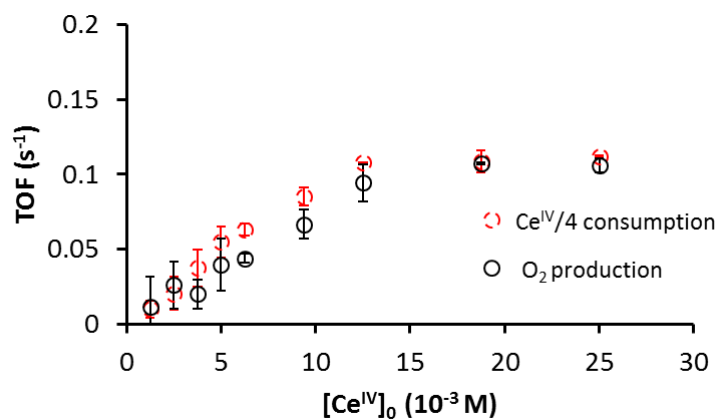
Supplementary Figure 13. Initial rates of O_2 evolution (circles, black) and $[Ce^{IV}]/4$ consumption (squares, red) versus $[Ce^{IV}]_0$.

SI.1.2.2 Titration of 2-α with Ce^{IV}
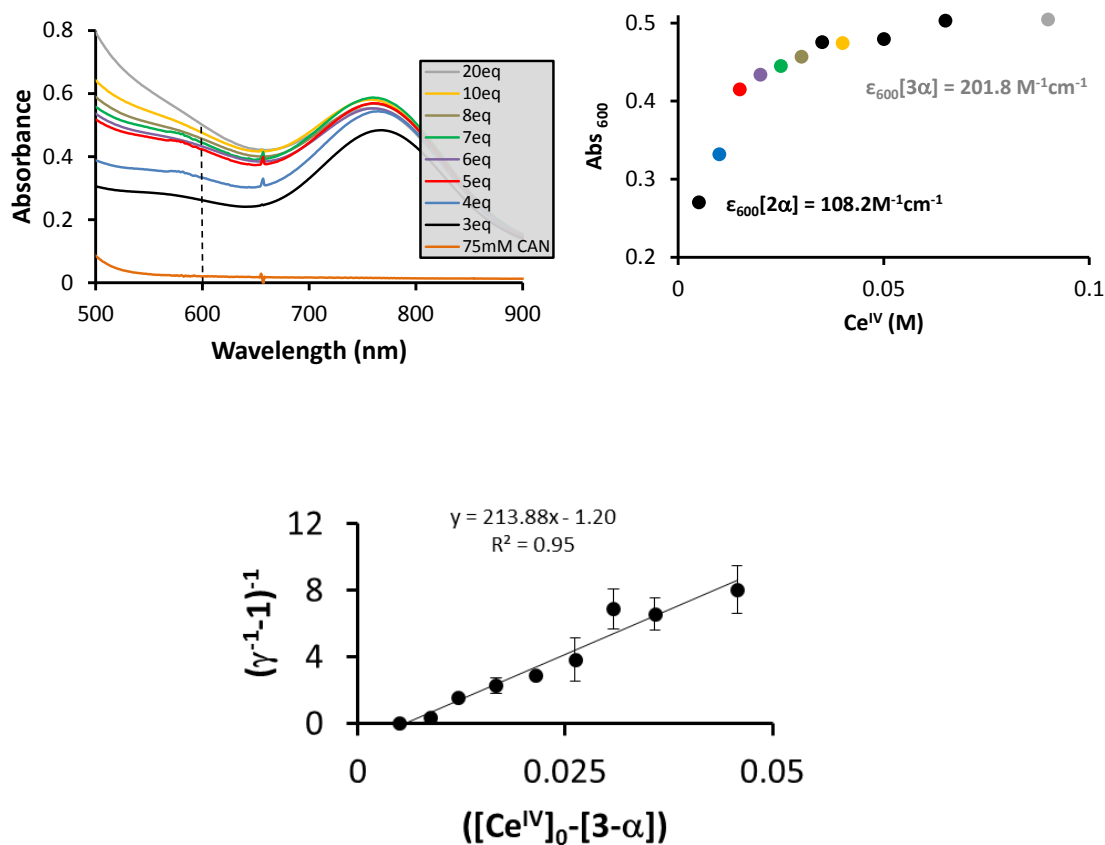
Supplementary Figure 14. Titration of [2-α] (5.0 mM) with CAN (5-100 mM) at pH 1 in H$_2$O:MeCN (1:1 v/v) at 265 K. Top) Raw UV-Vis spectra (left) and absorbance at λ = 600 nm versus the concentration of Ce^{IV} (15-100 mM) (right). Bottom) Plot of $(\gamma^{-1}-1)^{-1}$ vs ([Ce^{IV}]$_0$– [**3-α**]) to determine the Ce^{IV} binding constant to **2-α** to form **3-α** (K = [**3-α**] / [**2-α**] [Ce^{IV}]). γ = [**3-α**] / [**2-α**]. Every CAN addition was carried out on freshly prepared samples of Fe^{II} to completely avoid decomposition of the intermediates. Absorbance values were obtained from the averages of 2-3 experiments. The absorbance was measured in the range of 0-10 s after the addition of Ce^{IV}. ε$_{600}$ (at 600 nm) for 2-α and 3-α were calculated assuming 100% of conversion when 3 eq and 20 eq of Ce^{IV} were added to **1-α** respectively.

SI.1.2.3 HRMS and rRaman analysis
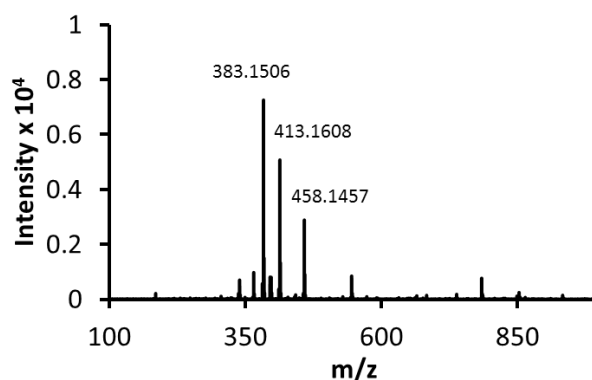
Supplementary Figure 15. CSI-HRMS spectrum recorded immediately after the addition of 75 eq of CAN to an aqueous solution of **1-β** (1 mM), using a cryospray probe coupled with a TOF analyzer (dry gas and nebulizer gas temperatures were set at 25 ºC). The most intense peaks correspond to $[Fe^{IV}O(OH)(mcp)]^+$ (413.1627 m/z) and $[Fe^{IV}(O)(NO_3)(mcp)]^+$ (458.1463 m/z).

HRMS analysis of 3-α

HRMS of Intermediate **3-α** presents a prominent peak at m/z 738.0235 (**M$_3$**) which shows a complex isotopic pattern. First of all, the experimental m/z obtained matches the m/z value calculated for the formulation of **3-α** as $\{[Fe^{IV}(O)(mcp)(\mu\text{-}O)Ce^{IV}(NO_3)_3]\}^+$ with an error lower than 1.5 ppm (calc. 738.0245 m/z).The individual peak separations for this peak cluster were found to be m/z $\pm$ 1, indicating a mono-charged positive ion. Further information was gained by taking a closer look at its isotopic distribution pattern. The isotopic pattern related to the prominent peak at m/z 738.0235 (**M$_3$**) can be only correctly described by taking into account the natural isotopic distribution and abundance of both the Fe and the Ce atoms (Figure SI.14A). For instance the peak at m/z **M$_3$** - 2 (736.0244) accounting for 6.5% of the **M$_3$** peak, is indicative of the presence of one iron atom (isotopes and natural abundance of iron: 53.9, 5.8%; 55.9, 91.8%; 56.9, 2.1% and 57.9, 0.3%) in the molecule (Figure SI.14B). However, m/z 739.0274 and 740.0283 peaks are experimentally more intense than expected according to the simulation, suggesting the presence of some amount of Fe(III)-OH (the presence of Fe(III)-OH was also observed in the spectra of **2-α**). Taking into account the presence of 16 % of Fe(III)-OH, peak at 739.0274 reaches its expected intensity (Figure SI.14C). In addition, peaks at 740.0283 and 741.0305 have lower intensities than expected if only

the 139.9 cerium isotope is taking into account. By taking into account the natural abundance of cerium (isotopes and natural abundance of cerium 135.9, 0.2%; 137.9, 0.2%; 139.9 88.45% and 141.9, 11.1%) these peaks match the isotopic pattern in the experimental spectrum, indicating the presence of this element in the formulation of **3-α** (Figure SI.14D).
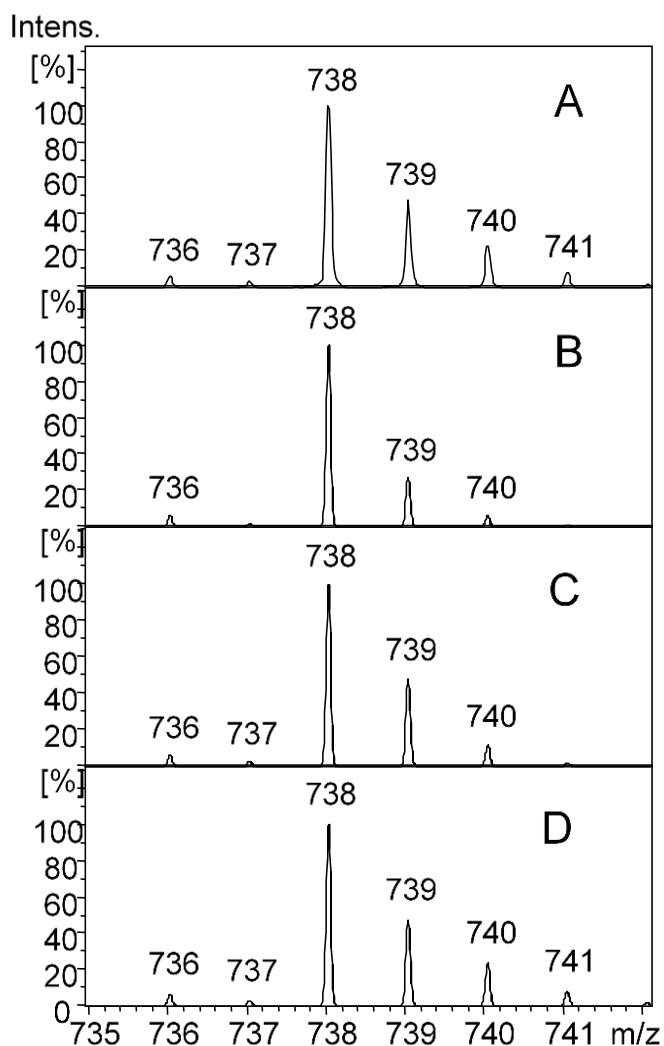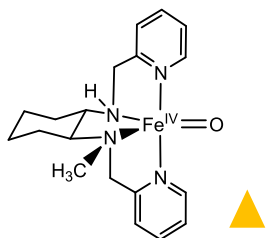

Supplementary Figure 16. A) Experimental spectrum of **3-α**. B) Simulated spectrum of pure $\{[Fe^{IV}(O)(mcp)(\mu\text{-}O)Ce^{IV}(NO_3)_3]\}^+$ using monoisotopic Ce (139.9). C) Simulated spectrum of a mixture of $\{[Fe^{IV}(O)(mcp)(\mu\text{-}O)Ce^{IV}(NO_3)_3]\}^+$ (84%) and $\{[Fe^{III}(OH)(mcp)(\mu\text{-}O)Ce^{IV}(NO_3)_3]\}^+$ (16%) using monoisotopic Ce (139.9). D) Simulated spectrum of pure $\{[Fe^{IV}(O)(mcp)(\mu\text{-}O)Ce^{IV}(NO_3)_3]\}^+$ using the natural isotope distributions of Fe and Ce.
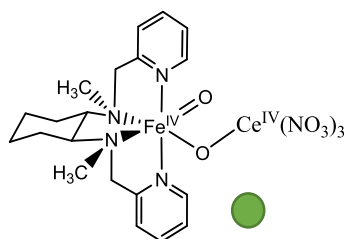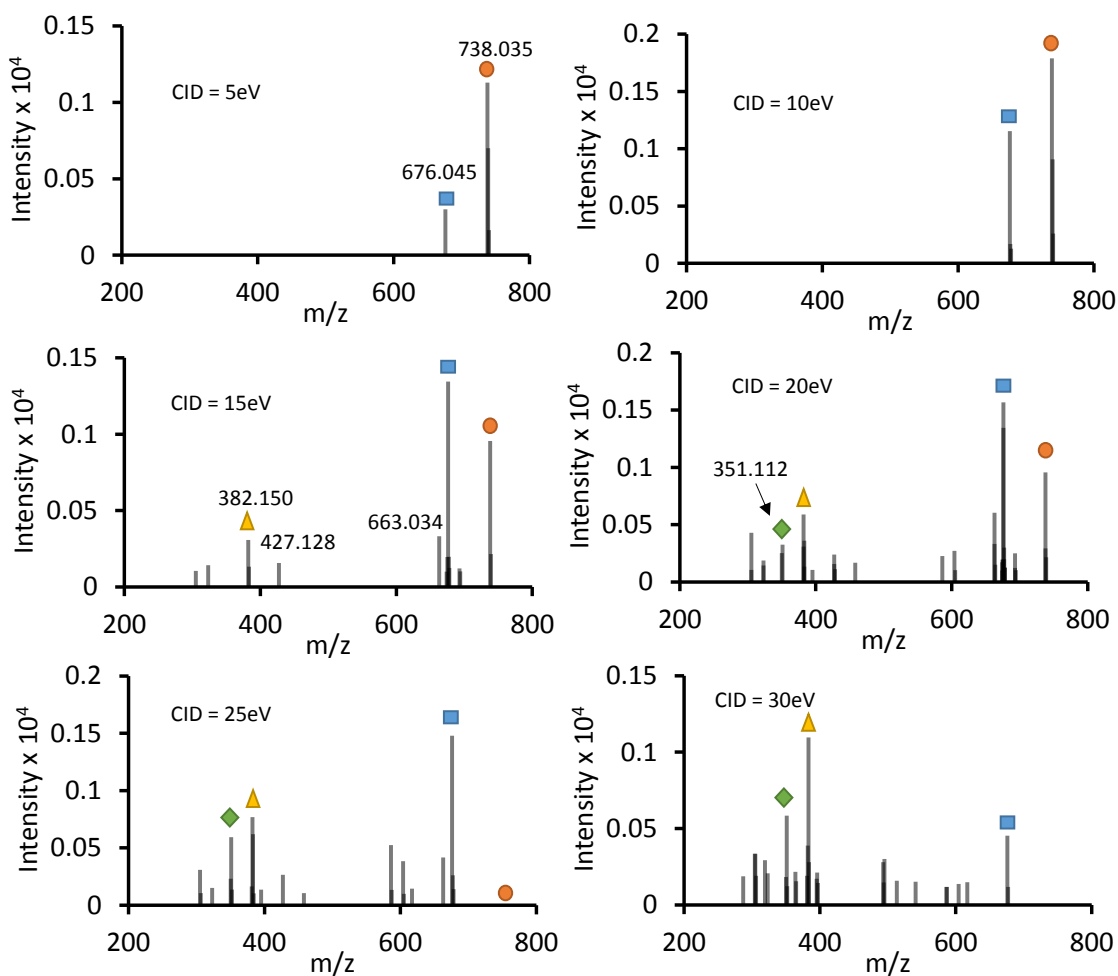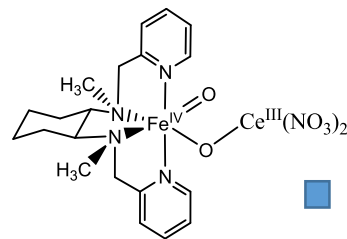
Supplementary Figure 17. Effect of the collision-induced dissociation (CID) for the MS/MS spectrum of **3-α** (738.035 m/z).
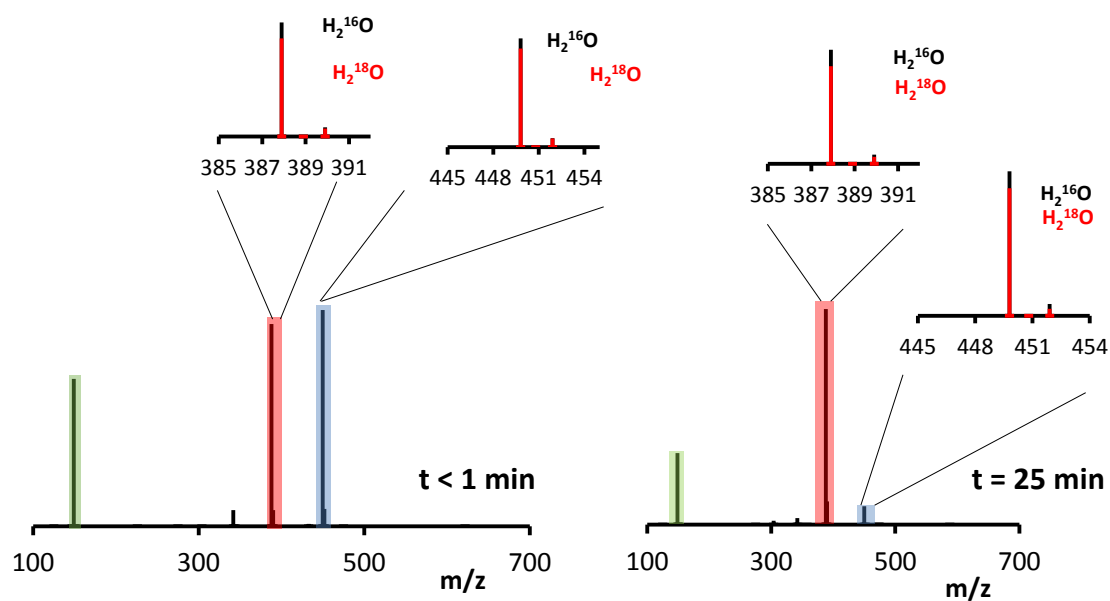
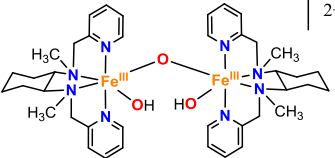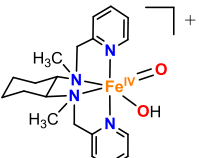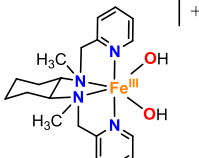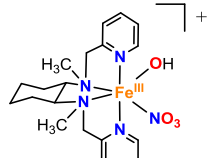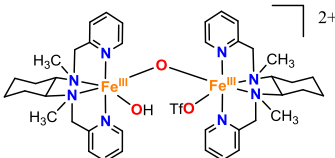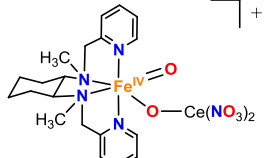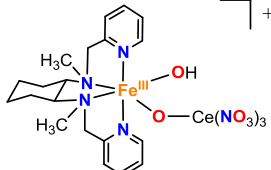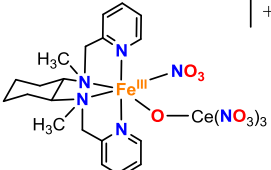| Species	Exp (m/z)	Theo (m/z)
[Ce^{IV}(NO$_3$)$_5$]$^-$	449.8496	449.8451
[Ce^{III}(NO$_3$)$_4$]$^-$	387.8610	387.8573
[OTf]$^-$	148.9543	148.9520

Supplementary Figure 18. Negative mode HRMS recorded immediately (< 1min, left) and 25 min (right) after the addition of CAN (75 eq.) to [Fe(mcp)(OTf)$_2$] (0.5 mM) in Milli-Q H$_2$O (magnification, black spectra) and 98% H$_2$^{18}O (magnification, red spectra). Labelled and non-labelled m/z values for the main species are included in the table below.
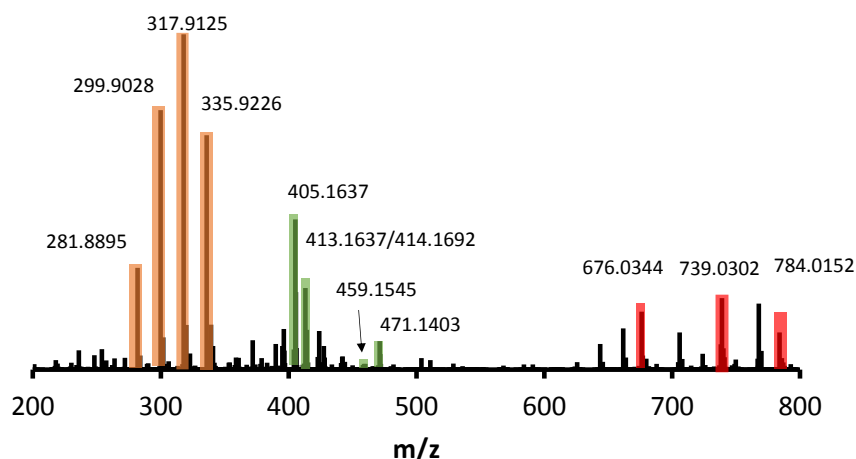
Supplementary Figure 19. Positive mode HRMS recorded after complete decay of **3-α** formed by addition of CAN (75 eq.) to [Fe(mcp)(OTf)$_2$] (1 mM) in Milli-Q H$_2$O. m/z peaks highlighted in orange are derived from the cerium since are present in the CAN blank HRMS experiments, in green are monomeric iron species and in red Fe-Ce heterobimetallic species. Labelled and non-labelled m/z values for the main species are included in the table below.

2+ Sim. 405.1665 (810.3331) Exp H$_2$O 405.1637 Exp. D$_2$O 406.1728 Exp H$_2$^{18}O 408.1732	**+** Sim. 413.1634 Exp H$_2$O 413.1627 Exp. D$_2$O 414.1703 Exp H$_2$^{18}O 417.1720	**+** Sim. 414.1718 Exp. H$_2$O 414.1692 Exp. D$_2$O 416.1848 Exp. H$_2$^{18}O 418.1764
+ Sim. 459.1569 Exp H$_2$O 459.1545 Exp. D$_2$O 460.1628 Exp H$_2$^{18}O 461.1556	**2+** Sim. 471.1406 (942.2824) Exp H$_2$O 471.1403 Exp. D$_2$O 471.6453 Exp H$_2$^{18}O 473.1459	**+** Sim. 676.0367 Exp H$_2$O 676.0353 Exp D$_2$O 676.0369 Exp H$_2$^{18}O 680.0444
+ Sim. 739.0329 Exp H$_2$O 739.0302 Exp. D$_2$O 740.0339 Exp H$_2$^{18}O 743.0398	**+** Sim. 784.0180 Exp H$_2$O 784.0147 Exp. D$_2$O 784.0191 Exp H$_2$^{18}O 786.0214	
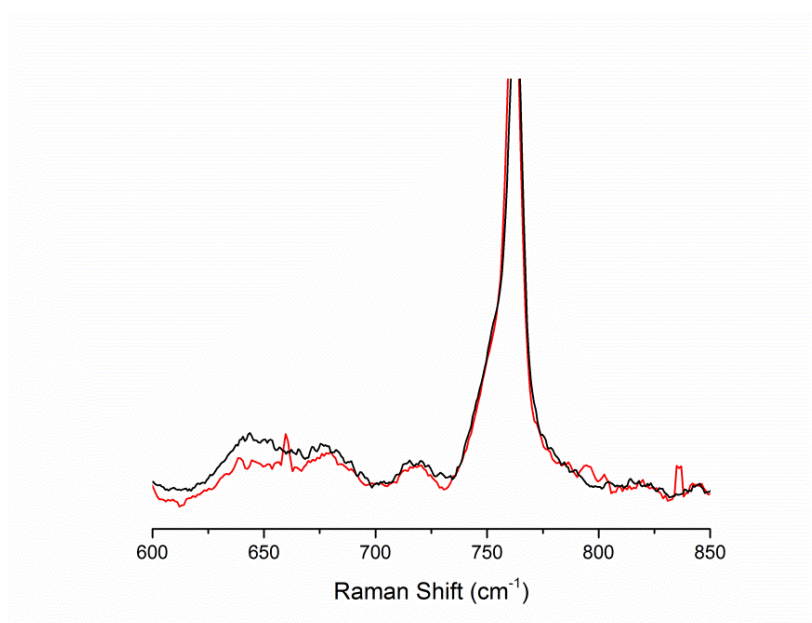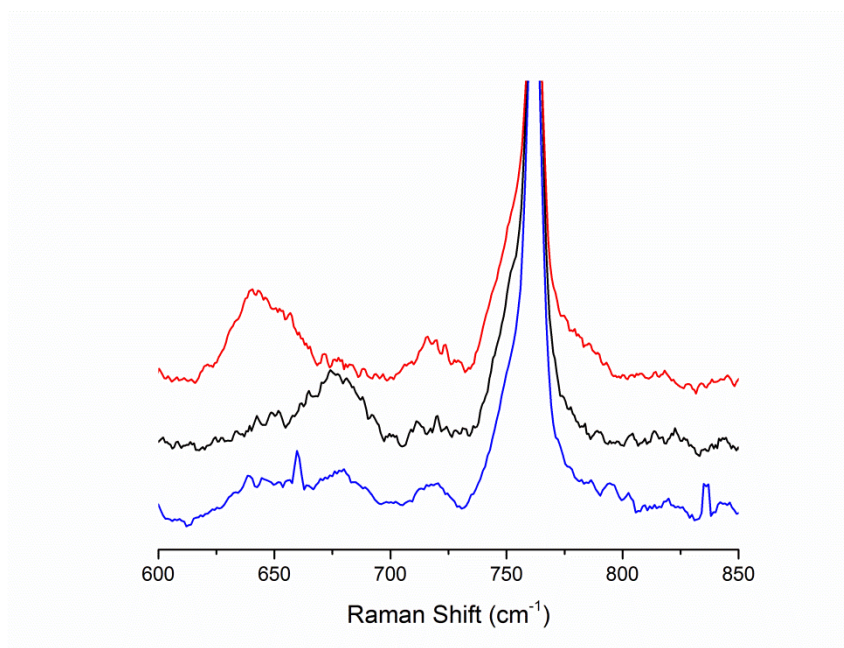
Supplementary Figure 20. Top) Resonance Raman spectra of **3-α** (λ_{ex} 514.5 nm, 140 mW) prepared upon addition of 9 eq. of CAN to a 6-mM solution of **1-α** in 1:1 H_2O:MeCN. $H_2^{16}O$: Black. $H_2^{18}O$: Red. 1:1 $H_2^{16}O$: $H_2^{18}O$: Blue. **Bottom)** Resonance Raman spectra of **3-α** (λ_{ex} 514.5 nm, 140 mW) prepared upon addition of 9 eq. of CAN to a 6 mM solution of **1-α** in 1:1 H_2O:MeCN. 1:1 $H_2^{16}O$: $H_2^{18}O$: Red. Sum of individual $H_2^{16}O$ and $H_2^{18}O$ spectra divided by 2: black.
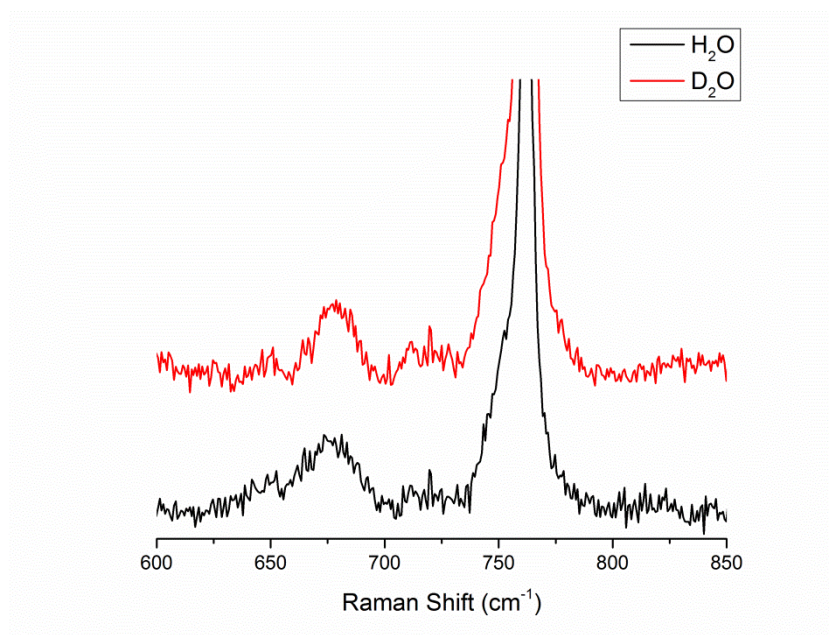
Supplementary Figure 21. Resonance Raman spectra of **3-α** (λ_{ex} 514.5 nm, 140 mW) prepared upon addition of 9 eq. of CAN to a 6 mM solution of **1-α** in 1:1 H_2O:MeCN. H_2O: Black D_2O: Red.
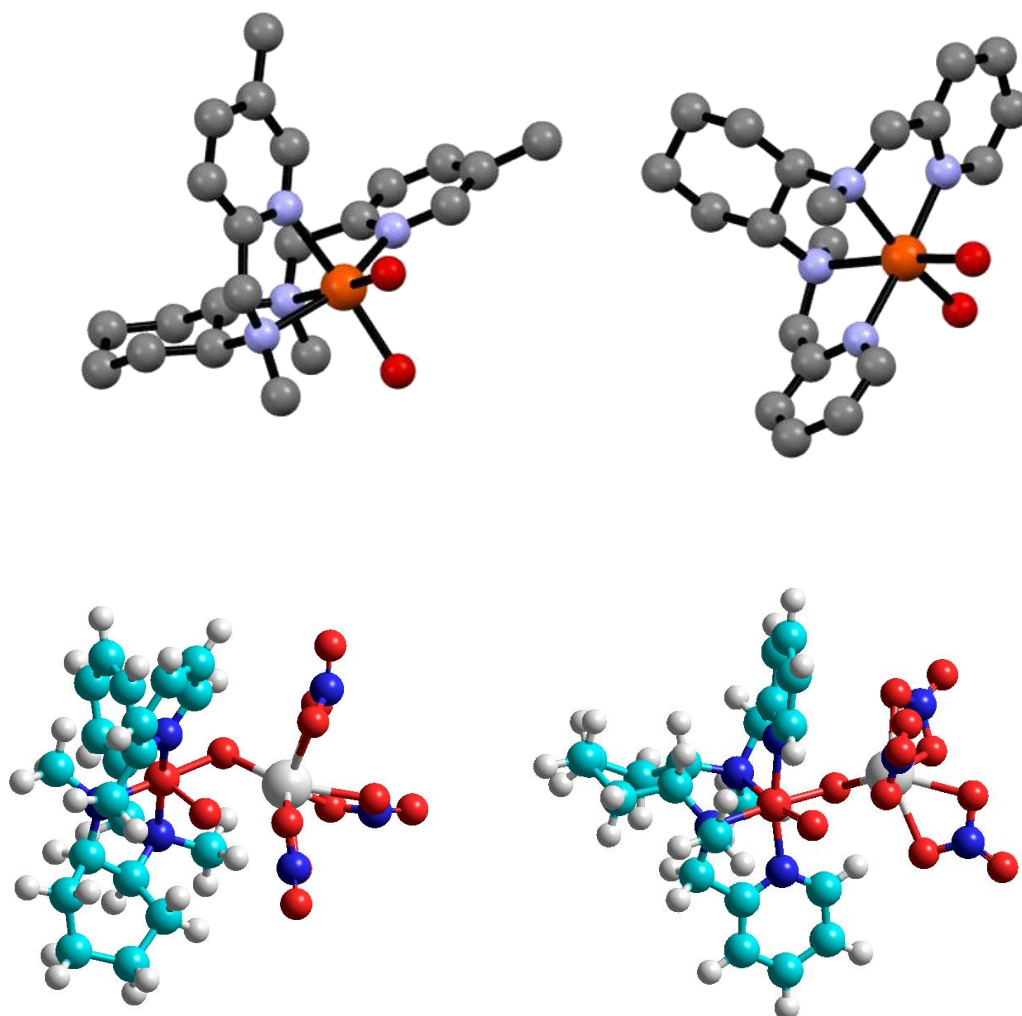
Supplementary Figure 22. Top) Ball and stick models obtained from the XRD structures of **1-β** (left) and 1-α (right). Bottom) Molecular Mechanics models of **3-β** (left) and **3-α** (right).

SI.2 Supplementary References

1. M. Costas, J. Que, L., Ligand Topology Tuning of Iron-Catalyzed Hydrocarbon Oxidations. *Angew Chem. Int. Ed.* **41**, 2179-2181 (2002).
2. M. Costas, A. K. Tipton, K. Chen, D.-H. Jo, L. Que, Modeling Rieske Dioxygenases: The First Example of Iron-Catalyzed Asymmetric cis-Dihydroxylation of Olefins. *J. Am. Chem. Soc.* **123**, 6722-6723 (2001).
3. J. Lloret Fillol, Z. Codolà, I. Garcia-Bosch, L. Gómez, J. J. Pla, M. Costas, Efficient water oxidation catalysts based on readily available iron coordination complexes. *Nat Chem* **3**, 807-813 (2011).
4. Z. Codolà, I. Garcia-Bosch, F. Acuña-Parés, I. Prat, J. M. Luis, M. Costas, J. Lloret-Fillol, Electronic Effects on Single-Site Iron Catalysts for Water Oxidation. *Chemistry – A European Journal* **19**, 8042-8047 (2013).